
Topological Magnon Materials and Transverse Magnon Transport

DISSERTATION ZUR ERLANGUNG DES DOKTORGRADES
DER NATURWISSENSCHAFTEN (DR. RER. NAT.)

der

*Naturwissenschaftlichen Fakultät II
Chemie, Physik und Mathematik*

der

*Martin-Luther-Universität
Halle-Wittenberg*

VORGELEGT VON HERRN

ALEXANDER MOOK
geboren am 26.10.1989 in Magdeburg

Erstgutachterin: Prof. Dr. Ingrid Mertig
Zweitgutachter: Prof. Dr. Steffen Trimper
Drittgutachter: Prof. Dr. Piet Brouwer

Tag der Eröffnung des Promotionsverfahrens: 31.05.2017
Tag der öffentlichen Verteidigung: 9.10.2017
Vorsitzender der Promotionskommission: Prof. Dr. Roland Scheer

The present thesis reports on a theoretical study of fundamental topological properties of magnons. Magnon spectra of two- and three-dimensional magnets are characterized by topological invariants calculated within the framework of linear spin-wave theory. Magnonic counterparts of electronic topological Chern insulators, Weyl semimetals, and nodal-line semimetals are identified. They respectively host topologically protected edge magnons, magnon arcs, and magnon drumhead surface states. It is shown that the nontrivial topology of magnon spectra leads to transverse magnon transport, e. g., a thermal magnon Hall effect. To complement the results obtained in the limit of non-interacting magnons, a method for the computation of the magnon transport properties is developed, which is based on classical atomistic spin dynamics simulations and the Kubo formula. It is applied to the topological magnon insulator Cu(1,3-benzenedicarboxylate) and to skyrmion crystals that exhibit the topological magnon Hall effect.

In dieser Arbeit werden fundamentale topologische Eigenschaften von Magnonen theoretisch untersucht. Die Magnonenspektren zwei- und dreidimensionaler Magneten werden durch topologische Invarianten charakterisiert, die im Rahmen der linearen Spinwellen-Näherung berechnet werden. Magnonische Gegenstücke zu elektronischen topologischen Chern-Isolatoren, Weyl-Semimetallen und Semimetallen mit Knotenlinien werden ermittelt. Ihre jeweiligen Ränder oder Oberflächen weisen topologisch geschützte Randmagnonen, *magnon arcs* und *drumhead*-Zustände auf. Es wird gezeigt, dass die nichttriviale Topologie der Magnonenspektren zu transversalem Transport führt, beispielsweise zu einem thermischen Magnon-Hall-Effekt. Um die Ergebnisse, die im Grenzfall nichtwechselwirkender Magnonen erhalten wurden, zu ergänzen, wird eine Methode zur Berechnung des Magnonentransportes entwickelt, die auf klassischen, atomistischen Spindynamiksimulationen und der Kubo-Formel beruht. Sie wird verwendet, um den transversalen Transport im topologischen Magnon-Isolator Cu(1,3-Benzen-Dicarboxylat) und in Skyrmionkristallen, die den topologischen Magnon-Hall-Effekt aufzeigen, zu untersuchen.

Abstract	i
1. Introduction	1
2. Interacting Spins in the Heisenberg Model	3
2.1. Motivation of the Heisenberg Model	3
2.2. Types of Interactions	4
2.3. Magnetic Ground States and the Luttinger-Tisza Method	6
2.4. Magnetic Excitations: Magnons	8
3. Topology in Magnetism	13
3.1. Berry's Geometrical Phase	13
3.2. Topological Materials and Their Realization by Magnons	15
3.3. Transverse Transport Caused by Nontrivial Topology	23
3.4. Topologically Nontrivial Magnetic Textures: Skyrmions	30
4. Numerical Methods	35
4.1. Magnonic Structure of Semi-infinite Crystals	35
4.2. Monte Carlo Simulations	37
4.3. Stochastic Landau-Lifshitz-Gilbert Equation	40
5. Publications	43
5.1. List of Publications	43
5.2. Thermal Magnon Hall Effect	45
5.3. Three-Dimensional Topological Magnon Materials	63
5.4. Magnon Transport from Atomistic Spin Dynamics Simulations	78
6. Conclusion and Outlook	101
A. Numerical calculation of the skyrmion number	103
List of Publications	115
Curriculum Vitae	117

Electronic and spin-electronic devices respectively utilize the charge and the spin of electrons to transmit information [1]. They rule today's technology in the form of, e. g., complementary metal-oxide-semiconductor (CMOS) integrated circuits [2] and read heads of computer hard drives, the latter based either on the giant [3, 4] or tunnel magnetoresistance [5]. Naturally, for the electron currents to flow, these devices are based on (semi)conductors.

In insulators, however, the electrons are not free to move but bound to the atomic cores. Still, their magnetic moments interact with each other by effective local magnetic fields. This interaction can lead to magnetic ordering below a certain temperature and to spin-wave excitations, whose quanta are quasiparticles. These *magnons* also carry information and, thus, can be utilized in logic devices, which are studied in the research area of spin-electronics in insulators: *magnonics* [6, 7]. Such devices are free of ohmic heating, because there is no flow of electrons, making them very attractive with regard to low waste energy production and power consumption. For their successful engineering, it is necessary to understand the fundamental (transport) properties of magnons.

A relevant question is, for example, whether magnons exhibit transverse transport phenomena similar to those of electrons. For example, electrons show the anomalous (thermal) Hall effect: an electric current through, e. g., a magnetic iron sample leads to a transverse voltage drop [8] and a transverse temperature gradient [9]. On a microscopic level, the transverse conductivities can be related to the geometric properties of the electron Bloch states [10, 11], more precisely, to their "Berry curvature" in reciprocal space [12, 13].

In 2010, Onose *et al.* [14] studied the thermal conductivity of the electric *insulator* $\text{Lu}_2\text{V}_2\text{O}_7$, whose vanadium sublattice is a network of corner-sharing tetrahedra, a pyrochlore lattice [see Fig. 1.1(a)]. Below the Curie temperature $T_C \approx 70$ K the vanadium spins order ferromagnetically. Surprisingly, a nonzero transverse heat conductivity was measured in the ferromagnetic phase [see Fig. 1.1(b)]: applying a temperature gradient leads to a *transverse* temperature gradient. Since both electron and phonon contributions to transverse transport can be ruled out, only magnons come into question as carriers of the transverse heat current [14] [see Fig. 1.1(c)].

This *thermal* Hall effect of magnons was predicted by Katsura *et al.* [15], who showed that spin-orbit interaction in the form of Dzyaloshinskii-Moriya interactions [16, 17] can originate nonzero Berry curvature of the magnon wave functions. As in the case of the anomalous (thermal) Hall effect of electrons, the (intrinsic) transverse thermal conductivity can be related to this Berry curvature [15, 18–21]. Thus, the thermal Hall effect is a transverse transport phenomenon occurring for electrons as well as magnons [22].

Interestingly, the parallel between electrons and magnons does not end here. Zhang *et al.* [23] realized that nonzero Berry curvature must be connected to nontrivial topological invariants of the magnon bulk states. They demonstrated that a ferromagnet on the two-dimensional kagome lattice, which is a (111)-layer of the pyrochlore lattice [red triangles in Fig. 1.1(a)], hosts topologically protected edge magnons. Such modes are known from the quantum Hall effect [24, 25] or from electronic topological Chern insulators, as introduced by Haldane [26]. They unidirectionally revolve the sample; based on that, theoretical ideas to utilize them as beam splitters [27, 28] or a magnonic Fabry-Perot interferometer [27] have been put forward.

Thus, envisioning a future application of topologically protected magnons for magnonic devices calls for a fundamental analysis of *topological magnon materials* and their *transverse magnon transport* properties, an enterprise the present thesis contributes to. The key issues addressed are the following:

- ▷ The topological invariants of electronic Chern insulators are robust against smooth changes of the band structure. Only changes leading to a closing and reopening of a band gap can alter them, i. e., can cause a *topological phase transition*. If the Fermi energy lies within such a band gap, the transverse electric conductivity sharply changes during the transition, because the number of conducting edge channels varies in integer steps. This *quantization* of conductivity is due to the Fermi-Dirac statistics and is, thus, not expected in topological magnon materials: the Bose-Einstein statistics makes *all* states contribute to transport. Thus, the influence of topological phase transitions on transverse *magnon* conductivities is inherently different from the fermionic case.

1. Introduction

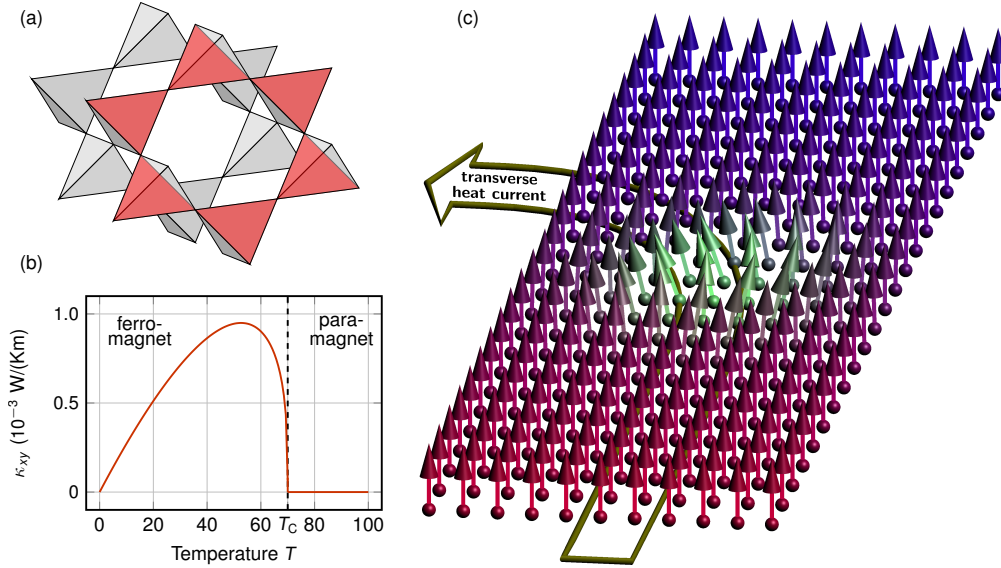


Fig. 1.1.: Thermal magnon Hall effect in the ferromagnetic pyrochlore oxide $\text{Lu}_2\text{V}_2\text{O}_7$. (a) Pyrochlore lattice with a (111)-plane (kagome plane) indicated in red. (b) Sketch of the experimentally measured transverse thermal conductivity κ_{xy} versus temperature (after Ref. [14]); $T_C \approx 70 \text{ K}$ Curie temperature. (c) Simplified picture: a magnon wave packet (greenish spins) propagates from the hot (red) to the cold (blue) side of the ferromagnetic sample and is deflected, resulting in a transverse heat current (bend arrow; exaggerated for visualization).

- ▷ There are electronic topological materials apart from topological Chern insulators, for instance, topological semimetals. One representative of this class, the *Weyl semimetal* [29], hosts singular Berry curvature at the Fermi energy and exhibits a negative magnetoresistance [30, 31]: when applying a magnetic field parallel to the electric field, the electric resistivity drops for increasing magnetic fields [32]. Motivated by such unusual transport properties, it is a natural question to ask for magnon realizations of topological semimetals.
- ▷ In contrast to electrons, which are successfully described as noninteracting particles as long as correlation effects can be neglected, magnons are bosons and their interactions increase with temperature. Thus, the single-particle ansatz and the definition of a Berry curvature are restricted to low temperatures. There are, however, topologically interesting magnetic phases, such as skyrmion lattices, which do not necessarily exist at zero temperature but are stabilized at elevated temperatures. Thus, their magnon transport properties have to be accessed by an approach different from single-particle Berry curvature theory.

This thesis is structured as follows. A brief primer on the Heisenberg model (Sec. 2.1), spin-spin interactions (Sec. 2.2), magnetic ground states (Sec. 2.3), and the theory of magnons (Sec. 2.4) is followed by an introduction to topology in magnetism (Sec. 3). The main ideas of the Berry phase (Sec. 3.1) are the basis for the presentation of selected topological materials: topological Chern insulators (Sec. 3.2.1), Weyl semimetals (Sec. 3.2.2), and nodal line semimetals (Sec. 3.2.3). Thereafter, a dual electrodynamics for magnetic moments in magnetic fields is constructed and an “electron-magnon duality shortcut” is taken to obtain the transverse magnon conductivities within the Boltzmann approach to transport (Sec. 3.3). A discussion of skyrmion crystals and the topological Hall effects of electrons and magnons (Sec. 3.4) closes the chapter on the theoretical background. It is followed by the presentation of the numerical methods (Sec. 4), comprising Green function renormalization (Sec. 4.1), Monte-Carlo (Sec. 4.2) and atomistic spin dynamics simulations (Sec. 4.3).

The results of this thesis are given in form of six original publications *Pubs. 1-6* (Sec. 5), which appeared in peer-reviewed journals (Sec. 5.1). Each of them addresses one of the three aforementioned key issues. They demonstrate, for example, that both temperature and a topological phase transition can lead to a sign reversal of the transverse thermal conductivity (Sec. 5.2), that $\text{Lu}_2\text{V}_2\text{O}_7$ is the magnonic pendant to an electronic Weyl semimetal (Sec. 5.3), and that the transverse transport of magnons can be accessed by atomistic spin dynamics simulations without evaluation of a Berry curvature (Sec. 5.4). A conclusion and an outlook are given in Sec. 6.

A fundamental building block of this work is the Heisenberg model of localized spins [33], which is derived in the following (Sec. 2.1). The introduction of several types of interactions between spins (Sec. 2.2) is followed by the evaluation of the classical ground state by introducing the Luttinger-Tisza method (Sec. 2.3). This chapter closes with the discussion of excitations of magnetically ordered systems: the spin waves or magnons (Sec. 2.4).

2.1. Motivation of the Heisenberg Model

Following a standard textbook on magnetism [34], one begins with the observation that in the absence of a magnetic field the interaction of two indistinguishable electrons of mass m at position \mathbf{r}_1 and \mathbf{r}_2 and with momenta \mathbf{p}_1 and \mathbf{p}_2 , respectively, is described by the Hamiltonian

$$\tilde{H} = \frac{1}{2m} (\mathbf{p}_1^2 + \mathbf{p}_2^2) + V(\mathbf{r}_1, \mathbf{r}_2), \quad (2.1)$$

where $V(\mathbf{r}_1, \mathbf{r}_2)$ is an interaction potential. The following argumentation aims at mapping the spin-independent Hamiltonian (2.1) onto an equivalent Hamiltonian which only includes interactions between spins. Two Hamiltonians are regarded “equivalent”, if they have the same set of eigenfunctions and eigenvalues.

As dictated by the Pauli exclusion principle, no two electrons can occupy the same quantum state. Thus, their respective wave function $|\psi\rangle$ is antisymmetric under electron exchange. $|\psi\rangle$ is a product of a spin-independent position part $|\mathbf{r}\rangle$ and a spin-dependent part $|S; m_S\rangle$, where the total spin S can be 0 or 1 and the magnetic quantum number m_S is an integer within the interval $[-S, S]$. Encoding symmetry by (\pm) , where $+$ ($-$) denotes symmetric (antisymmetric) character, the eigenstates of eq. (2.1) read

$$|\psi_1\rangle^{(-)} = |\mathbf{r}\rangle^{(+)}|0; 0\rangle, \quad \text{and} \quad (2.2)$$

$$|\psi_2\rangle^{(-)} = |\mathbf{r}\rangle^{(-)}|1; m_S\rangle. \quad (2.3)$$

Here, $|0; 0\rangle$ is the antisymmetric singlet state, while $|1; m_S\rangle$ is the symmetric triplet state. Both are multiplied by the position-dependent wave function of the respective opposite symmetric character. \tilde{H} acts only on the positions, giving the corresponding eigenenergies $\epsilon^{(+)}$ and $\epsilon^{(-)}$, respectively,

$$\tilde{H}|\psi_1\rangle^{(-)} = \epsilon^{(+)}|\mathbf{r}\rangle^{(+)}|0; 0\rangle, \quad \text{and}$$

$$\tilde{H}|\psi_2\rangle^{(-)} = \epsilon^{(-)}|\mathbf{r}\rangle^{(-)}|1; m_S\rangle.$$

Now, a new Hamiltonian H is looked for, which provides the same eigenenergies but does not act on the positions. Denoting the operator of spin i by s_i ($i = 1, 2$), one shows [34] that

$$H = J_0 - J_{12}s_1 \cdot s_2, \quad \text{with} \quad J_0 = \frac{1}{4}(\epsilon^{(+)} + 3\epsilon^{(-)}) \quad \text{and} \quad J_{12} = \frac{1}{\hbar^2}(\epsilon^{(+)} - \epsilon^{(-)}), \quad (2.4)$$

is the sought solution: the eigenvalue of s_i reads $s_i^2 = \hbar^2 s_i (s_i + 1) = 3\hbar^2/4$ and that of the total spin $\mathbf{S} = \mathbf{s}_1 + \mathbf{s}_2$ is

$$\mathbf{S}^2 = s_1^2 + s_2^2 + 2s_1 \cdot s_2 = \frac{3}{2}\hbar^2 + 2s_1 \cdot s_2 = \hbar^2 S (S + 1);$$

one obtains

$$s_1 \cdot s_2 = \frac{\hbar^2}{2} S (S + 1) - \frac{3}{4}\hbar^2.$$

2. Interacting Spins in the Heisenberg Model

Thus, the eigenenergy of $|\psi_1\rangle^{(-)}$, which contains the singlet state $|0; 0\rangle$ ($S = 0$), reads

$$H|\psi_1\rangle^{(-)} = |r\rangle^{(+)} H|0; 0\rangle = |r\rangle^{(+)} \left(J_0 + \frac{3}{4} \hbar^2 J_{12} \right) |0; 0\rangle = \epsilon^{(+)} |\psi_1\rangle^{(-)},$$

where eq. (2.4) was used. Similarly, one shows that $H|\psi_2\rangle^{(-)} = \epsilon^{(-)} |\psi_2\rangle^{(-)}$, proving the equivalence of H and \tilde{H} .

The Heisenberg model for localized spins on a lattice is obtained by generalizing H to *all* pairs of spins [33, 35, 36]. Dropping constant terms yields

$$H = - \sum_{ij} J_{ij} \mathbf{s}_i \cdot \mathbf{s}_j, \quad (2.5)$$

where J_{ij} is the exchange integral, which parametrizes the interaction between the i -th and j -th spin. Concerning real materials, the J_{ij} 's can be evaluated by *ab initio* methods (e.g., Refs. [37, 38]). Here, the J_{ij} 's are used as parameters (see *Pubs. 1-4*, and *6*) or experimentally determined values are taken (see *Pub. 5*).

Notice that the generalization that led to eq. (2.5) can also generalize the “spin” operators \mathbf{s}_i to account for both spin *and* orbital degrees of freedom (i.e., the spin magnetic moment and the orbital magnetic moment) [36]. In the following, however, it is not distinguished between the two and the term “spin” is kept.

2.2. Types of Interactions

The generalization of the Heisenberg Hamiltonian does not have to stop at the level of eq. (2.5): one can introduce an interaction matrix l_{ij} between spins i and j , [39, 40]

$$H = \sum_{ij} \mathbf{s}_i^T l_{ij} \mathbf{s}_j, \quad (2.6)$$

with $l_{ij} = l_{ji}^T$, which allows for rich physics; a brief (and by no means exhaustive) overview is provided in the following.

In general, l_{ij} can be decomposed as [41]

$$l_{ij} = \mathbf{J}_{ij} + \mathbf{D}_{ij} + \mathbf{S}_{ij}, \quad (2.7)$$

where \mathbf{J}_{ij} is the isotropic diagonal part (Sec. 2.2.1), \mathbf{D}_{ij} the traceless antisymmetric anisotropic part (Sec. 2.2.2), and \mathbf{S}_{ij} the traceless symmetric anisotropic part (Sec. 2.2.3).

2.2.1. Exchange Interaction and Anisotropy

If $l_{ij} = \mathbf{J}_{ij} = -\text{diag}(J_{ij}, J_{ij}, J_{ij})$, only isotropic symmetric exchange is considered. Assuming all spins equivalent and equally spaced, one has $J_{ij} = J$ for all i and j which are nearest neighbors (indicated by $\langle ij \rangle$), thus

$$H = -J \sum_{\langle ij \rangle} \mathbf{s}_i \cdot \mathbf{s}_j. \quad (2.8)$$

The sign of J determines the favored orientation of neighboring spins, i. e., the magnetic ground state. For $J > 0$ a collinear ferromagnetic alignment is energetically favored, whereas $J < 0$ originates antiferromagnetic ground states. The latter are strongly influenced by the lattice geometry: bipartite lattices allow for the Néel ground state, a collinear configuration where neighboring spins are antiparallel, while nonbipartite lattices cause “frustration” (see textbooks such as Ref. [42]). Frustration is easily understood for three spins arranged on a triangle: each pair of the three spins could be arranged antiparallel, such that the third spin cannot be antiparallel to both of them. Instead of a collinear order, noncollinear order minimizes the total energy in this case. Although the focus of this thesis is on ferromagnets, the subject of frustrated exchange interaction for classical spins is touched in Sec. 2.3 and *Pub. 6*.

While the above already hints at the complexity of spin Hamiltonians, one can further set $l_{ij} = \mathbf{J}_{ij} + \mathbf{S}_{ij} = -\text{diag}(J_{ij}^x, J_{ij}^y, J_{ij}^z)$ to make the symmetric exchange anisotropic; this is *two-ion anisotropy* [39]. In particular, for

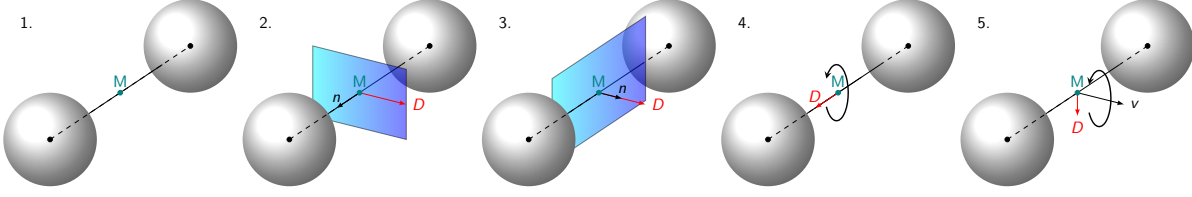


Fig. 2.1.: Moriya's symmetry rules [17] for the determination of the DM vector \mathbf{D}_{ij} (red) between atoms i and j in the presence of (1) an inversion center at M , (2,3) mirror planes through M , and (4,5) rotational axes through M .

$J_{ij}^x = J_{ij}^y = 0$, only the z component of the spins determines the energy, describing the case of the Ising model [43]. If $J_{ij}^z = J^z > 0$, the ferromagnetic state is the ground state but in contrast to the isotropic case the magnetization is forced to point in z direction to minimize energy. Thus, the Hamiltonian of the Ising model lacks the continuous rotational symmetry in spin space.

Furthermore, the exchange interaction can be anisotropic with respect to direction: the interaction in x direction might be different from the interaction in y direction, which is readily understood when considering a rectangular lattice and recalling that the exchange interaction depends on the distance of two spins. Consequences of such a directional anisotropy are addressed in *Pub. 4*.

Another anisotropic contribution is the crystal-field *single-ion anisotropy* (or magnetocrystalline anisotropy) [44]

$$H_{\text{single-aniso}} = \frac{K}{2} \sum_i (\mathbf{s}_i \cdot \hat{\mathbf{n}}_i)^2,$$

where $\hat{\mathbf{n}}_i$ is the unit vector of a local distinguished direction. For $K < 0$, it becomes energetically favorable for the spin to align with the *easy axis* $\pm \hat{\mathbf{n}}_i$. In contrast, for $K > 0$, the case of an *easy-plane* anisotropy is encountered, because the spin avoids the direction $\hat{\mathbf{n}}_i$ and is consequently forced to the plane normal to $\hat{\mathbf{n}}_i$.

2.2.2. Dzyaloshinskii-Moriya Interaction

l_{ij} might contain the skew-symmetric contribution

$$\mathbf{D}_{ij} = \begin{pmatrix} 0 & -D_{ij}^z & D_{ij}^y \\ D_{ij}^z & 0 & -D_{ij}^x \\ -D_{ij}^y & D_{ij}^x & 0 \end{pmatrix},$$

[confer eq. (2.7)] which can be written as

$$H = \sum_{ij} \mathbf{D}_{ij} \cdot (\mathbf{s}_i \times \mathbf{s}_j), \quad (2.9)$$

with $\mathbf{D}_{ij} = (D_{ij}^x, D_{ij}^y, D_{ij}^z)^T$. Such an interaction is known as Dzyaloshinskii-Moriya (DM) interaction [16, 17] and the DM vector \mathbf{D}_{ij} is antisymmetric, i. e., $\mathbf{D}_{ij} = -\mathbf{D}_{ji}$; it favors spin canting due to the cross product in eq. (2.9).

DM interaction (DMI) is derived from second-order perturbation theory for the spin-orbit interaction [17, 45] and relies on broken inversion symmetry. While the magnitude of \mathbf{D}_{ij} has to be estimated from *ab initio* calculations or experiments, its direction can be worked out by Moriya's symmetry rules [17], which are visualized in Fig. 2.1. For two magnetic ions i and j (gray spheres) connected by a vector \mathbf{r} with the midpoint denoted by M , they read:

1. If M is a center of inversion, it is $\mathbf{D}_{ij} = \mathbf{0}$ (see 1. of Fig. 2.1).
2. If M is on a mirror plane with normal $\mathbf{n} \parallel \mathbf{r}$, it is $\mathbf{D}_{ij} \perp \mathbf{r}, \mathbf{n}$ (see 2. of Fig. 2.1).
3. If M is on a mirror plane with normal $\mathbf{n} \perp \mathbf{r}$, it is $\mathbf{D}_{ij} \parallel \mathbf{n}$ (see 3. of Fig. 2.1).
4. If \mathbf{r} is an m -fold rotational axis, it is $\mathbf{D}_{ij} \parallel \mathbf{r}$ (see 4. of Fig. 2.1).
5. If there is a two-fold rotational axis \mathbf{v} passing through M with $\mathbf{v} \perp \mathbf{r}$, it is $\mathbf{D}_{ij} \perp \mathbf{v}, \mathbf{r}$ (see 5. of Fig. 2.1).

DMI is the origin of nontrivial topology in ferromagnets (see Sec. 3.1.2) and chiral skyrmions (see Sec. 3.4).

2. Interacting Spins in the Heisenberg Model

2.2.3. Other Interactions

Under the influence of an external homogeneous magnetic field \mathbf{B} there is an additional contribution to the energy, the so-called Zeeman energy

$$H_{Zee} = -\mathbf{B} \cdot \sum_i \boldsymbol{\mu}_i, \quad (2.10)$$

where $\boldsymbol{\mu}_i$ is the magnetic moment of the i -th spin. If H_{Zee} is added to the Hamiltonian (2.8), the ground state is ferromagnetic ($J > 0$) with the magnetic moments pointing in the direction of \mathbf{B} ¹.

While exchange and DMI are of quantum-mechanical origin, it is also possible to include the effects of the classical dipole-dipole interaction. Its contribution to the interaction matrix is given by (see, e. g., Ref. [46])

$$I_{\text{dd},ij}^{\alpha\beta} = -F_{ij} r_{ij}^3 \frac{3r_{ij}^\alpha r_{ij}^\beta - r_{ij}^2 \delta_{\alpha\beta}}{r_{ij}^5}, \quad \text{with} \quad F_{ij} = \frac{\mu_0 \mu^2}{4\pi r_{ij}^3},$$

where \mathbf{r}_{ij} is the difference vector between the i -th and j -th spin and μ_0 is the permeability of free space. Using typical values for μ ($\sim 1\mu_B$) and r_{ij} ($\sim 1\text{\AA}$), one finds that the energy scale F_{ij} is in the order of μeV , which is much smaller than typical values for the exchange interaction ($> 1\text{ meV}$). Therefore, dipole-dipole interactions and their consequences (e. g., shape anisotropy) are neglected in the following.

The form of eq. (2.6) only comprises bilinear interactions, that is, terms with two spin operators. Interactions including higher orders of spin operators are, for instance, the biquadratic exchange $\propto (\mathbf{s}_i \cdot \mathbf{s}_j)^2$ (e.g., Ref. [47]) and ring exchange (e.g., Ref. [48]). Such interactions are, however, not considered here.

2.3. Magnetic Ground States and the Luttinger-Tisza Method

One center piece of magnetism is the determination of the magnetic ground state, because it determines many relevant properties of the magnetic system; the most obvious example is the presence (or absence) of a net magnetization. Here, the Luttinger-Tisza (LT) method for the determination of the *classical* magnetic ground state for a given spin Hamiltonian is presented and exemplarily applied to a two-dimensional antiferromagnet on a triangular lattice.

Originally, Luttinger and Tisza studied crystals with magnetic dipole-dipole interactions (see Sec. 2.2.3) but they already noted that their method can be generalized to all quadratic interactions (i. e., interactions of the form $\mathbf{s}_i^T \mathbf{I}_{ij} \mathbf{s}_j$) [49]; Luttinger later showed an application to antiferromagnets [50].

In the following, only Bravais lattices and isotropic exchange-only spin Hamiltonians are considered; the most general case of the LT method can be found in the review of Litvin [51]. The starting point is to treat the spin operators as classical (cl) vectors recasting the Hamilton operator as a Hamilton functional

$$H^{\text{cl}} = - \sum_{ij} J_{ij} \mathbf{s}_i^{\text{cl}} \cdot \mathbf{s}_j^{\text{cl}}, \quad (2.11)$$

which has to be minimized under the condition $|\mathbf{s}_i^{\text{cl}}| = s$. Obviously, this is only an approximation to the quantum-mechanical reality, which is, however, reasonable for large s . In the following, the superscript ‘‘cl’’ is dropped to lighten up the notation. A Fourier transformation brings eq. (2.11) to the form

$$H = \sum_q J(\mathbf{q}) \mathbf{s}_q \cdot \mathbf{s}_{-q},$$

with

$$J(\mathbf{q}) = - \sum_{\delta} J(\delta) \exp(-i\mathbf{q} \cdot \delta), \quad (2.12)$$

¹The spin \mathbf{s}_i and the spin magnetic moment $\boldsymbol{\mu} = -g\mu_B \mathbf{s}/\hbar$ are antiparallel (μ_B Bohr’s magneton, and g -factor $g \approx 2$). However, the Zeeman term is often condensed to $H_{Zee} = -\mathbf{B}' \cdot \sum_i \mathbf{s}_i$ for simplicity. Here, $\mathbf{B}' = -g\mu_B \mathbf{B}$ ($\hbar = 1$) is measured in units of energy. Nonetheless, \mathbf{B}' is called the external magnetic field.

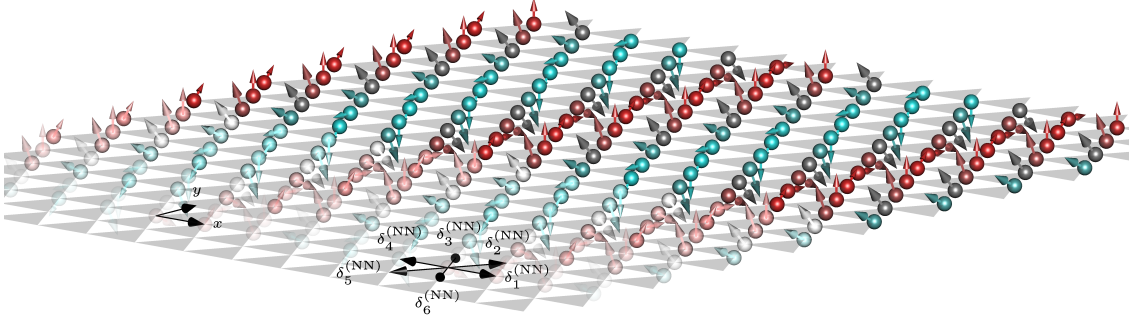


Fig. 2.2.: Spin spiral with a pitch of $\lambda = 7a$ on a triangular lattice with lattice constant a . The vectors to nearest neighbors read $\delta_1^{(NN)} = -\delta_4^{(NN)} = a(1, 0)^T$, $\delta_2^{(NN)} = -\delta_5^{(NN)} = a(1/2, \sqrt{3}/2)^T$, and $\delta_3^{(NN)} = -\delta_6^{(NN)} = a(-1/2, \sqrt{3}/2)^T$. The vectors to third-nearest neighbors are given by $\delta_i^{(3NN)} = 2\delta_i^{(NN)}$ ($i = 1, \dots, 6$).

where δ is a difference vector to an interacting neighboring spin.

If \mathbf{q}_{\min} is the wave vector which minimizes $J(\mathbf{q})$, and the Fourier components $s_{\mathbf{q}_{\min}}$ and $s_{-\mathbf{q}_{\min}}$ are nonzero but all others vanish (that is, $s_{\mathbf{q}} = 0$ for $\mathbf{q} \neq \mathbf{q}_{\min}$), then the Hamilton functional H is minimized. The ground state spin texture can then be determined by an inverse Fourier transformation.

To illustrate the LT method, a two-dimensional triangular lattice with spin Hamiltonian

$$H = -J_1 \sum_{\langle ij \rangle} \mathbf{s}_i \cdot \mathbf{s}_j - J_3 \sum_{\langle\langle ij \rangle\rangle} \mathbf{s}_i \cdot \mathbf{s}_j \quad (2.13)$$

is considered. J_1 (J_3) is the isotropic exchange interaction of nearest (third-nearest) neighbors, which is indicated by $\langle ij \rangle$ and $\langle\langle ij \rangle\rangle$, respectively. This model was featured in Ref. [52] and studied in the context of skyrmions (see Sec. 3.4). It is introduced here, because it is the basis of *Pub. 6*.

With the vectors connecting nearest (NN) and third-nearest neighbors (3NN) shown in Fig. 2.2, eq. (2.12) reads

$$J(\mathbf{q}) = -2 \sum_{i=1}^3 \left[J_1 \cos(\mathbf{q} \cdot \delta_i^{(NN)}) + J_3 \cos(\mathbf{q} \cdot \delta_i^{(3NN)}) \right]. \quad (2.14)$$

Since $J(\mathbf{q})$ inherits the six-fold rotational symmetry of the lattice, the search for the minimum is restricted to the q_x direction ($q_y = 0$). For $J_3 < 0$, minima of $J(\mathbf{q})$ are at

$$q_{x,\min} = \begin{cases} 0 & \text{for } \frac{J_1}{J_3} < -4 & \text{ferromagnet} \\ \frac{2}{a} \arccos \left[\frac{1}{4} \left(1 + \sqrt{1 - \frac{2J_1}{J_3}} \right) \right] & \text{for } -4 < \frac{J_1}{J_3} < 0 & \text{spin spiral} \\ \frac{4}{3a} \pi & \text{for } 0 < \frac{J_1}{J_3} & \text{antiferromagnet} \end{cases}. \quad (2.15)$$

Thus, the magnetic ground state of Hamiltonian (2.13) is a uniform ferromagnetic state ($|\mathbf{q}| = 0$) for $J_1/J_3 < -4$ ($J_3 < 0$), and a spin spiral for $-4 < J_1/J_3 < 0$, whose pitch $\lambda = 2\pi/|\mathbf{q}_{\min}|$ shrinks as J_1/J_3 approaches zero from below (see Fig. 2.2, where a spin spiral with $\lambda = 7a$ is depicted; a lattice constant). Due to the six-fold rotational symmetry the ordering vector \mathbf{q} can point in any nearest-neighbor direction. For $J_1/J_3 > 0$ ($J_3 < 0$), \mathbf{q}_{\min} coincides with the K (and K') points of the hexagonal Brillouin zone; a noncollinear antiferromagnetic phase is formed.

This result is returned to in Secs. 4.2.2 and 5.4.2, where the classical Hamiltonian (2.13) is studied in the context of Monte Carlo simulations and spin dynamics simulations, respectively. It is shown that elevated temperatures and an external magnetic field stabilize a coherent superposition of spin spirals, which is called ‘‘skyrmion lattice’’ (see Sec. 3.4). This magnetic texture possesses nontrivial winding and causes transverse transport phenomena of magnons (see Sec. 3.3).

2.4. Magnetic Excitations: Magnons

While the previous section introduced a *classical* way to determine the ground state, the focus is now on the quantum-mechanical formulation. Once the magnetic ground state is identified, it is possible to analyze low-lying excited states. Here, the isotropic Hamiltonian

$$H = -J \sum_{\langle ij \rangle} \mathbf{s}_i \cdot \mathbf{s}_j \quad (2.16)$$

is considered on a Bravais lattice. When $J > 0$, the spins align parallel, forming the ferromagnetic ground state $|0\rangle$. Note that for a ferromagnet, the quantum-mechanical ground state coincides with the classical ground state [53].

2.4.1. Ferromagnetic Ground State

In quantum mechanics, $|0\rangle$ is a product state built from local eigenstates $|s, s_z\rangle_i$ of the s^2 and s_z operator with maximal s_z eigenvalue s for all lattice sites i : [54]

$$|0\rangle = \bigotimes_i^N |s, s_z = s\rangle_i, \quad s_z |s, s_z = s\rangle_i = s |s, s_z = s\rangle_i$$

($\hbar = 1$). All spins have identical length. To show that $|0\rangle$ is an eigenstate of H , one introduces the ladder operators

$$s_i^\pm = s_i^x \pm i s_i^y,$$

which—owing to the angular momentum algebra $[s_i^\alpha, s_j^\beta] = i\epsilon_{\alpha\beta\gamma} s_i^\gamma \delta_{ij}$ —obey

$$[s_i^+, s_j^-] = 2s_i^z \delta_{ij}, \quad (2.17a)$$

$$[s_i^2, s_j^\pm] = 0, \quad (2.17b)$$

$$[s_i^z, s_j^\pm] = \pm s_i^\pm \delta_{ij}. \quad (2.17c)$$

s_i^\pm are called *ladder* operators, because they increase (+) or decrease (−) the s_z quantum number: [54]

$$s_i^\pm |s, s_z\rangle_i = \sqrt{(s \mp s_z)(s \pm s_z + 1)} |s, s_z \pm 1\rangle_i.$$

Note that $s_i^\pm |s, s_z = s\rangle_i = 0$, which means that the s_z component is maximal. Using

$$s_i^x s_j^x + s_i^y s_j^y = \frac{1}{2} (s_i^+ s_j^- + s_i^- s_j^+)$$

in eq. (2.16), leads to

$$H|0\rangle = -s^2 z J N |0\rangle = E_0 |0\rangle,$$

where $E_0 = -s^2 z J N$ is the ground-state energy (z number of nearest neighbors). Thus, $|0\rangle$ is an eigenstate of H . Furthermore, it has to be the ground state, because any other state with a nonmaximal s_z quantum number for one of the lattice sites has an energy larger than E_0 [54].

2.4.2. One-magnon States

To identify excited states of H , one introduces [54]

$$|r_i\rangle = (2s)^{-1/2} s_i^- |0\rangle,$$

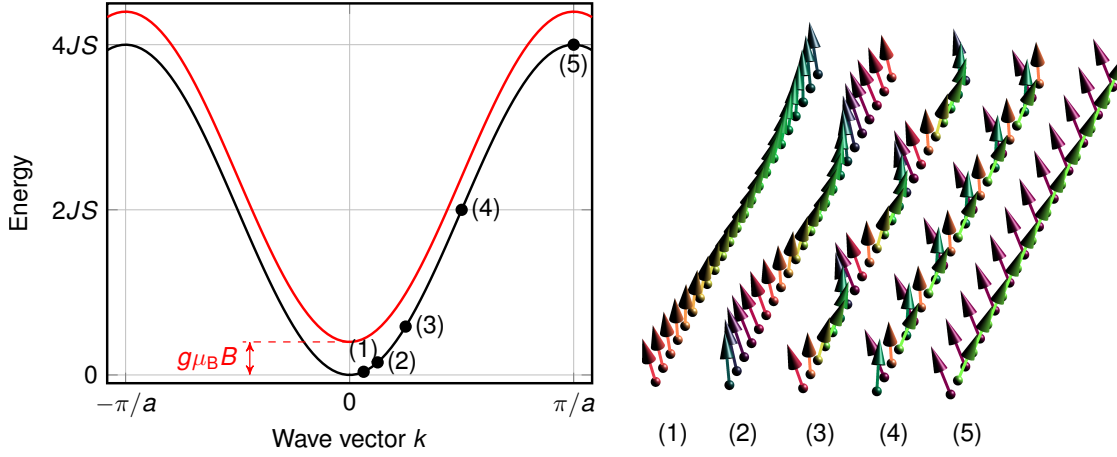


Fig. 2.3.: (Left) Magnon dispersion relation $E(k)$ [eq. (2.19)] of a ferromagnetic chain with lattice spacing a without (black) and with (red) an external magnetic field B , which causes a rigid energy shift of $g\mu_B B$. (1)–(5) Snapshots of spin waves with selected wavenumbers k as indicated in the dispersion relation.

which is a state similar to the ground state but with the s_z quantum number reduced by 1 at the i -th lattice site with position \mathbf{r}_i . Although $|\mathbf{r}_i\rangle$ is not an eigenstate of H , because the action of the term

$$s_j^- s_i^+ |\mathbf{r}_i\rangle = 2s |\mathbf{r}_j\rangle$$

in the Hamiltonian shifts the spin deviation from the i -th to the j -th site, one uses $|\mathbf{r}_i\rangle$ to construct a Bloch sum [54]

$$|\mathbf{k}\rangle = \frac{1}{\sqrt{N}} \sum_i^N \exp(i\mathbf{r}_i \cdot \mathbf{k}) |\mathbf{r}_i\rangle. \quad (2.18)$$

This superposition includes spin deviations on *all* lattice sites, and *is* an eigenstate of H :

$$H|\mathbf{k}\rangle = [E_0 + E(\mathbf{k})] |\mathbf{k}\rangle.$$

Here,

$$E(\mathbf{k}) = Js \sum_{\delta}^z [1 - \cos(\boldsymbol{\delta} \cdot \mathbf{k})] \quad (2.19)$$

is the \mathbf{k} -dependent excitation energy, with z denoting the number of nearest neighbors and the $\boldsymbol{\delta}$'s are the vectors connecting nearest neighbors [54]. Fig. 2.3 shows $E(\mathbf{k})$ (black curve) for a spin chain ($\mathbf{k} \rightarrow k$, $\boldsymbol{\delta} \rightarrow \pm a$, a lattice spacing). For $k \ll \pi/a$, the dispersion is quadratic in k .

To obtain a physical understanding of the quasiparticles described by $|\mathbf{k}\rangle$, one analyzes some expectation values. The s_i^z expectation value [34]

$$\begin{aligned} \langle s_i^z \rangle &= \langle \mathbf{k} | s_i^z | \mathbf{k} \rangle = \frac{1}{N} \sum_{m,n} \exp[i\mathbf{k} \cdot (\mathbf{r}_n - \mathbf{r}_m)] \langle \mathbf{r}_m | s_i^z | \mathbf{r}_n \rangle = \frac{1}{N} \left[\sum_{m=n \neq i} \langle \mathbf{r}_m | s_i^z | \mathbf{r}_n \rangle + \sum_{m=n=i} \langle \mathbf{r}_m | s_i^z | \mathbf{r}_n \rangle \right] \\ &= \frac{1}{N} [(N-1)s + (s-1)] = s - \frac{1}{N} \end{aligned}$$

turns out to be site-independent, which indicates that the quasiparticle is a collective excitation. By construction, the overall spin deviation is 1, which is uniformly distributed over all N spins, and the quasiparticles are *bosons*.

2. Interacting Spins in the Heisenberg Model

Moreover, the expectation value of the transverse correlation [34]

$$\begin{aligned}\langle s_i^\perp s_j^\perp \rangle &= \frac{1}{2} \langle \mathbf{k} | s_i^+ s_j^- + s_i^- s_j^+ | \mathbf{k} \rangle = \frac{1}{2N} \sum_{m,n} \exp[i\mathbf{k} \cdot (\mathbf{r}_n - \mathbf{r}_m)] \left(\underbrace{\langle \mathbf{r}_m | s_i^+ s_j^- | \mathbf{r}_n \rangle}_{2s\delta_{in}\delta_{jm}} + \underbrace{\langle \mathbf{r}_m | s_i^- s_j^+ | \mathbf{r}_n \rangle}_{2s\delta_{jn}\delta_{im}} \right) \\ &= \frac{2s}{N} \cos[\mathbf{k} \cdot (\mathbf{r}_i - \mathbf{r}_j)],\end{aligned}$$

reveals that the angle between the orientation of the transverse spin component of two spins at \mathbf{r}_i and \mathbf{r}_j , respectively, is $\phi = \mathbf{k} \cdot (\mathbf{r}_i - \mathbf{r}_j)$. This pattern reappears after the period $\lambda = 2\pi/|\mathbf{k}|$. This shows that the quasiparticle is like a wave propagating along \mathbf{k} .

Thus, the eigenstate $|\mathbf{k}\rangle$ describes a *spin wave* whose quanta are called *magnons*; $|\mathbf{k}\rangle$ is a *one-magnon* state, because *one* spin deviation is included. It can be classically visualized as precessing spins, where two neighboring spins show a phase difference ϕ [see (1)-(5) in Fig. 2.3]. A spin wave with infinite wavelength (wave vector $\mathbf{k} = 0$, thus $\phi = 0$) is just a reorientation of the ferromagnetic ground state, indicating that a magnon can be excited by an infinitesimal amount of energy [34]. This can also be seen from the magnon energy $E(\mathbf{k})$ in eq. (2.19) that goes to zero as $\mathbf{k} \rightarrow 0$. This is—according to the Nambu-Goldstone theorem [55–57]—a result of the spontaneously broken continuous rotational symmetry of the Hamiltonian (2.16) in the ferromagnetic ground state [58]. The spin Hamiltonian (2.16) is SU(2) symmetric: a global rotation in spin space leaves the Hamiltonian invariant. In contrast, the ferromagnetic ground state possesses only U(1) symmetry, that is, it is invariant under a rotation about the magnetization direction.

However, a U(1)-symmetric Hamiltonian, that is, a spin Hamiltonian that includes a magnetic field or an anisotropy, also features the U(1)-symmetric ferromagnetic ground state, which does not lower the symmetry of the Hamiltonian in this case. The Hamiltonian’s symmetry is *not* broken and a Goldstone mode is *not* expected. For instance, a magnetic field B rigidly shifts the magnon spectrum: $E(\mathbf{k}) \rightarrow E(\mathbf{k}) + g\mu_B B$ (see red curve in Fig. 2.3). This effect is also known as the “freezing” of spins: it costs a finite amount of energy to excite a magnon, because one has to “work against the magnetic field”.

Note that *two-magnon* states are not eigenstates of H , because magnons do not obey the superposition principle. Physically, this is intuitively understood by considering $s = 1/2$ spins, where it is impossible to locate a spin deviation of 2 on a single spin [59]. Thus, magnons interact and repel each other (“kinematic” interaction in the terms of Dyson², see Ref. [60]). Mathematically speaking, the set of two-magnon states is overdetermined and cannot be orthogonalized [59].

2.4.3. Bosonization of Spins

The “spin language” makes working out the magnon excitations for generic spin Hamiltonians very tedious, which comes down to the problem that the commutator of spin operators is itself an operator [61]; see eqs. (2.17a)-(2.17c). A more efficient way of studying magnons was introduced by Holstein and Primakoff [62]. They proposed to map the entirety of spins onto a boson model, where vacuum accounts for the ground state, that is, the absence of magnons. The Holstein-Primakoff (HP) transformation reads [62]

$$s_i^z = s - n_i, \quad s_i^+ = \sqrt{2s} \sqrt{1 - \frac{n_i}{2s}} a_i, \quad s_i^- = \sqrt{2s} a_i^\dagger \sqrt{1 - \frac{n_i}{2s}},$$

where $n_i = a_i^\dagger a_i$ is the magnon number operator. The operators a_i (a_i^\dagger), which annihilate (create) a magnon, obey the boson commutation relations,

$$[a_i, a_j^\dagger] = \delta_{ij}, \quad [a_i^\dagger, a_j^\dagger] = [a_i, a_j] = 0.$$

That s_i^z has the eigenvalues $-s, -s + 1, \dots, s - 1, s$ leads to the constraint $n_i \leq 2s$. It is much easier to work with the boson commutators than with spin commutators, because the former are complex numbers.

The HP transformation, although being exact, comes at a high price because the factors $[1 - n_i/(2s)]^{1/2}$ contain the square root of an operator. However, at low temperatures—which is the case of interest here— $n_i/(2s) \ll 1$,

²Dyson differentiated a “kinematic” from a “dynamical” interaction of magnons, where the latter describes magnon scattering [60].

because n_i , the number of thermally excited magnons, is small. Thus, only the first term of the square root Taylor series is kept and the approximate HP transformation reads

$$s_i^- = s - n_i, \quad s_i^+ \approx \sqrt{2s}a_i, \quad s_i^- \approx \sqrt{2s}a_i^\dagger.$$

Following Refs. [61, 63], this results for a nearest-neighbor spin Hamiltonian (2.16) in

$$H \approx -J \sum_{\langle ij \rangle} [(s - n_i)(s - n_j) + sa_i^\dagger a_j + sa_j a_i^\dagger].$$

The diagonalizable bilinear Hamiltonian $H_{(2)}$, that is, that part of H , in which the boson operators appear in pairs, is found by dropping the term $n_i n_j$, which is a fourth-order term, and the ground state energy $NzJs^2$, which is a zero-order term:

$$H_{(2)} = Js \sum_{\langle ij \rangle} (n_i + n_j - a_i^\dagger a_j - a_j a_i^\dagger).$$

Fourier-transforming the annihilation and creation operators,

$$a_i = \frac{1}{\sqrt{N}} \sum_{\mathbf{k}} \exp(i\mathbf{k} \cdot \mathbf{r}_i) a_{\mathbf{k}}, \quad a_i^\dagger = \frac{1}{\sqrt{N}} \sum_{\mathbf{k}} \exp(-i\mathbf{k} \cdot \mathbf{r}_i) a_{\mathbf{k}}^\dagger,$$

where \mathbf{r}_i is the position of site i , yields

$$H_{(2)} = \frac{Js}{N} \sum_{\langle ij \rangle} \sum_{\mathbf{k}\mathbf{k}'} (\exp[i(\mathbf{k}' - \mathbf{k}) \cdot \mathbf{r}_i] a_{\mathbf{k}}^\dagger a_{\mathbf{k}'} + \exp[i(\mathbf{k}' - \mathbf{k}) \cdot \mathbf{r}_j] a_{\mathbf{k}}^\dagger a_{\mathbf{k}'} \\ - \exp[-i\mathbf{k} \cdot \mathbf{r}_i] \exp[i\mathbf{k}' \cdot \mathbf{r}_j] a_{\mathbf{k}}^\dagger a_{\mathbf{k}'} - \exp[i\mathbf{k} \cdot \mathbf{r}_i] \exp[-i\mathbf{k}' \cdot \mathbf{r}_j] a_{\mathbf{k}} a_{\mathbf{k}'}^\dagger).$$

With $\sum_i^N \exp[i(\mathbf{k} - \mathbf{k}') \cdot \mathbf{r}_i] = N\delta_{\mathbf{k}\mathbf{k}'}$ and $\boldsymbol{\delta} = \mathbf{r}_j - \mathbf{r}_i$ one finds [63]

$$H_{(2)} = \frac{Js}{2} \sum_{\boldsymbol{\delta}} \sum_{\mathbf{k}} (2a_{\mathbf{k}}^\dagger a_{\mathbf{k}} - \exp(i\mathbf{k} \cdot \boldsymbol{\delta}) a_{\mathbf{k}}^\dagger a_{\mathbf{k}} - \exp(-i\mathbf{k} \cdot \boldsymbol{\delta}) a_{\mathbf{k}} a_{\mathbf{k}}^\dagger) = \sum_{\mathbf{k}} E(\mathbf{k}) n_{\mathbf{k}},$$

where

$$E(\mathbf{k}) = Js \sum_{\boldsymbol{\delta}} [1 - \cos(\mathbf{k} \cdot \boldsymbol{\delta})]$$

is the energy of the magnons. Note that $[a_{\mathbf{k}}, a_{\mathbf{k}}^\dagger] = 1$ and the fact that on a Bravais lattice all sites are inversion centers were used [63]. The result is similar to that obtained in Sec. 2.4.2 [see eq. (2.19)], because the bilinear Hamiltonian describes noninteracting magnons (i. e., one-magnon states).

Above, a lattice with one spin per unit cell was considered, but the formalism can be generalized to the case of n spins in the unit cell. One has to keep track of the basis index and rewrite the $a_i \rightarrow a_{\mathbf{r}_i + \mathbf{t}_\mu}$, where \mathbf{r}_i is the vector to the i -th unit cell and \mathbf{t}_μ the basis vector to the μ -th spin in the unit cell ($\mu = 1, \dots, n$). Doing so, $H_{(2)}$ can always be written in the form

$$H_{(2)} = (a_{\mathbf{k},1}^\dagger, \dots, a_{\mathbf{k},n}^\dagger) \mathbf{H}_{\mathbf{k}} \begin{pmatrix} a_{\mathbf{k},1} \\ \vdots \\ a_{\mathbf{k},n} \end{pmatrix},$$

with $a_{\mathbf{k},\mu}$ being the Fourier-transformed annihilation operator on the μ -th basis atom. The linear spin-wave matrix

$$\mathbf{H}_{\mathbf{k}} = \begin{pmatrix} H_{\mathbf{k}}^{11} & \dots & H_{\mathbf{k}}^{1n} \\ \vdots & \ddots & \vdots \\ H_{\mathbf{k}}^{n1} & \dots & H_{\mathbf{k}}^{nn} \end{pmatrix},$$

2. Interacting Spins in the Heisenberg Model

contains the interaction between the μ -th and ν -th spin in the unit cell via its entries $H_k^{\mu\nu} = (H_k^{\nu\mu})^*$. The matrix H_k has n eigenvalues $E_\mu(\mathbf{k})$, the associated eigenvectors $\mathbf{u}_\mu(\mathbf{k})$ are (generalized) one-magnon wavefunctions.

In the course of this thesis the free-magnon picture is used (see *Pubs. 1-4*). It is formally equivalent to the single-particle description of electrons and the wave functions can be studied with respect to topology as is discussed in the following chapter. The formal equivalence to electrons is traced back to the absence of magnon-number nonconserving terms in the bilinear Hamiltonian $H_{(2)}$; terms of the form $a_i a_j$ or $a_i^\dagger a_j^\dagger$ are missing. However, such terms are found in ferromagnets with *elliptical* magnons (where an anisotropy deforms the formerly circular precession) or in non-ferromagnets. In these cases the Hamiltonian looks like a Bogoliubov-de-Gennes Hamiltonian, which is known from superconductivity, and a Bogoliubov-Valatin transformation [64, 65] is necessary to diagonalize the Hamiltonian with respect to the bosonic commutation rules [66]. Although the theory of the following chapters can be generalized to such cases [20, 27], this thesis concentrates on ferromagnets (with circular magnons).

Magnon-magnon interactions, which become important at higher temperatures, can also be treated in the “boson language” by analyzing higher-than-bilinear contributions. Their effect is two-fold: they renormalize the magnon energies and cause a finite-lifetime broadening due to damping [61]. These effects are indirectly addressed in *Pubs. 5*, and *6*. However, due comments on the influence of interactions are given at the appropriate places.

Topology conquered condensed matter physics in the 1980s with the discovery of the quantum Hall effect [25], when Thouless, Kohmoto, Nightingale, and den Nijs found that the quantization of the electrical Hall conductivity could be put in terms of an integer topological invariant [24]. Sir Michael Berry's seminal work on the geometrical phase in quantum mechanics [12] was the decisive factor for understanding topological phenomena in quantum and solid state physics. The Aharonov-Bohm effect [67] could be rephrased in terms of a Berry phase [68], and Zak defined a Berry phase for the dynamics of electrons in periodic solids [13]. This, in combination with Haldane's model [26] (see Sec. 3.2.1) and its extension by Kane and Mele [69], laid the foundation for the concept of topological electronic matter (for instance, topological insulators [70]), a still-growing zoo of materials. The interest in the geometrical (or topological) properties of materials is partly attributed to their spectacular transport properties. For instance, the (intrinsic) anomalous Hall effect [10, 11], which comprises a voltage drop transverse to the direction of electrical current (in the absence of an externally applied magnetic field), can be calculated solely from the electronic Berry phases.

In this chapter, Berry's geometrical phase [12] and its appearance in electronic states [13] (Sec. 3.1.1) is presented, and it is shown how it allows to classify topological Chern insulators (Sec. 3.2.1) and semimetals (Secs. 3.2.2 and 3.2.3). This motivates the search for magnonic equivalents, that is, electrically insulating magnetic materials, whose magnon excitations show the same topological features as their electronic counterparts. Therefore, the Haldane model [26] is discussed in detail and "rebuilt" with localized spins (Sec. 3.2.1). Then, a connection is drawn to transverse transport phenomena: starting from the electronic anomalous transport, results are carried over to magnonic anomalous transport by invoking an "electron-magnon duality" on the single-particle level (Sec. 3.3). Consequently, anomalous magnon transport is also expressed in terms of geometrical properties of the one-magnon wavefunctions.

Finally, the research area of skyrmionics is shortly introduced, which is concerned with topologically nontrivial magnetic "whirls" (Sec. 3.4). The review of the "emergent electrodynamics" for electrons [71, 72] and magnons [73] leads to the discussion of another transverse transport phenomenon: the topological Hall effect. Here, the topological nontriviality of the magnetic texture is the origin of an additional (emergent) magnetic field, which exerts a Lorentz force on the electrons, causing a topological contribution to the Hall effect. These sections lay the theoretical foundation for *Pubs. 1-6*.³

3.1. Berry's Geometrical Phase

3.1.1. Derivation of the Berry Phase and Chern Number

The introduction to the Berry phase tightly follows Berry's original work [12]. Consider a quantum mechanical system described by a Hamiltonian $H(\mathbf{X})$ depending on a parameter \mathbf{X} . The instantaneous discrete basis of the Hilbert space of $H(\mathbf{X})$ are the eigenstates $|n(\mathbf{X})\rangle$ obeying the stationary Schrödinger equation [12]

$$H(\mathbf{X})|n(\mathbf{X})\rangle = E_n(\mathbf{X})|n(\mathbf{X})\rangle, \quad (3.1)$$

with eigenvalues $E_n(\mathbf{X})$. With nondegenerate $E_n(\mathbf{X})$'s, an adiabatic evolution of \mathbf{X} in time t does not allow for an inter-state transition and, consequently, the instantaneous eigenstates of $H[\mathbf{X}(t)]$ read $|n[\mathbf{X}(t)]\rangle$.

The solution of the time-dependent Schrödinger equation

$$H[\mathbf{X}(t)]|\varphi(t)\rangle = i\hbar \frac{\partial |\varphi(t)\rangle}{\partial t} \quad (3.2)$$

³The topic "topology in magnetism" is not exhausted by Sec. 3. "Spin ices" [74, 75] or "spin liquids" [76], subjects with their own notions of topology, remain unconsidered.

3. Topology in Magnetism

takes the form

$$|\varphi(t)\rangle = \exp\left(\frac{i}{\hbar} \int_0^t E_n[\mathbf{X}(t')]\mathrm{d}t'\right) \exp(i\gamma_n(t)) |n[\mathbf{X}(t)]\rangle, \quad (3.3)$$

where the first exponential is the dynamic phase and the second exponential the *geometric* phase. Inserting eq. (3.3) into eq. (3.2) yields [12]

$$\dot{\gamma}_n(t) = i \langle n(\mathbf{X}) | \nabla_{\mathbf{X}} n(\mathbf{X}) \rangle \cdot \dot{\mathbf{X}}(t),$$

which can be integrated along a closed loop C in parameter space,

$$\gamma_n(C) = \oint_C \mathbf{A}_n(\mathbf{X}) \cdot \mathrm{d}\mathbf{X}. \quad (3.4)$$

The integrand

$$\mathbf{A}_n(\mathbf{X}) = i \langle n(\mathbf{X}) | \nabla_{\mathbf{X}} n(\mathbf{X}) \rangle \quad (3.5)$$

is a geometric “vector potential” called *Berry connection*⁴ [12]. Its curl,

$$\mathbf{\Omega}_n(\mathbf{X}) = \nabla_{\mathbf{X}} \times \mathbf{A}_n(\mathbf{X}) = i \langle \nabla_{\mathbf{X}} n(\mathbf{X}) | \times | \nabla_{\mathbf{X}} n(\mathbf{X}) \rangle, \quad (3.6)$$

describes a geometric “magnetic field” dubbed *Berry curvature* [12]. As in electromagnetism, the vector potential is gauge dependent, while the magnetic field is not: the gauge transformation $|n(\mathbf{X})\rangle \rightarrow |n'(\mathbf{X})\rangle = \exp(i\Lambda(\mathbf{X})) |n(\mathbf{X})\rangle$ yields $\mathbf{A}_n(\mathbf{X}) \rightarrow \mathbf{A}'_n(\mathbf{X}) = \mathbf{A}_n(\mathbf{X}) - \nabla_{\mathbf{X}} \Lambda(\mathbf{X})$ but $\mathbf{\Omega}_n(\mathbf{X}) \rightarrow \mathbf{\Omega}'_n(\mathbf{X}) = \mathbf{\Omega}_n(\mathbf{X})$ [12].

A more illustrative expression for Berry’s curvature is obtained by insertion of the completeness relation $1 = \sum_m |m(\mathbf{X})\rangle \langle m(\mathbf{X})|$:

$$\mathbf{\Omega}_n(\mathbf{X}) = i \sum_m \langle \nabla_{\mathbf{X}} n(\mathbf{X}) | m(\mathbf{X}) \rangle \times \langle m(\mathbf{X}) | \nabla_{\mathbf{X}} n(\mathbf{X}) \rangle,$$

which with

$$\langle m(\mathbf{X}) | \nabla_{\mathbf{X}} n(\mathbf{X}) \rangle = \frac{\langle m(\mathbf{X}) | \nabla_{\mathbf{X}} H | n(\mathbf{X}) \rangle}{E_n(\mathbf{X}) - E_m(\mathbf{X})}$$

($m \neq n$) becomes [12]

$$\mathbf{\Omega}_n(\mathbf{X}) = i \sum_{m \neq n} \frac{\langle n(\mathbf{X}) | \nabla_{\mathbf{X}} H | m(\mathbf{X}) \rangle \times \langle m(\mathbf{X}) | \nabla_{\mathbf{X}} H | n(\mathbf{X}) \rangle}{[E_n(\mathbf{X}) - E_m(\mathbf{X})]^2}. \quad (3.7)$$

It can be seen that $\sum_n \mathbf{\Omega}_n(\mathbf{X}) = 0$ and that $\mathbf{\Omega}_n(\mathbf{X})$ is largest, when $[E_n(\mathbf{X}) - E_m(\mathbf{X})]^2$ is small.

By virtue of Stoke’s theorem, one rewrites eq. (3.4) as [77]

$$\gamma_n(C) = \oint_C \mathbf{A}_n(\mathbf{X}) \cdot \mathrm{d}\mathbf{X} = \iint_S \mathbf{\Omega}_n(\mathbf{X}) \cdot \mathrm{d}\mathbf{S} + 2\pi p = \iint_{S'} \mathbf{\Omega}_n(\mathbf{X}) \cdot \mathrm{d}\mathbf{S} + 2\pi p',$$

where S and S' are nonidentical surfaces, whose boundary is the loop C . Berry’s phase is periodic in 2π and, thus, both p and p' are integer (but not necessarily the same). C is the seam of a closed surface \mathcal{S} constructed from surfaces S and S' . Thus, the integral of Berry’s curvature over \mathcal{S} , [77]

$$\begin{aligned} C_n &= \frac{1}{2\pi} \iint_S \mathbf{\Omega}_n(\mathbf{X}) \cdot \mathrm{d}\mathbf{S} \\ &= \frac{1}{2\pi} \left(\iint_S \mathbf{\Omega}_n(\mathbf{X}) \cdot \mathrm{d}\mathbf{S} - \iint_{S'} \mathbf{\Omega}_n(\mathbf{X}) \cdot \mathrm{d}\mathbf{S} \right) = \frac{1}{2\pi} (\gamma_n - 2\pi p - \gamma_n + 2\pi p') = p' - p, \end{aligned} \quad (3.8)$$

is integer. The minus sign between the two integrals reflects the directedness of C . C_n is called *Chern number* of the n -th eigenstate and is—due to its integer nature—a topological invariant: smooth transformations of H leave C_n invariant as long as there are no degeneracies of the n -th state with another state on the integration surface \mathcal{S} [according to eq. (3.7), Berry’s curvature would be singular in this case].

⁴Berry himself did not speak of a “Berry connection”. This phrasing became popular in the publications building on his work.

3.1.2. Berry Phase in Band Structure Theory

Crystalline materials show translational symmetry (quasicrystals excluded) which allows to characterize the single-particle states $\psi_{n,\mathbf{k}}(\mathbf{r})$ by their crystal momentum $\hbar\mathbf{k}$ and to decompose them as

$$\psi_{n,\mathbf{k}}(\mathbf{r}) = \exp(i\mathbf{k} \cdot \mathbf{r}) u_{n,\mathbf{k}}(\mathbf{r})$$

according to the Bloch theorem [54]. $u_{n,\mathbf{k}}(\mathbf{r})$ is lattice periodic and an eigenstate of the \mathbf{k} -dependent Hamiltonian

$$H(\mathbf{k}) \equiv \exp(-i\mathbf{k} \cdot \mathbf{r}) H \exp(i\mathbf{k} \cdot \mathbf{r})$$

with eigenenergy $E_n(\mathbf{k})$ [13]. The kinetic energy term of $H(\mathbf{k})$ reads $(\mathbf{p} + \hbar\mathbf{k})^2/(2m)$, demonstrating the parametric influence of \mathbf{k} . For translationally invariant solids, the crystal momentum \mathbf{k} takes over the role of the parameter \mathbf{X} . The Berry connection and curvature in eqs. (3.5) and (3.6), respectively, read [13]

$$\begin{aligned} \mathbf{A}_n(\mathbf{k}) &= i \langle u_n(\mathbf{k}) | \nabla_{\mathbf{k}} u_n(\mathbf{k}) \rangle, \\ \boldsymbol{\Omega}_n(\mathbf{k}) &= i \langle \nabla_{\mathbf{k}} u_n(\mathbf{k}) | \times | \nabla_{\mathbf{k}} u_n(\mathbf{k}) \rangle \end{aligned}$$

in reciprocal space.

Band structures reflect the symmetry of the crystal. Two major symmetries are space inversion symmetry, also called parity symmetry ($\mathcal{P} : \mathbf{r} \rightarrow -\mathbf{r}$), and time-reversal symmetry ($\mathcal{T} : t \rightarrow -t$), both of which project \mathbf{k} onto $-\mathbf{k}$. Thus, both symmetries require $E_n(\mathbf{k}) = E_n(-\mathbf{k})$, ignoring the spin-degree of freedom. Under time-reversal symmetry, Berry's curvature is an odd function in momentum, $\boldsymbol{\Omega}_n(\mathbf{k}) = -\boldsymbol{\Omega}_n(-\mathbf{k})$, while it is even in the presence of parity symmetry, $\boldsymbol{\Omega}_n(\mathbf{k}) = \boldsymbol{\Omega}_n(-\mathbf{k})$ [78]. Thus, the presence of both \mathcal{T} and \mathcal{P} symmetry renders the curvature zero everywhere [except for band crossings, confer eq. (3.7)].

3.2. Topological Materials and Their Realization by Magnons

A material is considered "topological", if it is characterized by nonzero topological invariants, such as the Chern number [see eq. (3.8)]. Here, several topological materials are introduced, which are known from *electronic* band theory: topological Chern insulators (Sec. 3.2.1), Weyl semimetals (Sec. 3.2.2), and nodal-line semimetals (Sec. 3.2.3). It is demonstrated how to construct analog materials from localized spins, meaning that the respective magnon spectra show the same topological features as their electronic pendants. The following three subsections provide the theoretical background to *Pubs. 1-4*, respectively.

3.2.1. Topological Chern Insulators

The Chern number defined in eq. (3.8) is of particular importance for band structures, because the reciprocal space is periodic in all k -directions. Thus, the Brillouin zone (BZ) is a closed surface *in two dimensions*. The Chern number of band n thus reads [24, 26]

$$C_n = \frac{1}{2\pi} \iint_{\text{BZ}} \Omega_{n,z}(\mathbf{k}) d^2k. \quad (3.10)$$

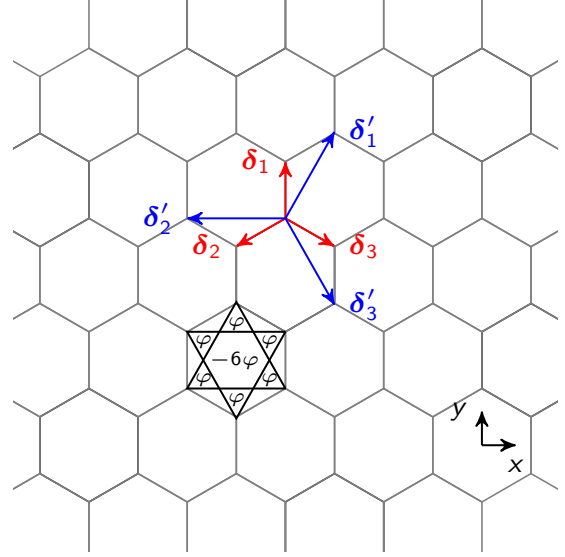
Since Berry's connection only has x and y components in two dimensions, $\Omega_{n,z} = \partial_{k_x} A_{n,y} - \partial_{k_y} A_{n,x}$ is the only nonzero component of the curvature.

Haldane's Model

A very famous minimal model for the analysis of topologically trivial ($C_n = 0 \forall n$) and nontrivial ($C_n \neq 0 \exists n$) band structures is Haldane's model of spinless electrons on a honeycomb lattice [26], which is a staple in the introduction to topological insulators (see Fig. 3.1). It can be considered a minimal graphene tight-binding model, because one orbital per lattice site is taken into consideration, making it a two-band model (graphene has two sublattices $\beta = 1, 2$). Here, the reviews by Fruchart and Carpentier [79], by Cayssol [80], and by Kane [81] are followed.

3. Topology in Magnetism

Fig. 3.1: Haldane's honeycomb-lattice model for a topological Chern insulator. Vectors to nearest δ_i and second-nearest neighbors δ'_i ($i = 1, 2, 3$) are indicated by red and blue arrows, respectively. A textured magnetic flux, which breaks time-reversal symmetry, is indicated by the black kagome-like plaquettes. As in Ref. [79], $\varphi = \phi/2$ for notational simplicity.



The tight-binding Hamiltonian reads

$$H = -t \sum_{\langle ij \rangle} a_i^\dagger a_j, \quad (3.11)$$

where t is the hopping amplitude of nearest neighbors (indicated by $\langle ij \rangle$), and a_i^\dagger (a_i) creates (destroys) a particle at site i . Eq. (3.11) is diagonalized by Fourier transforming these operators, resulting in

$$H = \sum_{\alpha, \beta=1}^2 \sum_{\mathbf{k}} H_{\alpha\beta}(\mathbf{k}) c_{\alpha, \mathbf{k}}^\dagger c_{\beta, \mathbf{k}}, \quad (3.12)$$

with $c_{\beta, \mathbf{k}}$ destroying a mode with wavevector \mathbf{k} on the β sublattice. $H_{\alpha\beta}(\mathbf{k})$ is an element of the Hamilton matrix [81]

$$H(\mathbf{k}) = \mathbf{d}(\mathbf{k}) \cdot \boldsymbol{\sigma}, \quad \text{with} \quad \mathbf{d}(\mathbf{k}) = \begin{pmatrix} -t \sum_{i=1}^3 \cos(\mathbf{k} \cdot \boldsymbol{\delta}_i) \\ -t \sum_{i=1}^3 \sin(\mathbf{k} \cdot \boldsymbol{\delta}_i) \\ 0 \end{pmatrix}. \quad (3.13)$$

Here, $\boldsymbol{\sigma} = (\sigma_x, \sigma_y, \sigma_z)^T$ is the vector of Pauli matrices and $\mathbf{d}(\mathbf{k})$ contains sums over all vectors $\boldsymbol{\delta}$ to nearest neighbors: $\boldsymbol{\delta}_1 = (0, 1)^T$, $\boldsymbol{\delta}_2 = (-\sqrt{3}/2, -1/2)^T$, and $\boldsymbol{\delta}_3 = (\sqrt{3}/2, -1/2)^T$ (red arrows in Fig. 3.1). The form of Hamiltonian (3.13) is generic for two-level systems [79]. Since $\mathbf{d}(\mathbf{k})$ is zero at the K and K' points of the hexagonal Brillouin zone, the two bands [given by the eigenvalues of $H(\mathbf{k})$] are degenerate and form Dirac cones [81] [see Fig. 3.2(a)].

Both parity symmetry and time-reversal symmetry are intact (see Sec. 3.1.2) [79–81]. Parity \mathcal{P} interchanges the sublattices and acts as $\mathcal{P} : (\sigma_x, \sigma_y, \sigma_z) \rightarrow (\sigma_x, -\sigma_y, -\sigma_z)$ [80]. Thus, the parity operation can be written as $\mathcal{P} = \sigma_x$. The Hamiltonian (3.13) is parity-invariant, because $\mathcal{P}H(\mathbf{k})\mathcal{P}^{-1} = H(-\mathbf{k})$.

Time-reversal symmetry (TRS) of spinless electrons takes the wave functions to their complex conjugates and it acts as $\mathcal{T} : (\sigma_x, \sigma_y, \sigma_z) \rightarrow (\sigma_x, -\sigma_y, \sigma_z)$ [80], such that its operation reads $\mathcal{T} = \sigma_0 \mathcal{K}$ (σ_0 is the 2-by-2 unit matrix), where \mathcal{K} denotes complex conjugation. $H(\mathbf{k})$ is time-reversal symmetric, because $\mathcal{T}H(\mathbf{k})\mathcal{T}^{-1} = H(-\mathbf{k})$. Note that this TRS is a pseudospin TRS (sublattice TRS) and not the same as the true TRS for spinful electrons. The latter obeys $\mathcal{T}^2 = -1$ and is responsible for the Kramer's degeneracy of electron bands, while pseudospin TRS obeys $\mathcal{T}^2 = +1$ [80].

The effects of the above symmetries on topology can be studied by analyzing the Berry curvature [79–81]

$$\Omega_{\pm, z}(\mathbf{k}) = \mp \frac{1}{2} \hat{\mathbf{d}}(\mathbf{k}) \cdot \left(\frac{\partial \hat{\mathbf{d}}(\mathbf{k})}{\partial k_x} \times \frac{\partial \hat{\mathbf{d}}(\mathbf{k})}{\partial k_y} \right) \quad (3.14)$$

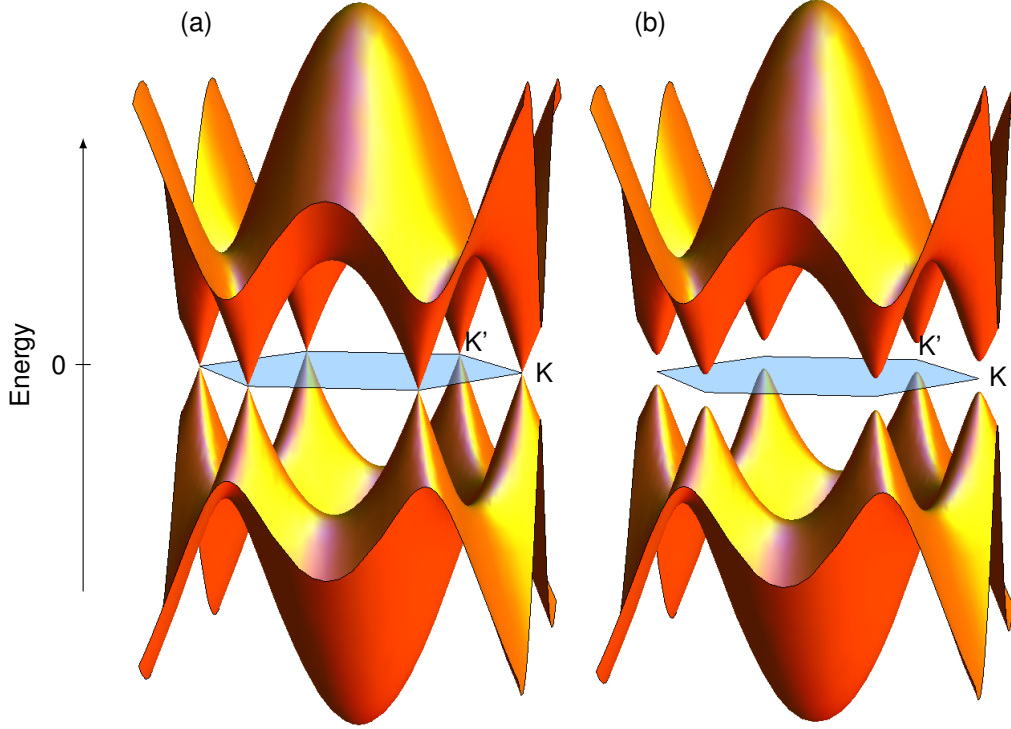


Fig. 3.2.: Electronic band structure of the Haldane model. (a) In the simultaneous presence of parity and time-reversal symmetry, the dispersion exhibits Dirac cones at the K and K' points of the hexagonal Brillouin zone (light blue hexagon). (b) If parity or time-reversal symmetry is broken, the Dirac points are lifted and there is a finite band gap.

in a two-level system, where $+$ ($-$) corresponds to the upper (lower) band. The unit vector $\hat{\mathbf{d}}(\mathbf{k}) = \mathbf{d}(\mathbf{k})/|\mathbf{d}(\mathbf{k})|$ defines a point on a sphere for every \mathbf{k} [except for $\mathbf{d}(\mathbf{k}) = 0$] and is directly connected to the Berry phase that is given by half of the solid angle swept out by $\hat{\mathbf{d}}(\mathbf{k})$ [12, 81]. Using eq. (3.13), one verifies that $\Omega_{\pm,z}(\mathbf{k}) = 0$ [for $\mathbf{d}(\mathbf{k}) \neq 0$]. For $\mathbf{d}(\mathbf{k}) = 0$, Berry's curvature is ill-defined and can have Dirac-delta contributions (confer Sec. 3.2.3).

To lift the Dirac points at the K and K' points [see Fig. 3.2(b)], either one of \mathcal{P} or \mathcal{T} (or both) must be broken by introducing a σ_z mass term in the Hamiltonian (3.13) [81]. \mathcal{P} is lifted by adding a sublattice-asymmetric on-site potential, such that $d_z(\mathbf{k}) = d_z \neq 0$ [81]. However, the resulting band structure is topologically trivial, because $\Omega_{\pm,z}(\mathbf{k}) = -\Omega_{\pm,z}(-\mathbf{k})$ (Chern numbers $C_{\pm} = 0$).

To obtain a topologically nontrivial insulating phase, TRS has to be lifted, which is done by invoking a textured magnetic field which preserves the symmetry of the lattice (see Fig. 3.1) [26, 79–81]. When the electron “hops” from site i to site j , it acquires an Aharonov-Bohm phase ϕ due to the magnetic flux [67, 79]. Hopping in the reversed direction (which is the time-reversed process), the phase is reversed $\phi \rightarrow -\phi$. This introduces a \mathbf{k} -dependent mass [79, 81]

$$d_z(\mathbf{k}) = -t_2 \sin(\phi) \sum_{\delta'} \sin(\mathbf{k} \cdot \delta'), \quad (3.15)$$

where δ' are the vectors to second-nearest neighbors and t_2 is the strength of second-neighbor hopping. $\Omega_{\pm,z}(\mathbf{k}) = \Omega_{\pm,z}(-\mathbf{k})$ becomes an even function in \mathbf{k} , provided that parity symmetry is recovered [otherwise $\Omega_{\pm,z}(\mathbf{k})$ is neither even nor odd]. The Chern numbers $C_{\pm} = \mp \text{sgn}(\sin \phi)$ are nonzero [79], indicating a topologically nontrivial scenario.

3. Topology in Magnetism

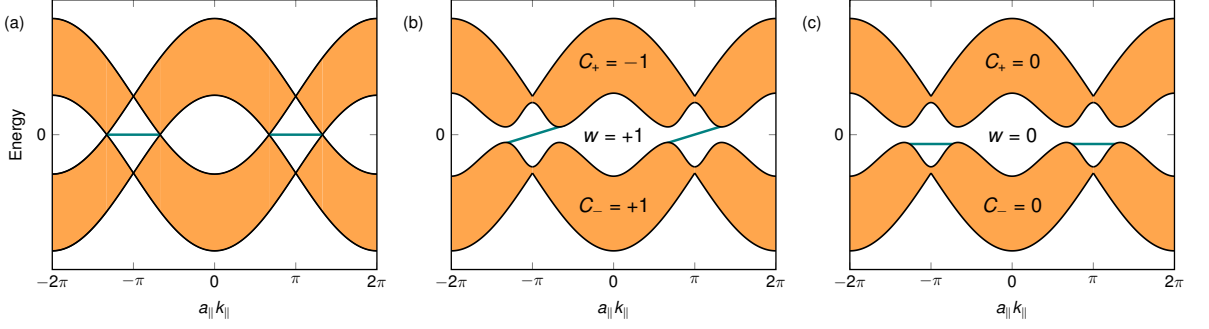


Fig. 3.3.: Bulk-boundary correspondence. Electronic edge spectra at the zig-zag edge of the honeycomb lattice are shown for (a) \mathcal{P} and \mathcal{T} symmetry, (b) \mathcal{P} symmetry, and (c) \mathcal{T} symmetry. Extended orange areas are the projection of the bulk states, while the sharp greenish feature is the edge mode. Chern numbers C_{\pm} and the winding number w are indicated. a_{\parallel} is the lattice constant of, and k_{\parallel} the momentum parallel to the edge unit cell. The edge Brillouin zone spreads from $a_{\parallel}k_{\parallel} = -\pi$ to $+\pi$.

Bulk-boundary Correspondence

Nonzero Chern numbers of the bulk states dictate electronic properties of a boundary, a connection known as *bulk-boundary correspondence*. As rigorously shown by Hatsugai [82, 83], the *winding number* w_i of band gap i ,

$$w_i = \sum_{j \leq i} C_j. \quad (3.16)$$

tells the difference in the number of left-propagating and right-propagating edge states within the i -th band gap. For the Haldane model, there is no band gap when \mathcal{P} and \mathcal{T} symmetry are preserved. The projections of the magnon bulk states onto, for example, the zig-zag edge of the honeycomb lattice, show touching points, which are the projected Dirac points [see orange area in Fig. 3.3(a)]. There is a flat state (green line at zero energy) connecting the Dirac point projections. Its wave function decays exponentially towards the bulk, hence the name *edge mode*.

Breaking \mathcal{T} symmetry leads to a band gap opening and nonzero Chern numbers. The winding number of the band gap is equal to the Chern number of the lower band, $w = C_-$. If the Aharonov-Bohm phase is chosen such that $w = C_- = +1$, one finds that there is one *right*-propagating edge mode (one mode with positive group velocity per edge Brillouin zone), which connects adjacent bulk band projections [see green line in Fig. 3.3(b)]. In the opposite case, $C_- = -1$, there would be one *left*-propagating edge mode (negative group velocity).

A finite Chern-insulator sample is unidirectionally revolved by the topological edge modes. Manipulation of the model's parameter at the edge can change the dispersion of the edge mode, but cannot destroy its topological nature, that is, it will *always* connect adjacent bulk bands and revolve the sample. Furthermore, it is robust against all smooth changes to the Hamiltonian which do not alter the Chern numbers, and, hence, the winding numbers.

Broken \mathcal{P} symmetry also lifts the Dirac cones, but the Chern numbers remain zero. The edge state does not cross the band gap, in agreement with $w = 0$. The edge state clings to the same bulk band projection [see Fig. 3.3(c)].

Haldane's Model "Rebuilt" with Localized Spins

To "rebuild" Haldane's model with localized spins one replaces the electrons by spins. Note that chronologically this was not the first model considered to study topological properties of magnons (see comments at the end of this section), but it makes the equivalence to electrons the most obvious. The following argumentation is based on Refs. [84–86] but rephrased with respect to the above introduced two-level system.

Localized spins on the honeycomb lattice obey the spin Hamiltonian [84, 86]

$$H = -J \sum_{\langle ij \rangle} \mathbf{s}_i \cdot \mathbf{s}_j + \sum_{\langle\langle ij \rangle\rangle} \mathbf{D}_{ij} \cdot (\mathbf{s}_i \times \mathbf{s}_j) - \sum_i \mathbf{B} \cdot \mathbf{s}_i, \quad (3.17)$$

Table 3.1.: Comparison of symmetry-breaking mechanisms for the electronic and magnonic Haldane model.

symmetry	breaking mechanism	
	electrons	magnons
parity \mathcal{P}	sublattice-asym. on-site energy	different spin lengths, fields, or anisotropies
time reversal \mathcal{T}	antisym. next-nearest neighbor hopping	next-nearest neighbor DMI

with nearest neighbor exchange J , second-nearest neighbor DMI with vector $\mathbf{D}_{ij} = (0, 0, D_{ij})^T$, and a magnetic field $\mathbf{B} = (0, 0, B)^T$, which is measured in units of energy (see Sec. 2.2.3).

Since the model is strictly two-dimensional, say, in the xy plane, it is a mirror plane by definition; only z components of the DM vectors are allowed according to the third Moriya rule in Sec. 2.2.2. The honeycomb lattice allows for a second-nearest neighbor DMI, because the midpoint of the second-nearest neighbor bond is no center of inversion (first Moriya rule). A nearest-neighbor DMI is not included, because the midpoint of nearest-neighbor bonds is a center of inversion⁵.

The out-of-plane magnetic field ensures the out-of-plane magnetization in the ferromagnetic ground state, about which the Holstein-Primakoff transformation (see Sec. 2.4.3) is performed. The Hamiltonian (3.17) is rewritten as [84, 86]

$$H_{(2)} = -Js \sum_{\langle ij \rangle} (a_i a_j^\dagger + a_i^\dagger a_j) + is \sum_{\langle\langle ij \rangle\rangle} D_{ij} (a_i a_j^\dagger - a_i^\dagger a_j) + Js \sum_{\langle ij \rangle} (a_i^\dagger a_i + a_j^\dagger a_j) + B \sum_i a_i^\dagger a_i, \quad (3.18)$$

where only the bilinear part $H_{(2)}$ is kept as discussed in Sec. 2.4.3. Comparing $H_{(2)}$ with the electronic tight-binding model, the exchange sum takes over the role of nearest-neighbor hopping [$t = Js$, see eq. (3.11)], while the DMI sum mimics imaginary antisymmetric second-nearest neighbor hopping ($D_{ij} = -D_{ji}$), being the equivalent of the Aharonov-Bohm phase ϕ . The only fundamental differences to the electronic case are the third and fourth sum, which ensure that the magnon spectrum is non-negative. Fourier transforming the boson operators leads to the two-level system Hamiltonian (3.13) [84, 86]

$$H = d_0 \sigma_0 + \mathbf{d}(\mathbf{k}) \cdot \boldsymbol{\sigma}, \quad \text{with} \quad \mathbf{d}(\mathbf{k}) = \begin{pmatrix} -Js \sum_{\delta} \cos(\mathbf{k} \cdot \boldsymbol{\delta}) \\ -Js \sum_{\delta} \sin(\mathbf{k} \cdot \boldsymbol{\delta}) \\ 2Ds \sum_{\delta'} \sin(\mathbf{k} \cdot \boldsymbol{\delta}') \end{pmatrix}. \quad (3.19)$$

The on-site energy enters as $d_0 = B + 3Js$; for the discussion of topology, d_0 can be ignored, because it only rigidly shifts the magnon spectrum and does not change the eigenfunctions. Thus, the situation of the electronic Haldane model is recovered. It is concluded that out-of-plane DMI breaks the TRS of the free-magnon Hamiltonian, causing topologically nontrivial magnon bands. Notice that it is neither the magnetic ordering itself nor the magnetic field which acts as the relevant time-reversal breaking mechanism: without DMI the magnon bands form Dirac cones at the K and K' points, just as for the electrons, and Berry's curvature is zero. To reiterate, TRS breaking means pseudospin TRS breaking.

Although not contained in eq. (3.17), the parity-symmetry breaking asymmetric on-site potential could be obtained either by choosing different spin lengths on the sublattices [85] (a ferrimagnet with $J > 0$ to ensure parallel ordering), by making the magnetic field sublattice-dependent, or by introducing sublattice-dependent single-ion anisotropy (see Sec. 2.2.1). All cases would lead to a k -independent σ_z term. Confer Tab. 3.1 for a comparison of the symmetry-breaking ingredients in the electronic and magnonic Haldane model.

A ferromagnet with a magnon spectrum with nonzero Chern numbers is called a *topological magnon (Chern) insulator* [23] as homage to electronic Chern insulators. It is stressed that the term ‘‘insulator’’ has no physical meaning for magnons (or generally bosons). Here, ‘‘insulator’’ refers to the spectrum featuring band gaps.

Historically, TMIs were discovered by Katsura *et al.* [15] and Zhang *et al.* [23] on the kagome lattice. They respectively demonstrated the existence of nonzero Berry curvature [15] and topological edge magnons [23]. The

⁵However, if the honeycomb lattice was considered the two-dimensional interface of a three-dimensional bulk or was not a mirror plane of a three-dimensional crystal, Rashba-like DMI, that is, in-plane DM vectors, would be allowed for *nearest* neighbors. Such DMI was considered in Ref. [87], but is not accounted for here.

3. Topology in Magnetism

kagome lattice, which is built from corner-sharing equilateral triangles [confer red triangles in Fig. 1.1(a)], has the fundamental advantage that it allows for nearest-neighbor DMI. As noted in Sec. 2.2.2, DMI is a result of spin-orbit coupling and is usually much smaller than the exchange interaction; even more so for further-than-nearest neighbors. Thus, the Haldane model—although being an excellent illustration of the concept—is quite unrealistic for magnons⁶. In contrast, the ferromagnetic kagome model was recently found to be realized by the metal-organic magnet Cu(1,3-benzenedicarboxylate) [89]. Thus, the kagome model was of central interest of the present thesis and it is featured in *Pubs. 1, 2, and 5*.

As demonstrated in Ref. [27], the concept of topological magnon insulators can be generalized to nonferromagnets. Over the years, some theoretical proposals for an experimental realization have been put forward. They feature, for example, magnonic crystals, whose classical dipole-dipole interaction takes over the TRS-breaking role of the DMI [27], or noncoplanar spin textures [90].

3.2.2. Weyl Semimetal

For each closed surface S in three-dimensional reciprocal space, a Chern number can be calculated. If the Berry curvature vector field is divergence free, the Chern integral is zero; there is zero *topological charge*, at which the Berry curvature field lines could start or end. If, however, a Berry curvature monopole is enclosed by S , the Chern number yields nonzero *topological charge* $q = \pm 1$, where the sign differentiates between a source and a sink of Berry curvature. To obtain a Berry curvature monopole, either \mathcal{P} or \mathcal{T} symmetry (or both) must be broken to make Berry's curvature nonzero in the first place, *and* two bands have to touch each other, such that the denominator in eq. (3.7) becomes zero. These touching points are called Weyl points, as proposed in the seminal work of Wan *et al.* [29]⁷. Weyl points carry a topological charge (a nonzero Chern number) and they are robust: smooth perturbations of the Hamiltonian do modify the band structure, but the Weyl points cannot be lifted, because of the associated annihilation of topological charge [29].

Weyl points always come in pairs as indicated in Fig. 3.4 by the red and blue spheres. An intuitive way to see so is as follows. Suppose one wishes to calculate the Chern number over the surface S of the three-dimensional Brillouin zone⁸ (indicated by the cuboid in Fig. 3.4). If the Berry curvature field punctures a surface element of S with normal \mathbf{n} , there is another surface element on S with opposite normal $-\mathbf{n}$ but with the same Berry curvature field due to translational symmetry. Thus, the Chern number integral is zero. Consequently, for each Weyl point with positive topological charge, there exists a Weyl point with negative charge, such that the total topological charge is zero. When smoothly varying the Hamiltonian (by tuning some parameter), the only way to remove the Weyl points is by moving them to the same k point, such that their opposite charges can annihilate [29].

If \mathcal{P} is broken but \mathcal{T} is not, $E(\mathbf{k}) = E(-\mathbf{k})$ and $\mathbf{\Omega}(\mathbf{k}) = -\mathbf{\Omega}(-\mathbf{k})$. Thus, when there is a Weyl point at \mathbf{k} with topological charge q , there is another Weyl point with charge q at $-\mathbf{k}$ [29]. Thus, there must exist another pair of Weyl points, with each point carrying charge $-q$; there are at least *four* Weyl points.

If \mathcal{T} is broken but \mathcal{P} is not, $E(\mathbf{k}) = E(-\mathbf{k})$ and $\mathbf{\Omega}(\mathbf{k}) = \mathbf{\Omega}(-\mathbf{k})$. Thus, each Weyl point at \mathbf{k} with topological charge q has its opposite partner ($-q$) at $-\mathbf{k}$ [29]. The minimal number of Weyl points is *two*, a scenario sketched in Fig. 3.4.

Concerning the topological surface state associated with Weyl points, the argument given in Ref. [29] is reviewed in the following paragraph. Since the Chern number integral only depends on the topological charges enclosed by the surface S , one can choose S cylindric, such that it forms a torus in k space (cylinder in Fig. 3.4). This cylinder describes a two-dimensional subsystem with bands separated by a band gap, because the Weyl point, i. e., the gap closing, does not lie on S . Thus, a Chern number can be calculated for each band of this subsystem, recovering the case of a Chern insulator, discussed in Sec. (3.2.1). Consequently, when introducing an edge to this cylinder (a surface to the three-dimensional crystal), the cylinder forms a loop in the surface Brillouin zone (elliptic loop in Fig. 3.4). This loop encloses the projection of a Weyl point and it can be regarded the edge of a two-dimensional Chern insulator. Thus, one invokes the bulk-boundary correspondence, dictating that there is an

⁶Actually, even the electronic case is far from a solid-state realization. However, an experimental realization was demonstrated in Ref. [88], where ultracold fermionic atoms in a periodically modulated optical honeycomb lattice were studied.

⁷The low-energy physics about a Weyl point at \mathbf{k}_0 obeys the Weyl equation $H_W = E_0\sigma_0 + v_0 \cdot \mathbf{q}\sigma_0 + \sum_{i=1}^3 v_i \cdot \mathbf{q}\sigma_i$. Here, E_0 is the position of the Weyl point in energy, $\mathbf{q} = \mathbf{k} - \mathbf{k}_0$, and the v_i 's are velocities. The 2-by-2 Weyl-Hamiltonian H_W has a cone-like dispersion. In contrast to Dirac fermions, a mass gap cannot be introduced [29].

⁸It is indirectly assumed that all faces are infinitesimally smoothly rounded, such that the normal of the surface is well-defined.

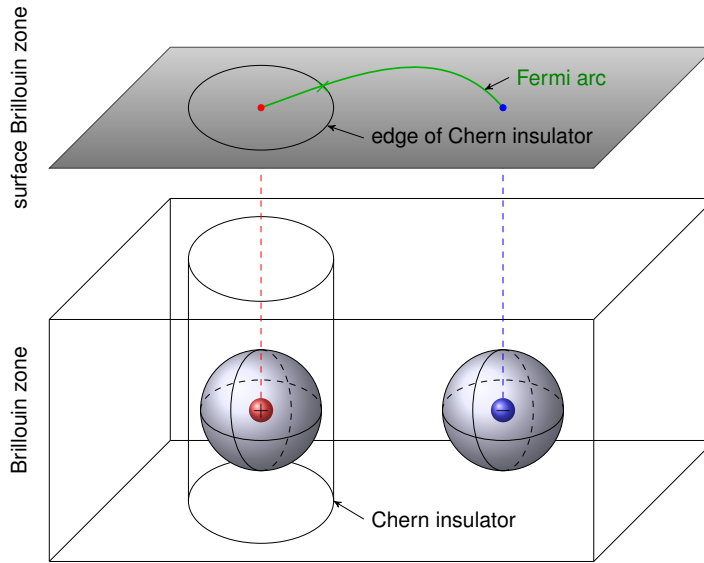


Fig. 3.4.: Weyl points and Fermi arc. The touching points, called Weyl points, of two bulk bands are source or sink of the Berry curvature vector field (red and blue spheres). They always appear in pairs: one Weyl point with positive and one with negative topological charge. A special closed surface enclosing a Weyl point is a cylindric tube, which forms a torus due to the periodicity of the three-dimensional Brillouin zone. Since the Weyl point does not lie on the tube's surface, the cylinder hosts a two-dimensional Chern insulator with a well-defined band gap. When projected onto a surface whose normal is parallel to the tube's axis, the tube forms a loop, encircling the projection of a Weyl point. Due to the bulk-boundary correspondence there must be an edge state crossing the Fermi energy in the band gap on this loop (green cross). This argument can be invoked for any tube and one can trace the crossing point, where the edge state crosses the Fermi energy on the respective loop in the surface Brillouin zone. Connected, these crossing points form a Fermi arc (green line), which starts at a projection of one Weyl point and ends at the projection of an oppositely charged Weyl point.

edge state crossing the band gap on the loop. In particular, this edge state will cross the Fermi energy, which lies within the band gap. In Fig. 3.4 this crossing point is indicated by the green cross. Since this argument is true for every loop, the shape of the cylinder can be varied, allowing to trace the point where the edge state crosses the Fermi energy. When connected, these points form a *Fermi arc*, which starts at the projection of one Weyl point and ends at the projection of an oppositely charged Weyl point.

Over the years, several materials have been proposed to host Weyl points, among the first were $\text{Y}_2\text{Ir}_2\text{O}_7$ [29] and $\text{TlBi}(\text{S}_{1-x}\text{Se}_x)_2$ [91]. In TaAs [92, 93] Weyl points were first experimentally confirmed [94, 95]. Additionally, TaAs was shown to exhibit a negative magnetoresistance due to the chiral anomaly [30, 31]: when applying a magnetic field parallel to the electric field, the electric resistivity drops for increasing magnetic fields in Weyl semimetals as proposed in Ref. [32].

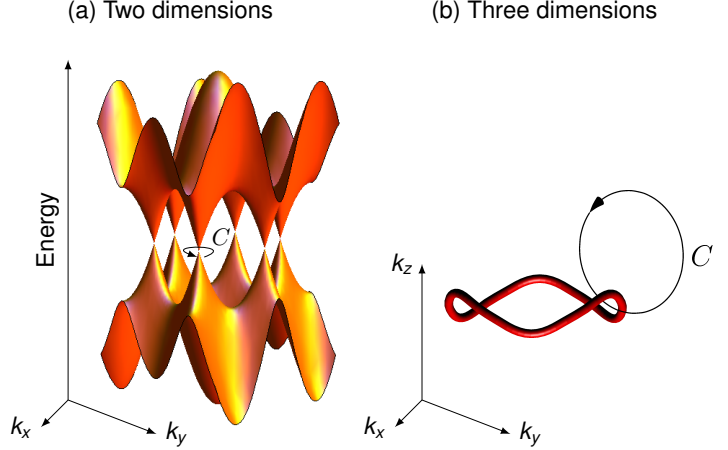
In *Pub. 3* it is demonstrated how to construct a magnon spectrum with Weyl points. To that end, the spin Hamiltonian of a pyrochlore ferromagnet is taken and (pseudo-spin) time-reversal symmetry is broken by introduction of symmetry-allowed DMI. One finds the minimal number of two oppositely charged Weyl points and the associated surface state, a *magnon arc*. The pyrochlore oxide $\text{Lu}_2\text{V}_2\text{O}_7$, which shows the (thermal) magnon Hall effect (see Sec. 1), is proposed to be a “magnon Weyl semimetal”.

3.2.3. Nodal-line Semimetal

A question remains whether the simultaneous presence of parity \mathcal{P} and time-reversal symmetry \mathcal{T} , which renders Berry's curvature zero everywhere, automatically implies a topologically trivial situation. This is not necessarily the case as can be understood from the Haldane model. It was shown that there are Dirac points at the K and K'

3. Topology in Magnetism

Fig. 3.5: Nodes and nodal lines. (a) The two-dimensional spectrum of the Haldane model under simultaneous presence of parity and time-reversal symmetry shows Dirac points, at which the two bands touch each other. The Berry phase over loop C yields π , because C encloses a Dirac point. (b) In three dimensions two bands can touch along a closed line in k -space, forming a *nodal line* (red). The Berry phase over loops interconnected with the nodal line is π .



points if \mathcal{P} and \mathcal{T} are present [see Fig. 3.5(a)]. Thus, closed loops in the two-dimensional Brillouin zone which contain a Dirac point [loop C in Fig. 3.5(a)] are different from those which do not. In the remainder of this section, the meaning of “different” is elaborated by following the review by Fang *et al.* [96], leading to the introduction of nodal-line semimetals.

All closed loops C in the two-dimensional k -space can be classified by a \mathbb{Z}_2 invariant $\nu_n(C)$, which is either 0 or 1 (in contrast, a Chern number is a \mathbb{Z} invariant; it can take all integer values). Here, 0 indicates a topologically trivial situation, while 1 indicates a topologically nontrivial situation. Consider

$$(-1)^{\nu_n(C)} = \exp\left(i \sum_{m \leq n} \gamma_m(C)\right), \quad \text{where} \quad \gamma_m(C) = \iint_S \Omega_m^z(\mathbf{k}) d^2k \quad (3.20)$$

is the Berry phase of the m -th band along the closed loop C ($\partial S = C$). Acting with \mathcal{PT} on $\gamma_m(C)$ yields $-\gamma_m(C)$. Thus, $\gamma_m(C) = -\gamma_m(C) + 2\pi p$ (p integer), when \mathcal{PT} symmetry is present. It follows that $\gamma_m(C) = p\pi$, where $p = 0$ indicates the situation that Berry’s curvature is zero everywhere, while $p \neq 0$ is only possible, if there are p Dirac points enclosed by C , all of which contribute as a δ distribution to the curvature [in Fig. 3.5(a) there is one Dirac point enclosed by C , yielding $p = 1$].

With this result, eq. (3.20) becomes

$$(-1)^{\nu_n(C)} = \exp\left(i\pi \sum_{m \leq n} p_m(C)\right)$$

where $p_m(C)$ counts the number of Dirac points in the m -th band enclosed by C . Thus, $\nu_n(C)$ is either 0 or 1, representing a \mathbb{Z}_2 invariant that characterizes every closed loop C with respect to the n -th band.

This invariant can be extended to three dimensions, classifying loops C in the three-dimensional Brillouin zone [96]. However, a Dirac point is no longer sufficient to make the situation topologically nontrivial. While in two dimensions there is no way to contract C if it encloses a Dirac point, this is obviously possible in three dimensions by contracting C on a plane that does not contain the Dirac point. This argument tells that one needs a one-dimensional “Dirac loop”, which has to be intertwined with C [96] [visualized in Fig. 3.5(b)]. These loops are called *nodal lines* and electronic materials with a nodal line at the Fermi level are *nodal-line semimetals* [96].

If C is not intertwined with a nodal line, the respective $\nu_n(C)$ is zero. If C is intertwined with a nodal line, $\nu_n(C)$ can be 0 (accidental nodal line) as well as 1 (topological nodal line). An accidental nodal line can be lifted by a symmetry-preserving infinitesimally small perturbation, while a topological nodal line cannot [96].

With respect to the bulk-boundary correspondence, it is obvious that \mathcal{P} symmetry is always lifted at a surface, breaking the protecting symmetry of a nodal line. Thus, the bulk-boundary correspondence cannot be applied and there is no dictation of a typical surface state of a bulk nodal line [96]. However, many numerical studies have seen the so-called *drumhead* surface state, a weakly dispersive surface state located in the interior or exterior of the surface projection of the nodal line [96], which is sensitive to the surface termination [97]. A drumhead

surface state can be understood as the generalization of the nondispersive edge mode of the Haldane model in the presence of \mathcal{P} and \mathcal{T} symmetry [see Fig. 3.3(a)].

Note that there are other types of nodal lines, which are protected by mirror symmetry (and are thus forced to appear within the respective mirror planes) [96, 98] or by a screw axis [99] rather than by \mathcal{P} and \mathcal{T} symmetry. Moreover, it was shown experimentally that PbTaSe₂ [100] and ZrSiS [101] are electronic nodal-line semimetals. PbTaSe₂ hosts a doubly-degenerate line node protected by mirror symmetry [100], while ZrSiS features a fourfold-degenerate line node (also called Dirac line node due to spin-degeneracy [86]).

In *Pub. 4* the magnon analog of a nodal-line semimetal is introduced. Considering a ferromagnet on the pyrochlore lattice, the limit of vanishingly small DMI is studied to preserve time-reversal symmetry. Topological and accidental nodal lines are identified and their topological invariants are calculated; the magnon surface spectrum is shown to feature a drumhead surface state. The study of the evolution of the nodal lines upon variation of exchange parameters reveals a topological phase transition from a “closed” nodal line to an “open” nodal line; for the meaning of “closed” and “open”, please confer *Pub. 4*.

3.2.4. Other Topological Materials

There are many other classes of topological materials not covered in this thesis. The most prominent are

- \mathbb{Z}_2 topological insulators, where time-reversal symmetry in the presence of spin-orbit interaction protects “helical” edge states, meaning that the topological edge states of spin-up and spin-down electrons revolve the sample in opposite direction [70],
- topological crystalline insulators without the necessity of spin-orbit interaction, where a crystal symmetry protects topological surface modes [102],
- materials with nonsymmorphic symmetries, which feature “hourglass” fermions [103],
- and topological Dirac semimetals with time-reversal and parity symmetry, which can be understood as Weyl semimetals without broken symmetries. The bands forming the Dirac cone are two-fold spin degenerate, causing a four-fold degeneracy of the Dirac point [104].

Notice that the time-reversal symmetry mentioned here is not the pseudo time-reversal symmetry but that of spinful electrons.

3.3. Transverse Transport Caused by Nontrivial Topology

The history of transverse transport dates back to 1879 when E. Hall discovered a voltage drop across a bar of metal situated in a magnetic field, when an electrical current is flowing along the bar [105]. Today, this phenomenon is known as Hall effect or, more precisely, as the *normal* Hall effect, because Hall also measured the aforementioned voltage drop across a bar of a metal with a magnetization (but without magnetic field) [8]. Due to the lack of the magnetic field, the latter effect is known as *anomalous* Hall effect. While the normal effect can be understood intuitively as a result of the deflection of electrons in the magnetic field (Lorentz force), the anomalous effect remained a mystery for quite some time; please see Ref. [11] for an extensive review of the anomalous Hall effect. In short, it was found by Sundaram and Niu [10] that the idea of Karplus and Luttinger to include an “anomalous velocity” [106] could be elegantly explained in terms of Berry curvature $\mathbf{\Omega}_n(\mathbf{k})$ (n band index) of electron Bloch wave functions (confer Sec. 3.1.2). The equations of motion for an electron wave packet in electromagnetic fields (\mathbf{E} electrical field, and \mathbf{B} magnetic field) thus read [10]

$$\dot{\mathbf{r}} = \frac{1}{\hbar} \frac{\partial \varepsilon_n(\mathbf{k})}{\partial \mathbf{k}} - \dot{\mathbf{k}} \times \mathbf{\Omega}_n(\mathbf{k}), \quad (3.21)$$

$$\hbar \dot{\mathbf{k}} = q\mathbf{E} + q\dot{\mathbf{r}} \times \mathbf{B}, \quad (3.22)$$

where $\mathbf{v}_n(\mathbf{k}) = \hbar^{-1} \partial \varepsilon_n(\mathbf{k}) / \partial \mathbf{k}$ is the group velocity [$\varepsilon_n(\mathbf{k})$ electron energy] and $-\dot{\mathbf{k}} \times \mathbf{\Omega}_n(\mathbf{k})$ the anomalous velocity; $q = -e$ is the electron charge. Notice that the anomalous velocity makes the equations of motion symmetric: the Berry curvature is the \mathbf{k} -space analog of a magnetic field [78].

3. Topology in Magnetism

It can be seen right away that the anomalous velocity causes transverse transport. In two dimensions the wavepacket motion is restricted to the xy plane and $\mathbf{\Omega}_n(\mathbf{k})$ has only an out-of-plane component. Thus, in the presence of an electrical field, the vector resulting from the cross product of $\dot{\mathbf{k}} = \hbar^{-1}q\mathbf{E}$ and $\mathbf{\Omega}_n(\mathbf{k})$ lies in the xy plane and orthogonal to \mathbf{E} .

In the following, the application of the Boltzmann transport equation is reviewed to find expressions for the transverse conductivities in the linear-response limit for electrons (see Sec. 3.3.1). Thereafter, the construction of a dual electrodynamics for magnons is presented, which is utilized to carry over the results from electron to magnon transport (Sec. 3.3.2). On the single-particle level the major difference between electrons and magnons is given by the statistics (Fermi-Dirac versus Bose-Einstein distribution). Thus, as in the case of electrons, the transverse conductivities associated with magnon transport can be calculated from the Berry curvature. A nomenclature of magnon transport phenomena closes this section (Sec. 3.3.2).

3.3.1. Boltzmann Equation and Linear Response Theory

To study transport of an ensemble of particles, the Boltzmann equation is utilized (see, for instance, Refs. [107] and [108]), which is an integro-differential equation for the distribution function $\rho(\mathbf{r}, \mathbf{k}, t)$ depending on space (\mathbf{r}), momentum (\mathbf{k}), and time (t) [108]:

$$\left[\frac{\partial}{\partial t} + \dot{\mathbf{r}} \cdot \frac{\partial}{\partial \mathbf{r}} + \dot{\mathbf{k}} \cdot \frac{\partial}{\partial \mathbf{k}} \right] \rho(\mathbf{r}, \mathbf{k}, t) = \left. \frac{\partial \rho(\mathbf{r}, \mathbf{k}, t)}{\partial t} \right|_{\text{coll}}.$$

$\partial \rho(\mathbf{r}, \mathbf{k}, t) / \partial t|_{\text{coll}}$ denotes a collision term (or ‘‘collision integral’’), which describes scattering processes on impurities or other (quasi-)particles. While the left-hand side follows from the total time derivative of $\rho(\mathbf{r}, \mathbf{k}, t)$, the collision term on the right-hand side is introduced by physical reasoning: only collisions can balance the drift terms on the left-hand side in a steady state [$\partial \rho(\mathbf{r}, \mathbf{k}, t) / \partial t = 0$]. For the evaluation of the collision term, detailed knowledge of the quantum-mechanical scattering processes is necessary in principle. However, restriction to a phenomenological level is possible by invoking the relaxation-time approximation [108]. By decomposing the distribution function $\rho(\mathbf{r}, \mathbf{k}, t) = \rho^0(\mathbf{r}, \mathbf{k}, t) + \delta \rho(\mathbf{r}, \mathbf{k}, t)$ into the local equilibrium distribution $\rho^0(\mathbf{r}, \mathbf{k}, t)$ and a deviation $\delta \rho(\mathbf{r}, \mathbf{k}, t)$, one assumes that the scattering is proportional to the deviation,

$$\left. \frac{\partial \rho(\mathbf{r}, \mathbf{k}, t)}{\partial t} \right|_{\text{coll}} = -\frac{\delta \rho(\mathbf{r}, \mathbf{k}, t)}{\tau(\mathbf{r}, \mathbf{k})}$$

where $\tau(\mathbf{r}, \mathbf{k})$ is the relaxation time. Thus, in a stationary [$\partial \rho(\mathbf{r}, \mathbf{k}, t) / \partial t = 0$] and homogeneous case [$\partial \rho(\mathbf{r}, \mathbf{k}, t) / \partial \mathbf{r} = 0$, and $\tau(\mathbf{r}, \mathbf{k}) = \tau(\mathbf{k})$] it follows

$$\dot{\mathbf{k}} \cdot \frac{\partial \rho(\mathbf{k})}{\partial \mathbf{k}} = -\frac{\delta \rho(\mathbf{k})}{\tau(\mathbf{k})}, \quad (3.23)$$

which is linearized by setting $\rho(\mathbf{k}) \approx \rho^0(\mathbf{k})$. In the absence of a magnetic field, eq. (3.22) yields $\dot{\mathbf{k}} = q\mathbf{E}/\hbar$, leading to

$$\delta \rho = -q\tau \mathbf{E} \cdot \mathbf{v} \frac{\partial \rho^0}{\partial \varepsilon};$$

$\partial \rho^0 / \partial \mathbf{k} = \hbar \mathbf{v} \partial \rho^0 / \partial \varepsilon$ was used and the functional dependencies and band indices were dropped for simplicity.

Defining a (two-dimensional) particle current density $\mathbf{j} = (2\pi)^{-2} \int_{\text{BZ}} \dot{\mathbf{r}} \rho \, d^2k$ and using eq. (3.21), one finds

$$\mathbf{j} = \frac{1}{(2\pi)^2} \int_{\text{BZ}} \dot{\mathbf{r}} (\rho^0 + \delta \rho) \, d^2k = \frac{1}{(2\pi)^2} \int_{\text{BZ}} \left(\mathbf{v} - \frac{q}{\hbar} \mathbf{E} \times \mathbf{\Omega} \right) \left(\rho^0 - q\tau \mathbf{E} \cdot \mathbf{v} \frac{\partial \rho^0}{\partial \varepsilon} \right) d^2k.$$

The integral over $\mathbf{v} \rho^0$ is zero. Considering small electrical fields, that is, terms quadratic in \mathbf{E} are neglected, the current in x -direction reads

$$j_x = -\frac{1}{(2\pi)^2} \int_{\text{BZ}} \left(qv_x^2 \tau E_x \frac{\partial \rho^0}{\partial \varepsilon} + \frac{q}{\hbar} E_y \Omega_z \rho^0 \right) d^2k \quad (3.24)$$

3.3. Transverse Transport Caused by Nontrivial Topology

($\Omega_y = 0$ for a two-dimensional sample in the xy plane). Here, the first term is the “normal” longitudinal transport: an electric field in x direction causes a current in x direction. The second part, however, describes an anomalous Hall effect, because an electric field in y direction causes a transverse current in x direction, provided Ω_z is nonzero and not odd in \mathbf{k} .

For electrons ($q = -e$), the electrical current density $\mathbf{j}^e = -e\mathbf{j}$ obeys Ohm’s law

$$\mathbf{j}^e = \sigma \mathbf{E}, \quad (3.25)$$

where σ is the electrical conductivity tensor. Utilizing eq. (3.24), one can write $j_x^e = \sigma_{xx}E_x + \sigma_{xy}E_y$ to identify the longitudinal conductivity

$$\sigma_{xx} = \frac{e^2}{(2\pi)^2} \sum_{n \in \text{bands}} \int_{\text{BZ}} v_{n,k,x}^2 \tau_{n,k} \left(-\frac{\partial \rho^0}{\partial \varepsilon} \right) \Big|_{\varepsilon = \varepsilon_{n,k}} d^2k, \quad (3.26)$$

and the transverse conductivity

$$\sigma_{xy} = -\frac{e^2}{(2\pi)^2 \hbar} \sum_{n \in \text{bands}} \int_{\text{BZ}} \Omega_{z,n,k} \rho_{n,k}^0 d^2k,$$

where the band indices were recovered.

At zero temperature the equilibrium Fermi-Dirac distribution function $\rho_{n,k}^0$ is the Heaviside function with the step located at the Fermi energy. If the Fermi energy is within the m -th band gap, the integral over Berry’s curvature is the winding number w_m [confer eq. (3.16)]:

$$\sigma_{xy} = -\frac{e^2}{2\pi\hbar} \sum_{n \leq m} \frac{1}{2\pi} \int_{\text{BZ}} \Omega_{z,n,k} d^2k = -\frac{e^2}{h} \sum_{n \leq m} C_n = -\frac{e^2}{h} w_m,$$

where the m -th band is the first band below the Fermi level. Thus, the transverse electrical conductivity is quantized.

Considering thermal transport, one obtains the thermal conductivity and conductivities that connect an electrical current with a temperature gradient ∇T and an electric field with a heat current \mathbf{j}^{th} . The derivation of these *thermoelectric* conductivities can be carried out by the same routine as sketched above [108, 109]. This leads to the linear-response matrix

$$\begin{pmatrix} \mathbf{j} \\ \mathbf{j}^{\text{th}} \end{pmatrix} = \begin{pmatrix} qL_0 & L_1 \\ qL_1 & L_2 \end{pmatrix} \begin{pmatrix} \mathbf{E} \\ -\frac{\nabla T}{T} \end{pmatrix}, \quad (3.27)$$

where the L_i ($i = 0, 1, 2$) are the generalized transport tensors [108]. Without Berry curvature and magnetic field they read

$$L_i = \frac{1}{(2\pi)^2} \sum_{n \in \text{bands}} \int_{\text{BZ}} (\mathbf{v}_{n,k} \mathbf{v}_{n,k}^T) \tau_{n,k} (\varepsilon_{n,k} - \varepsilon_0)^i \left(-\frac{\partial \rho^0}{\partial \varepsilon} \right) \Big|_{\varepsilon = \varepsilon_{n,k}} d^2k$$

in two dimensions (ε_0 chemical potential). By comparison with Ohm’s law in eq. (3.25) one identifies

$$\sigma = q^2 L_0.$$

The thermal conductivity tensor relates the heat current density and a temperature gradient by Fourier’s law

$$\mathbf{j}^{\text{th}} = \kappa (-\nabla T). \quad (3.28)$$

In experiments it is usually measured in the absence of particle current (open boundary conditions), such that accumulated charge creates a counteracting electrical field $\mathbf{E} = L_0^{-1} L_1 \nabla T / (qT) = S \nabla T$; $S = L_0^{-1} L_1 / (qT)$ is the thermopower (or Seebeck coefficient). Thus, the thermal conductivity tensor reads

$$\kappa = \frac{1}{T} (L_2 - qT L_1 S) = \frac{1}{T} (L_2 - L_1 L_0^{-1} L_1). \quad (3.29)$$

An overview over the nomenclature of electronic transport phenomena is provided in Table 3.2.

3. Topology in Magnetism

Table 3.2.: Nomenclature of longitudinal and anomalous transverse electron transport phenomena.

force	electrical current response		thermal current response	
	longitudinal	transverse	longitudinal	transverse
\mathbf{E}	Ohm's law	anomalous Hall effect	Peltier effect	anomalous Ettingshausen effect
∇T	Seebeck effect	anomalous Nernst effect	Fourier's law	anomalous Righi-Leduc effect

Linear Response Theory

In most general terms, transport theory is concerned with a (generalized) response \mathbf{J} (a current) to a (generalized) force \mathbf{F} . For small \mathbf{F} , one keeps only terms linear in \mathbf{F} ,

$$\mathbf{J} \approx L\mathbf{F}$$

(L transport tensor). Such linear-response laws appear quite often, see, for instance, Ohm's law in eq. (3.25) or Fourier's law in eq. (3.28).

While transport phenomena belong to the realm of nonequilibrium thermodynamics, Kubo has shown in 1957 [110] that linear processes close to the thermal equilibrium, that is, when the external perturbing forces are small, can be put in terms of time-correlation functions

$$C(A, B) = \langle A(0)B(t) \rangle, \quad (3.30)$$

evaluated in equilibrium. $\langle \cdot \rangle$ denotes the canonical ensemble average, and A and B are ‘‘molecular’’ properties, e. g., velocities, currents, dipole orientations, *et cetera* [111]. Repeating eq. (3.27) in this context,

$$\begin{pmatrix} \langle \mathbf{j}^e \rangle \\ \langle \mathbf{j}^{\text{th}} \rangle \end{pmatrix} = \begin{pmatrix} L_{11} & L_{12} \\ L_{21} & L_{22} \end{pmatrix} \begin{pmatrix} \mathbf{E} \\ -\frac{\nabla T}{T} \end{pmatrix}, \quad (3.31)$$

the expressions $\langle \mathbf{j}^e \rangle$ and $\langle \mathbf{j}^{\text{th}} \rangle$ are the macroscopically measurable averaged current densities in nonequilibrium. They are related to the instantaneous current densities $\mathbf{j}^e(t)$ and $\mathbf{j}^{\text{th}}(t)$ in equilibrium via the $L_{ij}^{\alpha,\beta}$ ($\alpha, \beta = x, y, z$; $i, j = 1, 2$), which are given by the (classical) Green-Kubo relations [109]

$$L_{11}^{\alpha,\beta} = \frac{1}{k_B T} \int_0^\infty \lim_{V \rightarrow \infty} VC(j_\alpha^e, j_\beta^e) dt, \quad (3.32a)$$

$$L_{12}^{\alpha,\beta} = L_{21}^{\alpha,\beta} = \frac{1}{k_B T} \int_0^\infty \lim_{V \rightarrow \infty} VC(j_\alpha^{\text{th}}, j_\beta^e) dt, \quad (3.32b)$$

$$L_{22}^{\alpha,\beta} = \frac{1}{k_B T} \int_0^\infty \lim_{V \rightarrow \infty} VC(j_\alpha^{\text{th}}, j_\beta^{\text{th}}) dt \quad (3.32c)$$

(V volume of sample). The equivalence of L_{12} and L_{21} is an instance of Onsager's reciprocity relation [111, 112], who rigorously showed that $L_{ij} = L_{ji}$ is true in the absence of time-reversal-symmetry-breaking magnetic fields.

3.3.2. Electron-magnon Duality Shortcut to Magnon Transport

While transverse magnon transport has been predicted in Ref. [15] and its theory was refined in Refs. [18–21], those derivations are not repeated here in detail here. Instead a shortcut to magnon transport in ferromagnets is taken, which is based on the duality of the electrodynamics of a charged particle and the ‘‘dual’’ electrodynamics of a magnetic dipole.

A Dual Electrodynamics for Magnetic Dipoles

The nonrelativistic Hamiltonian of a particle with charge q , momentum \mathbf{p} , and mass m in electromagnetic fields $\mathbf{E} = -\nabla V - \partial_t \mathbf{A}$ and $\mathbf{B} = \nabla \times \mathbf{A}$ is

$$H = \frac{1}{2m} (\mathbf{p} - q\mathbf{A})^2 + qV;$$

V and \mathbf{A} denote the scalar and the vector potential, respectively. In the following, the effects of a magnetic field are neglected, thus,

$$H = \frac{1}{2m} \mathbf{p}^2 + qV. \quad (3.33)$$

The dual situation is studied mostly within the framework of the Aharonov-Casher effect [113], in which a neutral particle with a permanent magnetic dipole $\boldsymbol{\mu}$ is moving in electromagnetic fields. Here, the Zeeman interaction $-\boldsymbol{\mu} \cdot \mathbf{B}$ is considered but the electric field, which would cause a minimal-coupling-like term [114] and the Aharonov-Casher effect [113], is dropped⁹. The remaining Hamiltonian reads

$$H = \frac{1}{2m} \mathbf{p}^2 - \boldsymbol{\mu} \cdot \mathbf{B}. \quad (3.34)$$

Writing the magnetic moment as $\boldsymbol{\mu} = QX\hat{\boldsymbol{\mu}}$ ($\hat{\boldsymbol{\mu}}$ unit vector), in which Q has the unit of electric charge, and X contains everything else, H reads

$$H = \frac{1}{2m} \mathbf{p}^2 + Q(-X\hat{\boldsymbol{\mu}} \cdot \mathbf{B}). \quad (3.35)$$

A comparison with eq. (3.33) suggests to define the ‘‘dual’’ scalar potential $\mathcal{V} = -X\hat{\boldsymbol{\mu}} \cdot \mathbf{B}$, yielding the ‘‘dual’’ electric field $\mathcal{E} = -\nabla\mathcal{V} = X\nabla(\hat{\boldsymbol{\mu}} \cdot \mathbf{B})$. If the (true) electric field \mathbf{E} was kept, there would also appear a dual magnetic field [116]. However, this is not necessary for the anomalous transverse transport of magnons.

Application to Ferromagnetic Insulators

Magnons are electrically neutral quasiparticles with magnetic dipoles. In ferromagnets, the magnon dispersion is quadratic about the Γ point ($\mathbf{k} = \mathbf{0}$), resembling free nonrelativistic electrons. Thus, these magnons obey the single-particle Hamiltonian (3.35) at temperatures well below the ordering temperature, at which magnon-magnon interactions can be neglected [116].

Restricting oneself to uniform ferromagnets with saturation magnetization along \hat{z} [ensured by a magnetic field $\mathbf{B} = (0, 0, B_z)^T$], the magnetic moment of the magnons is in opposite direction; $\hat{\boldsymbol{\mu}} = -\hat{z}$. Thus, the dual electric field reads

$$\mathcal{E} = -X\nabla B_z. \quad (3.36)$$

Furthermore, the magnetic dipole of the magnons is torque-free, because it is antiparallel to \mathbf{B} . Thus, the dynamics is in complete similarity to that of a point charge; the semiclassical equations of motion

$$\dot{\mathbf{r}} = \frac{1}{\hbar} \frac{\partial \varepsilon_n(\mathbf{k})}{\partial \mathbf{k}} - \dot{\mathbf{k}} \times \boldsymbol{\Omega}_n(\mathbf{k}), \quad (3.37)$$

$$\hbar \dot{\mathbf{k}} = Q\mathcal{E}, \quad (3.38)$$

agree with those in eqs. (3.21) and (3.22) without the magnetic contribution to the Lorentz force.

One can now take results for electron transport and replace the electron charge by Q , the (true) electric field by the dual \mathcal{E} , and the Fermi-Dirac by the Bose-Einstein distribution function to obtain the transport phenomena of magnons. Examples are given in the following, using $\mu = QX = g\mu_B$:

1. The equation of motion for $\dot{\mathbf{k}}$ of a magnon wavepacket reads [cf. eqs. (3.36) and (3.38)]

$$\hbar \dot{\mathbf{k}} = q\mathbf{E} \quad \rightarrow \quad \hbar \dot{\mathbf{k}} = Q\mathcal{E} = -QX\nabla B_z = g\mu_B (-\nabla B_z).$$

Obviously, the magnetic-field gradient ‘‘plays the role’’ of an electric field. This can also be understood intuitively by the following consideration. The magnetic field ‘‘freezes out’’ the spins, meaning that a deviation from the spin’s equilibrium orientation costs the more energy the larger the magnetic field. For a sample with a magnetic-field gradient, there is one side with ‘‘stiff’’ spins (larger magnetic field) and another

⁹For a theoretical treatment of anomalous magnetic moments, e. g., the magnetic moment of a spin- $\hbar/2$ particle, see Ref. [115].

3. Topology in Magnetism

side with “loose” spins (smaller magnetic field). This “freezing” effect is equivalent to the rigid energy shift of the magnon spectrum to higher energies (see Fig. 2.3). For the Bose-Einstein distribution function, shifting the spectrum upwards in energy is the same as introducing a negative chemical potential. Thus, the magnetic-field gradient can formally be translated into a chemical-potential gradient, causing magnon diffusion.

2. Rewriting Ohm’s law

$$j_x = \sigma_{xx} E_x \quad \rightarrow \quad j_x = \sigma_{xx} \mathcal{E}_x = X \sigma_{xx} (-\partial_x B_z) = \sigma_{xx}^{\text{mag}} (-\partial_x B_z),$$

the longitudinal magnon conductivity σ_{xx}^{mag} can be derived from the particle conductivity¹⁰ [confer eq. (3.26)]

$$\sigma_{xx} = Q \sum_{n \in \text{bands}} \int_{\text{BZ}} \frac{d^2 k}{(2\pi)^2} \tau_{n,k} v_{x,n,k}^2 \left(-\frac{\partial \rho^0}{\partial \varepsilon} \right) \Big|_{\varepsilon = \varepsilon_{n,k}}$$

(ρ^0 equilibrium Fermi-Dirac distribution function). One finds

$$\sigma_{xx}^{\text{mag}} = X \sigma_{xx} = g \mu_B \sum_{n \in \text{bands}} \int_{\text{BZ}} \frac{d^2 k}{(2\pi)^2} \tau_{n,k} v_{x,n,k}^2 \left(-\frac{\partial \rho^0}{\partial \varepsilon} \right) \Big|_{\varepsilon = \varepsilon_{n,k}}$$

(now, ρ^0 equilibrium Bose-Einstein distribution function). This result is in agreement with those presented in Refs. [117] and [118].

3. The transport tensor elements for the anomalous Hall, Nernst, and Righi-Leduc effect of electrons read [119–121]

$$L_0^{xy} = \frac{Q}{\hbar} C_0, \quad L_1^{xy} = \frac{k_B}{\hbar} T C_1, \quad L_2^{xy} = -\frac{(k_B T)^2}{\hbar} C_2,$$

with

$$C_\nu = \sum_{n \in \text{bands}} \int_{\text{BZ}} \frac{d^2 k}{(2\pi)^2} \Omega_{n,z}(\mathbf{k}) \int_{\varepsilon_{n,k} - \varepsilon_0}^{\infty} \left(\frac{\varepsilon_{n,k}}{k_B T} \right)^\nu \left(-\frac{\partial \rho^0}{\partial \varepsilon} \right) \Big|_{\varepsilon = \varepsilon_{n,k}} d\varepsilon, \quad \nu = 0, 1, 2,$$

and the chemical potential ε_0 . Note that L_0^{xy} and L_1^{xy} are transport tensor elements respectively relating an electrical field and a temperature gradient with the electron *particle* current. The above replacements lead to

$$\begin{Bmatrix} L_0^{xy} \\ L_1^{xy} \\ L_2^{xy} \end{Bmatrix} = \frac{1}{(2\pi)^2 \hbar} \begin{Bmatrix} g \mu_B \\ k_B T \\ -(k_B T)^2 \end{Bmatrix} \int_{\text{BZ}} \Omega_{n,z}(\mathbf{k}) \begin{Bmatrix} c_0 \\ c_1 \\ c_2 \end{Bmatrix} d^2 k \quad (3.39)$$

for magnons ($\varepsilon_0 = 0$), in which

$$\begin{aligned} c_0 &= \rho_{n,k}^0, \\ c_1 &= (1 + \rho_{n,k}^0) \log(1 + \rho_{n,k}^0) - \rho_{n,k}^0 \log(\rho_{n,k}^0), \\ c_2 &= (1 + \rho_{n,k}^0) \log^2 \frac{(1 + \rho_{n,k}^0)}{\rho_{n,k}^0} - \log^2(\rho_{n,k}^0) - 2\text{Li}_2(-\rho_{n,k}^0). \end{aligned}$$

Eq. (3.39) is to be read line by line. These are exactly the formulas for anomalous transverse magnon transport found in Refs. [15, 18–21, 122], where they were derived with greater mathematical expenditure (but also for more general magnets than ferromagnets; see also Ref. [123] for the prediction of a spin-wave Hall effect in frustrated magnets with long-range order¹¹).

¹⁰Particle conductivity and electrical conductivity differ by a factor of q .

¹¹Long-range order is necessary for the magnon approximation to hold. Note that a thermal Hall effect was measured in the electrically insulating “quantum spin ice” $\text{Tb}_2\text{Ti}_2\text{O}_7$ [124], which does not exhibit long-range order. Thus, quasiparticles different from magnons must be responsible.

Matsumoto and Murakami obtained the formula for L_2^{xy} by using the confining-potential “trick” [18–20]. Since magnons are charge-neutral, electromagnetic fields do not exert a force on magnons. Thus, $\hbar\dot{\mathbf{k}} = 0$ in eq. (3.38), when not utilizing the dual electrodynamics. Yet, considering a finite sample, there has to exist a confining potential U preventing the magnons from leaving the sample: $\hbar\dot{\mathbf{k}} = -\nabla U$. Thus, the anomalous velocity $-\dot{\mathbf{k}} \times \boldsymbol{\Omega}_n(\mathbf{k}) = \nabla U \times \boldsymbol{\Omega}_n(\mathbf{k})/\hbar$ only exists at the edges of the sample, where ∇U is sizable; this originates equilibrium magnon edge currents. Consequently, when applying a temperature gradient, the edge current on the hotter side is larger than that on the colder side, leading to a transverse net heat current.

In contrast, Han and coworkers [21, 122] later obtained the formulas in eq. (3.39) from the linear response formalism within the “spin language” (also applicable to paramagnets). They did not formulate equations of motion for magnon wavepackets and there is no such thing as a confining potential. Consequently, there are no magnon edge currents involved in their physical interpretation of transverse magnon transport.

According to eq. (3.39), the transverse conductivities are given by \mathbf{k} -space integrals over Berry’s curvature weighted by c_0 , c_1 or c_2 . As expected, there is no anomalous transverse transport for zero curvature, thus, magnon spectra with simultaneous presence of parity and time-reversal symmetry (e. g., spectra with nodal lines as explained in Sec. 3.2.3) do not feature anomalous Hall-type transport. Similarly, in the presence of time-reversal symmetry but broken parity symmetry, when the curvature is nonzero but odd in \mathbf{k} , the anomalous transport also vanishes, because the integral over $\Omega_{n,z}(\mathbf{k}) c_\nu$ ($\nu = 0, 1, 2$) is zero (the magnon dispersion is even in \mathbf{k})¹².

In contrast, topological magnon insulators (Sec. 3.2.1) and magnon Weyl semimetals (Sec. 3.2.2) with broken time-reversal symmetry exhibit anomalous transport. This is readily clear from the observation that the integral over the unweighted curvature would yield nonzero Chern numbers. However, in contrast to electrons, magnon occupation follows the Bose statistics instead of the Fermi statistics. Thus, a quantization of the transverse transport, which occurs at low temperatures in electric topological insulators when only the edge states contribute to transport, is not expected.

A note on the definition of the thermal conductivity is in order. As defined in eq. (3.29), it consists of a nominal part $\kappa_{\text{nom}} = L_2/T$ and a magnetothermal correction $\kappa_{\text{corr}} = -L_1 L_0^{-1} L_1/T$. For electrons, κ_{corr} is negligibly small [54], because the internal energy scale (defined by the Fermi energy) is usually much larger than the energy scale of temperature. Bosons, however, do not come with such an internal energy scale, which is why the neglect of the magnetothermal correction is under debate. It was argued in Ref. [20] that the nonconserved number of magnons and the corresponding ill-definiteness of their particle current prevent the magnetothermal correction. Contrary arguments were put forward in very a recent work by Nakata *et al.* [126], in which it was shown that only this correction can restore a magnon Wiedemann–Franz law. Additionally, the problem of the definiteness of the spin current was addressed in Ref. [127]. Still, the common practice is to identify the transverse thermal conductivity of magnons as $\kappa_{xy} = \kappa_{\text{nom},xy}$, examples are Refs. [21, 84, 90, 122, 128, 129] and *Pubs. 1*, and 2.

In summary, nonzero Berry curvature of magnon states causes anomalous transverse magnon transport phenomena (please see below for the nomenclature), as is the case for electrons. In *Pub. 1* the transverse thermal transport of magnons in a two-dimensional topological magnon insulator is analyzed, and different topological phases and their influence on the thermal Hall effect of magnons are studied. In particular, a sign change of the Hall transport is predicted. Furthermore, a method to access the transverse magnon transport phenomena without evaluating the Berry curvature is presented in *Pubs. 5*, and 6. Instead, a direct numerical calculation of the Kubo relations (3.32a)–(3.32c) is performed: a cluster of classical spins is evolved according to the stochastic Landau–Lifshitz–Gilbert equation (see Sec. 4.3) and the time-correlation functions of the fluctuating magnetization and heat currents are evaluated.

Nomenclature of Magnon Transport Phenomena

The duality to the transport of electrons suggests a nomenclature of magnon transport phenomena, listed in Table 3.3. Although this nomenclature might be the most exact, there are different conventions in the literature. The most prominent example is the “anomalous magnon Righi–Leduc effect”, i. e., a transverse heat current upon application of a temperature gradient, which is often called “thermal magnon Hall effect” [15] or even “magnon Hall effect” [14]. In the present work, mainly the latter nomenclature is adopted to stay true to the literature.

¹²Note that only the *linear* transverse response vanishes. As shown in Ref. [125], when considering *nonlinear* transport, not the symmetry of the Berry curvature but that of its “dipole” becomes relevant, allowing for nonlinear Hall effects.

3. Topology in Magnetism

Table 3.3.: Nomenclature of magnon transport phenomena derived from their analogs in electron transport. Each phenomenon gets the specifier “magnon” to indicate the carrier.

force	magnetization current		thermal current	
	longitudinal	transverse	longitudinal	transverse
∇B_z	Ohm’s law	anomalous Hall	Peltier	anomalous Ettingshausen
∇T	Seebeck	anomalous Nernst	Fourier’s law	anomalous Righi-Leduc

However, there arises the problem of naming the effect describing a transverse magnetization current due to an applied magnetic-field gradient (“anomalous magnon Hall effect” in Tab. 3.3), because “magnon Hall” is already assigned in the alternative nomenclature scheme in Table 3.4. One could name this effect “magnon spin Hall effect” to stress the transport of spin (or magnetization). Yet, this phenomenon has nothing to do with the spin Hall effect of electrons. This became a problem after the discovery of the “magnon spin Nernst effect” [130, 131], which indeed is related to the spin Hall effect of electrons.

In summary, the developing field of magnon transport phenomena has no fully consistent nomenclature. In the following and, in particular, in *Pubs. 1-6* the nomenclature in Table 3.4 is used; additionally, all effects under consideration are introduced to avoid confusion or ambiguity.

3.4. Topologically Nontrivial Magnetic Textures: Skyrmions

Topology enters magnetism in various ways, not only as a k -space Berry curvature. In recent years, *skyrmions* have become a major research field; these are particle-like magnetic textures with nontrivial winding. The name “skyrmion” has been borrowed from nuclear physics, for which T. Skyrme postulated stable topological soliton solutions related to baryons in the 1960s [132–135]. About 30 years later Bogdanov and Yablonskii showed that topological solitons are thermodynamically stable solutions of chiral magnets [136]. Finally, a skyrmion lattice—a regular array of skyrmions—was found in the A phase of the metal MnSi [137]. Since then, several materials with a skyrmion crystal phase have been identified, amongst others, the insulating compound Cu_2OSeO_3 [138]. From the perspective of magnon transport, the latter is particularly interesting, because the transport of electrons (which dominates over the magnon transport in metallic skyrmion crystals) can be ruled out.

The topological triviality or nontriviality of a magnetic texture $\mathbf{m}(\mathbf{r})$ of “hard” spins [$|\mathbf{m}(\mathbf{r})| = m$] is determined by the winding number (also called “skyrmion number” or “topological charge”) [139]

$$w = \frac{1}{4\pi} \frac{1}{m^3} \iint_{\mathbb{R}^2} \mathbf{m}(\mathbf{r}) \cdot \left[\frac{\partial \mathbf{m}(\mathbf{r})}{\partial x} \times \frac{\partial \mathbf{m}(\mathbf{r})}{\partial y} \right] dx dy, \quad (3.40)$$

which is integer. Since $\hat{\mathbf{m}}(\mathbf{r}) = \mathbf{m}(\mathbf{r})/m$ defines a point on a sphere, w measures how often $\hat{\mathbf{m}}(\mathbf{r})$ “winds” (or wraps) around the sphere, exactly as in the case of the $\hat{\mathbf{d}}(\mathbf{k})$ vector for a two-level system [see eq. (3.14)]. Thus, the topological charge w of a skyrmion is nothing but a real-space Chern number (or the topological charge of a Weyl point, see Sec. 3.2.2) and

$$B(\mathbf{r}) = \frac{1}{2} \hat{\mathbf{m}}(\mathbf{r}) \cdot \left[\frac{\partial \hat{\mathbf{m}}(\mathbf{r})}{\partial x} \times \frac{\partial \hat{\mathbf{m}}(\mathbf{r})}{\partial y} \right] \quad (3.41)$$

Table 3.4.: Alternative nomenclature of magnon transport phenomena derived from the transported quantity. Each phenomenon is “tagged” the specifier “magnon” to indicate the carrier.

force	magnetization current		thermal current	
	longitudinal	transverse	longitudinal	transverse
∇B_z	Ohm’s law	spin Hall	spin Peltier	spin Ettingshausen
∇T	spin Seebeck	spin Nernst	Fourier’s law	(thermal) Hall

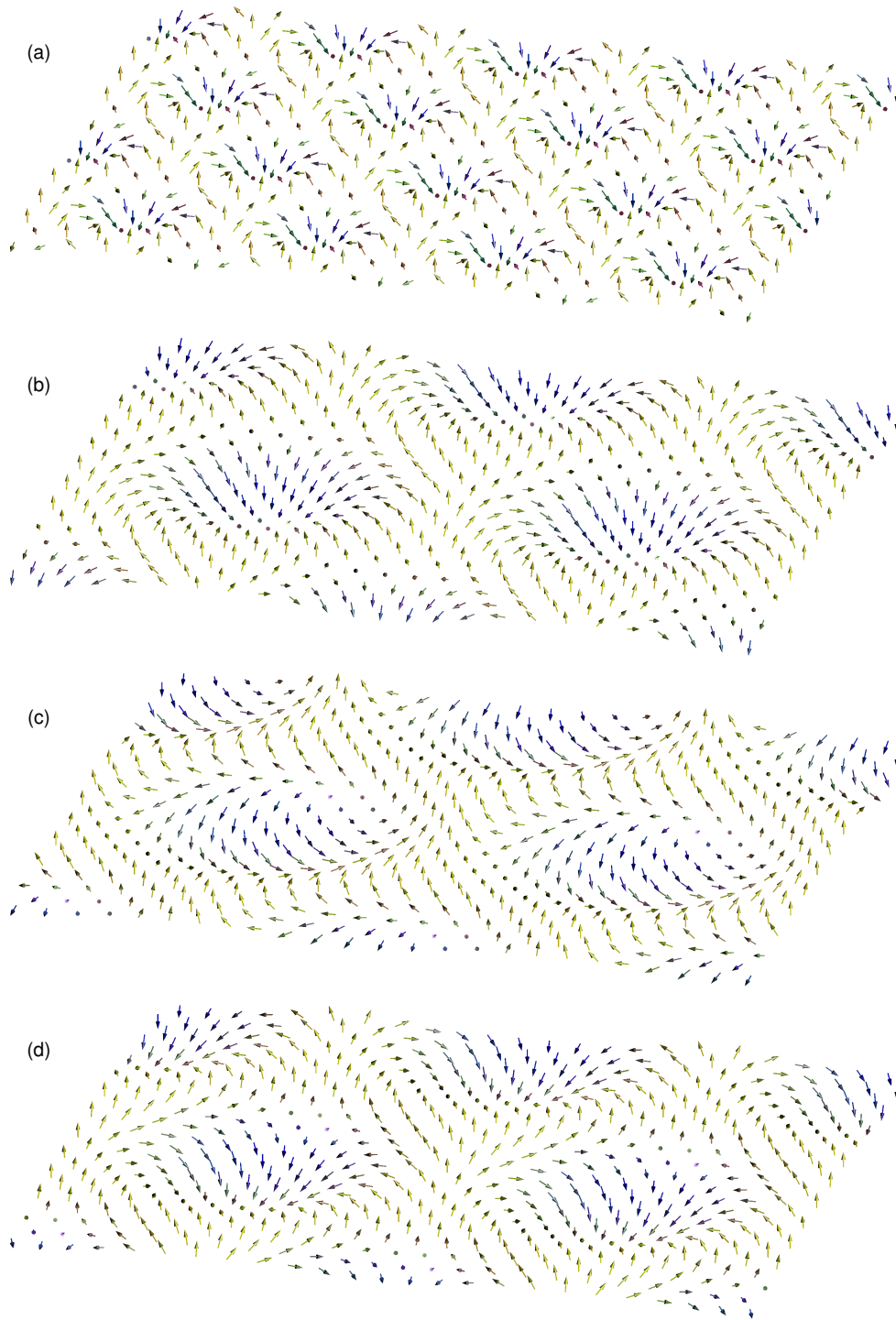


Fig. 3.6.: Two-dimensional skyrmion lattices—superposition of three spin spirals; every pair of spiral ordering vectors forms an angle of 120° . Each magnetic unit cell carries a unit of topological charge [see eq. (3.40)]. (a) Small Néel-type skyrmions. (b) Larger Néel-type skyrmions. (c) Bloch-type skyrmions. (d) Bloch-type antiskyrmions.

3. Topology in Magnetism

is a real-space Berry curvature. It is termed $B(\mathbf{r})$ to underline its relation to a real-space magnetic field as will become clear in Secs. 3.4.1 and 3.4.2, where the “topological Hall effect” of electrons [72] and magnons is explained, respectively.

Skyrmion crystals can be understood as superpositions of three spin spirals and a uniform component [52]; some examples are depicted in Fig. 3.6. They look like regular arrays of magnetic “whirls”, whose magnetization points opposite (blue) to the uniform background (yellow). Depending on the wavelength of the spin spirals, the whirls can be small or large [compare panel (a) and (b) in Fig. 3.6]. In Cu_2OSeO_3 , for example, the spiral’s pitch is about 60 nm [138].

Historically, one differentiates Bloch-type [Fig. 3.6(b)] from Néel-type skyrmions [139] [Fig. 3.6(c)], in analogy to Bloch-type and Néel-type domain walls [140]. When going from a skyrmion center (blue) radially to the skyrmion periphery (yellow), the magnetization rotates in the plane normal to the radial direction in Bloch-type skyrmions [Fig. 3.6(b)], while the magnetization rotates in the plane whose normal is orthogonal to the radial direction in Néel-type skyrmions [Fig. 3.6(c)]. This property is called *helicity* [139]. Skyrmions with fixed helicity are *chiral*. Usually, they are a result of DMI, originated by the noncentrosymmetry of the crystal [139]. Depending on the directions of the DM vectors, either Bloch-type skyrmions (e. g., MnSi [137]) or Néel-type skyrmions are featured (e. g., GaV_4S_8 [141]). In contrast, skyrmions which do not rely on DMI can be *nonchiral*, meaning that they are helicity-degenerate; a continuous transformation from Bloch-type to Néel-type skyrmions does not change the energy. Such nonchiral skyrmion crystals have been found in Ref. [52]; the authors of that study showed that the J_1 - J_3 model¹³, which was introduced in Sec. 2.3, features a skyrmion crystal at elevated temperatures under application of an external magnetic field. Since the spin spirals—which form the skyrmion crystal—are due to exchange frustration rather than DMI, their direction of rotation is not fixed. Thus, when equilibrating the magnetic system, Bloch-type skyrmions, Néel-type skyrmions, and all smooth configurations between the two are equally likely [52].

Skyrmions also have *vorticity* [139], which is the direction of the “wrapping”, that is, whether the magnetization direction wraps positively [Fig. 3.6(c)] or negatively [Fig. 3.6(d)] around the Bloch sphere¹⁴. It determines the topological charge of the skyrmion [see eq. (3.40)], which is why positively-wrapped and negatively-wrapped magnetic whirls, i. e., skyrmions and *antiskyrmions*, are each other’s antiparticle [139]. If they meet, they annihilate [142].

The following sections serve as an introduction to *Pub. 6*, in which the topological magnon transport on skyrmion crystals is studied in the limit of small *nonchiral* skyrmions. Here, literature concerning the topological Hall effect of electrons and magnons is reviewed. Please also see Sec. 4.2.2, where the magnetic phase diagram of the J_1 - J_3 model on the triangular lattice introduced in Ref. [52] is revisited by means of classical Monte Carlo simulations. In particular, the topological charge of the magnetic textures is calculated [see eq. (3.40)].

3.4.1. Emergent Electrodynamics for Electrons and the Topological Hall Effect

As demonstrated in Ref. [72], the Schrödinger equation for electrons traversing a space- and time-dependent, smooth magnetic texture $\mathbf{m}(\mathbf{r}, t) = m\hat{\mathbf{m}}(\mathbf{r}, t)$ [$\hat{\mathbf{m}}(\mathbf{r}, t)$ unit vector] reads

$$i\hbar \frac{\partial \psi(\mathbf{r}, t)}{\partial t} = \left(\frac{\mathbf{p}}{2M} I_{2 \times 2} - J\boldsymbol{\sigma} \cdot \hat{\mathbf{m}}(\mathbf{r}, t) \right) \psi(\mathbf{r}, t), \quad (3.42)$$

with M and \mathbf{p} denoting the electron’s mass and its momentum, respectively. $J = J'g\mu_B m\hbar/2$ is the strength of the coupling of the electron’s spin to the magnetic texture and $\psi(\mathbf{r}, t)$ is a Pauli spinor. $\boldsymbol{\sigma}$ is the vector of Pauli matrices; its product with the magnetic texture can be brought into a trivial form by locally rotating to the reference frame of the texture, such that the quantization axis is aligned with the texture. Such a local $\text{SU}(2)$ gauge transformation reads $\psi(\mathbf{r}, t) = U(\mathbf{r}, t)\phi(\mathbf{r}, t)$, where

$$U(\mathbf{r}, t) = \exp\left(-i \frac{\theta(\mathbf{r}, t)}{2} \boldsymbol{\sigma} \cdot \mathbf{n}(\mathbf{r}, t)\right),$$

¹³In Ref. [52] the J_1 - J_2 model on the triangular lattice was also studied (J_2 second-nearest neighbor interaction). The results are very similar to that of the J_1 - J_3 model.

¹⁴To study this “wrapping”, the magnetic texture is mapped onto a unit sphere by a stereographic projection.

is a unitary matrix [$\cos \theta(\mathbf{r}, t) = \hat{\mathbf{m}}(\mathbf{r}, t) \cdot \mathbf{z}$ and $\mathbf{n}(\mathbf{r}, t) = \hat{\mathbf{m}}(\mathbf{r}, t) \times \mathbf{z} / |\hat{\mathbf{m}}(\mathbf{r}, t) \times \mathbf{z}|$ denote the rotation angle and axis] [72]. This yields a Schrödinger equation for $\phi(\mathbf{r}, t)$, [72]

$$i\hbar \frac{\partial \phi(\mathbf{r}, t)}{\partial t} = \left[\frac{1}{2M} (\mathbf{p} - \hbar \mathbf{A}(\mathbf{r}, t)) - J\sigma_z - \hbar V(\mathbf{r}, t) \right] \phi(\mathbf{r}, t), \quad (3.43)$$

with the scalar and vector gauge potentials,

$$V(\mathbf{r}, t) = -iU^\dagger(\mathbf{r}, t)\partial_t U(\mathbf{r}, t), \quad \text{and} \quad \mathbf{A}(\mathbf{r}, t) = iU^\dagger(\mathbf{r}, t)\nabla U(\mathbf{r}, t),$$

respectively. They are nonzero only if $U(\mathbf{r}, t)$ shows temporal or spatial modulations [72]. In contrast to the Hamiltonian of a spinless charged particle in electromagnetic fields [U(1) gauge symmetry], the potentials are 2-by-2 matrices, allowing for spin flip processes. The latter can be neglected, if one considers textures, whose characteristic length ℓ is much larger than a lattice constant a ¹⁵. Then, the gauge potentials become approximately diagonal. Since they are also traceless, they must be proportional to σ_z and, thus, act oppositely on electrons with majority and minority spins [143]. This opposite action can be hidden in an emergent charge q_{em} (opposite for the two spin species), which suggests to define the emergent electromagnetic potentials [72]

$$V_{\text{em}}^\sigma(\mathbf{r}, t) = \frac{\hbar}{q_{\text{em}}} \langle \sigma | V(\mathbf{r}, t) | \sigma \rangle = -i \frac{\hbar}{q_{\text{em}}} \langle \psi_\sigma | \partial_t | \psi_\sigma \rangle,$$

$$\mathbf{A}_{\text{em}}^\sigma(\mathbf{r}, t) = \frac{\hbar}{q_{\text{em}}} \langle \sigma | \mathbf{A}(\mathbf{r}, t) | \sigma \rangle = i \frac{\hbar}{q_{\text{em}}} \langle \psi_\sigma | \nabla | \psi_\sigma \rangle,$$

where $|\sigma\rangle$ with $\sigma = \uparrow, \downarrow$ are the eigenstates of the unperturbed Hamiltonian, that is, Hamiltonian (3.43) without the potentials. With $|\psi_\sigma\rangle = U(\mathbf{r}, t)|\sigma\rangle$ the potentials $V_{\text{em}}^\sigma(\mathbf{r}, t)$ and $\mathbf{A}_{\text{em}}^\sigma(\mathbf{r}, t)$ take the form of a Berry connection [confer eq. (3.5)] in space-time (t, \mathbf{r}) . The corresponding Berry curvatures [confer eq. (3.6)] are electromagnetic fields $\mathbf{E}_{\text{em}}^\sigma(\mathbf{r}, t) = -\nabla V_{\text{em}}^\sigma(\mathbf{r}, t) - \partial_t \mathbf{A}_{\text{em}}^\sigma(\mathbf{r}, t)$ and $\mathbf{B}_{\text{em}}^\sigma(\mathbf{r}, t) = \nabla \times \mathbf{A}_{\text{em}}^\sigma(\mathbf{r}, t)$, with [72]

$$\mathbf{E}_{\text{em}}^{\sigma, \xi}(\mathbf{r}, t) = \mp \frac{\hbar}{2q_{\text{em}}} \hat{\mathbf{m}}(\mathbf{r}, t) \cdot \left[\partial_\xi \hat{\mathbf{m}}(\mathbf{r}, t) \times \partial_t \hat{\mathbf{m}}(\mathbf{r}, t) \right], \quad (3.44a)$$

$$\mathbf{B}_{\text{em}}^{\sigma, \xi}(\mathbf{r}, t) = \mp \frac{\hbar}{2q_{\text{em}}} \frac{\epsilon_{\xi\rho\zeta}}{2} \hat{\mathbf{m}}(\mathbf{r}, t) \cdot \left[\partial_\rho \hat{\mathbf{m}}(\mathbf{r}, t) \times \partial_\zeta \hat{\mathbf{m}}(\mathbf{r}, t) \right], \quad (3.44b)$$

(Einstein summation rule; $\epsilon_{\xi\rho\zeta}$ Levi-Civita symbol) where \mp corresponds to $\sigma = \uparrow, \downarrow$, respectively. The emergent charge reads $q_{\text{em}} = \pm 1/2$.

In summary, an electron traversing a texture feels both an emergent electric and magnetic field given by eqs. (3.44a) and (3.44b), respectively (up to prefactors). For a two-dimensional skyrmion crystal phase $\mathbf{B}_{\text{em}}(\mathbf{r}, t) = \mathbf{B}_{\text{em}}(\mathbf{r}) = [0, 0, B_{\text{em}}^z(\mathbf{r})]^T$ reduces to

$$B_{\text{em}}^z(\mathbf{r}) = \hbar \hat{\mathbf{m}}(\mathbf{r}) \cdot \left[\partial_x \hat{\mathbf{m}}(\mathbf{r}) \times \partial_y \hat{\mathbf{m}}(\mathbf{r}) \right],$$

which is proportional to the Berry curvature in eq. (3.41). Integrating over a magnetic unit cell (uc), which contains one skyrmion, the integrated magnetic field per unit cell [72],

$$\int_{\text{uc}} B_{\text{em}}^z(\mathbf{r}) d^2 r = 4\pi\hbar w,$$

is proportional to the topological charge w (real-space Chern number). This sets skyrmions apart from other generic magnetic textures, which might have a locally nonzero $B_{\text{em}}^z(\mathbf{r})$ but with zero average. Consequently, skyrmions give rise to an additional Lorentz force on electrons and, thus, generate a *topological* contribution to the Hall effect; this phenomenon is called ‘‘topological Hall effect’’. It was first experimentally verified in the skyrmion crystal phase of MnSi [144].

¹⁵The texture’s wave number $\sim 1/\ell$ is much smaller than the electron’s Fermi wave number $\sim 1/a$. Multiplying both wave numbers by $\hbar v_F$ (v_F Fermi velocity) shows that the energy scale of the electrons is much larger than that associated with the modulated texture [143].

3.4.2. Emergent Electrodynamics for Magnons

That an argumentation similar to that before can be invoked for magnons was demonstrated in Refs. [73, 128, 145]: in the classical limit of magnetization dynamics and smoothly varying two-dimensional magnetic textures, one may use the Landau-Lifshitz equation of motion¹⁶,

$$s\hbar\dot{\mathbf{m}} = \mathbf{m} \times \frac{\delta F(\mathbf{m}, \partial_j \mathbf{m})}{\delta \mathbf{m}}, \quad (3.45)$$

where $\mathbf{m}(\mathbf{r}, t)$ is the continuous unit vector magnetization field, s a constant spin density, and $F(\mathbf{m}, \partial_j \mathbf{m})$ ($j = x, y$) the free-energy functional, accounting for, e. g., exchange interaction and DMI.

Assuming that magnons are perturbatively small oscillations $\delta \mathbf{m}(\mathbf{r}, t)$ of a slowly-changing inhomogeneous magnetization background $\mathbf{m}_0(\mathbf{r}, t)$, the magnetization field is decomposed into $\mathbf{m}(\mathbf{r}, t) = \mathbf{m}_0(\mathbf{r}, t) + \delta \mathbf{m}(\mathbf{r}, t)$ [145]. To lowest order, $\mathbf{m}_0(\mathbf{r}, t) \cdot \delta \mathbf{m}(\mathbf{r}, t) = 0$. Following the idea for electrons, the local reference frame is aligned with the local direction of $\mathbf{m}_0(\mathbf{r}, t)$, such that $\mathbf{m}_0(\mathbf{r}, t) \rightarrow \mathbf{m}'_0(\mathbf{r}, t) = R(\mathbf{r}, t)\mathbf{m}_0(\mathbf{r}, t)$ appears constant (here: along the z' direction). The rotation matrix is given by $R(\mathbf{r}, t) = \exp[\theta(\mathbf{r}, t)J_x] \exp[\phi(\mathbf{r}, t)J_z]$, where J_β is the generator of rotation about the β axis ($\beta = x, z$) [145]. $\theta(\mathbf{r}, t)$ and $\phi(\mathbf{r}, t)$ are the space-time-dependent rotation angles.

In the new reference frame $\delta \mathbf{m}'(\mathbf{r}, t)$ is a vector in the $x'y'$ plane. The equation of motion for $\delta m'_\pm(\mathbf{r}, t) = \delta m'_x(\mathbf{r}, t) \pm i\delta m'_y(\mathbf{r}, t)$ is derived from eq. (3.45) by the substitution $\partial_\mu \rightarrow \partial'_\mu - [\partial'_\mu R(\mathbf{r}, t)]R(\mathbf{r}, t)$ ($\mu = t, x, y$) [73]:

$$i s [\partial_t - iV_{\text{em}}(\mathbf{r}, t)] m'_+(\mathbf{r}, t) = J [-i\partial_j + A_{\text{em},j}(\mathbf{r}, t)] m'_+(\mathbf{r}, t). \quad (3.46)$$

The emergent potentials

$$V_{\text{em}}(\mathbf{r}, t) = \cos \theta(\mathbf{r}, t) \partial_t \phi(\mathbf{r}, t), \quad A_{\text{em},j}(\mathbf{r}, t) = \cos \theta(\mathbf{r}, t) \partial_j \phi(\mathbf{r}, t),$$

($j = x, y$) define the emergent electromagnetic fields [73]

$$E_{\text{em},j}(\mathbf{r}, t) = -\partial_t A_{\text{em},j}(\mathbf{r}, t) - \partial_j V_{\text{em},j}(\mathbf{r}, t) = \mathbf{m}_0(\mathbf{r}, t) \cdot [\partial_t \mathbf{m}_0(\mathbf{r}, t) \times \partial_j \mathbf{m}_0(\mathbf{r}, t)], \quad (3.47a)$$

$$B_{\text{em},j}(\mathbf{r}, t) = \partial_k A_{\text{em},l}(\mathbf{r}, t) - \partial_l A_{\text{em},k}(\mathbf{r}, t) = \frac{1}{2} \epsilon_{jkl} \mathbf{m}_0(\mathbf{r}, t) \cdot [\partial_k \mathbf{m}_0(\mathbf{r}, t) \times \partial_l \mathbf{m}_0(\mathbf{r}, t)]. \quad (3.47b)$$

These fields are the same as for electrons [see eqs. (3.44a) and (3.44b)] and, thus, the magnons also “feel” an emergent Lorentz force that causes a “topological Hall effect” of magnons.

This effect has been indirectly experimentally verified. The authors of Ref. [146] shone laser light onto the insulating ferromagnet Cu_2OSeO_3 , which hosted a skyrmion crystal. The radial temperature gradient caused a radial magnon current, which got deflected by the skyrmions. Since there is a reaction to every action, the skyrmions are deflected as well, causing them to circle around the laser spot. This effect is similar to the skew-scattering of magnons at a single skyrmion, shown in Refs. [147–149].

In summary, the emergent electrodynamics theory for magnons requires two ingredients: a texture that negligibly varies on the length scale of the lattice constant [which justifies the continuous *ansatz* (3.45)], and small temperatures to treat the magnons as noninteracting particles [this approximation is implicitly included in the single-particle Schrödinger equation eq. (3.46)]. In *Pub. 6* an alternative method for the evaluation of magnon transport in noncollinear textures based on atomistic spin dynamics simulations is presented. In particular, the magnon thermal conductivity on a nonchiral skyrmion crystal is studied in dependence on the skyrmion size. It is found that the topological thermal magnon Hall effect vanishes for extremely small skyrmions, violating the requirements for the emergent electrodynamics.

¹⁶The atomistic version of the Landau-Lifshitz(-Gilbert) equation is introduced in Sec. 4.3.

In the framework of this thesis several numerical methods have been applied, which are briefly discussed in this chapter. The calculation of the spectral density at the surface of a semi-infinite crystal, presented in Sec. 4.1, features in *Pubs.* 2-4. Monte Carlo simulations and the stochastic Landau-Lifshitz-Gilbert equation, presented in Secs. 4.2 and 4.3, respectively, are the basis of *Pubs.* 5 and 6.

4.1. Magnonic Structure of Semi-infinite Crystals

The bulk-boundary correspondence states that topological invariants of the bulk cause inevitable features at the boundary (see Sec. 3.2.1). Thus, an efficient calculation method of the boundary spectrum is crucial for the study of topology. Boundary effects on the magnonic band structure can be included by considering a slab geometry, meaning that the sample is finite in one direction and infinite in the remaining directions. However, such a geometry introduces *two* opposite boundaries. From a topological perspective, this is critical, because the wavefunctions of the topological states at opposite edges could hybridize, leading to a small but nonzero artificial band gap. Increasing the thickness of the slab would reduce the effect, but comes at the price of increased computation costs. Thus, a semi-infinite geometry hosting only *one* boundary is pursued. This chapter introduces a Green function renormalization method established in Ref. [150] that can deal with the desired geometry.

Ref. [150] is followed for the remainder of this section. The magnonic band structure is determined by the bilinear free-magnon Hamiltonian $H_{(2)}$ in Sec. 2.4.3 [henceforth, the subscript (2) is dropped]. The Green function

$$G(\varepsilon + i\eta) = (\varepsilon + i\eta - H)^{-1}, \quad (4.1)$$

determines the density of states

$$N(\varepsilon) = -\frac{1}{\pi} \lim_{\eta \rightarrow 0^+} \{\text{Im} [\text{Tr} G(\varepsilon + i\eta)]\} \quad (4.2)$$

(an explicit dependence on the wavevector was dropped for notational simplicity). The small imaginary $i\eta$ ensures that singularities of G , which are located on the real axis, are not encountered. In computations, the limit $\lim_{\eta \rightarrow 0^+}$ is not taken, but η is chosen small compared to all other energy scales (e. g., the exchange parameters), causing a small broadening of all peaks.

A semi-infinite crystal consists of atomic layers parallel to its surface. By combining these layers to principal layers (PLs), which are chosen thick enough that interaction takes place only between adjacent PLs, eq. (4.1) can be written as [150]

$$\begin{pmatrix} z - H_s & -h_s & 0 & \cdots & \cdots \\ -h_s^\dagger & z - H_b & -h_b & 0 & \cdots \\ 0 & -h_b^\dagger & z - H_b & -h_b & \ddots \\ \vdots & 0 & -h_b^\dagger & z - H_b & \ddots \\ \vdots & \vdots & \ddots & \ddots & \ddots \end{pmatrix} \begin{pmatrix} G_{00} & G_{01} & G_{02} & \cdots & \cdots \\ G_{10} & G_{11} & G_{12} & G_{13} & \cdots \\ G_{20} & G_{21} & G_{22} & G_{23} & \ddots \\ \vdots & G_{31} & G_{32} & G_{33} & \ddots \\ \vdots & \ddots & \ddots & \ddots & \ddots \end{pmatrix} = \begin{pmatrix} 1 & 0 & 0 & \cdots & \cdots \\ 0 & 1 & 0 & 0 & \cdots \\ 0 & 0 & 1 & 0 & \ddots \\ \vdots & 0 & 0 & 1 & \ddots \\ \vdots & \ddots & \ddots & \ddots & \ddots \end{pmatrix}, \quad (4.3)$$

which is an infinite system of equations for the Green function blocks G_{ij} (PL indices i and j). H_s (H_b) denotes the Hamilton matrix for interactions within the surface (bulk-like) PLs. Interaction between adjacent PLs is comprised into h_s and h_b : the former is the inter-layer Hamilton matrix between the surface PL and the first bulk-like PL; the latter accounts for the interaction between bulk-like PLs.

4. Numerical Methods

Expanding eq. (4.3), one obtains, for example [150]

$$(z - H_s)G_{00} = 1 + h_s G_{10}, \quad (4.4)$$

$$(z - H_b)G_{10} = h_s^\dagger G_{00} + h_b G_{20}, \quad (4.5)$$

$$(z - H_b)G_{n,0} = h_b^\dagger G_{n-1,0} + h_b G_{n+1,0}, \quad (4.6)$$

$$(z - H_b)G_{n,n} = 1 + h_b^\dagger G_{n-1,n} + h_b G_{n+1,n}. \quad (4.7)$$

With eqs. (4.4) and (4.5) one eliminates G_{10} :

$$\left[(z - H_s) - h_s(z - H_b)^{-1}h_s^\dagger \right] G_{00} = 1 + h_s(z - H_b)^{-1}h_b G_{20}$$

and all odd-indexed Green function block matrices:

$$\begin{aligned} \left[(z - H_b) - h_b^\dagger(z - H_b)^{-1}h_b - h_b(z - H_b)^{-1}h_b^\dagger \right] G_{n,0} &= h_b^\dagger(z - H_b)^{-1}h_b^\dagger G_{n-2,0} + h_b(z - H_b)^{-1}h_b G_{n+2,0}, \\ \left[(z - H_b) - h_b^\dagger(z - H_b)^{-1}h_b - h_b(z - H_b)^{-1}h_b^\dagger \right] G_{n,n} &= 1 + h_b^\dagger(z - H_b)^{-1}h_b^\dagger G_{n-2,n} + h_b(z - H_b)^{-1}h_b G_{n+2,n}. \end{aligned}$$

With the definition

$$\begin{aligned} A_b^1 &\equiv h_b(z - H_b)^{-1}h_b, \\ B_b^1 &\equiv h_b^\dagger(z - H_b)^{-1}h_b^\dagger, \\ A_s^1 &\equiv h_s(z - H_b)^{-1}h_b, \\ B_s^1 &\equiv h_s^\dagger(z - H_b)^{-1}h_b^\dagger, \\ E_b^1 &\equiv (z - H_b) - h_b^\dagger(z - H_b)^{-1}h_b - h_b(z - H_b)^{-1}h_b^\dagger, \\ E_s^1 &\equiv (z - H_s) - h_s(z - H_b)^{-1}h_s^\dagger, \\ \tilde{E}_b^1 &\equiv (z - H_b) - h_b(z - H_b)^{-1}h_b^\dagger, \end{aligned}$$

one obtains equations that possess the form as the original ones, (4.4)–(4.7), but with *renormalized* interactions [150],

$$E_s^1 G_{00} = 1 + A_s^1 G_{20}, \quad (4.8)$$

$$E_b^1 G_{20} = B_s^1 G_{00} + A_b^1 G_{40}, \quad (4.9)$$

$$E_b^1 G_{n,0} = B_b^1 G_{n-2,0} + A_b^1 G_{n+2,0}, \quad (4.10)$$

$$E_b^1 G_{n,n} = 1 + B_b^1 G_{n-2,n} + A_b^1 G_{n+2,n}, \quad (4.11)$$

$$\tilde{E}_b^1 G_{n,0} = h_b^\dagger G_{n-1,0} + A_b^1 G_{n+4,0}. \quad (4.12)$$

Repeating the elimination procedure results in a renormalization prescription for the interaction matrices [150],

$$\begin{aligned} A_b^i &= A_b^{i-1}(E_b^{i-1})^{-1}A_b^{i-1}, \\ B_b^i &= B_b^{i-1}(E_b^{i-1})^{-1}B_b^{i-1}, \\ E_b^i &= E_b^{i-1} - B_b^{i-1}(E_b^{i-1})^{-1}A_b^{i-1} - A_b^{i-1}(E_b^{i-1})^{-1}B_b^{i-1}, \\ A_s^i &= A_s^{i-1}(E_b^{i-1})^{-1}A_b^{i-1}, \\ B_s^i &= B_s^{i-1}(E_b^{i-1})^{-1}A_b^{i-1}, \\ E_s^i &= E_s^{i-1} - A_s^{i-1}(E_b^{i-1})^{-1}B_b^{i-1}, \\ \tilde{E}_b^i &= \tilde{E}_b^{i-1} - A_b^{i-1}(E_b^{i-1})^{-1}B_b^{i-1}. \end{aligned}$$

In the limit of $i \rightarrow \infty$ the interlayer interaction becomes zero. Thus, the Green function block matrices read [150]

$$G_{00} = (E_s^\infty)^{-1}, \quad G_{nn} = (E_b^\infty)^{-1}, \quad \tilde{G}_{00} = (\tilde{E}_s^\infty)^{-1}, \quad (4.13)$$

where G_{00} is the surface Green function block, G_{nm} that of the bulk ($n \rightarrow \infty$). \tilde{G}_{00} is necessary to define transfer matrices [150]

$$T_b \equiv \tilde{G}_{00} h_b^\dagger, \quad T_b^\dagger \equiv h_b \tilde{G}_{00}, \quad T_s \equiv \tilde{G}_{00} h_s^\dagger, \quad T_s^\dagger \equiv h_s \tilde{G}_{00}, \quad (4.14)$$

which allow to calculate the Green function block matrix of *any* PL. The layer-resolved Bloch spectral function (layer index m) is finally obtained by [150]

$$N_m(\varepsilon, \mathbf{k}_\parallel) = -\frac{1}{\pi} \lim_{\eta \rightarrow 0^+} \{\text{Im} [\text{Tr} G_{mm}(\varepsilon + i\eta, \mathbf{k}_\parallel)]\} \quad (4.15)$$

(\mathbf{k}_\parallel wave vector in the surface Brillouin zone).

Thus, this procedure can access the density of magnon states of the bulk and of every PL m , in particular, that at the surface ($m = 0$), where topological boundary states are expected. In *Pubs. 2, 3, and 4* this renormalization scheme was utilized for the presentation of topological magnon edge/surface states. *Pubs. (a) and (b)*, which are not included in this thesis, demonstrate that interfaces of two semi-infinite magnets can be treated by an extended scheme for interfaces [151].

4.2. Monte Carlo Simulations

The determination of the magnetic ground state is key in the theory of magnetism. Unfortunately, the Luttinger-Tisza method (Sec. 2.3) works only at zero temperature (and is strictly reliable only for Bravais lattices). Thus, temperature has to be included by other means. In this respect, Monte Carlo simulations have become a staple method in the magnetism community because they are ideally suited for this purpose. For the introduction, Ref. [152] is reviewed.

4.2.1. Importance Sampling

The approach of randomly sampling all possible spin configurations to identify that with lowest energy can readily be discarded, because the phase space is just too large; the relevant configurations would not be sampled often enough [152]. Furthermore, the number of minima of the energy hyper-surface is extremely large, such that conventional gradient methods have to be dismissed, too. Instead, so-called *importance* sampling has to be applied, which generates a configuration from a previous configuration (Markov process) with a transition probability given by the Boltzmann weight [152].

The time-dependence of the probability $P_n(t)$ of the system being in state n at time t is given by the master equation [152]

$$\frac{\partial P_n(t)}{\partial t} = - \sum_{n \neq m} [P_n(t) W_{n \rightarrow m} - P_m(t) W_{m \rightarrow n}],$$

where $W_{n \rightarrow m}$ is the transition rate from state n to m . In equilibrium, $\partial P_n(t)/\partial t = 0$, which is fulfilled by the ‘‘detailed balance condition’’ $P_n(t) W_{n \rightarrow m} = P_m(t) W_{m \rightarrow n}$. In a classical system,

$$P_n(t) = \frac{1}{Z} \exp(-\beta E_n) \quad (4.16)$$

($\beta^{-1} = k_B T$), where $\exp(-\beta E_n)$ is the Boltzmann weight and E_n the energy of the n -th state. The partition function Z cannot be accessed in simulations. However, by generating a Markov chain of configurations, where each configuration is directly generated from the previous one, only the relative probability is relevant. Thus, only the energy difference $\Delta E = E_n - E_m$ is important [152]:

$$\frac{P_n(t)}{P_m(t)} = \exp(-\beta \Delta E) = \frac{W_{m \rightarrow n}}{W_{n \rightarrow m}}. \quad (4.17)$$

4. Numerical Methods

Here, the Metropolis update [153] is used; the transition rates are

$$W_{m \rightarrow n} = \begin{cases} \exp(-\beta\Delta E) & \text{if } \Delta E > 0 \\ 1 & \text{if } \Delta E < 0 \end{cases}. \quad (4.18)$$

Thus, given a classical spin configuration $\{s_i\}_m$ with energy E_m , one suggests an update to the i -th spin and calculates the new energy E_{m+1} (according to the Hamiltonian functional under consideration). If the new energy is smaller than the old ($E_{m+1} < E_m$) the update is always accepted; a new spin configuration $\{s_i\}_{m+1}$ is generated. In the opposite case, $E_{m+1} > E_m$, the update is accepted with the probability $\exp[-\beta(E_{m+1} - E_m)]$. Therefore, a random number $r \in (0, 1)$ is computed. If $r < \exp[-\beta(E_{m+1} - E_m)]$, the step is accepted, otherwise rejected. Then, this routine is repeated for the next spin and so on.

Since temperature T enters eq. (4.18) via β , its value determines the transition rate of energetically unfavourable steps ($\Delta E > 0$), thereby, simulating thermal fluctuations. If the simulation time is infinite, one is guaranteed to find the energetical minimum. To speed up simulations, an additional microcanonical (energy is preserved) update known as overrelaxation can be performed [154], which mirrors each spin about its local effective field.

4.2.2. Equilibration and Measurement

The equilibration process is typically performed by starting from a temperature much larger than the ordering temperature ($k_B T \gg J$) and performing $\sim 10^5$ cooling-down Metropolis steps, successively lowering temperature down to the target temperature T . Arrived at T , about 10^6 combined Metropolis-overrelaxation steps are performed.

Once equilibrium is reached (the cluster is “thermalized”), a “measurement” can be performed. “Measuring” is meant in the sense that a quantity of interest is averaged over hundreds of thousands of Metropolis steps (N number of measuring steps). Examples are the (normalized) magnetization $\mathbf{M} = (nN)^{-1} \sum_{i=1}^n \mathbf{m}_i$ of a cluster of $i = 1, \dots, n$ moments \mathbf{m}_i , the specific heat $c_v = (k_B T^2)^{-1} (\langle E^2 \rangle - \langle E \rangle^2)$, where E is the energy of the entire cluster given by the Hamilton functional, the susceptibility $\chi = (k_B T)^{-1} (\langle M^2 \rangle - \langle M \rangle^2)$, and the static structure factor $S_\alpha(\mathbf{k}) = n^{-1} \langle |\sum_{i=1}^n m_{\alpha,i} \exp(i\mathbf{k} \cdot \mathbf{r}_i)|^2 \rangle$ ($\alpha = x, y, z$), providing information about the spin texture [152].

Here, the focus is on the skyrmion number w given in eq. (3.40). Several algorithms for the numerical evaluation of w were implemented and tested (see Appendix A).

Example: Skyrmion Crystals in the J_1 - J_3 Model In Sec. 2.3, the J_1 - J_3 antiferromagnet on the triangular lattice was introduced. According to the Luttinger-Tisza method, the frustration causes a spin spiral ground state. Here, Monte Carlo simulations are briefly applied to this model. In particular, a skyrmion crystal phase is identified at elevated temperatures. These results are the basis of *Pub. 6*, where magnon transport on spin spirals and skyrmion crystals is numerically studied.

With J_1 and J_3 from Ref. [52], the phase diagram spanned by temperature T and magnetic field B was recalculated (see Fig. 4.1)¹⁷. The gray phase boundaries in Fig. 4.1 are taken from Ref. [52]. The spin spiral phase (single- q phase) is the ground state. At elevated temperatures (roughly about $0.42 k_B T / |J_3|$) the phase transition to the paramagnetic phase takes place. If a magnetic field is applied, the equilibrium can be a superposition of two (double- q phase) or even three (triple- q phase) spin spirals; the latter forms a skyrmion crystal (confer Sec. 3.4). Since the handedness of the spin spirals is not fixed (they are caused by frustration, not by DMI), the resulting skyrmion crystal can be built from skyrmions of any helicity and any vorticity; the skyrmions are nonchiral. In particular, skyrmion and antiskyrmion crystals are equally likely. However, once one type of skyrmion is randomly produced, it is the building block of the skyrmion crystal, that is, in equilibrium true (anti)skyrmion lattices are obtained. Repeating the simulation with exactly the same set of parameters does, in general, lead to a different skyrmion crystal.¹⁸

To evaluate the skyrmion numbers line scans for constant temperature or constant magnetic field (horizontal and vertical lines in Fig. 4.1, respectively) were conducted, and both the trigonometric and the conserving least-squares

¹⁷Monte Carlo simulations were performed by B. Göbel (coauthor of *Pub. 6*). Fig. 4.1 is taken from his master thesis [155]. More details can be found there. The results agree with those of Ref. [52].

¹⁸The energetic degeneracy between skyrmions and antiskyrmions might be responsible for the existence of the Z phase (small pocket in Fig. 4.1 right below the critical temperature). Here, skyrmions and antiskyrmions are simultaneously present. See Ref. [52] for a discussion of this magnetic phase.

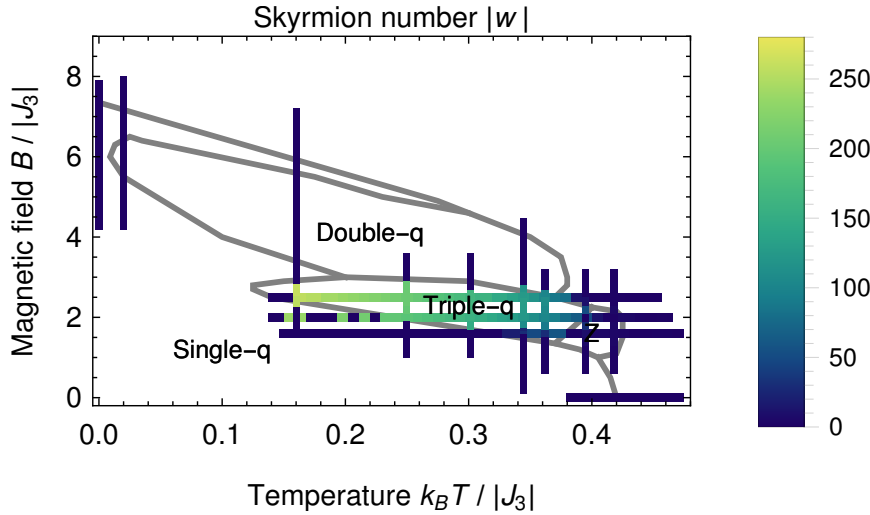


Fig. 4.1.: Magnetic phase diagram spanned by temperature T and magnetic field B of the J_1 - J_3 model for $J_1/J_3 = -1/3$. There are five distinct phases: single- q , double- q , triple- q , Z , and a paramagnetic phase. The first three are spin spiral states formed from one, two or three superimposed spin spirals, respectively; the Z phase is characterized by the coexistence of skyrmions and antiskyrmions. The paramagnetic phase is found at high temperatures (roughly about $0.42 k_B T / |J_3|$) and is continuously transformed into a field-polarized phase by application of the magnetic field (not indicated). The color of the lines quantifies the absolute value of the skyrmion number w (see color bar). Calculations were carried out on a 72×72 spin cluster. This graph is taken from Ref. [155] (labels translated into English); the data for the gray phase boundaries is taken from Ref. [52].

algorithm were utilized (Appendix A; the skyrmion numbers indicated at the colorbar in Fig. 4.1 are those obtained from the trigonometric algorithm). The absolute value of w is shown, because the skyrmion crystals phase can be equally likely built from skyrmions as well as antiskyrmions (opposite skyrmion number). The numerical calculations of $|w|$ comply very well with the phase boundaries (gray lines; data for the phase boundaries were taken from Ref. [52]): nonzero skyrmion number is found only in the triple- q phase, which is the skyrmion crystal phase.

Concentrating on this phase, note that for the ratio $J_1/J_3 = -1/3$ the spin spiral's pitch is $\lambda = 2\pi/|q| \approx 3.27a$ (a lattice constant) [confer eq. (2.15)], such that about 22 periods fit in an $N \times N = 72 \times 72$ spin cluster. Thus, $N_{\text{Sk}} = 3N^2/(4\lambda^2) \approx 364$ skyrmions are expected. On average, each skyrmion is "sampled" by $N^2/N_{\text{Sk}} \approx 14.24$ spins, which is a challenging small number for the numerical integration algorithms (Appendix A)¹⁹. The numerically determined skyrmion number (≈ 250) is clearly smaller than 364, because the topological charge of each magnetic unit cell is underestimated. Besides this numerical issue, the algorithms qualitatively identify the skyrmion crystal. Furthermore, the numerically evaluated skyrmion number drops with increasing temperature (yellow \rightarrow green \rightarrow light blue), which is unphysical, because w is determined by the cluster size. The origin of this decrease are strong thermal fluctuation at higher temperatures. However, even at the crossing to the Z or paramagnetic phase, a sharp transition from a light blue to a dark blue is identified. Thus, the integration algorithm reliably identifies a skyrmion crystal.

Similar phase diagrams are obtained when varying J_1/J_3 , which directly translates into the pitch of the spin spiral [see eq. (2.15)] and, consequently, into the size of the skyrmions. In *Pub. 6* cluster sizes which are commensurate with the skyrmion crystal were used.

¹⁹It is pointed out that the skyrmions studied here are even smaller than the smallest test skyrmion studied in Appendix A. There, the smallest skyrmion was built from $4 \times 4 = 16$ spins (confer Tab. A.1).

4.3. Stochastic Landau-Lifshitz-Gilbert Equation

The Monte Carlo method presented above does not grant access to the dynamics of the spin cluster, because there is no true but a “Monte Carlo time” that corresponds to the number of Monte Carlo steps per site²⁰. Therefore, the equation of motion, the Landau-Lifshitz-Gilbert equation, needs to be solved. Its presentation follows Refs. [40, 158–162].

4.3.1. Temporal Evolution of Magnetic Moments

The total magnetic moment of an electron is proportional to the sum of its orbital and its spin angular momentum. For simplicity, the discussion is restricted to the spin contribution. The spin magnetic moment $\mathbf{m} = -\gamma\mathbf{s}$ is related to the spin \mathbf{s} by the gyromagnetic ratio $\gamma = g\mu_B/\hbar$, with Bohr’s magneton μ_B and the g -factor ($g \approx 2$ for free electrons). To obtain the equation of motion of a spin \mathbf{s}_i , one starts from the Heisenberg equation $\hbar\dot{\mathbf{s}}_i = -i[\mathbf{s}_i, H]$. Expanding the spin Hamiltonian H in terms of spin operators, leads to [163]

$$\dot{\mathbf{s}}_i = -\mathbf{s}_i \times \frac{\partial H}{\partial \mathbf{s}_i} + O(\hbar).$$

In line with the Ehrenfest theorem one replaces all operators by their expectation values, drops the second term (classical limit), and obtains

$$\dot{\mathbf{m}}_i = -\gamma\mathbf{m}_i \times \mathbf{B}_i \quad (4.19)$$

for a classical magnetic moment (i. e., a vector in \mathbb{R}^3). $\mathbf{B}_i = -\partial H/\partial \mathbf{m}_i$ is the effective magnetic field due to the neighboring spins (H is no longer the Hamilton operator but the energy). Eq. (4.19) describes how the magnetic moment precesses about the local field. Its modulus stays constant and energy is conserved.

To incorporate dissipation, a phenomenological viscous damping term is added [164, 165], leading to the Landau-Lifshitz-Gilbert (LLG) equation

$$\dot{\mathbf{m}}_i = -\gamma\mathbf{m}_i \times \mathbf{B}_i + \frac{\alpha}{|\mathbf{m}_i|}\mathbf{m}_i \times \dot{\mathbf{m}}_i,$$

with Gilbert damping α ($\alpha \ll 1$). It can be rewritten as [161]

$$\dot{\mathbf{m}}_i = -\frac{\gamma}{1+\alpha^2} \left[\mathbf{m}_i \times \mathbf{B}_i + \frac{\alpha}{|\mathbf{m}_i|} \mathbf{m}_i \times (\mathbf{m}_i \times \mathbf{B}_i) \right], \quad (4.20)$$

which is now the LLG equation in Landau-Lifshitz form [166]²¹. The two terms are interpreted and visualized in Fig. 4.2. Besides the precession $\mathbf{m}_i \times \mathbf{B}_i$ of the magnetic moment \mathbf{m}_i about the effective field \mathbf{B}_i (red torque in Fig. 4.2), there is the damping $\mathbf{m}_i \times (\mathbf{m}_i \times \mathbf{B}_i)$ (green torque in Fig. 4.2), trying to align \mathbf{m}_i with \mathbf{B}_i .

Eq. (4.20) is a reasonable approximation for the dynamics of classical spins, because it captures the most relevant effects. Although the physical justification for the Gilbert damping term is difficult on the atomistic level [162], the LLG can be derived from time-dependent density functional theory [167] and the density matrix formalism [168]²². However, eq. (4.20) does not include (i) anisotropic and nonlocal damping, (ii) variations of the modulus of \mathbf{m}_i , (iii) quantum effects (quantization), and, up to now, (iv) temperature.

The last point is cured by adding a stochastic random magnetic field \mathbf{b}_i to \mathbf{B}_i [with $\mathbf{B}_i \rightarrow \mathbf{B}_i + \mathbf{b}_i$, eq. (4.20) becomes the stochastic LLG (sLLG)]. \mathbf{b}_i simulates the effect of temperature. For thermodynamic consistency, it has to obey the following conditions [159, 169]

$$\langle b_i^\xi(t) \rangle = 0, \quad \langle b_i^\xi(t)b_j^\zeta(t') \rangle = 2D\delta_{ij}\delta_{\xi\zeta}\delta(t-t'),$$

($\xi, \zeta = x, y, z$), i. e., it must follow a Gaussian distribution with zero average and a variance of $2D$. \mathbf{b}_i is uncorrelated in time, i. e., a *white noise* magnetic field. D determines the fluctuation amplitude and is, thus, related to temperature; from a mapping onto Langevin dynamics (and the related Fokker-Planck equation) one obtains $D = \alpha k_B T / (\gamma|\mathbf{m}|)$ [159, 169], where $|\mathbf{m}_i| = |\mathbf{m}|$ (all moments have length $|\mathbf{m}|$).

²⁰There are, however, efforts to develop a time-quantified Monte Carlo method [156, 157].

²¹Landau and Lifshitz did not add the term proportional to $\mathbf{m}_i \times \dot{\mathbf{m}}_i$ to the precessional motion, but directly the term proportional to $\mathbf{m}_i \times (\mathbf{m}_i \times \mathbf{B}_i)$ [166]. Then, the overall prefactor $(1+\alpha^2)^{-1}$ is missing, leading to unphysical behaviour in the limit of large damping [160].

²²Actually, the LLG is not derived in the Landau-Lifshitz-Gilbert form, but in the Landau-Lifshitz form, leading to a rescaling of the prefactors.

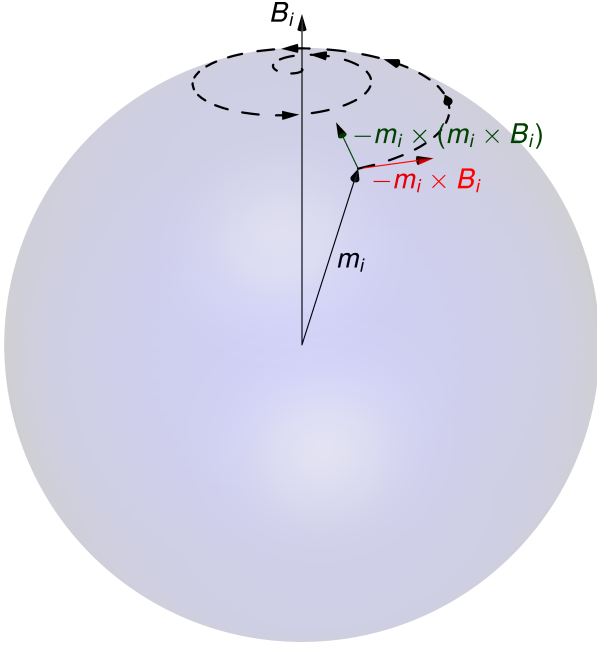


Fig. 4.2: Dynamics of a classical magnetic moment \mathbf{m}_i in an effective field \mathbf{B}_i as described by the Landau-Lifshitz-Gilbert equation (4.20). The term $-\mathbf{m}_i \times \mathbf{B}_i$ (red) causes a precession, while the term $-\mathbf{m}_i \times (\mathbf{m}_i \times \mathbf{B}_i)$ (dark green) tries to align \mathbf{m}_i with \mathbf{B}_i , resulting in a damping of the precession. Combined, the two mechanisms force \mathbf{m}_i onto the trajectory indicated by the dashed line.

4.3.2. Numerical Integration

Following Ref. [170] to obtain the dimensionless version of the sLLG, one sets $\mathbf{m} = m\mu_B \mathbf{n}$ (\mathbf{n} unit vector) and introduces a reference magnetic field $B_{\text{ref}} \approx 5.679044137$ T, which is chosen such that one unit of dimensionless time $\tau = \gamma B_{\text{ref}} t$ corresponds to one picosecond. Thus, eq. (4.20) reduces to

$$(1 + \alpha^2) d\mathbf{n}_i = -(1 + \alpha \mathbf{n}_i \times) \left[\mathbf{n}_i \times \left(\mathcal{B}_i d\tau + \frac{1}{B_{\text{ref}}} \mathbf{b}_i d\tau \right) \right], \quad (4.21)$$

with $\mathcal{B}_i = \mathbf{B}_i / B_{\text{ref}}$. Using $\mathbf{b}_i d\tau / B_{\text{ref}} = \tilde{D} d\mathbf{W}_i$, where \mathbf{W}_i is an isotropic vector Wiener process²³, and $\tilde{D}^2 = 2\alpha k_B T / (m\mu_B B_{\text{ref}})$ [160], one obtains

$$(1 + \alpha^2) d\mathbf{n}_i = -(1 + \alpha \mathbf{n}_i \times) \left[\mathbf{n}_i \times \left(\mathcal{B}_i d\tau + \tilde{D} d\mathbf{W}_i \right) \right]. \quad (4.22)$$

For the numerical evaluation of eq. (4.22), the implicit mid-point method [158, 160]

$$(1 + \alpha^2) (\mathbf{n}_i^{(k+1)} - \mathbf{n}_i^{(k)}) = - \left(1 + \alpha \mathbf{n}_i^{(k+\frac{1}{2})} \times \right) \left[\mathbf{n}_i^{(k+\frac{1}{2})} \times \mathcal{B}_i^{(k+\frac{1}{2})} \Delta\tau + \tilde{D} \mathbf{n}_i^{(k+\frac{1}{2})} \times (\mathbf{W}^{(k+1)} - \mathbf{W}^{(k)}) \right], \quad (4.23)$$

is used; $\Delta\tau = \tau^{(k+1)} - \tau^{(k)}$, $\mathbf{n}_i^{(k+1/2)} = (\mathbf{n}_i^{(k+1)} + \mathbf{n}_i^{(k)})/2$, and $\mathcal{B}_i^{(k+1/2)}$ is evaluated at $\mathbf{n}_i^{(k+1/2)}$.

Since the sLLG (4.22) is a stochastic differential equation with *multiplicative* noise, one is faced with the Itô-Stratonovich dilemma concerning the interpretation of a stochastic integral [171]. The two interpretations of eq. (4.22) lead to different magnetization dynamics, and only Stratonovich's conserves the spin length, which is why it is used here (the implicit midpoint scheme is compatible with the Stratonovich interpretation [158, 160])²⁴.

Tests of the Simulation Code

To test the thermodynamic consistency of the simulations, the energy per spin $E_i = |\mathbf{m}_i| |\mathbf{B}_i| - \mathbf{m}_i \cdot \mathbf{B}_i$ [170, 172] was computed. In equilibrium, E_i follows the Boltzmann distribution. The numerically obtained energy distribution

²³The cartesian components of $\mathbf{W}_i(t)$ are scalar Wiener processes $W_i^\beta(t)$ ($\beta = x, y, z$) with the properties that (a) $W_i^\beta(0) = 0$, (b) $W_i^\beta(t) - W_i^\beta(t')$ with $t > t' \geq 0$ is a gaussian random variable with zero mean and variance $t - t'$, and (c) its increments are uncorrelated [160].

²⁴Equivalence between Stratonovich's and Itô's interpretation can be achieved by adding a drift term to the sLLG, such that Itô's interpretation also conserves the spin length [158, 160].

4. Numerical Methods

Fig. 4.3: Numerically evaluated energy distribution of spins in a ferromagnetic 20×20 cluster at $T = 2$ K ($J = 1$ meV). Simulations were performed with a Gilbert damping $\alpha = 0.1$ (blue) and $\alpha = 0.5$ (red). The dashed line shows the analytic Boltzmann distribution function.

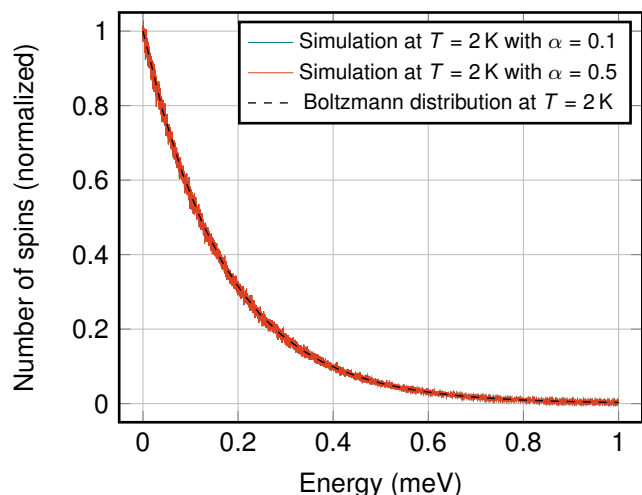


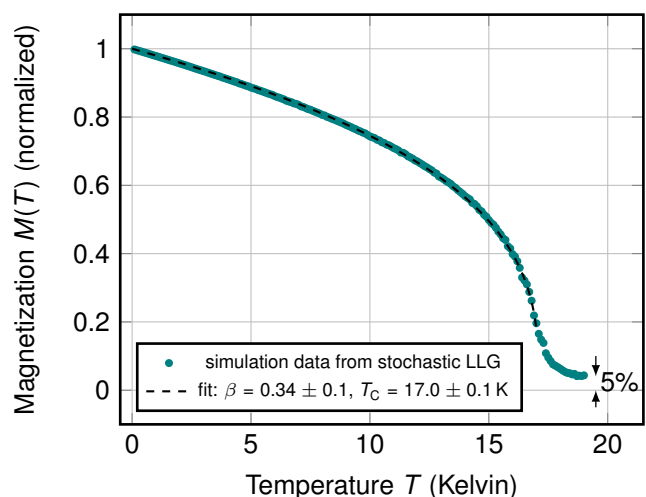
(Fig. 4.3) does not depend on the Gilbert damping α (blue curve: $\alpha = 0.1$; red curve: $\alpha = 0.5$) and agrees excellently with the Boltzmann distribution (dashed line). It is concluded that the simulations are thermodynamically consistent.

Additionally, the magnetization curve [magnetization versus temperature, $M(T)$] of a ferromagnetic three-dimensional simple cubic spin cluster was measured ($J = 1$ meV). Theory predicts that it exhibits a critical temperature of $T_C = J\lambda z/(3k_B) \approx 16.7$ K, where $z = 6$ is the number of nearest neighbors and $\lambda \approx 0.719$ the factor relating the mean-field Curie temperature to the actual Curie temperature of the classical three-dimensional Heisenberg model on a simple cubic lattice [173]; λ takes spin-wave corrections into account. The numerical data are shown in Fig. 4.4 and fitted by [174]

$$M(T) = \left(1 - \frac{T}{T_C}\right)^\beta, \quad (4.24)$$

where M is the normalized magnetization. For the classical three-dimensional Heisenberg model the critical exponent β is about 0.32–0.37 [174–176]. This fit yields results which are in good agreement with the theoretical predictions (relative error of about 5%), taking into account the finite size of the cluster. The residual magnetization of less than 5% at temperatures above the Curie temperature limits the accuracy.

Fig. 4.4: Numerical (normalized) magnetization versus temperature, numerical data blue, fit dashed black [eq. (4.24)]. A ferromagnetic ($J = 1$ meV) simple cubic lattice with $22 \times 22 \times 22 = 10648$ magnetic moments and periodic boundary conditions was simulated, yielding a finite-size error less than 5%; Gilbert damping $\alpha = 0.1$.



The publications of this thesis do not appear in chronological order but are arranged thematically. A short introduction precedes each publication, explaining the motivation and the central results of the respective study; reference is given to those chapters of the present thesis, which provide the theoretical background. A comment on the author's contribution to each publication is given below.

5.1. List of Publications

Publications Appearing in This Thesis

1. A. Mook, J. Henk, and I. Mertig
Magnon Hall effect and topology in kagome lattices: A theoretical investigation
Physical Review B **89**, 134409 (2014).
2. A. Mook, J. Henk, and I. Mertig
Edge states in topological magnon insulators
Physical Review B **90**, 024412 (2014).
3. A. Mook, J. Henk, and I. Mertig
Tunable magnon Weyl points in ferromagnetic pyrochlores
Physical Review Letters **117**, 157204 (2016).
4. A. Mook, J. Henk, and I. Mertig
Magnon nodal-line semimetals and drumhead surface states in anisotropic pyrochlore ferromagnets
Physical Review B **95**, 014418 (2017).
5. A. Mook, J. Henk, and I. Mertig
Spin dynamics simulations of topological magnon insulators: From transverse current correlation functions to the family of magnon Hall effects
Physical Review B **94**, 174444 (2016).
6. A. Mook, B. Göbel, J. Henk, and I. Mertig
Magnon transport in noncollinear spin textures: Anisotropies and topological magnon Hall effects
Physical Review B Rapid Communications **95**, 020401(R) (2017).

Comment on my contributions. For all publications, I developed the computer codes for the numerical simulations, interpreted the results, and wrote major parts of the manuscripts. Additionally, I initiated the research presented in *Pubs. 3, 4, 5, and 6*. JH provided the original code for the Green's functions renormalization (see Sec. 4.1 and Ref. [150]), which I implemented by myself; he participated in the writing process of the manuscripts. IM and JH initiated the research presented in *Pubs. 1, and 2*. BG performed the Monte Carlo simulations which are the basis of *Pub. 6*. All authors discussed the results and commented on the manuscripts.

5. Publications

Publications Not Appearing in This Thesis

- (a) A. Mook, J. Henk, and I. Mertig
Topologically nontrivial magnons at an interface of two kagome ferromagnets
Physical Review B **91**, 224411 (2015).
- (b) A. Mook, J. Henk, and I. Mertig
Magnon waveguide with nanoscale confinement constructed from topological magnon insulators
Physical Review B **91**, 174409 (2015).
- (c) A. Mook, J. Henk, and I. Mertig
Topological Magnon Insulators: Chern numbers and surface magnons
Proceedings SPIE 9931, Spintronics IX, 993134 (2016).
- (d) B. Göbel, A. Mook, J. Henk, and I. Mertig
Unconventional topological Hall effect in skyrmion crystals caused by the topology of the lattice
Physical Review B **95**, 094413 (2017).
- (e) B. Göbel, A. Mook, J. Henk, and I. Mertig
Signatures of Lattice Geometry in Quantum and Topological Hall Effect
Preprint on arXiv:1704.00567, submitted to the New Journal of Physics (2017).

Comment on my contribution. For *Pubs. (a), (b), and (c)*, I set up the computer code for the numerical simulations, and interpreted the results. I wrote major parts of the manuscripts of *Pubs. (a)*, and *(b)*, and participated in the writing process of *Pubs. (c), (d), and (e)*. All authors initiated the research, discussed the results, and commented on the manuscripts.

5.2. Thermal Magnon Hall Effect

As already pointed out in the introduction (Sec. 1), the thermal magnon Hall effect (or “magnon Hall effect”, see Sec. 3.3.2) was predicted [15] and experimentally verified [14] for the insulator $\text{Lu}_2\text{V}_2\text{O}_7$. A connection between the geometric properties of the magnon Bloch wave functions and the transverse magnon transport was established in Refs. [18–20]. The transverse thermal conductivity could be expressed as a \mathbf{k} -space integral over Berry’s curvature (Sec. 3.3) and the notion of “topological magnon (Chern) insulators” was born [23] (Sec. 3.2.1).

The aim of the following two publications was understanding the (thermal) magnon Hall effect in a two-dimensional topological magnon insulator on the kagome lattice in detail [see red triangles in Fig. 1.1(a)]. One of the most fundamental questions is that concerning the sign of the Hall transport, i. e., whether the current is deflected to the right or to the left. For electric topological insulators, only the metallic edge states contribute to transport. Thus, their number and propagation direction directly translates into the transverse conductivity. However, for magnons, the Bose-Einstein distribution function makes all states contribute. Thus, the transverse transport is fundamentally different.

Previous work did either focus on the magnon Hall effect caused by magnon states in the vicinity of the center of the Brillouin zone [14, 15, 18, 19] or on the contribution of the topologically protected edge magnons [23]. The dependence of the transverse thermal conductivity on the topological phase of the magnon spectrum, its detailed temperature dependence, and “tunability” remained unexplored.

5.2.1. Magnon Hall effect and topology in kagome lattices: A theoretical investigation

A kagome ferromagnet with nearest and second-nearest neighbor exchange and DM interaction was considered. Its magnon bulk bands were shown to possess nonzero Chern numbers, making it a topological magnon Chern insulator (see Secs. 3.2.1). Variation of the ratio between second-nearest and nearest-neighbor exchange interaction leads to *topological phase transitions*: the Chern numbers of the bulk bands change. In total, four topologically different phases were identified.

For exchange parameters chosen such that a topological phase boundary is touched, the magnon bulk bands are not separated by a band gap. Slight variation of the parameters leads to an opening of a band gap, a so-called “avoided crossing”. Since the energy gap is very small, the Berry curvature is very large [confer the denominator of eq. (3.7)]. Thus, the energy-resolved contribution to the transverse thermal conductivity shows “hot spots” at the avoided band crossings. When there is positive Berry curvature in the lower band of the avoided crossing, there is negative curvature in the upper band. If there were only two magnon bulk bands (as is the case in the Haldane model, Sec. 3.2.1), the lower one would always be the more populated one, such that its Berry curvature determines the sign of the thermal conductivity. However, the kagome Chern insulator possesses *three* magnon bulk bands, which allows for a more complex dependence on temperature and, in particular, for a sign change.

To illuminate the detailed dependence of the Hall transport on the different topological phases, a figure of merit was defined: the thermal conductivity at high temperatures. Although this limit is beyond the range of validity of the linear spin-wave approximation, this quantity turned out to be a very useful to estimate the direction of the transverse transport.

Magnon Hall effect and topology in kagome lattices: A theoretical investigationAlexander Mook,¹ Jürgen Henk,² and Ingrid Mertig^{1,2}¹Max-Planck-Institut für Mikrostrukturphysik, D-06120 Halle (Saale), Germany²Institut für Physik, Martin-Luther-Universität Halle-Wittenberg, D-06099 Halle (Saale), Germany

(Received 21 January 2014; revised manuscript received 27 March 2014; published 14 April 2014)

Ferromagnetic insulators with Dzyaloshinskii-Moriya interaction show the magnon Hall effect, i.e., a transverse heat current upon application of a temperature gradient. In this theoretical investigation we establish a close connection of the magnon Hall effect in two-dimensional kagome lattices with the topology of their magnon dispersion relation. From the topological phase diagram we predict systems which show a change of sign in the heat current in dependence on temperature. Furthermore, we derive the high-temperature limit of the thermal Hall conductivity; this quantity provides a figure of merit for the maximum strength of the magnon Hall effect. Eventually, we compare the temperature and field dependence of the magnon Hall conductivity of the three-dimensional pyrochlore $\text{Lu}_2\text{V}_2\text{O}_7$ with experimental results.

DOI: [10.1103/PhysRevB.89.134409](https://doi.org/10.1103/PhysRevB.89.134409)

PACS number(s): 66.70.-f, 75.30.-m, 75.47.-m, 85.75.-d

I. INTRODUCTION

The Hall and Nernst effects comprise a variety of phenomena, all showing a transverse current in response to a longitudinal external field [1–3]. In the case of Hall effects, this field is (typically) an applied voltage, whereas in the case of Nernst effects, this is a temperature gradient. For the conventional and anomalous effects, one observes an electric current; a spin current is measured for their “spin” counterparts, e.g., the spin Hall effect. Typically, one associates the observation of a transverse current with the term Hall effect or Hall geometry, rather than with a Nernst effect or Nernst geometry. An example of this notation is the phonon Hall effect [4] which describes a heat current perpendicular to a longitudinal temperature gradient.

The diversity of Hall effects has been extended by Onose *et al.* who discovered the magnon Hall effect (MHE) [5]. For the insulating ferromagnet $\text{Lu}_2\text{V}_2\text{O}_7$ with pyrochlore lattice [Fig. 1(a)] they found a transverse heat current upon application of a longitudinal temperature gradient. Theoretical understanding of this phenomenon has been provided by Matsumoto and Murakami, who explained the magnon Hall effect as a consequence of noncompensated magnon edge currents in a two-dimensional system [6,7]. Later on, Zhang *et al.* recognized that this net edge current results from the topology of the system, thereby confirming the existence of topological magnon insulators [8].

The magnon Hall effect is due to the spin-orbit interaction. In a magnetic system without inversion center—as in the pyrochlore lattice—it results in the Dzyaloshinskii-Moriya contribution to the exchange interaction of localized magnetic moments which opens up band gaps in the magnon dispersion relation. These avoided crossings give a nonzero Berry curvature and nonzero topological invariants (i.e., the Chern numbers). The transverse thermal conductivity κ^{xy} is consequently expressed as an integral of the Berry curvature over the Brillouin zone. The preceding information reveals a close similarity to the physics of electronic topological insulators in which spin-orbit-induced band inversions yield nonzero topological invariants and topologically protected surface or edge states [9–11]. The transverse thermal conductivity of the MHE is, thus,

in line with several other—mostly electronic—physical quantities that are expressed in terms of the Berry curvature and have been studied extensively in the past [12,13].

Although the fundamental physics of the MHE has been derived by Matsumoto and Murakami [6,7], a number of open questions needs to be answered. In our theoretical investigation reported in this paper we deduce a topological phase diagram for kagome systems. It turns out that for specific systems the transverse thermal conductivity changes sign in dependence on temperature; this implies that the orientation of the heat current can be reversed by tuning the temperature in a device. Furthermore, we derive the high-temperature limit of the thermal conductivity which provides a figure of merit for the strength of the magnon Hall effect. To come closer to experiment, we extend our analysis of two-dimensional lattices to the three-dimensional pyrochlore lattice by stacking non-interacting kagome layers. By comparison of the temperature and field dependence of the magnon Hall conductivity with the experimental results of Onose *et al.* [5], we determine the Dzyaloshinskii-Moriya parameters of $\text{Lu}_2\text{V}_2\text{O}_7$.

The paper is organized as follows. In Sec. II we outline the quantum-mechanical description of magnons in kagome lattices (Sec. II A) and derive an expression for the transverse thermal conductivity (Sec. II B). Results are presented in Sec. III: topology and magnon band structure (Sec. III A), the topological phase diagram (Sec. III B), the high-temperature limit of the thermal conductivity (Sec. III C), and a comparison with experiments for $\text{Lu}_2\text{V}_2\text{O}_7$ (Sec. III D). We conclude with Sec. IV.

II. THEORY OF THE MAGNON HALL EFFECT**A. Model Hamiltonian for magnons**

For the description of magnons in kagome lattices, we use the quantum-mechanical Heisenberg model [14]. In the Hamiltonian

$$\mathcal{H}_H = -\frac{1}{2} \sum_{n \neq m} J_m^n \hat{s}_m \cdot \hat{s}_n \quad (1)$$

spin operators \hat{s}_n and \hat{s}_m at lattice sites n and m are coupled by exchange parameters J_m^n . The latter account for

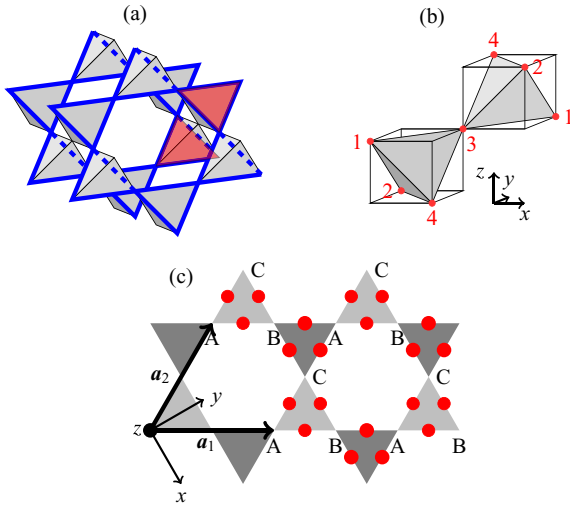


FIG. 1. (Color online) Pyrochlore and kagome lattices. (a) Three-dimensional pyrochlore lattice, with (111) planes representing stacked two-dimensional kagome lattices (marked by blue bold lines). (b) Atomic positions, labeled by numbers, in the pyrochlore lattice. (c) Two-dimensional kagome lattice with lattice vectors \mathbf{a}_1 and \mathbf{a}_2 . Atoms A, B, and C are placed at the corners of the triangles. Dzyaloshinskii-Moriya vectors are aligned normal to the lattice plane and are represented by red dots: along $+z$ ($-z$) for a counterclockwise (clockwise) chirality: A-B-C (C-B-A).

isotropic symmetric spin-spin interactions, typically termed “Heisenberg” exchange. The eigenvectors of \mathcal{H}_H ,

$$|\mathbf{k}\rangle = \frac{1}{\sqrt{N}} \sum_m e^{i\mathbf{k}\cdot\mathbf{R}_m} |\mathbf{R}_m\rangle, \quad (2)$$

are called “one-magnon states”, where N is the total number of spins, \mathbf{R}_m is the vector pointing to lattice site m , and $|\mathbf{R}_m\rangle$ denotes the state with all spins aligned along the ferromagnetic ground state except the one at lattice site m ; its z component is reduced by \hbar .

As mentioned above, the spin-orbit interaction is essential for the MHE; it contributes in two ways to the Hamiltonian: the magnetocrystalline anisotropy, which is not considered in this paper, and the Dzyaloshinskii-Moriya interaction [15,16]. The Dzyaloshinskii-Moriya (DM) contribution is anisotropic as well as antisymmetric and can be written as

$$\mathcal{H}_{\text{DM}} = \frac{1}{2} \sum_{m \neq n} \mathbf{D}_m^n (\hat{\mathbf{s}}_m \times \hat{\mathbf{s}}_n). \quad (3)$$

\mathbf{D}_m^n is the DM vector between sites m and n ($\mathbf{D}_m^n = -\mathbf{D}_n^m$).

The coupling to an external magnetic field \mathbf{H} is introduced by a Zeeman term,

$$\mathcal{H}_{\text{ext}} = -g\mu_B \sum_n \mathbf{H} \cdot \hat{\mathbf{s}}_n. \quad (4)$$

g and μ_B denote the g factor of electrons and Bohr’s magneton, respectively. The complete Hamiltonian then reads

$$\mathcal{H} = \mathcal{H}_H + \mathcal{H}_{\text{DM}} + \mathcal{H}_{\text{ext}}. \quad (5)$$

For the time being, we consider only one-magnon states and, thereby, exclude the kinematic [17] interaction that originates from the impossibility of locating more than $2s$ deviations at a

single spin s . We also do not account for the dipole-dipole interaction and for higher-order spin interactions (e.g., Ref. [18]).

By means of Moriya’s symmetry rules [16], the DM vectors of the pyrochlore lattice can be expressed as

$$\begin{aligned} \mathbf{D}_{12} &= \frac{\tilde{D}}{\sqrt{2}}(-y - z), & \mathbf{D}_{13} &= \frac{\tilde{D}}{\sqrt{2}}(-x + y), \\ \mathbf{D}_{14} &= \frac{\tilde{D}}{\sqrt{2}}(x + z), & \mathbf{D}_{24} &= \frac{\tilde{D}}{\sqrt{2}}(-x - y), \\ \mathbf{D}_{43} &= \frac{\tilde{D}}{\sqrt{2}}(-y + z), & \mathbf{D}_{23} &= \frac{\tilde{D}}{\sqrt{2}}(x - z), \end{aligned} \quad (6)$$

where \tilde{D} denotes the DM constant of adjacent sites. The site labels 1–4 and the unit vectors \mathbf{x} , \mathbf{y} , and \mathbf{z} of the Cartesian coordinate system are defined in Fig. 1(b) (cf. Refs. [19] and [20]).

In the experiment by Onose *et al.* [5], an external magnetic field \mathbf{H} is applied along the [111] direction. Only the components of the DM vectors along this direction contribute to the MHE; the other components do not contribute up to second order in the spin deviation from the [111] direction (cf. the supplemental online material of Ref. [5]). With $\sqrt{3}\mathbf{n} = \mathbf{x} + \mathbf{y} + \mathbf{z}$ we arrive at

$$D \equiv -\mathbf{n} \cdot \mathbf{D}_{12} = \mathbf{n} \cdot \mathbf{D}_{14} = -\mathbf{n} \cdot \mathbf{D}_{24} = \frac{2}{\sqrt{6}} \tilde{D}, \quad (7a)$$

$$0 = \mathbf{n} \cdot \mathbf{D}_{13} = \mathbf{n} \cdot \mathbf{D}_{23} = \mathbf{n} \cdot \mathbf{D}_{43}. \quad (7b)$$

Hence, only spins at sites that form a kagome lattice within the (111) plane are coupled by the DM interaction (here, sites 1, 2, and 4). This suggests a study of (two-dimensional) kagome lattices instead of (three-dimensional) pyrochlore lattices, as is done in this paper.

To simplify the calculation for the kagome lattice, we use the coordinate system shown in Fig. 1(c), in which the kagome lattice and the xy plane coincide and the [111] direction is along z . The lattice vectors read

$$\mathbf{a}_1 = (1, \sqrt{3}) \frac{a}{2}, \quad (8a)$$

$$\mathbf{a}_2 = (-1, \sqrt{3}) \frac{a}{2} \quad (8b)$$

(a is the lattice constant) in Cartesian coordinates. The DM vectors are then along the z direction. Their orientation is given by the chirality of the triangles in the kagome lattice: those with counterclockwise (clockwise) chirality point along the $+z$ ($-z$) direction [cf. the red dots in Fig. 1(c)]. The length of the DM vectors is D .

By means of ladder operators $\hat{\mathbf{s}}^\pm \equiv \hat{\mathbf{s}}^x \pm i\hat{\mathbf{s}}^y$ and the definition

$$\tilde{J}_m^n \exp(i\phi_m^n) \equiv J_m^n + iD_m^n \quad (9)$$

the Hamiltonian reads [5]

$$\begin{aligned} \mathcal{H} &= -\frac{1}{4} \sum_{m \neq n} \tilde{J}_m^n [e^{i\phi_m^n} \hat{\mathbf{s}}_m^- \hat{\mathbf{s}}_n^+ + e^{-i\phi_m^n} \hat{\mathbf{s}}_m^+ \hat{\mathbf{s}}_n^-] \\ &\quad - \frac{1}{2} \sum_{m \neq n} J_m^n \hat{\mathbf{s}}_m^z \hat{\mathbf{s}}_n^z - g\mu_B H \sum_m \hat{\mathbf{s}}_m^z. \end{aligned} \quad (10)$$

H is the strength of the external magnetic field.

From Eq. (9) it is obvious that a magnon accumulates an additional phase ϕ_m^n upon propagation from site m to n , which is brought about by the spin-orbit interaction. This can be viewed as a result of a textured flux within the plaquettes of the kagome lattice [21], similar to the Haldane model for an electronic topological insulator [22]. Thus, we are concerned with a nonzero Berry curvature $\Omega(\mathbf{k})$ (Ref. [23]) and with topological invariants.

For a given set of parameters $\{J_m^n, D_m^n\}$, we solve the eigenproblem of the complete Hamiltonian \mathcal{H} , yielding the magnon dispersion relations $\varepsilon_i(\mathbf{k})$ [wave vector $\mathbf{k} = (k_x, k_y, 0)$, band index i] and the Berry curvature

$$\Omega_j(\mathbf{k}) \equiv i \sum_{i \neq j} \frac{\langle i(\mathbf{k}) | \nabla_{\mathbf{k}} \mathcal{H}(\mathbf{k}) | j(\mathbf{k}) \rangle \times \langle j(\mathbf{k}) | \nabla_{\mathbf{k}} \mathcal{H}(\mathbf{k}) | i(\mathbf{k}) \rangle}{[\varepsilon_i(\mathbf{k}) - \varepsilon_j(\mathbf{k})]^2}. \quad (11)$$

$|i(\mathbf{k})\rangle$ and $\varepsilon_i(\mathbf{k})$ are the eigenvectors and eigenvalues of \mathcal{H} , respectively.

B. Transverse thermal conductivity and Chern numbers

Having solved the magnon Hamiltonian, the transverse thermal conductivity can be computed as follows. By formulating semiclassical equations of motion for magnon wave packets which include the anomalous velocity in terms of the Berry curvature, the intrinsic contribution¹ to the transverse thermal conductivity is expressed as

$$\kappa^{xy} = \frac{k_B^2 T}{(2\pi)^2 \hbar} \sum_i \int_{\text{BZ}} c_2(\varrho_i) \Omega_i^z(\mathbf{k}) dk^2. \quad (12)$$

The sum runs over all bands i in the magnon dispersion relation, and the integral is over the Brillouin zone (BZ). The Bose distribution function ϱ_i enters the function c_2 which is given by

$$c_2(x) \equiv (1+x) \left(\ln \frac{1+x}{x} \right)^2 - (\ln x)^2 - 2 \text{Li}_2(-x). \quad (13)$$

Li_2 is the dilogarithm or Spence function [6,7]. c_2 is depicted in Fig. 2; it accounts via the Bose distribution for the temperature dependence of κ^{xy} .

The transverse thermal conductivity and the Chern number of band i ,

$$C_i \equiv \frac{1}{2\pi} \int_{\text{BZ}} \Omega_i^z(\mathbf{k}) dk^2, \quad (14)$$

differ by constant factors and by the c_2 function in the integrand. This establishes a close connection of the magnon Hall effect with the topology of the magnon dispersion relation in the kagome lattice.

C. Numerical aspects

To calculate the Chern numbers and the transverse thermal conductivity [cf. Eqs. (14) and (12)], a k -space integration has to be performed. All results of this paper are obtained for Gaussian meshes with 2500 points. This gives an accuracy

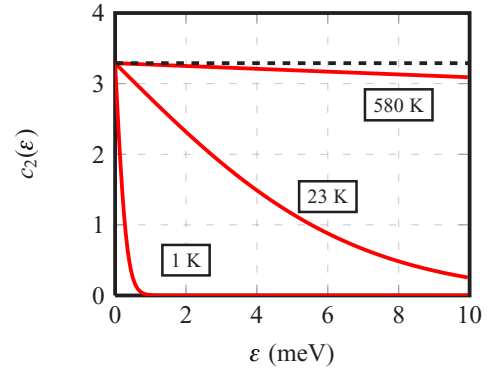


FIG. 2. (Color online) Function $c_2(\varepsilon)$, as defined in Eq. (13), versus energy ε for selected temperatures (as indicated). The broken line marks the high-temperature limit of $\pi^2/3 \approx 3.28987$.

of the (integer) Chern numbers better than 10^{-5} . For almost closed band gaps the Berry curvature gets locally very large [cf. the denominator in Eq. (11)]; in these cases, a refined mesh has to be used: 40 000 points for band gaps less than 0.1 meV.

III. RESULTS AND DISCUSSION

In the following analysis we assume a kagome lattice with all three basis atoms being identical, i.e., identical spin and exchange parameters. We consider the Heisenberg exchange between nearest (J_N) and next-nearest (J_{NN}) sites; the Dzyaloshinskii-Moriya parameters account only for nearest-neighbor interactions (D).

A. Magnon dispersion relation and topological invariants

First, we address the close connection of the magnon band structure, the Chern numbers, and the thermal conductivity. For this purpose, we introduce Chern numbers of isoenergy surfaces

$$C_i(\varepsilon) \equiv \frac{1}{2\pi} \int_{\text{BZ}} \delta(\varepsilon_i - \varepsilon) \Omega_i^z(\mathbf{k}) dk^2 \quad (15)$$

[cf. Eq. (14)] and the corresponding energy-dependent contribution to the transverse thermal conductivity

$$\kappa^{xy}(\varepsilon) = \frac{k_B^2 T}{(2\pi)^2 \hbar} \sum_i \int_{\text{BZ}} \delta(\varepsilon_i - \varepsilon) c_2(\varrho_i) \Omega_i^z(\mathbf{k}) dk^2 \quad (16)$$

[cf. Eq. (12)].

Inspection of Fig. 3 provides that the main contributions to the Chern numbers appear at the band edges of spin-orbit-induced band gaps, that is, where the Berry curvature is largest [cf. the denominator in Eq. (11)]. The total Chern numbers are $C_1 = 1$, $C_2 = 0$, and $C_3 = -1$, indicating that the topological phase of the magnon dispersion is characterized by $(1, 0, -1)$ (the sum over all Chern numbers is zero in any case).

Because the thermal conductivity is mainly given by the Chern numbers weighted by the c_2 function, $\kappa^{xy}(\varepsilon)$ shows the same features as the Chern numbers. However, it decreases towards higher energies due to the energy dependence of c_2 (see Fig. 2). Furthermore, adjacent peaks show opposite signs, leading to a partial cancellation in the total conductivity.

¹The skew scattering contribution is not considered in this paper.

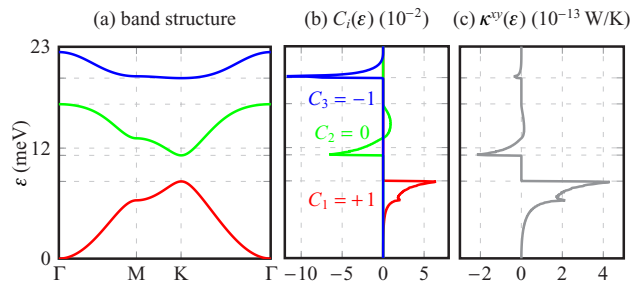


FIG. 3. (Color online) Relation between magnon band structure, Chern numbers, and thermal conductivity. The magnon dispersion relation for $J_N = 4$ meV, $D = 1$ meV, and $J_{NN} = 0$ is shown in (a). The band- and energy-resolved Chern numbers $C_i(\varepsilon)$ and the energy-resolved thermal conductivity $\kappa^{xy}(\varepsilon)$ at $T = 30$ K are displayed in (b) and (c), respectively. The step width of the energy mesh is $1/20$ meV. The energy scale is compressed to account for the finite temperature (cf. Sec. III D).

These findings suggest a way to maximize the thermal conductivity. The requirements comprise (i) a wide energy gap provided by (ii) a large DM constant to obtain large c_2 differences for the band edges, and (iii) a flat first band for a large c_2 . These features yield an absolute boundary of the transverse thermal conductivity at low temperatures. Considering only the first band, i.e., assuming a wide band gap, and approximating the lowest band by $\varepsilon_1(\mathbf{k}) = 0$, for which $c_2(0) = \pi^2/3$ (Fig. 2), one arrives at

$$|\kappa^{xy}| = \left| \sum_n \kappa_n^{xy} \right| < |\kappa_1^{xy}| < \frac{k_B^2 \pi}{6\hbar} T |C_1|, \quad (17)$$

where C_1 is the Chern number of the first band.

B. Topological phase diagram

A topological phase transition is closely related to a band inversion that appears due to a variation of parameters that enter the Hamiltonian: a band gap closes and reopens again, which is accompanied by a (discrete) change of the respective topological invariants (cf. Ref. [24] for an electronic topological insulator). In this section, we discuss the topological phase diagram of the magnon Hamiltonian. Each system is characterized by a set of constants D , J_N , and J_{NN} , from which a point $(J_{NN}/J_N, D/J_N)$ in phase space is defined. It is conceivable that deformation of the lattice or magnetic doping are means to change the topological phase. Some regions of the phase diagram cannot be realized in practice because $D < J_N$ in real systems.

To derive phase boundaries, we write the Hamiltonian as a 3×3 matrix,

$$\mathfrak{H}(\mathbf{k}) = \begin{pmatrix} \mathfrak{H}_{AA}(\mathbf{k}) & \mathfrak{H}_{AB}(\mathbf{k}) & \mathfrak{H}_{AC}(\mathbf{k}) \\ \mathfrak{H}_{AB}^*(\mathbf{k}) & \mathfrak{H}_{AA}(\mathbf{k}) & \mathfrak{H}_{BC}(\mathbf{k}) \\ \mathfrak{H}_{AC}^*(\mathbf{k}) & \mathfrak{H}_{BC}^*(\mathbf{k}) & \mathfrak{H}_{AA}(\mathbf{k}) \end{pmatrix}, \quad (18)$$

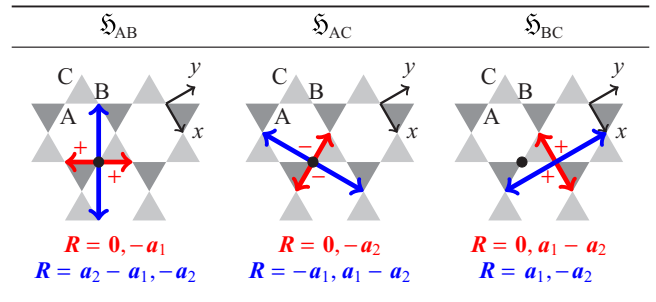


FIG. 4. (Color online) Dzyaloshinskii-Moriya interaction in a kagome lattice. Lattice vectors \mathbf{R} from atom $i = A, B, C$ to the basis of both nearest (red) and next-nearest (blue) neighbors of type $j = A, B, C$ are given by arrows. \pm represent the signs of the Dzyaloshinskii-Moriya interaction, in accordance with the chirality. Lattice vectors \mathbf{a}_1 and \mathbf{a}_2 are defined in Fig. 1(c). The dot (\bullet) denotes the origin of the coordinate system.

with A, B, and C indicating the basis atoms (cf. Figs. 1 and 4). The matrix elements read

$$\mathfrak{H}_{AA}(\mathbf{k}) = 0, \quad (19)$$

$$\mathfrak{H}_{AB}(\mathbf{k}) = -(J_N + iD)s(1 + e^{i(-k_x - \sqrt{3}k_y)/2}) - J_{NN}s(e^{-ik_x} + e^{i(k_x - \sqrt{3}k_y)/2}), \quad (20)$$

$$\mathfrak{H}_{AC}(\mathbf{k}) = -(J_N - iD)s(1 + e^{i(k_x - \sqrt{3}k_y)/2}) - J_{NN}s(e^{ik_x} + e^{i(-k_x - \sqrt{3}k_y)/2}), \quad (21)$$

$$\mathfrak{H}_{BC}(\mathbf{k}) = -(J_N + iD)s(1 + e^{ik_x}) - 2J_{NN}s e^{ik_x/2} \cos\left(\frac{\sqrt{3}}{2}k_y\right). \quad (22)$$

s is the fixed length of the spin vectors ($\hbar = 1$).

A topological phase boundary is obtained by requiring two eigenvalues to be equal. At the K point of the Brillouin zone, e.g., at $\mathbf{k}_K = (-4\pi/3, 0)$, \mathfrak{H} has the form

$$\mathfrak{H}(\mathbf{k}_K) = \begin{pmatrix} 0 & x & x^* \\ x^* & 0 & x \\ x & x^* & 0 \end{pmatrix} \quad (23)$$

with

$$x \equiv -(J_N + iD)s(1 + e^{2\pi i/3}) - 2J_{NN}s e^{2\pi i/3}. \quad (24)$$

Its eigenvalues are

$$\lambda_1 = 2\text{Re}(x), \quad (25)$$

$$\lambda_{2,3} = -\text{Re}(x) \pm \sqrt{3}|\text{Im}(x)|. \quad (26)$$

Thus, the topological phase boundary in terms of the exchange parameters is given by

$$\frac{D}{J_N} = \sqrt{3} \left| 2 \frac{J_{NN}}{J_N} - 1 \right|. \quad (27)$$

Since the degeneracy occurs at each K and K' point of the Brillouin zone, the Chern number of the associated bands changes by $\Delta C = \pm 2$ when crossing this boundary.

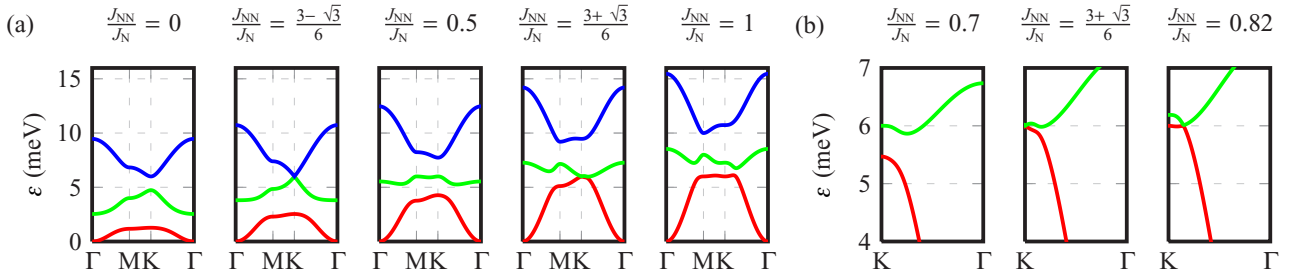


FIG. 5. (Color online) Magnon band structures of a kagome lattice for selected nearest- (N) and next-nearest- (NN) neighbor Heisenberg exchange parameters (as indicated). The Dzyaloshinskii-Moriya parameter D equals $J_N = 1$ meV. (a) Closing and reopening of a band gap at K , from left to right, according to the phase boundary given by Eq. (27). (b) Degeneracy along the Γ - K line. The bands are distinguished by colors.

A numerical analysis of the band structure (Fig. 5) yields two additional phase boundaries [Fig. 6(a)]: a linear and a nonlinear one. The latter approaches the boundary derived analytically as $J_{NN}/J_N \searrow 0.5$. All band degeneracies are located along the Γ - K and Γ - K' lines, respectively. These are parametrized by $\zeta \in [0, 1]$ with $\zeta = 0$ and 1 for Γ and K , respectively [Fig. 6(b)]. The accumulation at the K point arises due to the analytically derived boundary, while the one at Γ is identified with the linear boundary in Fig. 6(a); the eigenvalue analysis of $\mathfrak{H}(0)$ results in

$$\frac{D}{J_N} = \sqrt{3} \left| \frac{J_{NN}}{J_N} + 1 \right|. \quad (28)$$

The nonlinear boundary is associated with the descending curve in Fig. 6(b), indicating that this degeneracy moves

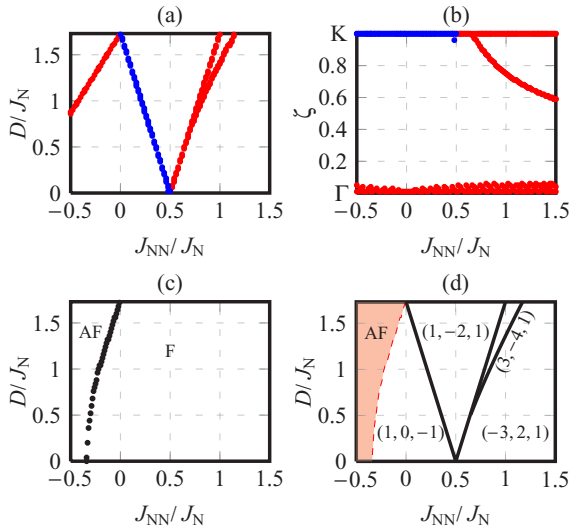


FIG. 6. (Color online) Analysis of band degeneracies. (a) Parameter combinations D/J_N and J_{NN}/J_N for which two neighboring bands are degenerate; red (blue) lines indicate degeneracy of the lower (upper) two bands 1 and 2 (2 and 3). (b) Point of degeneracy, ζ , along Γ - K line as a function of the parameter ratio J_{NN}/J_N . (c) Boundary between antiferromagnetic (AF) and ferromagnetic (F) phases. (d) Complete topological phase diagram with regions characterized by sets (C_1, C_2, C_3) of Chern numbers. The antiferromagnetic phase is colored red.

along Γ - K and Γ - K' [cf. Fig. 5(b) for $D = J_N = 1$ meV and $J_{NN}/J_N = 0.82$]. Because this degeneracy appears six times within the first BZ the Chern numbers of the associated bands change by $\Delta C = \pm 6$. The additional phase boundary caused by a degeneracy at Γ is not of interest for the present study as it is located within the antiferromagnetic phase [Fig. 6(c)]; the antiferromagnetic phase is identified by negative magnon energies at nonzero \mathbf{k} . The resulting topological phase diagram is given in Fig. 6(d).

C. High-temperature limit of the transverse thermal conductivity

In this section we derive the high-temperature limit of the transverse thermal conductivity,

$$\kappa_{\text{lim}}^{xy} \equiv \lim_{T \rightarrow \infty} \kappa^{xy}(T). \quad (29)$$

Although we disregard a ferromagnet-to-paramagnet transition and the influence of magnon-magnon interaction, it turns out that this quantity is helpful in describing MHE systems.

In the rewritten expression

$$\kappa_{\text{lim}}^{xy} = \lim_{T \rightarrow \infty} \left(\frac{\kappa^{xy}(T)}{T} \bigg/ \frac{1}{T} \right), \quad (30)$$

both $\kappa^{xy}(T)/T$ and $1/T$ tend to zero because $c_2(\varrho(\varepsilon, T)) \rightarrow \pi^2/3$ for all ε and the sum of the Chern numbers of all bands vanishes, $\sum_i C_i = 0$. Thus,

$$\lim_{T \rightarrow \infty} \left(\frac{\kappa^{xy}(T)}{T} \right) = \frac{k_B^2}{2\pi\hbar} \frac{\pi^2}{3} \sum_i C_i = 0. \quad (31)$$

By means of l'Hôpital's rule it follows that

$$\begin{aligned} \kappa_{\text{lim}}^{xy} &= \lim_{T \rightarrow \infty} \left(-T^2 \frac{\partial}{\partial T} \frac{\kappa^{xy}(T)}{T} \right) \\ &= -\frac{k_B^2}{(2\pi)^2 \hbar} \lim_{T \rightarrow \infty} \sum_i \int_{\text{BZ}} T^2 \frac{\partial c_2(Q_i)}{\partial T} \Omega_i^z(\mathbf{k}) d\mathbf{k}^2, \end{aligned} \quad (32)$$

with the final expression

$$\kappa_{\text{lim}}^{xy} = -\frac{k_B}{(2\pi)^2 \hbar} \sum_i \int_{\text{BZ}} \varepsilon_i(\mathbf{k}) \Omega_i^z(\mathbf{k}) d\mathbf{k}^2. \quad (34)$$

Even though the high-temperature limit $T \rightarrow \infty$ will never be reached within the ferromagnetic phase, κ_{lim}^{xy} can be used

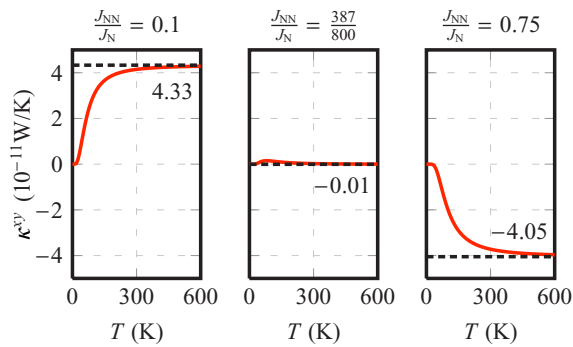


FIG. 7. (Color online) Transverse thermal conductivity κ^{xy} versus temperature T (solid lines) for $D/J_N = 1/4$ and selected ratios J_{NN}/J_N (as indicated), with $J_N = 4$ meV. The values of κ_{lim}^{xy} are given within each panel and represented by broken lines.

as a figure of merit to estimate the maximum magnitude of the thermal conductivity, because $\kappa^{xy}(T)$ rapidly approaches κ_{lim}^{xy} (Fig. 7). In the present cases, κ_{lim}^{xy} is reached at about $T = 300$ K. For the parameters $J_N = 4D = 4$ meV and $J_{NN}/J_N = 387/800$ the high-temperature conductivity is two orders of magnitude smaller than those for the other parameters shown in Fig. 7. The overall width of the conductivity as a function of temperature exceeds the limit insignificantly. A system's high-temperature-limit thermal conductivity is therefore a convenient approximation for the strength of its magnon Hall effect. Systems with high Curie temperature (i.e., of the order of room temperature for the presented results) allow for quantitative prediction as the limit is almost approached. It turns out, however, that for some regions in the phase space κ_{lim}^{xy} does not reproduce the correct sign of the thermal conductivity as a function of temperature, as will be discussed in the following paragraphs. Only the topological phases $(1, 0, -1)$ and $(-3, 2, 1)$ show conductivities with the same sign as the associated high-temperature limit.

To motivate a relation of the high-temperature limit κ_{lim}^{xy} of the transverse thermal conductivity with the topological phase space, we assume a magnonic system with two flat bands; $\varepsilon_i(\mathbf{k}) = \bar{\varepsilon}_i$ ($i = 1, 2$). This approximation yields

$$\kappa_{\text{lim}}^{xy} \propto -\frac{1}{2\pi} \sum_{i=1}^2 \bar{\varepsilon}_i \int_{\text{BZ}} \Omega_i^z(\mathbf{k}) dk^2 = C_1 \Delta\varepsilon, \quad (35)$$

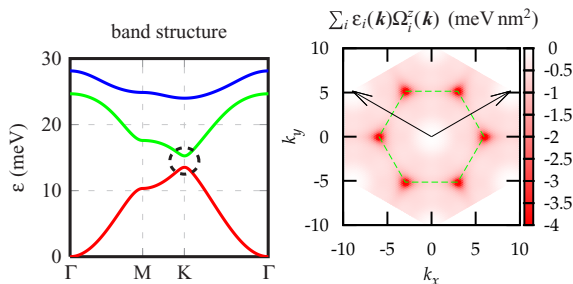


FIG. 8. (Color online) Band structure (left) and integrand of Eq. (34) (right). Arrows represent the reciprocal lattice vectors and the dashed green line indicates the Brillouin zone. $J_N = 10J_{NN} = 8D = 4$ meV.

where $\Delta\varepsilon = \bar{\varepsilon}_2 - \bar{\varepsilon}_1$ denotes the energy gap. This expression states that the sign of κ_{lim}^{xy} is given by the sign of the first band's Chern number C_1 .

In the case of a kagome lattice the above constant-energy approximation is justified as follows. The integrand $\varepsilon_i(\mathbf{k})\Omega_i^z(\mathbf{k})$ contributes sizably to the entire integral mainly in regions of the BZ in which the Berry curvature is large (Sec. III A), that is, at avoided crossings as shown in Fig. 8. If there is a single avoided crossing in each irreducible part of the Brillouin zone (cf. the dashed circle in Fig. 8), the band structure can be approximated as constant at the avoided crossings (in contrast to two or more avoided crossings that are different in energy). By this approximation, κ_{lim}^{xy} reads

$$\kappa_{\text{lim}}^{xy} \propto \begin{cases} -(\bar{\varepsilon}_1 - \bar{\varepsilon}_3) > 0 & (1, 0, -1), \\ -(\bar{\varepsilon}_1 - 2\bar{\varepsilon}_2 + \bar{\varepsilon}_3) & (1, -2, 1), \\ -(3\bar{\varepsilon}_1 - 4\bar{\varepsilon}_2 + \bar{\varepsilon}_3) & (3, -4, 1), \\ -(3\bar{\varepsilon}_1 + 2\bar{\varepsilon}_2 + \bar{\varepsilon}_3) < 0 & (-3, 2, 1). \end{cases}$$

The sign is unique only within the phases $(1, 0, -1)$ and $(-3, 2, 1)$ since $\bar{\varepsilon}_3 > \bar{\varepsilon}_2 > \bar{\varepsilon}_1$. In the other phases, the sign of the conductivity depends on the ratios of the energies $\bar{\varepsilon}_i$ and is not fixed. This, admittedly, crude approximation is corroborated by the numerical results shown in Fig. 9, where the line of vanishing high-temperature-limit conductivity is found within the phase $(1, -2, 1)$.

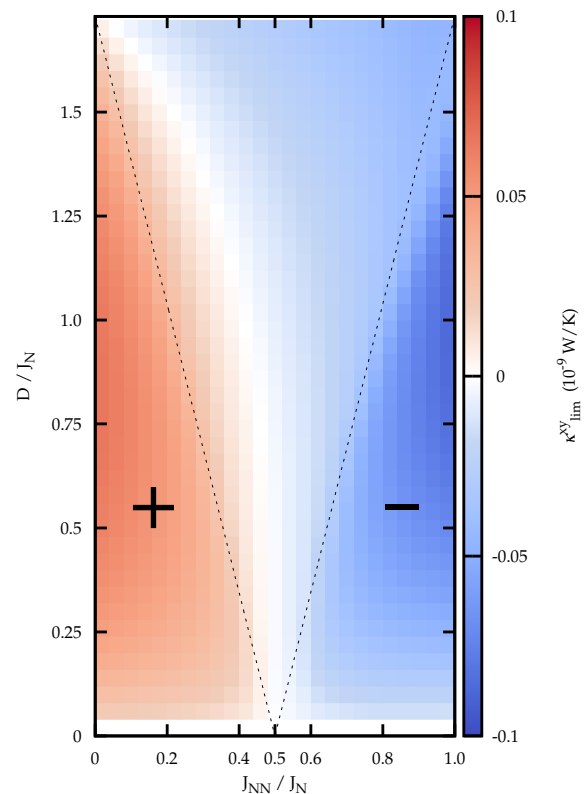


FIG. 9. (Color online) Topological phase diagram of the high-temperature transverse thermal conductivity κ_{lim}^{xy} , shown as color scale (right). Regions with positive (negative) values are marked + (-). The broken lines represent the analytically derived phase boundaries given by Eq. (27).

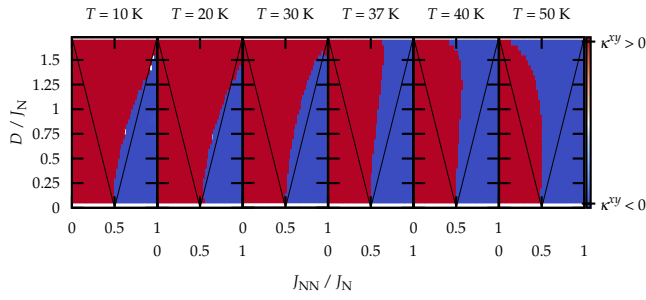


FIG. 10. (Color online) Sign of the transverse thermal conductivity κ^{xy} within the topological phase space for selected temperatures T (as indicated). $J_N = 4$ meV.

The above findings open up possibilities of changing a system's transverse thermal conductivity and heat current direction. Traversing through the phase diagram will lead to a change of the magnitude or even the sign of the thermal conductivity. Only systems with specific combinations of exchange parameters show a change of sign of the thermal conductivity with temperature. These combinations are located within the region that is covered by the line of zero κ^{xy} versus temperature (Fig. 10). In this phase-space region the conductivity shows a positive local maximum at low temperatures, although it converges to a negative limit (Fig. 11).

D. Application to $\text{Lu}_2\text{V}_2\text{O}_7$

Having studied the fundamental properties of the MHE in two-dimensional kagome lattices in the preceding sections, we proceed with an application to the three-dimensional pyrochlore $\text{Lu}_2\text{V}_2\text{O}_7$. Instead of considering a “true” three-dimensional lattice, we treat the system as a stack of non-interacting kagome layers. This allows the application of the methods derived so far, in particular the classification by Chern numbers [cf. the topological phase diagram in Fig. 6(d)].

To come closer to the experiment, the temperature dependence of the magnetization has to be considered. This could be done within a microscopic picture, that is, by considering the thermal fluctuations of the local spins which could enter the

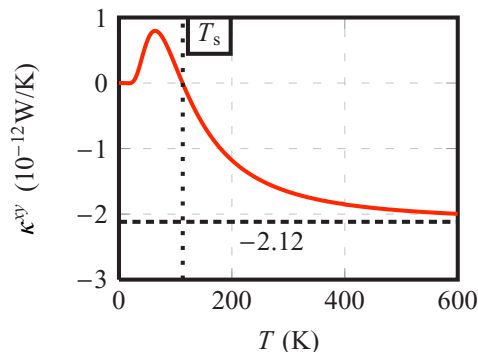


FIG. 11. (Color online) Transverse thermal conductivity κ^{xy} versus temperature T for $J_{\text{NN}}/J_N = 1/2$, $D/J_N = 1/4$, and $J_N = 4$ meV (solid line). The dashed line represents the limit $\kappa_{\text{lim}}^{xy} = -2.12 \times 10^{-12}$ W/K; the dotted line marks the temperature $T_s = 113$ K of vanishing conductivity.

exchange parameters [25,26]. For the time being, we restrict ourselves to a macroscopic picture. To be more specific, we assume that the spins s scale with temperature in the same way as the magnetization,

$$s \rightarrow s \left(1 - \frac{T}{T_C}\right)^\beta, \quad (36)$$

with the critical temperature $T_C = 70$ K (Ref. [5]) and the critical exponent $\beta = 0.362$ (Ref. [27]).

From the Curie temperature T_C , the spin-wave stiffness $D_S = 21$ meV \AA^2 , and the lattice constant $a = 7.024$ \AA , we determine the Heisenberg exchange parameter to $J_N = 3.405$ meV. J_{NN} is set to zero, so that there is no interaction between adjacent kagome planes.

To compare the thermal conductivity $\kappa_{2\text{D}}^{xy}$ of a two-dimensional system with that of the associated three-dimensional one, $\kappa_{3\text{D}}^{xy}$, we introduce a characteristic length l which equals the spacing of (111) lattice planes. The red triangles in Fig. 1(a) suggest that l is twice as large as the height of a tetrahedron with an edge length of $a/2$; hence, $\kappa_{3\text{D}}^{xy} = \kappa_{2\text{D}}^{xy}/l$ with $l = \sqrt{6}a/3$.

Now we compare the theoretical transverse thermal conductivity with its experimental counterpart [5], with the strength D of the DM interaction as the only parameter. For realistic values of D , $\text{Lu}_2\text{V}_2\text{O}_7$ is within the $(1, 0, -1)$ topological phase and exhibits a MHE with positive transverse thermal conductivity, in agreement with experiment.

The comparison is shown in Fig. 12, for two selected values of $D = \sqrt{6}/2\tilde{D}$ [cf. Eq. (6)]. The magnetic field was chosen slightly larger than the saturation field determined by Onose *et al.* (Ref. [5]). Reasonable agreement is found for $\tilde{D}/J_N = 0.39\% - 0.56\%$, that is, for parameters two orders of magnitude smaller than those deduced by Onose *et al.*, who derived $\tilde{D}/J_N = 32\%$. A density functional calculation for

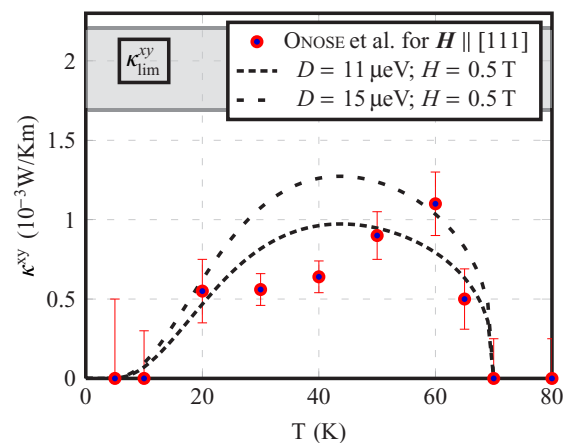


FIG. 12. (Color online) Transverse thermal conductivity κ^{xy} of $\text{Lu}_2\text{V}_2\text{O}_7$ versus temperature T . Theoretical data for Dzyaloshinskii-Moriya interactions $D = 11$ μeV (dashed line) and 15 μeV (wide-dashed line) are compared with experimental data from Ref. [5] (dots). The external magnetic field of 0.5 T is chosen slightly larger than the saturation field in the experiment. The range of the high-temperature limits of κ^{xy} is indicated by the gray area.

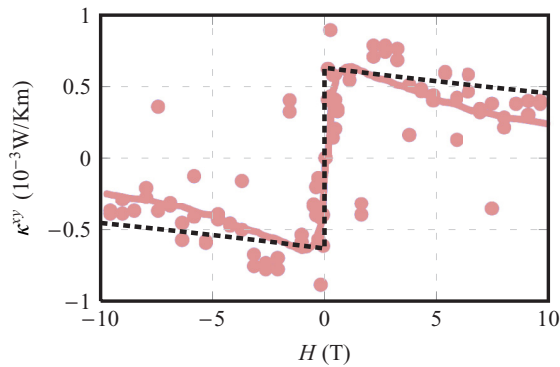


FIG. 13. (Color online) Transverse thermal conductivity κ^{xy} of $\text{Lu}_2\text{V}_2\text{O}_7$ versus applied magnetic field H along [111] at $T = 20$ K. The theoretical result has been obtained for Dzyaloshinskii-Moriya interaction $D = 15 \mu\text{eV}$ (broken line). Experimental data (red dots) for the magnetic field direction along [100] are reproduced from Ref. [5].

$\text{Y}_2\text{V}_2\text{O}_7$, which possesses magnetic properties similar to those of $\text{Lu}_2\text{V}_2\text{O}_7$, by Xiang *et al.* (Ref. [28]), yields $\tilde{D}/J_N = 5\%$.

We attribute the mismatch between our \tilde{D}/J_N ratio and the one obtained in Ref. [5] to the approximation of the three-dimensional systems by a stacking of noninteracting kagome planes. For example, disregarding the fourth basis atom of the pyrochlore basis reduces the bandwidths of the magnons; as a consequence, avoided crossings which give the major contributions to the conductivity are too low in energy. Thus, the c_2 function is too large, which has to be compensated by a reduced DM interaction.

In contrast, the approximation in Ref. [5] causes an overestimation of the DM interaction: in a model for a pyrochlore lattice, only contributions of the lowest-energy band at the Γ point (Goldstone mode) have been considered. Thus, the sizable contributions of the avoided crossings at higher energies are omitted (cf. Fig. 3). This approximation is valid for very small temperatures, as is evident from the rapid decrease of c_2 ; it is questionable for elevated temperature because c_2 is sizable at higher energies (compare $T = 1$ K with

$T = 23$ K in Fig. 2). We recall that the experimental data used for estimating D/J in Ref. [5] were taken at $T = 20$ K, for which c_2 cannot be safely neglected at the avoided crossings. To compensate for the missing contributions, the value of the Berry curvature around the Γ point is estimated too large and so the DM constant \tilde{D} is overestimated.

Neither the approximation in Ref. [5] nor ours takes into account magnon-magnon or magnon-phonon interactions which may influence the transverse thermal conductivity of $\text{Lu}_2\text{V}_2\text{O}_7$ at temperatures close to its Curie temperature. The mismatches of the \tilde{D}/J_N ratio can be explained by the approximations discussed in the preceding paragraphs.

Finally, we address the dependence of the transverse thermal conductivity on the strength of the applied magnetic field (Fig. 13). The experimental data were obtained for a magnetic field applied in the [100] direction, in contrast to theory ([111] direction), thus complicating a quantitative analysis. Nevertheless, the overall trend—namely, the gradual decrease of the conductivity (in absolute value) for increasing magnetic field—is reproduced. It is explained by the Zeeman term in the Hamiltonian [Eq. (10)] which shifts the entire magnonic band structure towards larger energies and, therefore, to regions with smaller c_2 (Fig. 2).

IV. OUTLOOK

Having analyzed kagome lattices in this paper, an evident extension of our study is to pyrochlore crystals in which all exchange interactions are considered. An important issue is the negative transverse thermal conductivity of $\text{In}_2\text{Mn}_2\text{O}_7$ (Ref. [29]), in contrast to the positive ones of $\text{Lu}_2\text{V}_2\text{O}_7$ and $\text{Ho}_2\text{V}_2\text{O}_7$; this needs to be explained by a topological phase diagram. With a phase diagram at hand, one should be able to predict systems with a strong magnon Hall effect.

It appears of great interest to find a kagome system with exchange parameters that are located in a region in which the conductivity changes sign. In this paper we have given a recipe for such a material. Its overall transverse thermal conductivity is, however, one order of magnitude smaller than that of $\text{Lu}_2\text{V}_2\text{O}_7$, which calls for advanced measurement techniques.

-
- [1] C. L. Chien and C. R. Westgate, *The Hall Effect and Its Applications* (Plenum, New York, 1980).
 - [2] *CRC Handbook of Thermoelectrics*, edited by D. M. Rowe (CRC Press, Boca Raton, FL, 1995).
 - [3] R. S. Popovic, *Hall Effect Devices* (IOP Publishing, London, 2004).
 - [4] C. Strohm, G. L. J. A. Rikken, and P. Wyder, *Phys. Rev. Lett.* **95**, 155901 (2005).
 - [5] Y. Onose, T. Ideue, H. Katsura, Y. Shiomi, N. Nagaosa, and Y. Tokura, *Science* **329**, 297 (2010).
 - [6] R. Matsumoto and S. Murakami, *Phys. Rev. Lett.* **106**, 197202 (2011).
 - [7] R. Matsumoto and S. Murakami, *Phys. Rev. B* **84**, 184406 (2011).
 - [8] L. Zhang, J. Ren, J.-S. Wang, and B. Li, *Phys. Rev. B* **87**, 144101 (2013).
 - [9] H. Hasan and C. Kane, *Rev. Mod. Phys.* **82**, 3045 (2010).
 - [10] X.-L. Qi and S.-C. Zhang, *Rev. Mod. Phys.* **83**, 1057 (2011).
 - [11] M. Z. Hasan and J. E. Moore, *Annu. Rev. Condens. Matter Phys.* **2**, 55 (2011).
 - [12] D. Xiao, M.-C. Chang, and Q. Niu, *Rev. Mod. Phys.* **82**, 1959 (2010).
 - [13] R. Resta, *Rev. Mod. Phys.* **66**, 899 (1994).
 - [14] W. Heisenberg, *Z. Phys.* **49**, 619 (1928).
 - [15] I. Dzyaloshinsky, *J. Phys. Chem. Solids* **4**, 241 (1958).
 - [16] T. Moriya, *Phys. Rev.* **120**, 1 (1960).
 - [17] F. J. Dyson, *Phys. Rev.* **102**, 1217 (1956).
 - [18] Y. Yoshida, S. Schröder, P. Ferriani, D. Serrate, A. Kubetzka, K. von Bergmann, S. Heinze, and R. Wiesendanger, *Phys. Rev. Lett.* **108**, 087205 (2012).
 - [19] M. Elhajal, B. Canals, R. Sunyer, and C. Lacroix, *Phys. Rev. B* **71**, 094420 (2005).

- [20] V. N. Kotov, M. Elhadj, M. E. Zhitomirsky, and F. Mila, *Phys. Rev. B* **72**, 014421 (2005).
- [21] H. Katsura, N. Nagaosa, and P. A. Lee, *Phys. Rev. Lett.* **104**, 066403 (2010).
- [22] F. D. M. Haldane, *Phys. Rev. Lett.* **61**, 2015 (1988).
- [23] M. V. Berry, *Proc. R. Soc. London, Ser. A* **392**, 45 (1984).
- [24] P. Barone, T. Rauch, D. Di Sante, J. Henk, I. Mertig, and S. Picozzi, *Phys. Rev. B* **88**, 045207 (2013).
- [25] D. Böttcher, A. Ernst, and J. Henk, *J. Magn. Magn. Mater.* **324**, 610 (2012).
- [26] A. Szilva, M. Costa, A. Bergman, L. Szunyogh, L. Nordström, and O. Eriksson, *Phys. Rev. Lett.* **111**, 127204 (2013).
- [27] C. Holm and W. Janke, *Phys. Rev. B* **48**, 936 (1993).
- [28] H. J. Xiang, E. J. Kan, M. H. Whangbo, C. Lee, S.-H. Wei, and X. G. Gong, *Phys. Rev. B* **83**, 174402 (2011).
- [29] T. Ideue, Y. Onose, H. Katsura, Y. Shiomi, S. Ishiwata, N. Nagaosa, and Y. Tokura, *Phys. Rev. B* **85**, 134411 (2012).

5.2.2. Edge states in topological magnon insulators

While the previous publication focused on the transverse thermal conductivity, this publication is concerned with topologically protected magnons. Green function renormalization (see Sec. 4.1) is used to calculate the magnon edge spectrum of a semi-infinite kagome crystal. Again, the ratio of the exchange interaction between nearest and second-nearest neighbors is used as a parameter to traverse the topological phase diagram.

Extending Ref. [23], where the kagome Chern insulator was studied without second-nearest neighbor exchange interaction, the validity of the bulk-boundary correspondence [82, 83] is demonstrated for topological magnon insulators (Sec. 3.2.1). Irrespective of the details of the edge, there are $w_j = \sum_{i<j} C_i$ topological edge magnons within the j -th band gap, where C_i is the Chern number of the i -th band. The “details” of the edge not only comprise the edge’s normal but also perturbations renormalizing the exchange constants. If the exchange and DM interactions at the edge differ from those in the bulk, the dispersion of the edge magnons (topologically trivial as well as nontrivial) is severely influenced. However, the fundamental property of the topologically nontrivial states, more precisely, that they connect adjacent bulk bands, is protected. In particular, the hybridization of a topologically nontrivial mode with a trivial mode is demonstrated, resulting in a nontrivial mode with doubled periodicity in reciprocal space. Thus, this work demonstrated that the topological properties of electronic Chern insulators are expected also for magnonic Chern insulators (at low temperatures, when the single-magnon picture is valid).

Furthermore, it is shown that the propagation direction of the topological edge magnons is connected with the sign of the thermal Hall conductivity (see *Pub. 1*), although all states (especially, those in the bulk) contribute to transport. Thus, within certain topological phases the Chern numbers (and the winding numbers) allow to estimate the direction of the Hall transport. It is pointed out, however, that the reverse is not true: edge magnons are *not* necessary for thermal magnon Hall transport. Topologically trivial magnon bulk bands (all Chern numbers zero) can possess nonzero Berry curvature²⁵. Thus, there are no topologically protected edge magnons but a nonvanishing thermal Hall transport (see, e. g., Ref. [177]).

²⁵This is the case, for example, in the Haldane model by tuning the \mathcal{P} and \mathcal{T} symmetry breaking parameters (see Sec. 3.2.1).

Edge states in topological magnon insulators

Alexander Mook,¹ Jürgen Henk,² and Ingrid Mertig^{1,2}

¹Max-Planck-Institut für Mikrostrukturphysik, D-06120 Halle (Saale), Germany

²Institut für Physik, Martin-Luther-Universität Halle-Wittenberg, D-06099 Halle (Saale), Germany

(Received 15 May 2014; revised manuscript received 27 June 2014; published 18 July 2014)

For magnons, the Dzyaloshinskii-Moriya interaction accounts for spin-orbit interaction and causes a nontrivial topology that allows for topological magnon insulators. In this theoretical investigation we present the bulk-boundary correspondence for magnonic kagome lattices by studying the edge magnons calculated by a Green function renormalization technique. Our analysis explains the sign of the transverse thermal conductivity of the magnon Hall effect in terms of topological edge modes and their propagation direction. The hybridization of topologically trivial with nontrivial edge modes enlarges the period in reciprocal space of the latter, which is explained by the topology of the involved modes.

DOI: [10.1103/PhysRevB.90.024412](https://doi.org/10.1103/PhysRevB.90.024412)

PACS number(s): 66.70.-f, 75.30.-m, 75.47.-m, 85.75.-d

I. INTRODUCTION

Understanding the physics of electronic topological insulators has developed enormously over the past 30 years: spin-orbit interaction induces band inversions and, thus, yields nonzero topological invariants as well as edge states that are protected by symmetry [1–3]. During this development the concept of Berry curvature [4] and Chern numbers has arisen in various contexts and laws of condensed matter physics. This led for example to the formulation of the bulk-boundary correspondence [5]. Topological arguments and concepts—gained mostly from studies of electronic systems [6]—are applicable to phononic and magnonic systems as well: the phonon Hall effect [7] was successfully explained in terms of Berry curvature and topology [8,9].

Recently, the magnon Hall effect (MHE) was discovered in the insulating ferromagnet $\text{Lu}_2\text{V}_2\text{O}_7$ with pyrochlore lattice structure [10]. The transverse heat current upon application of a longitudinal temperature gradient was explained by uncompensated net magnon edge currents that are mathematically described in terms of the Berry curvature [11,12]. The edge currents originate from the topology of the “topological magnon insulator” [13]. The nontrivial topology is brought about by the spin-orbit interaction which manifests itself as Dzyaloshinskii-Moriya (DM) contribution to the exchange interaction of localized magnetic moments. The Dzyaloshinskii-Moriya interaction shows up in systems without inversion center—as is the case in the aforementioned pyrochlore lattice or in its two-dimensional counterpart, the kagome lattice (Fig. 1).

The rich topology of the kagome lattice not only puts forward itself for an investigation of the bulk-boundary correspondence but also affects crucially the magnon Hall effect. Therefore, a detailed understanding of the MHE in the kagome lattice is a prerequisite for investigations of pyrochlore lattices, such as $\text{Lu}_2\text{V}_2\text{O}_7$.

In this paper, we report on such a study. We focus on two topological phases in which the sign of the transverse thermal conductivity—and hence the direction of the resulting heat current—is unique [14]. We explicitly show the correspondence of thermal Hall conductivity with the propagation direction of the nontrivial edge states. Furthermore, we establish that hybridization of topologically trivial with nontrivial edge

modes causes a doubling of the period of the latter in reciprocal space.

The paper is organized as follows. In Sec. II we sketch the quantum-mechanical description of magnons in kagome lattices (Sec. II A), Berry curvature and Chern number (Sec. II B), and the Green function renormalization method for calculating edge states in semi-infinite systems (Sec. II C). Results are presented in Sec. III: edge states of the semi-infinite kagome lattice for different edges and different topological phases (Sec. III A), the connection between the edge modes and the sign of the thermal Hall conductivity (Sec. III B), as well as the hybridization of topologically trivial and nontrivial edge states (Sec. III C). An outlook is given in Sec. IV.

II. THEORY

A. Model Hamiltonian for magnons in a kagome lattice

A two-dimensional kagome lattice is composed of a three-atomic basis which is arranged at the corners of an equilateral triangle with side length equal to half of the lattice constant a (Fig. 1). The lattice vectors read

$$\mathbf{a}_1 = \frac{a}{2}(\mathbf{x} + \sqrt{3}\mathbf{y}), \quad (1a)$$

$$\mathbf{a}_2 = \frac{a}{2}(-\mathbf{x} + \sqrt{3}\mathbf{y}) \quad (1b)$$

in Cartesian coordinates.

Magnons in the kagome lattice are described by a quantum-mechanical Heisenberg model [15] with Hamiltonian

$$\mathcal{H} = \mathcal{H}_H + \mathcal{H}_{DM} + \mathcal{H}_{\text{ext}}. \quad (2)$$

In the isotropic symmetric spin-spin interaction, i.e., the Heisenberg exchange

$$\mathcal{H}_H = - \sum_{n \neq m} J_m^n \hat{\mathbf{s}}_m \cdot \hat{\mathbf{s}}_n, \quad (3)$$

two spin operators $\hat{\mathbf{s}}_m$ and $\hat{\mathbf{s}}_n$ at sites n and m are coupled by symmetric exchange parameters $J_m^n = J_n^m$. The eigenvectors

$$|\mathbf{k}\rangle = \frac{1}{\sqrt{N}} \sum_m e^{i\mathbf{k}\cdot\mathbf{R}_m} |\mathbf{R}_m\rangle \quad (4)$$

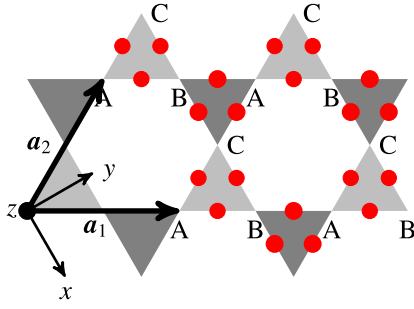


FIG. 1. (Color online) Kagome lattice with lattice vectors \mathbf{a}_1 and \mathbf{a}_2 in the xy plane. Identical atoms A, B, and C are placed at the corners of the triangles. Dzyaloshinskii-Moriya vectors are aligned normal to the lattice plane and are represented by red dots: along $+z$ ($-z$) for a counterclockwise (clockwise) chirality: A-B-C (C-B-A).

of \mathcal{H}_H are “one-magnon states”; they expose magnons as collective excitations because the spin deviation of \hbar is distributed uniformly over all N spins. \mathbf{R}_m is the vector pointing to lattice site m and $|\mathbf{R}_m\rangle$ denotes the state with all spins aligned along the ferromagnetic ground state except the one at lattice site m ; its z component is reduced by \hbar .

The second contribution in Eq. (2),

$$\mathcal{H}_{\text{DM}} = \sum_{m \neq n} \mathbf{D}_m^n (\hat{\mathbf{s}}_m \times \hat{\mathbf{s}}_n), \quad (5)$$

accounts for the antisymmetric Dzyaloshinskii-Moriya (DM) interaction [16,17]. \mathbf{D}_m^n is the DM vector between sites m and n ($\mathbf{D}_m^n = -\mathbf{D}_n^m$).

For completeness, we introduce the coupling to an external magnetic field \mathbf{H} ,

$$\mathcal{H}_{\text{ext}} = -g\mu_B \sum_n \mathbf{H} \cdot \hat{\mathbf{s}}_n. \quad (6)$$

g and μ_B denote the g factor of electrons and Bohr’s magneton, respectively. For the problems treated in this study, this contribution is irrelevant; it is, however, needed in the description of the magnon Hall effect (e.g., Ref. [14]). Likewise, neither magnetocrystalline anisotropy nor magnon-magnon interaction are considered in this paper.

B. Berry curvature and Chern numbers

According to Moriya’s symmetry rules [17], the DM vectors \mathbf{D}_m^n are perpendicular to the kagome lattice, that is, they are aligned along the z direction. Their orientation is given by the chirality of the triangles in the kagome lattice: those with counterclockwise (clockwise) chirality point along $+z$ ($-z$) direction (cf. the red dots in Fig. 1).

Because of the DM interaction a magnon accumulates an additional phase upon propagation from site m to n (cf. the supplemental online material of Ref. [10]). This can be viewed as a result of a textured flux within the plaquettes of the kagome lattice [18], in analogy to the Haldane model for an electronic topological insulator [19]. Thus we are concerned with a nonzero Berry curvature $\mathbf{\Omega}(\mathbf{k})$ (Ref. [4]) and with topological invariants. Please note the difference to models for strongly correlated electrons on a kagome lattice with spin anisotropy,

in which the Berry phase and the electronic edge modes are brought about by statically tilted spins [20].

For a given set of parameters $\{J_m^n, \mathbf{D}_m^n\}$, we solve the eigenproblem for the Hamiltonian \mathcal{H} . From the computed eigenvectors $|i(\mathbf{k})\rangle$ and dispersion relations $\varepsilon_i(\mathbf{k})$ [wave vector $\mathbf{k} = (k_x, k_y)$, band index i] the Berry curvature

$$\mathbf{\Omega}_j(\mathbf{k}) \equiv \mathbf{i} \sum_{i \neq j} \frac{\langle i(\mathbf{k}) | \nabla_{\mathbf{k}} \mathcal{H}(\mathbf{k}) | j(\mathbf{k}) \rangle \times \langle j(\mathbf{k}) | \nabla_{\mathbf{k}} \mathcal{H}(\mathbf{k}) | i(\mathbf{k}) \rangle}{[\varepsilon_i(\mathbf{k}) - \varepsilon_j(\mathbf{k})]^2} \quad (7)$$

and the Chern numbers

$$C_j \equiv \frac{1}{2\pi} \int_{\text{BZ}} \Omega_j^z(\mathbf{k}) dk^2 \quad (8)$$

are calculated for each band j . We recall that these are determined solely by the magnonic band structure of the bulk.

C. Edge magnons

For investigating magnonic edge modes we consider a semi-infinite solid. Thereby, finite-size effects that show up in a slab (stripe) calculation are avoided; for example, hybridization of edge states at opposite edges could result in artificial band gaps.

The magnon band structure is analyzed in terms of the spectral density:

$$N_n(\varepsilon, \mathbf{k}) = -\frac{1}{\pi} \lim_{\eta \rightarrow 0^+} \text{Im tr } G_{nm}(\varepsilon + i\eta, \mathbf{k}) \quad (9)$$

for site n . The limit $\eta \searrow 0$ is not taken but $\eta = 0.005$ meV.

The blocks G_{nm} of the Green function of the semi-infinite system are computed by a renormalization technique [21] which is briefly sketched now. The system is decomposed into principal layers for which the exchange interaction is only among adjacent principal layers. Restricted to nearest- and next-nearest-neighbor interactions, the thinnest principal layers possible are shown in Fig. 2 for two different edges.

In terms of the principal layers, the blocks of the Green’s matrix for the semi-infinite system fulfill

$$\delta_{nm} = \sum_{j=0}^{\infty} (z \delta_{nj} - H_{nj}) \cdot G_{jm}, \quad n, m \geq 0, \quad (10)$$

where $z = \varepsilon + i\eta$. The dimension of each block matrix is the number of basis atoms in a principal layer. The diagonal blocks H_{nn} comprise the intralayer interactions within the n th principal layer; in particular, H_{00} is the Hamilton matrix with interactions within the surface layer (red layer in Fig. 2 labeled “0th layer”). The interlayer couplings are comprised in $H_{n,n+1}$; for example, H_{01} is for the interaction between the surface layer and the subsurface layer (red and blue in Fig. 2). By construction of the principal layers, $H_{nm} = 0$ for $|n - m| \geq 2$.

From Eq. (10), one eliminates all blocks G_{nm} with odd principal-layer indices (e.g., the blue layers in Fig. 2); the result is an equation with identical form but with renormalized blocks H_{nm} . By repeating this elimination process, the interlayer interactions can iteratively be reduced ($\|H_{nm}\| \rightarrow 0$). From the renormalized Hamilton matrix which is effectively block diagonal, we calculate the layer-diagonal Green-function

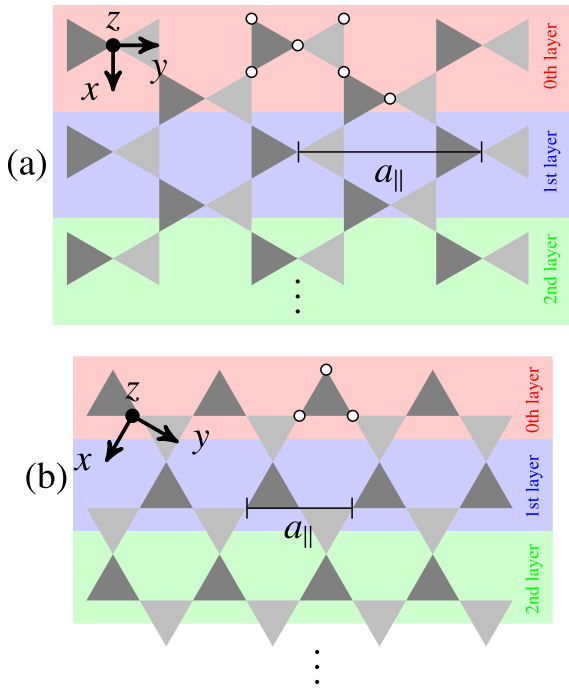


FIG. 2. (Color online) Edges of the kagome lattice. For two different terminations of the bulk system, (a) and (b), the semi-infinite lattice is divided into the thinnest principal layers possible if only nearest- and next-nearest-neighbor interactions are present. White dots show the basis consisting of six (a) and three (b) sites, respectively. The lattice constants a_{\parallel} are indicated.

blocks by

$$G_{nn} = (z - H_{nn})^{-1}. \quad (11)$$

All other G_{nm} are accessible by transfer matrices.

III. RESULTS AND DISCUSSION

In the following analysis we assume a kagome lattice with all three basis atoms being identical, i.e., with identical spin and exchange parameters; an exception is Sec. III C. We consider the Heisenberg exchange between nearest (J_N) and next-nearest (J_{NN}) sites; the Dzyaloshinskii-Moriya parameters account only for nearest-neighbor interactions (D).

A. Bulk-boundary correspondence

As investigated recently [14], the kagome lattice with ferromagnetic ground state shows four topologically different phases, with variables J_{NN}/J_N and D/J_N . These phases are distinguished by the triple of Chern numbers (C_1, C_2, C_3) of the three magnon bulk bands (Fig. 3) [22]. Note that the phase diagram results from analyzing an infinite crystal (bulk).

We now consider semi-infinite systems by introducing an edge according to Fig. 2(a). The local spectral density $N_n(\varepsilon, \mathbf{k})$ is calculated for four different sets of parameters which put the system into the four different topological phases [Figs. 4(a)–4(d)]. More precisely, we chose $\{J_{NN}/J_N, D/J_N\} = \{0, 1\}$, $\{\frac{1}{2}, 1\}$, $\{0.81, 1\}$, and $\{1, 1\}$, all of which are marked by the red dots in Fig. 3.

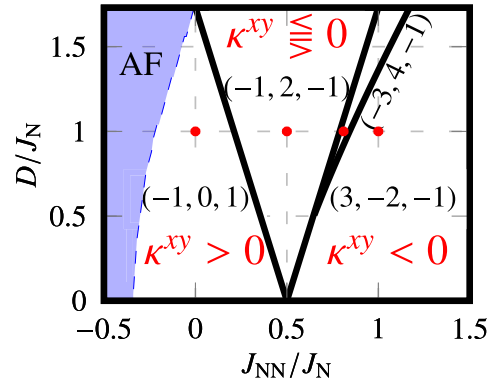


FIG. 3. (Color online) Topological phase diagram of the kagome lattice with regions characterized by sets (C_1, C_2, C_3) of Chern numbers. The antiferromagnetic (AF) phase is colored blue. Red dots mark those variable sets $\{J_{NN}/J_N, D/J_N\}$ for which local densities of states are calculated. The sign of the transverse thermal conductivity κ^{xy} of the magnon Hall effect is given in red; it is unique for the phases $(-1, 0, 1)$ and $(3, -2, -1)$.

The three magnon bulk bands are separated from each other by gaps generated by the Dzyaloshinskii-Moriya interaction. Topologically nontrivial edge modes are easily identified as bands that cross these band gaps and, thus, connect adjacent bulk bands. Furthermore, they are robust against variations of the exchange parameters at the edge. The edge states are singly degenerate and decay rapidly towards the bulk (Fig. 5). The atomic-layer-resolved spectral density clearly shows a localization of the edge state at the first 20 atomic layers (blue histogram in Fig. 5). The magnon edge resonance shows features up to the 300th atomic layer (green histogram in Fig. 5).

In contrast to electronic \mathbb{Z}_2 topological insulators—which rely on time-reversal invariance—magnonic edge modes do not occur in Kramers pairs. This is readily explained by the fact that a single spin orientation is present in the system (here: ferromagnetic ground state with spins along the $+z$ direction). We recall that time reversal changes the sign of \mathbf{k} and reverses the spin orientation. A reversal of the spin orientation alters the signs of all Chern numbers, which has the consequence that the propagation direction of the topologically nontrivial edge modes is reversed as well. These “reversed” edge states can be regarded as the time-reversed (Kramers) partners in an electronic \mathbb{Z}_2 topological insulator.

The topological phase—specified by its set of Chern numbers—is of particular importance for the topologically nontrivial edge modes as it determines both their propagation direction and their number. This is the “bulk-boundary correspondence” [1, 5, 23]: a bulk property, i.e., the Chern numbers, dictates surface properties, i.e., the edge magnons. The sum of Chern numbers up to the i th band,

$$v_i \equiv \sum_{j \leq i} C_j, \quad (12)$$

is the “winding number” of the edge states in band gap i (cf. Refs. [5] and [23]). In other words, $|v_i|$ is the number of topologically nontrivial edge states in the i th band gap; their propagation direction is given by $\text{sgn}(v_i)$. We emphasize that

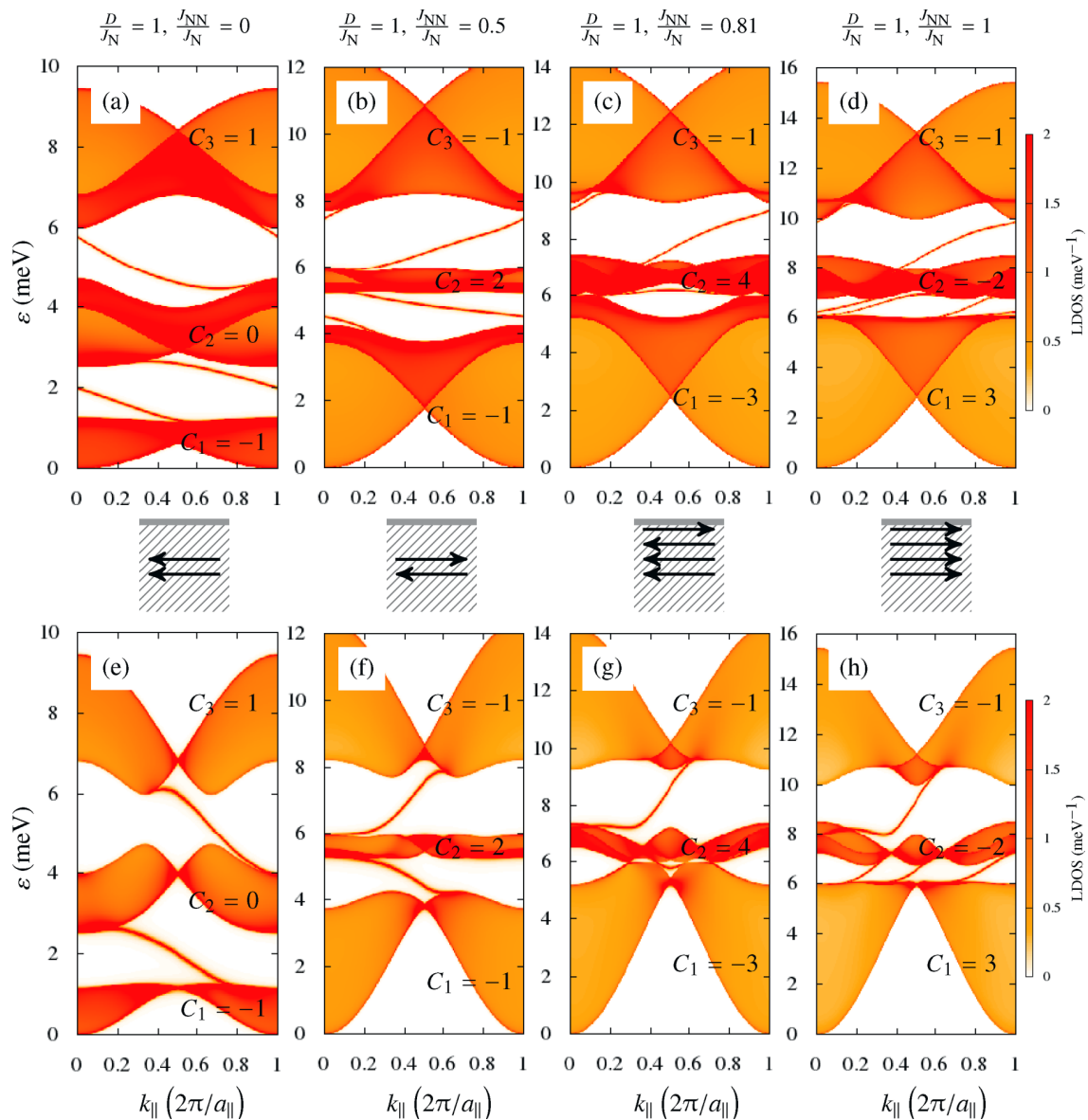


FIG. 4. (Color online) Edge magnons in a kagome lattice. The spectral density of states of an edge site is shown as color scale [“local density of states” (LDOS), right] for the edge geometries of Fig. 2(a) [top row, (a)–(d)] and Fig. 2(b) [bottom row, (e)–(h)] in the entire edge Brillouin zone. Bulk magnons appear as extended regions separated by band gaps (“projected bulk band structure”), while edge magnons bridge these band gaps. The topological phases are characterized by their bulk-band-resolved Chern numbers C_i ($i = 1, 2, 3$) given in each panel; the respective exchange parameters are given as well ($J_N = 1$ meV). The topologically nontrivial edge magnon modes and their propagation direction are sketched in the central row.

the geometry of the edge is irrelevant for these fundamental features.

We illuminate the above rule by considering as an example the topological phase $(-1, 2, -1)$. For both edge geometries [Figs. 4(b) and 4(f)], there is a single nontrivial edge mode with negative dispersion (slope) within the lowest energy gap because $\nu_1 = C_1 = -1$. In the second band gap there is a single edge mode with positive dispersion, in accordance with $\nu_2 = C_1 + C_2 = 1$. Because the sum over all Chern numbers vanishes— $\nu_n = \sum_i^n C_i = 0$, where $n = 3$ is the total number of bands—there are never topological nontrivial edge states above the uppermost band. These relations hold also for the

other topological phases, as is evident from the other panels of Fig. 4.

B. Edge modes and magnon Hall effect

The magnon Hall effect (MHE) is a transverse heat current upon application of a temperature gradient which was discovered for the ferromagnetic insulator $\text{Lu}_2\text{V}_2\text{O}_7$ by Onose *et al.* (Ref. [10]). The pyrochlore $\text{Lu}_2\text{V}_2\text{O}_7$ consists of stacked two-dimensional kagome lattices separated by an additional monatomic layer. Matsumoto and Murakami explained the MHE by uncompensated magnon edge currents

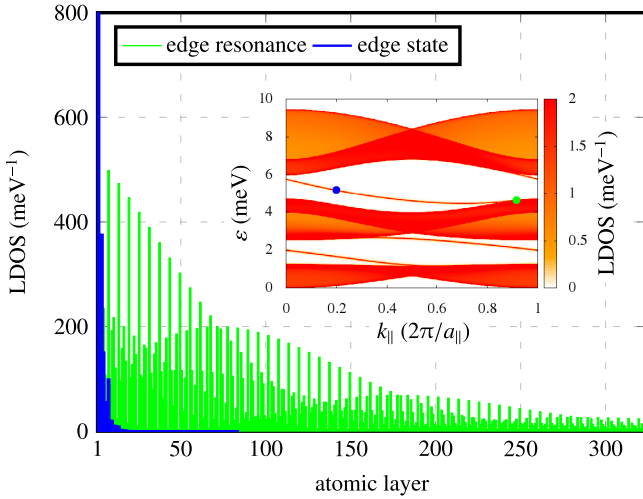


FIG. 5. (Color online) Edge localization of magnons. The site-resolved spectral density (“LDOS”) is shown versus layer index (edge = layer 1) for an edge magnon [blue; the respective $(\varepsilon, \mathbf{k})$ is marked by the blue dot in the inset] and an edge resonance (green; cf. the green dot in the inset). $D/J_N = 1$, $J_{NN}/J_N = 0$, and $J_N = 1$ meV, as in Fig. 4(a).

in two dimensions [11,12]. The intrinsic contribution to the transverse thermal conductivity,

$$\kappa^{xy} = -\frac{k_B^2 T}{(2\pi)^2 \hbar} \sum_i \int_{\text{BZ}} c_2(Q_i) \Omega_i^z(\mathbf{k}) dk^2, \quad (13)$$

is intimately related to the Chern numbers defined in Eq. (8). The sum runs over all bands i in the magnon dispersion relation, and the integral is over the Brillouin zone (BZ). The energy- and temperature-dependent Bose distribution function Q_i enters the function

$$c_2(x) \equiv (1+x) \left(\ln \frac{1+x}{x} \right)^2 - (\ln x)^2 - 2 \text{Li}_2(-x). \quad (14)$$

Li_2 is the dilogarithm.

The magnon Hall effect in kagome lattices has extensively been discussed in Ref. [14]. In particular, the sign of κ^{xy} has been shown to depend on the topological phase of the bulk system. In that publication, an explanation was given by means of Chern numbers and a high-temperature limit of κ^{xy} . However, this dependence can be understood in terms of edge modes and their propagation direction as well, as we will show in the following.

In the phase $(-1, 0, 1)$ there are two topologically nontrivial edge modes, both with negative dispersion [Figs. 4(a) and 4(e)]. As a consequence, heat transport can only proceed in one direction which is towards the left, as sketched in the center row of Fig. 4. Likewise, the phase $(3, -2, -1)$ shows four edge modes, all of which with positive dispersion; thus the heat transport is towards the right [panels (d) and (h)]. Because all nontrivial edge modes propagate in the same direction, the sign of the thermal Hall conductivity is fixed within these topological phases; its sign does not depend on the temperature.

The other two phases, $(-1, 2, -1)$ and $(-3, 4, -1)$, support edge modes of both propagation directions [panels (b), (c), (f), and (g) in Fig. 4]. Thus the sign of κ^{xy} depends on the occupation probability of the edge magnons, that is, on temperature. At low temperatures, edge modes in the first band gap are more occupied than edge modes in the second band gap. Thus the heat transport is dominated by the former edge modes; here: towards the left. Upon increasing the temperature, the edge modes in the second band gap become increasingly populated, with the consequence that the heat current is mainly mediated by these magnons, provided that the absolute values of their velocities are larger than those of the magnons in the first band gap; hence it is toward the right. This finding—a change of sign in κ^{xy} with temperature—is in full agreement with the analysis in Ref. [14].

C. Hybridization of edge modes

Topologically nontrivial edge magnons are protected by symmetry because their existence is dictated by the topology of the bulk system. However, their detailed dispersion relation may change under perturbations, for example, surface relaxation and reconstruction as well as adsorption of magnetic sites. All these modifications alter the exchange parameters at the edge with respect to those of the bulk. In the following, we account for such effects by changing the interaction parameters J_N within the very first principal layer but keeping the bulk parameters constant ($D/J_N = 0.1$).

It turns out that even for the ideal (unperturbed) edge there exists a trivial edge mode in the second band gap, close to the wedge-shaped region at $k_{\parallel} = 0.5 \times 2\pi/a_{\parallel}$ and $\varepsilon \approx 5.3$ meV [Fig. 6(a)]. For increasing J_N^{edge} this trivial mode is shifted towards higher energies [(b)–(d)]. Eventually, it hybridizes with the topologically nontrivial mode (d).

This hybridization of trivial with nontrivial edge modes shows severe consequences for the topologically nontrivial edge state. For the ideal edge, it connects the third with the second bulk band within a k_{\parallel} range of less than one edge Brillouin zone. More precisely, it “leaves” the third bulk band at about $k_{\parallel} = 0.3 \times 2\pi/a_{\parallel}$ and “enters” the second bulk band at about $0.8 \times 2\pi/a_{\parallel}$ [Fig. 6(a)]. In the case of hybridization, however, this period is enlarged by $2\pi/a_{\parallel}$, that is by the entire extension of one Brillouin zone [Fig. 6(d)]. The periodicity of the band structure remains unchanged with $2\pi/a_{\parallel}$, as is obvious within an extended zone scheme.

The effect of hybridization on the periodicity of the edge states can be understood by making use of the periodicity of the Brillouin zone. By identifying $k_{\parallel} = 0$ and $k_{\parallel} = 2\pi/a_{\parallel}$ the edge Brillouin zone becomes a cylinder (Fig. 7). Within this representation bulk bands form broad rings encircling the cylinder’s surface. In the systems of Fig. 6 two edge modes show up. The topologically nontrivial mode corresponds to the blue thread in Fig. 7(a) labeled “nontrivial edge mode.” By twisting the cylinder (i.e., rotation of its top or bottom) the nontrivial mode is continuously transformed into a line parallel to the rotational axis of the cylinder. However, the trivial mode [green thread in Fig. 7(a) labeled “trivial edge mode”] forms a closed loop around the cylinder’s surface and, therefore, will not change under twisting.

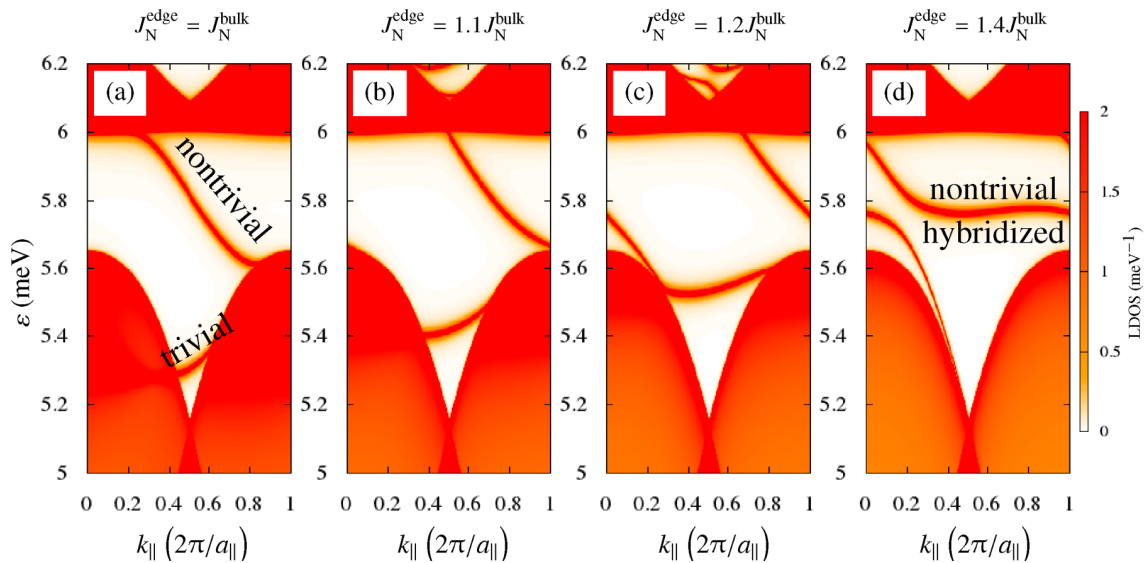


FIG. 6. (Color online) Hybridization of a topologically nontrivial with a trivial edge magnon. The local density of states (LDOS) for the edge geometry of Fig. 2(a) is shown as a color scale for several exchange parameters of the edge sites [(a)–(d); as indicated at the top of each panel]. $D/J_N = 0.1$, $J_N = 1$ meV, and $J_{NN} = 0$.

For the unperturbed edge [Fig. 6(a)] the trivial mode is located at a lower energy than the nontrivial mode; it is concealed almost entirely by the lower bulk band. For increasing perturbation J_N^{edge} , this trivial mode is shifted towards higher energies and, eventually, approaches the energy

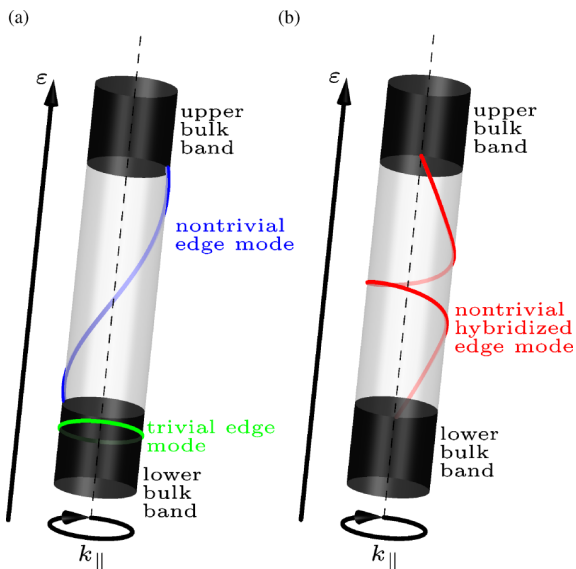


FIG. 7. (Color online) Topology and hybridization of a topologically nontrivial with a trivial edge magnon. Cylinder representation of a system with two bulk bands (black). The dashed line indicates the “seam” at $k_{||} = 0 = 2\pi/a_{||}$. (a) Sketch of the band structure in Fig. 6(a). Trivial edge modes (green) circle around the cylinder; nontrivial edge modes (blue) connect the bulk bands. The trivial modes’ energy is not located within the energy range of the nontrivial mode. (b) Sketch of the band structure in Fig. 6(d). A hybridization of a trivial and nontrivial edge mode generates a nontrivial mode circulating the cylinder (red).

range covered by the nontrivial mode. Thus the topologically trivial and nontrivial mode hybridize with each other [red thread labeled “nontrivial hybridized edge mode” in Fig. 7(b)]. As a result, a nontrivial edge mode is formed that not only connects the two bulk bands but also encircles the cylinder’s surface for another entire circulation; an additional extension of the Brillouin zone ($2\pi/a_{||}$) is necessary to traverse the band gap. Mathematically the hybridization can be understood as a Dehn twist [24] applied to the cylinder about the trivial mode modifying the nontrivial mode. As Dehn twists are self-homeomorphisms the topology of the cylinder stays untouched. We note in passing that a further increase of J_N^{edge} shifts the trivial edge mode into the upper bulk band and the original nontrivial mode with simple periodicity is recovered.

The above argumentation is readily generalized: if a nontrivial mode hybridizes with n trivial modes, its period is increased by $n \times 2\pi/a_{||}$ since n Dehn twists are applied. In any case, the resulting mode is always nontrivial due to its topology determined by the bulk. Therefore, a twisting of the cylinder will always transform the hybridized mode into a line parallel to the cylinder’s rotational axis.

A similar hybridization has been observed in electronic topological insulators: for Bi_2Te_3 covered by a monolayer of Au, the Dirac surface state of Bi_2Te_3 hybridizes with sp states of Au (Ref. [25]), thereby increasing its period in full analogy to the magnon case presented here.

IV. OUTLOOK

Having analyzed in detail the topology of edge modes in kagome lattices, it is obvious to extend such an investigation to three-dimensional systems, especially to ferromagnetic insulators with pyrochlore structure.

Our investigation of the edge modes in kagome systems calls for experimental verification. The dispersion relation could be mapped by spin-polarized electron energy loss

spectroscopy (SPEELS) [26] or time-resolved spectroscopies [27]. Within this respect, materials with different topological phases are desirable, for example, $\text{Lu}_2\text{V}_2\text{O}_7$ with positive and $\text{In}_2\text{Mn}_2\text{O}_7$ with negative thermal Hall conductivity [28]; these should exhibit nontrivial surface modes with opposite slope of the dispersion.

Recently, Matsumoto, Shindou, and Murakami derived a theory of the thermal Hall effect in magnets with dipolar interaction and in antiferromagnets [29]. In such systems, pairs of edge states could occur that can be regarded as time-reversed partners of each other, which calls for their detailed investigation.

-
- [1] H. Hasan and C. Kane, *Rev. Mod. Phys.* **82**, 3045 (2010).
 [2] X.-L. Qi and S.-c. Zhang, *Rev. Mod. Phys.* **83**, 1057 (2011).
 [3] M. Z. Hasan and J. E. Moore, *Annu. Rev. Condens. Matter Phys.* **2**, 55 (2011).
 [4] M. V. Berry, *Proc. R. Soc. A* **392**, 45 (1984).
 [5] Y. Hatsugai, *Phys. Rev. Lett.* **71**, 3697 (1993).
 [6] D. Xiao, M.-C. Chang, and Q. Niu, *Rev. Mod. Phys.* **82**, 1959 (2010).
 [7] C. Strohm, G. L. J. A. Rikken, and P. Wyder, *Phys. Rev. Lett.* **95**, 155901 (2005).
 [8] L. Zhang, J. Ren, J.-S. Wang, and B. Li, *Phys. Rev. Lett.* **105**, 225901 (2010).
 [9] L. Zhang, J. Ren, J.-S. Wang, and B. Li, *J. Phys. Condens. Matter* **23**, 305402 (2011).
 [10] Y. Onose, T. Ideue, H. Katsura, Y. Shiomi, N. Nagaosa, and Y. Tokura, *Science* **329**, 297 (2010).
 [11] R. Matsumoto and S. Murakami, *Phys. Rev. Lett.* **106**, 197202 (2011).
 [12] R. Matsumoto and S. Murakami, *Phys. Rev. B* **84**, 184406 (2011).
 [13] L. Zhang, J. Ren, J.-S. Wang, and B. Li, *Phys. Rev. B* **87**, 144101 (2013).
 [14] A. Mook, J. Henk, and I. Mertig, *Phys. Rev. B* **89**, 134409 (2014).
 [15] W. Heisenberg, *Z. Phys.* **49**, 619 (1928).
 [16] I. Dzyaloshinsky, *J. Phys. Chem. Solids* **4**, 241 (1958).
 [17] T. Moriya, *Phys. Rev.* **120**, 1 (1960).
 [18] H. Katsura, N. Nagaosa, and P. A. Lee, *Phys. Rev. Lett.* **104**, 066403 (2010).
 [19] F. D. M. Haldane, *Phys. Rev. Lett.* **61**, 2015 (1988).
 [20] K. Ohgushi, S. Murakami, and N. Nagaosa, *Phys. Rev. B* **62**, R6065(R) (2000).
 [21] J. Henk and W. Schattke, *Comput. Phys. Commun.* **77**, 69 (1993).
 [22] The Chern numbers have been defined with opposite sign in Ref. [14]. In this paper, the definition of the Berry curvature yields a sign of the thermal Hall conductivity, Eq. (13), in agreement with Refs. [11] and [12].
 [23] Y. Hatsugai, *Phys. Rev. B* **48**, 11851 (1993).
 [24] M. Dehn, *Acta Math.* **69**, 135 (1938).
 [25] F. Muñoz, J. Henk, and I. Mertig (unpublished).
 [26] K. Zakeri, Y. Zhang, T.-H. Chuang, and J. Kirschner, *Phys. Rev. Lett.* **108**, 197205 (2012).
 [27] S. O. Demokritov and B. Hillebrands, in *Spin Dynamics in Confined Magnetic Structures*, edited by B. Hillebrands and K. Ounadjela, Topics in Applied Physics (Springer, Berlin, 2002), Chap. 3, p. 65.
 [28] T. Ideue, Y. Onose, H. Katsura, Y. Shiomi, S. Ishiwata, N. Nagaosa, and Y. Tokura, *Phys. Rev. B* **85**, 134411 (2012).
 [29] R. Matsumoto, R. Shindou, and S. Murakami, *Phys. Rev. B* **89**, 054420 (2014).

5.3. Three-Dimensional Topological Magnon Materials

Perfectly two-dimensional materials are rare. Thus, the models considered in the previous publications must be understood as approximations to quasi two-dimensional materials²⁶. Truly three-dimensional topological magnon materials, however, must be considered separately. Here, it is shown that they allow for completely new topological classes of magnonic matter: topological magnon “semimetals”.

5.3.1. Tunable magnon Weyl points in ferromagnetic pyrochlores

Li *et al.* [178] considered noncollinear spin textures on the breathing pyrochlore lattice²⁷ and showed that the magnon spectra exhibit zero-dimensional crossings, so-called Weyl points (Sec. 3.2.2).

Motivated by their finding, this publication was dedicated to three-dimensional *ferromagnets* on the regular, that is, “non-breathing”, pyrochlore lattice. It was predicted that $\text{Lu}_2\text{V}_2\text{O}_7$ and $\text{In}_2\text{Mn}_2\text{O}_7$, two of the pyrochlore representatives showing the thermal magnon Hall effect [14, 179], are “magnon Weyl semimetals” with broken pseudo-time-reversal symmetry (Sec. 3.2.2). The minimal number of two Weyl points was found and their projections onto the surface are connected by a topologically protected magnon, whose constant-energy cut looks like an arc.

In contrast to Li *et al.* [178], where the topological nontriviality is brought about by the noncollinearity of the ground state, the present model relies on the ferromagnetic ground state and on DMI. Thus, it is the direct generalization of the topological magnon insulator on the kagome lattice to three dimensions. An external magnetic field determines the direction of the magnetization in the ferromagnetic ground state and, thereby, those components of the DM vectors contributing to the magnon spectrum at the linear spin-wave level. Consequently, if the magnetic field direction is rotated, the Weyl points (and the surface arcs) are rotated likewise. The DM vector components orthogonal to the magnetization direction enter the calculations as magnon damping and band broadening, possibly blurring the magnon spectrum in experiment as discussed in Ref. [180]. Therefore, a difference technique for the mapping of topological surface magnons was proposed in *Pub. (c)*. By a surface sensitive experiment one might obtain a constant-energy cut of surface magnon spectrum as shown in Fig. 5.1(a), where broad green features stem from the projected bulk bands and the sharp feature is due to the topological surface state. If the magnetization is reversed, the bulk spectrum does not change but the DM interaction is effectively inverted, leading to opposite Chern numbers and the mapping $\mathbf{k} \rightarrow -\mathbf{k}$ for the topological surface magnons, which is indicated in Fig. 5.1(b). If one now takes the signal difference of the oppositely magnetized samples, the bulk contribution cancels out, while the contribution of the topological surface magnon remains as an antisymmetric feature [cf. Fig. 5.1(c)], giving clear evidence of its topological origin.

The discovery of Weyl points in the magnon spectra of ferromagnets opens up the route to transport signatures of these topological objects. The question whether there might be a magnonic relative of the negative magnetoresistance of electrons in Weyl semimetals (see Sec. 3.2.2) is left for the future.

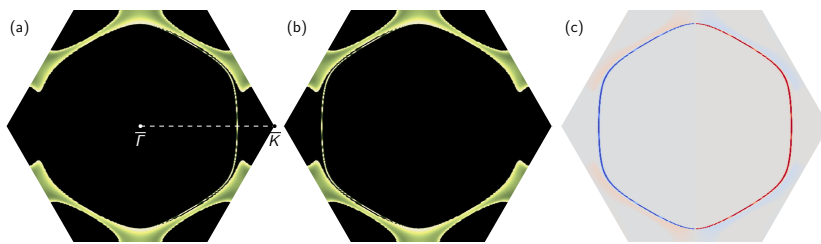


Fig. 5.1.: Suggested difference technique for the mapping of topological surface magnons by a surface-sensitive experiment. (a) and (b) Constant-energy cuts of the surface magnon spectrum for opposite magnetization directions, corresponding to opposite external magnetic fields. The bulk contribution (broad green features) stays unaffected, while the surface magnon (sharp line) is reflected from \mathbf{k} to $-\mathbf{k}$. (c) Difference of the spectra shown in (a) and (b), highlighting the topological surface magnon by its antisymmetric feature (red: positive; blue: negative).

²⁶Stacking of layers results in a three-dimensional crystal, but if the layers exhibit negligible interaction, they might be treated independently.

²⁷The term “breathing” means that the tetrahedra of the pyrochlore lattice alternate in size.

Tunable Magnon Weyl Points in Ferromagnetic Pyrochlores

Alexander Mook,¹ Jürgen Henk,² and Ingrid Mertig^{1,2}

¹Max-Planck-Institut für Mikrostrukturphysik, D-06120 Halle (Saale), Germany

²Institut für Physik, Martin-Luther-Universität Halle-Wittenberg, D-06099 Halle (Saale), Germany

(Received 25 June 2016; revised manuscript received 17 August 2016; published 7 October 2016)

The dispersion relations of magnons in ferromagnetic pyrochlores with Dzyaloshinskii-Moriya interaction are shown to possess Weyl points, i. e., pairs of topologically nontrivial crossings of two magnon branches with opposite topological charge. As a consequence of their topological nature, their projections onto a surface are connected by magnon arcs, thereby resembling closely Fermi arcs of electronic Weyl semimetals. On top of this, the positions of the Weyl points in reciprocal space can be tuned widely by an external magnetic field: rotated within the surface plane, the Weyl points and magnon arcs are rotated as well; tilting the magnetic field out of plane shifts the Weyl points toward the center $\bar{\Gamma}$ of the surface Brillouin zone. The theory is valid for the class of ferromagnetic pyrochlores, i. e., three-dimensional extensions of topological magnon insulators on kagome lattices. In this Letter, we focus on the (111) surface, identify candidates of established ferromagnetic pyrochlores which apply to the considered spin model, and suggest experiments for the detection of the topological features.

DOI: 10.1103/PhysRevLett.117.157204

Introduction.—Ferromagnetic pyrochlores attracted attention with the experimental discovery of the magnon Hall effect [1]. This transverse transport is explained by a Berry curvature [2–4] which is introduced by the Dzyaloshinskii-Moriya (DM) interaction [5,6]. In addition, the Chern numbers of magnon bulk bands are nonzero, and in accordance with the bulk-boundary correspondence [7,8] topological magnons are found at the edges of two-dimensional kagome lattices [9,10]. Hence, systems featuring topological magnon states are dubbed “topological magnon insulators” (TMIs) [9], because they exhibit many features of electronic topological insulators [11].

In this Letter, we predict that ferromagnetic pyrochlores exhibit features of another important class of topologically nontrivial systems, namely electronic Weyl semimetals [12,13]. Their magnon dispersion relations possess a pair of Weyl points on a line in reciprocal space which is along an external magnetic field; the Weyl points possess opposite topological charges of ± 1 .

At a surface, magnon surface states connect the surface-projected Weyl points; since the associated constant-energy cuts are open they are analogs of Fermi arcs in electronic Weyl semimetals. These arcs turn out to be tunable: upon rotating the magnetic field within the surface plane they follow the likewise rotated Weyl points. An out-of-plane rotation reduces the length of the arcs until they collapse at the center $\bar{\Gamma}$ of the surface Brillouin zone (when the field is perpendicular to the surface), a feature calling for experimental verification.

We recall that recently magnon Weyl points have been predicted in breathing pyrochlore lattices with spin anisotropy and a noncollinear ground state [14]. However, the present model relies on a ferromagnetic ground state

and on the DM interaction; it is thus a natural extension of TMIs on kagome lattices [9,10] to three dimensions.

Model and spin-wave analysis.—The pyrochlore lattice is a face-centered cubic (fcc) lattice of corner-sharing tetrahedra, with four atoms in its basis [Fig. 1(a)]. Lacking inversion symmetry with respect to the midpoints of bonds, it features DM interactions. Moriya’s symmetry rules [6] indicate that the DM vectors \mathbf{D}_{ij} are perpendicular to the bond that links site i with site j ; they are situated at the faces of cubes that enclose tetrahedra [Fig. 1(b)] [1,15,16].

The minimal magnetic Hamiltonian which includes isotropic symmetric exchange J_{ij} , DM interactions \mathbf{D}_{ij} , and a Zeeman term with external magnetic field \mathbf{B} reads

$$H = -\sum_{ij} J_{ij} \mathbf{s}_i \cdot \mathbf{s}_j + \sum_{ij} \mathbf{D}_{ij} \cdot (\mathbf{s}_i \times \mathbf{s}_j) - \sum_i \mathbf{B} \cdot \mathbf{s}_i, \quad (1)$$

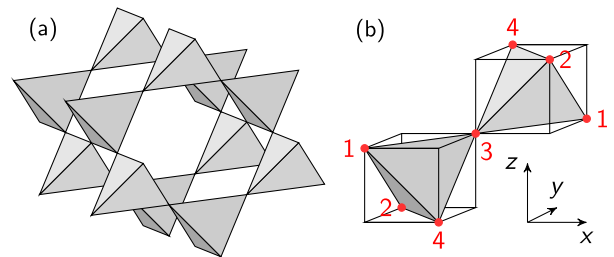


FIG. 1. Pyrochlore lattice. (a) Part of the crystal structure. (b) Four basis sites (1–4) with the nearest-neighbor DM vectors given by $\mathbf{D}_{12} = D/\sqrt{2}(0, -1, -1)$, $\mathbf{D}_{13} = D/\sqrt{2}(-1, 1, 0)$, $\mathbf{D}_{14} = D/\sqrt{2}(1, 0, 1)$, $\mathbf{D}_{23} = D/\sqrt{2}(1, 0, -1)$, $\mathbf{D}_{24} = D/\sqrt{2}(-1, -1, 0)$, and $\mathbf{D}_{43} = D/\sqrt{2}(0, -1, 1)$.

where s_i is the spin operator at site i . For $J_{ij} > 0$ the ferromagnetic state is the ground state with order parameter $\mathbf{n} = \mathbf{B}/B$; the collinearity is stable against the DM interaction [1]. In the following, the (tiny) rigid energy shift due to the Zeeman energy is neglected and only \mathbf{n} is kept for simplicity, that is, the limit $B \rightarrow 0^+$ is considered.

As argued in Ref. [1], only the component of \mathbf{D}_{ij} parallel to \mathbf{n} contributes to the linear spin-wave Hamiltonian. The spin-wave approximation is performed in an orthonormal basis $\{\mathbf{l}, \mathbf{m}, \mathbf{n}\}$, where ladder operators $s_i^\pm = s_i^l \pm i s_i^m$ are introduced. After an adequate Holstein-Primakoff [17] transformation, a Fourier transformation of the boson operators yields the 4×4 spin-wave Hamilton matrix $H_{\mathbf{k}}$. Allowing for nearest-neighbor interactions with strength J_N as well as next-nearest-neighbor interactions with strength J_{NN} , the matrix elements read $H_{\mathbf{k},\mu\nu} = 6s(J_N + J_{NN})$, and $H_{\mathbf{k},\mu\nu} = -2s(J_N + iD_{\mu\nu}^n) \cos(\mathbf{k} \cdot \boldsymbol{\delta}_{\mu\nu}^N) - 2sJ_{NN} \cos(\mathbf{k} \cdot \boldsymbol{\delta}_{\mu\nu}^{NN})$ for $\mu \neq \nu$; here, $D_{\mu\nu}^n \equiv \mathbf{D}_{\mu\nu} \cdot \mathbf{n}$ and $\boldsymbol{\delta}_{\mu\nu}^N$ ($\boldsymbol{\delta}_{\mu\nu}^{NN}$) connects nearest (next-nearest) basis sites μ and ν ($\mu, \nu = 1, 2, 3, 4$). To mimic pyrochlore systems, we set $s = 1/2$ for all basis sites.

We now analyze magnon spectra $\varepsilon_{\nu\mathbf{k}}$ and Berry curvatures [3,4,9,18–20]

$$\Omega_{\nu\mathbf{k}} \equiv i \sum_{\mu \neq \nu} \frac{\langle \mathbf{u}_{\nu\mathbf{k}} | \partial_{\mathbf{k}} H_{\mathbf{k}} | \mathbf{u}_{\mu\mathbf{k}} \rangle \times \langle \mathbf{u}_{\mu\mathbf{k}} | \partial_{\mathbf{k}} H_{\mathbf{k}} | \mathbf{u}_{\nu\mathbf{k}} \rangle}{(\varepsilon_{\nu\mathbf{k}} - \varepsilon_{\mu\mathbf{k}})^2}, \quad (2)$$

where $|\mathbf{u}_{\nu\mathbf{k}}\rangle$ is an eigenvector of $H_{\mathbf{k}}$ with energy $\varepsilon_{\nu\mathbf{k}}$. $\Omega_{\nu\mathbf{k}}$ encodes the nontrivial topology of the bulk bands which is related to global symmetries: inversion symmetry \mathcal{I} (time-reversal symmetry \mathcal{T}) causes $\Omega_{\nu\mathbf{k}}$ to be even (odd) in \mathbf{k} .

Typical results are summarized in Figs. 2(a)–(d). (a) For $J_{NN} = 0$ and $D = 0$, the four magnon bands are not gapped, the third and fourth band are dispersionless and degenerate. $\Omega_{\nu\mathbf{k}}$ vanishes in the entire Brillouin zone (BZ)

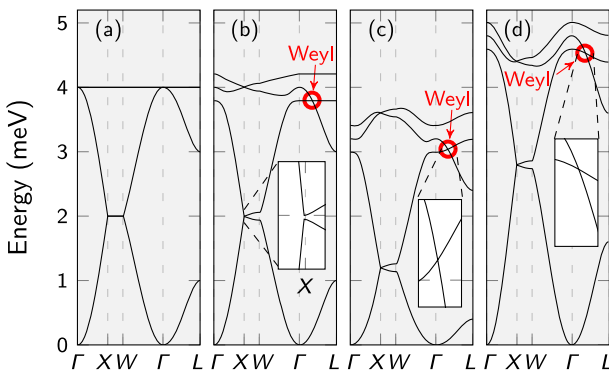


FIG. 2. Magnon spectrum of ferromagnetic pyrochlores for $J_N = 1$ meV and (a) $J_{NN} = D = 0$, (b) $J_{NN} = 0$, $D = 0.28$ meV, (c) $J_{NN} = -0.1$ meV, $D = 0.28$ meV, and (d) $J_{NN} = +0.1$ meV, $D = 0.28$ meV. The magnetic field points along $\mathbf{n} = (1, 1, 1)/\sqrt{3}$, i. e., along $\Gamma \rightarrow L$. Red circles in (b), (c), and (d) mark Weyl points. See Fig. 3(a) for the high-symmetry points of the fcc BZ.

since \mathcal{I} and \mathcal{T} are conserved. The direction \mathbf{n} of the magnetic field does not affect the spectrum. (b) \mathcal{T} is broken for $D > 0$, the upper two magnon branches become dispersive, and $\Omega_{\nu\mathbf{k}}$ is nonzero for all bands. The band structure depends sensitively on \mathbf{n} . As long as \mathbf{n} is *not* within a $\{100\}$ plane, a tiny fundamental gap between the first and second band shows up (inset). More strikingly, on any line in reciprocal space through the origin Γ and parallel to \mathbf{n} , the second and the third band cross each other at two \mathbf{k} . These \mathbf{k} lie symmetrically to Γ , their spacing is determined by \mathbf{n} and $|D|$. As we will show, these band crossings are *Weyl points* [red circle; cf. Fig. 3(a)]. (c) The Weyl points are robust against $J_{NN} \neq 0$ (inset) as \mathcal{I} remains preserved. For antiferromagnetic J_{NN} ($J_{NN} < 0$, small enough to retain the ferromagnetic ground state), the Weyl points are located in energy so that no other bulk band has the same energy (for any \mathbf{n}), that is, they are type-I Weyl points [21]. (d) The Weyl cones are tilted upon varying \mathbf{n} or J_{NN} . In particular type-II Weyl points [21] can occur for $J_{NN} > 0$.

Topology of bulk bands.—The nontrivial topology is brought about by the DM interaction, as is evident from expanding Eq. (1) in terms of small deviations $\boldsymbol{\delta}$ from the ferromagnetic ground state (the following arguments are in line with Refs. [1,2,22,23]). Without loss of generality, we take $\mathbf{n} = \hat{z}$ and $s_i = \hat{z} + \boldsymbol{\delta}_i$. Neglecting for the moment prefactors, a constant, and the Zeeman energy, the deviations yield $\delta H = \delta H_{\text{ex}} + \delta H_{\text{DM}}$, with $\delta H_{\text{ex}} = -\sum_{ij} J_{ij} (\delta_i^z + \delta_j^z + \boldsymbol{\delta}_i \cdot \boldsymbol{\delta}_j)$ and $\delta H_{\text{DM}} = \sum_{ij} D_{ij} (\delta_i^x \delta_j^y - \delta_i^y \delta_j^x)$. Terms in first order in $\boldsymbol{\delta}_i$ in δH_{DM} cancel because $\sum_j D_{ij} = 0$.

The inversion \mathcal{I} interchanges $i \leftrightarrow j$, it is obeyed by both δH_{ex} and δH_{DM} (note that $D_{ij} = -D_{ji}$). δH_{ex} also obeys the pseudotime-reversal \mathcal{T} which is a spin flip $\boldsymbol{\delta}_i \rightarrow -\boldsymbol{\delta}_i$ followed by a rotation in spin space by π about an axis perpendicular to \hat{z} . However, this does *not* apply to δH_{DM} .

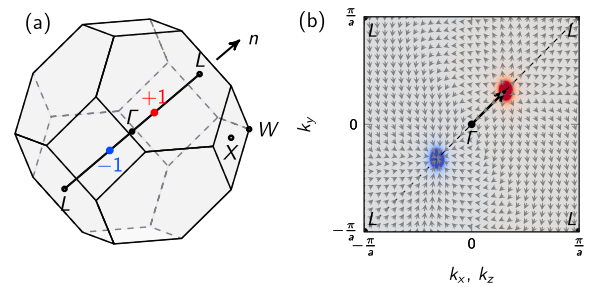


FIG. 3. Weyl points and Berry curvature. (a) Fcc BZ with high-symmetry points, field direction \mathbf{n} , and Weyl points (dots). (b) Normalized dipole vector field $\Omega_{2\mathbf{k}}$ of band 2 in the $k_x = k_z$ plane, with Γ and L points indicated. The color scale depicts the divergence of the vector field (blue: negative; gray: zero; red: positive); the two Weyl points appear in the center of the blue and red spot, respectively. Parameters as in Fig. 2(c), $\mathbf{n} = (1, 1, 1)/\sqrt{3}$, i. e., along $\Gamma \rightarrow L$ (indicated by the black arrow).

With \mathcal{I} preserved and \mathcal{T} broken, a single pair of Weyl points is allowed [24]. As \mathcal{I} implies $\varepsilon_\nu(\mathbf{k}) = \varepsilon_\nu(-\mathbf{k})$ the two Weyl points appear at the same energy.

The above mechanism is at variance with that predicted in Ref. [14]. There, the nontrivial topology is brought about by a local spin anisotropy, and the resulting complicated ground state allows for more than two Weyl points.

In the remainder of this Letter, we present results obtained for the exchange parameters of Fig. 2(c), i. e., for type-I Weyl points.

An integer Chern number $C_\nu = (1/2\pi) \int_S \Omega_{\nu k} \cdot \tilde{\mathbf{n}} dS$ is calculated for each band ν ; S is a closed and oriented surface in the bulk BZ with surface normal $\tilde{\mathbf{n}}$. Letting $\tilde{\mathbf{n}} = \text{const.}$, S is a 2D slice of the 3D BZ. By moving the slice in the BZ, $C_\nu(\lambda)$ can be calculated as a function of the position λ of the slice [25].

$C_1(\lambda) = -\text{sgn}(D)$ is constant (here, $\tilde{\mathbf{n}} = \mathbf{n}$) because a fundamental band gap separates the lowest from the other bands [inset in Fig. 2(b)]. $C_2(\lambda)$ and $C_3(\lambda)$ are not globally but piece-wise constant because these bands touch each other at the Weyl points. The latter are monopoles of the Berry curvature vector field. To prove that the band crossings are Weyl points we show the Berry curvature vector field of band 2 [Fig. 3(b)]. There are two monopoles that appear as source (red spot, offset from Γ in the direction of the magnetic field) and sink (blue spot) of the vector field, providing evidence that the Weyl points have opposite topological charge q_2^{top} . Numerical integration yields $q_2^{\text{top}} = +1$ for the “red” (source) and $q_2^{\text{top}} = -1$ for the “blue” (sink) Weyl point [26].

Recapitulating, we have identified Weyl points in the bulk band structure of pyrochlore systems whose positions in reciprocal space and cone tilting can be tuned by an external magnetic field. A prominent feature of electronic Weyl semimetals are Fermi arcs which are surface states

that connect projections of Weyl points onto the surface BZ. We now show that pyrochlore systems exhibit the magnon analogs of the (electronic) Fermi arcs, that is magnon arcs.

Surface states.—The surface magnon dispersion is analyzed in terms of the spectral density for semi-infinite systems which is calculated by Green function renormalization [27]. We exemplarily study the (111) surface and choose a quite large DM interaction ($D/J_N = 0.5$) to provide a clear picture. We would like to stress that the discussion is qualitatively valid for all surfaces and all D .

The (111) surface of the pyrochlore lattice is a kagome lattice; the resulting surface BZ is a hexagon [Fig. 4(a)]. Note that a magnetic field with an in-plane component breaks the rotational symmetry of the surface BZ. The magnetic field is completely in plane along $[11\bar{2}]$; hence, the projections of the Weyl points are situated on the line $\bar{M}' - \bar{\Gamma} - \bar{M}'$ [Fig. 4(b)].

The bulk bands appear as broad features in (b). The gaps between band 1 and 2 as well as band 2 and 3 are bridged by two topological surface states, TSS(1) and TSS(2). The latter obey the bulk-boundary correspondence [7,8,10,28].

Since the Chern number of band 1 equals -1 , the winding number of the gap between band 1 and 2 equals -1 as well (the winding number is the sum of all Chern numbers of the bands below the considered gap). As the winding number dictates the number of topological surface states, there has to be one topological surface state: TSS(1). The bulk-boundary correspondence also holds for TSS(2), since the Weyl points carry topological charges (Chern numbers).

To show that TSS(1) and TSS(2) differ qualitatively, we present constant-energy cuts of the surface spectrum that cover the band gaps in which TSS(1) and TSS(2) are situated [(a) and (c)]. Both surface states are easily identified as bright lines clinging to the extended bulk features.

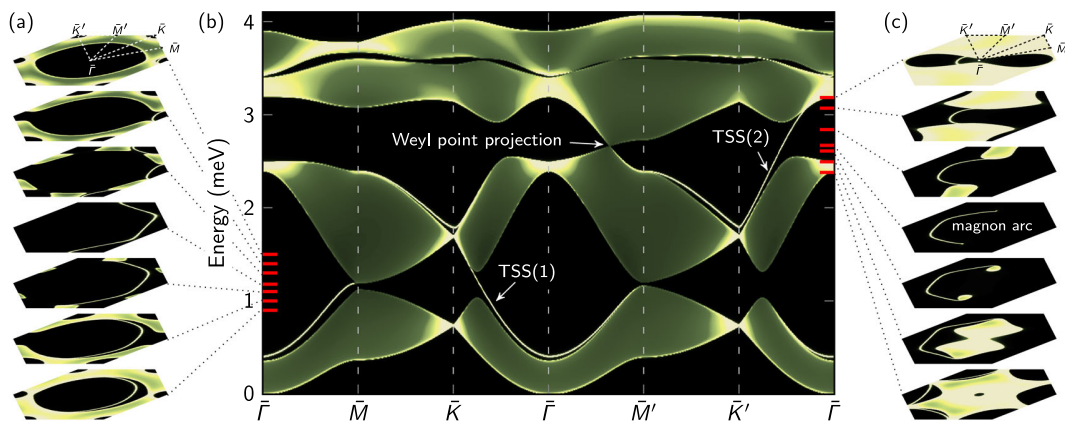


FIG. 4. Magnons at the (111) surface of a ferromagnetic pyrochlore. The surface spectral density is shown as color scale (black: zero; white: maximum). Bulk magnons appear as broad features, surface states as sharp lines. (a) and (c) show constant-energy cuts through the entire surface Brillouin zone for energies indicated by red lines in (b). (b) Spectral density along high-symmetry directions of the surface Brillouin zone. The projection of the Weyl points and two topological surface states (TSS) are indicated. Parameters as for Fig. 2(c), except $D = 0.5$ meV.

At $\varepsilon = 1.18$ meV bulk states do not contribute to the surface spectral density and only TSS(1) is visible [central cut in (a)]. Apparently, TSS(1) forms a closed line when considering the periodicity of the surface BZ.

Considering TSS(2), a similar scenario takes place at the energy of the Weyl points [$\varepsilon = 2.67$ meV, central cut of (c)]. Instead of a closed line, we find a *magnon arc* that connects the projections of the two Weyl points of opposite topological charge. Thus, pyrochlore ferromagnets host the magnon pendant to the Fermi arcs in electronic Weyl semimetals.

The Weyl points and the associated magnon arcs can be shifted—or tuned—by the magnetic field \mathbf{B} . The energy of the Weyl points is not affected by the rotation of \mathbf{B} ; hence, all of the constant-energy contours discussed in what follows are at the same energy (2.67 meV).

By rotating the field within the surface plane [Fig. 5(a)], the Weyl points follow the magnetic field and can be rotated arbitrarily. Consequently, the magnon arc trails the Weyl point projections and is rotated likewise [(b)–(e)]. The arc is not rotated rigidly: it shows the largest distances from $\bar{\Gamma}$ along $\bar{\Gamma} - \bar{M}$ as well as $\bar{\Gamma} - \bar{M}'$ directions, irrespective of the magnetic field’s azimuth. A sign change of either D or \mathbf{n} would change the signs of the Berry curvature and of the topological charges; the magnon arc would be reflected about the direction of the magnetic field.

Rotating the magnetic field from in-plane to out-of-plane (bottom row in Fig. 5), the Weyl point projections are shifted toward $\bar{\Gamma}$, thereby reducing the length of the magnon arc. The arc “collapses” when the magnetic field points along the surface normal [Fig. 5(j)].

Experimental considerations.—The pyrochlore oxides $\text{Lu}_2\text{V}_2\text{O}_7$, $\text{In}_2\text{Mn}_2\text{O}_7$, and $\text{Ho}_2\text{V}_2\text{O}_7$, all of which exhibit the magnon Hall effect [29], are the most promising candidates for experimental detection of magnon Weyl points. The first two are modeled very well by the Hamiltonian in Eq. (1). For $\text{Lu}_2\text{V}_2\text{O}_7$, the ratio D/J_N of DM interaction to exchange interaction has been

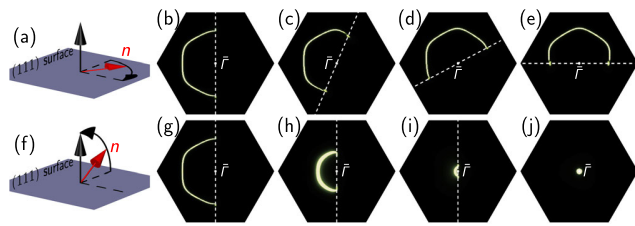


FIG. 5. Tuning magnon arcs in a pyrochlore ferromagnet by an external magnetic field. Top row (a)–(e): effect of rotating the magnetic field (\mathbf{n} , red) within the (111) surface (blue), as sketched in (a), on the magnon arc (b)–(e). Bottom row (f)–(j): as the top panels but for rotating \mathbf{n} out of plane, as sketched in (f). In (j) the field is perpendicular to the surface and the magnon arc “collapses.” The direction of \mathbf{n} projected onto the (111) surface is indicated by white dashed lines. Parameters as for Fig. 4, except \mathbf{n} which is varied.

determined recently, with values of 0.32 [1], 0.18 [30], 0.07 [31], and 0.05 [32]. Since the DM interaction determines the distance between the Weyl points and $\bar{\Gamma}$ in reciprocal space, a search for Weyl points can help to identify the exact ratio. The tunability of the Weyl points and magnon arcs can be exploited, for example, in inelastic neutron scattering experiments [30]: the shifts of the bulk band crossings upon variation of the external magnetic field can be traced. By probing a fixed line in reciprocal space through the origin, say \mathbf{q} , one will see a band gap closing and reopening at one point on \mathbf{q} upon evolution of the field’s azimuth. The closing, i. e., the occurrence of Weyl points, coincides with the alignment of the field and \mathbf{q} .

Electron energy loss spectroscopy, which is sensitive to the surface [33], could be applied for the detection of the magnon arcs. Upon inversion of the magnetic field a magnon arc is reflected, whereas the surface spectral density of the bulk states is not. Hence, subtracting spectra of oppositely magnetized samples yields clear evidence of topological surface states.

Since the transverse thermal conductivities of $\text{Lu}_2\text{V}_2\text{O}_7$ and $\text{In}_2\text{Mn}_2\text{O}_7$ differ in sign [29], it is likely that their DM constants D have opposite signs as well. Therefore, the magnon arcs of the two systems should roughly be mirror images for the same experimental setup.

Concerning transport experiments, signatures of the Weyl points are difficult to identify because magnons are bosons and all states contribute at elevated temperatures. On top of this, the Weyl points show up at a common energy; therefore, their contributions cancel each other in the integral of the transverse thermal conductivity [3,4] because they carry opposite topological charges. A mechanism which breaks the inversion symmetry allows for Weyl points with different energies; in this case, they would contribute to the transport.

Conclusion.—Ferromagnetic pyrochlores feature magnon Weyl points that can easily be tuned by an external magnetic field. Thus, the class of topologically nontrivial systems which comprises topological magnon insulators is extended to, loosely speaking, “magnon Weyl semimetals.” The latter consists of breathing pyrochlores with a non-collinear ground state, reported in Ref. [14], and ferromagnetic pyrochlores that belong to a different symmetry class, as predicted in this Letter. The effect of magnon Weyl points on magnon transport of both spin and heat as well as the formation of topological interface modes [28,34] and the influence of magnon damping of topological states [35] appear worth investigating in the future.

This work is supported by SPP 1666 of Deutsche Forschungsgemeinschaft (DFG).

[1] Y. Onose, T. Ideue, H. Katsura, Y. Shiomi, N. Nagaosa, and Y. Tokura, *Science* **329**, 297 (2010).

- [2] H. Katsura, N. Nagaosa, and P. A. Lee, *Phys. Rev. Lett.* **104**, 066403 (2010).
- [3] R. Matsumoto and S. Murakami, *Phys. Rev. B* **84**, 184406 (2011).
- [4] R. Matsumoto and S. Murakami, *Phys. Rev. Lett.* **106**, 197202 (2011).
- [5] I. Dzyaloshinsky, *J. Phys. Chem. Sol.* **4**, 241 (1958).
- [6] T. Moriya, *Phys. Rev.* **120**, 91 (1960).
- [7] Y. Hatsugai, *Phys. Rev. B* **48**, 11851 (1993).
- [8] Y. Hatsugai, *Phys. Rev. Lett.* **71**, 3697 (1993).
- [9] L. Zhang, J. Ren, J.-S. Wang, and B. Li, *Phys. Rev. B* **87**, 144101 (2013).
- [10] A. Mook, J. Henk, and I. Mertig, *Phys. Rev. B* **90**, 024412 (2014).
- [11] H. Hasan and C. Kane, *Rev. Mod. Phys.* **82**, 3045 (2010).
- [12] X. Wan, A. M. Turner, A. Vishwanath, and S. Y. Savrasov, *Phys. Rev. B* **83**, 205101 (2011).
- [13] S.-Y. Xu, N. Alidoust, I. Belopolski, Z. Yuan, G. Bian, T.-R. Chang, H. Zheng, V. N. Strocov, D. S. Sanchez, G. Chang *et al.*, *Nat. Phys.* **11**, 748 (2015).
- [14] F.-Y. Li, Y.-D. Li, Y. B. Kim, L. Balents, Y. Yu, and G. Chen, *Nat. Comm.* **7**, 12691 (2016).
- [15] M. Elhajal, B. Canals, R. Sunyer, and C. Lacroix, *Phys. Rev. B* **71**, 094420 (2005).
- [16] V. N. Kotov, M. Elhajal, M. E. Zhitomirsky, and F. Mila, *Phys. Rev. B* **72**, 014421 (2005).
- [17] T. Holstein and H. Primakoff, *Phys. Rev.* **58**, 1098 (1940).
- [18] M. V. Berry, *Proc. R. Soc. A* **392**, 45 (1984).
- [19] J. Zak, *Phys. Rev. Lett.* **62**, 2747 (1989).
- [20] J. H. Han and H. Lee, arXiv:1604.08290.
- [21] A. A. Soluyanov, D. Gresch, Z. Wang, Q. Wu, M. Troyer, X. Dai, and B. A. Bernevig, *Nature (London)* **527**, 495 (2015).
- [22] R. Cheng, S. Okamoto, and D. Xiao, arXiv:1606.01952 [*Phys. Rev. Lett.* (to be published)].
- [23] S. A. Owerre, *J. Phys. Condens. Matter* **28**, 386001 (2016).
- [24] A. A. Burkov and L. Balents, *Phys. Rev. Lett.* **107**, 127205 (2011).
- [25] M. Hermanns, K. O'Brien, and S. Trebst, *Phys. Rev. Lett.* **114**, 157202 (2015).
- [26] See Supplemental Material at <http://link.aps.org/supplemental/10.1103/PhysRevLett.117.157204> for additional plots of the Berry curvature vector field for different directions of \mathbf{n} .
- [27] J. Henk and W. Schattke, *Comput. Phys. Commun.* **77**, 69 (1993).
- [28] A. Mook, J. Henk, and I. Mertig, *Phys. Rev. B* **91**, 224411 (2015).
- [29] T. Ideue, Y. Onose, H. Katsura, Y. Shiomi, S. Ishiwata, N. Nagaosa, and Y. Tokura, *Phys. Rev. B* **85**, 134411 (2012).
- [30] M. Mena, R. S. Perry, T. G. Perring, M. D. Le, S. Guerrero, M. Storni, D. T. Adroja, C. Rüegg, and D. F. McMorrow, *Phys. Rev. Lett.* **113**, 047202 (2014).
- [31] K. Riedl, D. Guterding, H. O. Jeschke, M. J. P. Gingras, and R. Valenti, *Phys. Rev. B* **94**, 014410 (2016).
- [32] H. J. Xiang, E. J. Kan, M. H. Whangbo, C. Lee, S.-H. Wei, and X. G. Gong, *Phys. Rev. B* **83**, 174402 (2011).
- [33] K. Zakeri, Y. Zhang, and J. Kirschner, *J. Electron Spectroscopy Related Phenomena* **189**, 157 (2013).
- [34] A. Mook, J. Henk, and I. Mertig, *Phys. Rev. B* **91**, 174409 (2015).
- [35] A. L. Chernyshev and P. A. Maksimov, arXiv:1606.09249.

Tunable magnon Weyl points in ferromagnetic pyrochlores – Supplementary material

Alexander Mook,¹ Jürgen Henk,² and Ingrid Mertig^{1,2}

¹Max-Planck-Institut für Mikrostrukturphysik, D-06120 Halle (Saale), Germany

²Institut für Physik, Martin-Luther-Universität Halle-Wittenberg, D-06099 Halle (Saale), Germany

To prove that the Weyl points can be tuned arbitrarily, we provide additional plots showing the Berry curvature vector field of the second band. The directions of $\mathbf{n} = \mathbf{B}/|\mathbf{B}|$ are chosen as $\mathbf{n} = (1, 0, 0)$ [Fig. S1 (a) and (b)] and $(1, -1, 0)/\sqrt{2}$ [Fig. S1 (c) and (d)], respectively. The source and sink of the Berry curvature (red and blue dots, respectively), associated with the Weyl points, are clearly visible in the $k_z = 0$ plane.

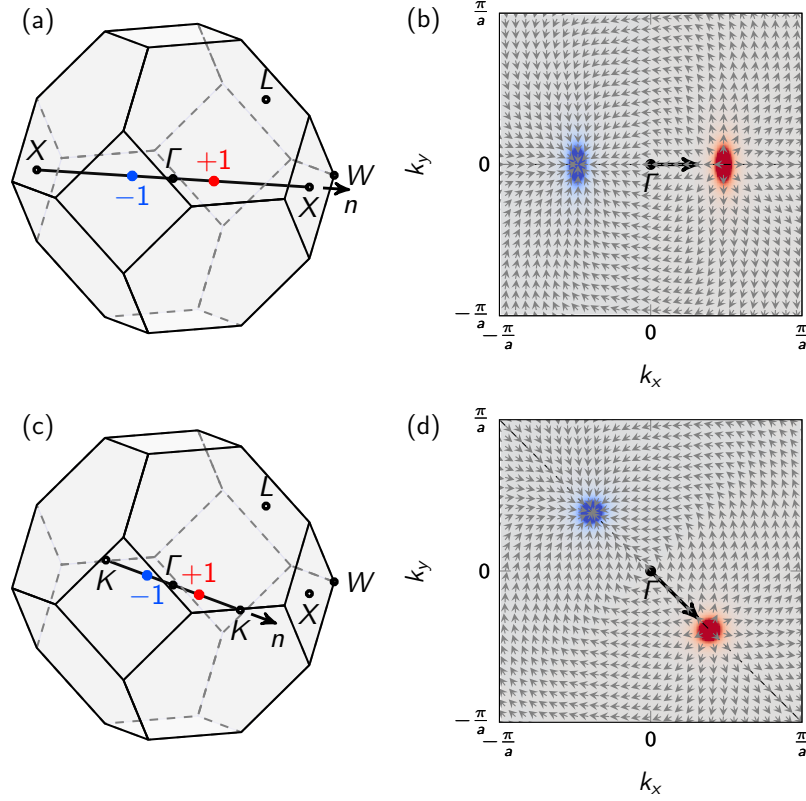


FIG. S1: Weyl points and Berry curvature. (a) and (c) Brillouin zone of the face-centered cubic lattice with high-symmetry points, field direction \mathbf{n} , and Weyl points (blue and red dots). (b) and (d) Normalized dipole vector field $\mathbf{\Omega}_{2k}$ of band 2 in the $k_z = 0$ plane. The color scale depicts the divergence of the vector field (blue: negative, gray: zero, red: positive); the two Weyl points appear in the center of the blue and red spot, respectively. Parameters as in Fig. 3 of the main article.

5.3.2. Magnon nodal-line semimetals and drumhead surface states in anisotropic pyrochlore ferromagnets

The existence of nonzero Berry curvature and the thermal Hall effect of magnons in, for example, $\text{Lu}_2\text{V}_2\text{O}_7$ is due to spin-orbit coupling in the form of DMI [14, 15]. This publication answers the question whether the magnon spectrum of a ferromagnet can remain topologically nontrivial in the absence of DMI, that is, in the presence of \mathcal{P} as well as \mathcal{T} symmetry. As discussed for electrons in Sec. 3.2.3, it is known that the simultaneous presence of the aforementioned two symmetries facilitates the existence of “nodal lines”, i. e., one-dimensional band degeneracies, forming a closed loop in reciprocal space.

It is shown that the concept of nodal-line semimetals can be carried over to magnon spectra, thereby introducing a novel state of matter: the “magnon nodal-line semimetal”. A case study based on a pyrochlore ferromagnet is presented: in the absence of DMI, that is, in the limit of negligible spin-orbit interaction, the magnon spectrum possesses \mathcal{T} as well as \mathcal{P} symmetry (Sec. 3.2.1). By assuming that the exchange coupling between kagome layers of the pyrochlore crystal is smaller than the exchange coupling within the kagome planes, a directional anisotropy is introduced. This anisotropy describes a pyrochlore ferromagnet strained along a [111] direction or an unstrained pyrochlore ferromagnet with two types of atoms, where one species occupies the kagome planes and the other species the triangular planes between the kagome planes. Crucially, this anisotropy leaves \mathcal{T} as well as \mathcal{P} symmetry intact²⁸, which is a prerequisite for nodal lines (see Sec. 3.2.3).

By tuning the strain parameter, several nodal lines are identified, two of which are topologically nontrivial (a third line is accidental and not topologically protected). This is corroborated by the calculation of the \mathbb{Z}_2 invariant introduced in Sec. 3.2.3. As in the case of electronic nodal-line semimetals, “drumhead states” exist at the surface. Furthermore, following the work of Kim *et al.* [181] on Dirac line nodes in inversion-symmetric crystals²⁹, strong and weak \mathbb{Z}_2 topological indices are calculated for the magnon nodal lines. A topological phase transition from a “strong” nodal line to a “weak” nodal line is observed.

Since Berry’s curvature is zero, the studied magnon nodal-line semimetal does not exhibit anomalous transverse transport. Moreover, up to now, a signature in transport was not found, which could serve as a hallmark of nodal-line magnons. Thus, direct mapping of the magnon band structure via inelastic neutron scattering seems to be the most promising method for their identification.

²⁸ \mathcal{P} symmetry stays intact, because every lattice site of the pyrochlore lattice is a center of inversion.

²⁹Electronic “Dirac line nodes” are four-fold degenerate due to time-reversal and parity symmetry (two spin-degenerate bands form the nodal line). In contrast, the magnon nodal lines are doubly degenerate. However, in the absence of spin-orbit interaction, the time-reversal operator of electrons only conjugates the wave function, just as the pseudo time-reversal operator introduced in Sec. 3.2.1. Thus, the work of Kim *et al.* [181] can be applied to the magnonic nodal-line semimetals.

Magnon nodal-line semimetals and drumhead surface states in anisotropic pyrochlore ferromagnetsAlexander Mook,¹ Jürgen Henk,² and Ingrid Mertig^{1,2}¹Max-Planck-Institut für Mikrostrukturphysik, D-06120 Halle (Saale), Germany²Institut für Physik, Martin-Luther-Universität Halle-Wittenberg, D-06099 Halle (Saale), Germany

(Received 30 September 2016; revised manuscript received 16 December 2016; published 17 January 2017)

We introduce a type of topological magnon matter: the magnonic pendant to electronic nodal-line semimetals. Magnon spectra of anisotropic pyrochlore ferromagnets feature twofold degeneracies of magnon bands along a closed loop in reciprocal space. These magnon nodal lines are topologically protected by the coexistence of inversion and time-reversal symmetry; they require the absence of spin-orbit interaction (no Dzyaloshinskii-Moriya interaction). We calculate the topological invariants of the nodal lines and show that details of the associated magnon drumhead surface states depend strongly on the termination of the surface. Magnon nodal-line semimetals complete the family of topological magnons in three-dimensional ferromagnetic materials.

DOI: [10.1103/PhysRevB.95.014418](https://doi.org/10.1103/PhysRevB.95.014418)**I. INTRODUCTION**

Recently, nontrivial topologies of magnon spectra have become a thriving field of research. In striking analogy to *electronic* topological matter [1], topological *magnon* matter has been identified. The drosophilae of such topological magnon insulators (TMIs) [2], which are the pendant to electronic Chern insulators, are (two-dimensional) ferromagnets on a kagome lattice with Dzyaloshinskii-Moriya interaction (DMI) [3–10]. This last causes complex hopping matrix elements in the free-boson Hamiltonian of magnons and thus breaks the time-reversal symmetry; this points towards the textured magnetic flux in the Haldane model [11]. As a result, Berry curvatures and Chern numbers are nonzero and cause topologically protected edge magnons. The last of these revolve unidirectionally the sample in accordance with the bulk-boundary correspondence [12,13]. Recently, Cu-(1,3-benzenedicarboxylate) was identified as a TMI which is very well approximated by the kagome model [14]; TMIs on the honeycomb lattice have been proposed as well [15].

The quest for topologically nontrivial systems has been initiated by the discovery of the magnon Hall effect [16,17] in ferromagnetic pyrochlore oxides, mostly because the transverse thermal Hall conductivity has been related to the Berry curvature of the bulk magnons [5,18,19]. The quite natural extension of the topological classification to three-dimensional systems led to the discovery of magnon Weyl semimetals [20,21], in which the crossing points of two magnon bands act as source and sink of Berry flux (again in close analogy to electronic systems [22,23]).

Here we complete the family of topological magnonic objects in three-dimensional ferromagnetic materials by predicting magnon nodal-line semimetals (magnon NLSMs), the magnon pendant of electronic NLSMs [24–30]. For this purpose, we consider a ferromagnetic pyrochlore lattice with anisotropic exchange interactions, but without spin-orbit interaction (SOI). We find two nodal lines, that is, two closed loops in reciprocal space along which two magnon bands are degenerate. On top of this, we identify the protecting symmetries and calculate the topological invariants of the nodal lines. Magnon spectra for the (111) surface feature drumhead surface states, i. e., the hallmarks of NLSMs.

The dispersion relations of these depend strongly on the termination of the surface. Eventually, we discuss the effect of a nonzero DMI on the spectra and suggest experiments to identify magnon NLSMs.

II. MODEL AND SPIN-WAVE ANALYSIS

The pyrochlore lattice consists of four interpenetrating face-centered cubic (fcc) lattices, resulting in a regular array of corner-sharing tetrahedra [see Fig. 1(a)]. Along the [111] direction, kagome layers alternate with triangular layers.

Considering only nearest-neighbor Heisenberg exchange interactions, there is only coupling between sites within a kagome layer [J_N , solid bonds in Fig. 1(a)] and between sites in a triangular layer with sites in the adjacent kagome layers [J'_N , dashed bonds in Fig. 1(a)]. To introduce anisotropic exchange, we assume that $0 < J'_N < J_N$. Thus, the Hamiltonian

$$H = -J_N \sum_{\langle ij \rangle}^{\text{kagome}} \mathbf{s}_i \cdot \mathbf{s}_j - J'_N \sum_{\langle ij \rangle}^{\text{triangular}} \mathbf{s}_i \cdot \mathbf{s}_j \quad (1)$$

includes only a symmetric exchange between spins \mathbf{s}_i and \mathbf{s}_j at sites i and j , respectively. An external magnetic field is not considered because it merely shifts the magnon spectrum towards higher energies. Moriya's symmetry rules [4] would, in principle, allow for a nonzero DMI [31,32] but for the time being we consider vanishing SOI.

A truncated Holstein-Primakoff transformation [33]

$$s_i^z \rightarrow s - n_i, \quad (2)$$

$$s_i^+ = s_i^x + is_i^y \rightarrow \sqrt{2s}a_i, \quad (3)$$

$$s_i^- = s_i^x - is_i^y \rightarrow \sqrt{2s}a_i^\dagger, \quad (4)$$

is applied (linear spin-wave approximation, i. e., no magnon-magnon interactions). The annihilation operators a_i and the creation operators a_i^\dagger obey the boson commutation rules; $n_i = a_i^\dagger a_i$ is the magnon number operator. This low-temperature

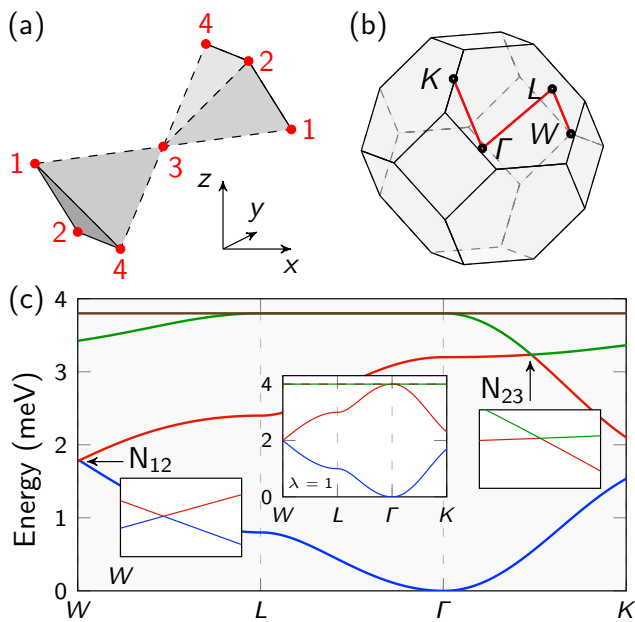


FIG. 1. (a) Corner-sharing tetrahedra of the pyrochlore lattice with basis sites (red dots, labeled 1, . . . , 4). Sites 1, 2, and 4 form a kagome lattice with nearest-neighbor interaction J_N (solid bonds); site 3 connects adjacent kagome layers by a weaker interaction J'_N (dashed bonds). (b) Brillouin zone of the fcc lattice with indicated high-symmetry points. (c) Magnon spectrum $[\varepsilon_n(\mathbf{k}), n = 1, \dots, 4]$ of the anisotropic pyrochlore ferromagnet along the red path depicted in (b) for $J_N = 1$ meV, $\lambda = 0.8$, and $s = 1/2$. Band crossings are marked N_{12} and N_{23} , with insets showing magnifications. The central inset displays the spectrum for the isotropic case ($\lambda = 1$).

approximation yields the free-magnon Hamiltonian matrix

$$H_{\text{free}} = -2sJ_N \begin{pmatrix} -2 - \lambda & c(y, -z) & \lambda c(x, y) & c(z, -x) \\ c(y, -z) & -2 - \lambda & \lambda c(x, z) & c(x, -y) \\ \lambda c(x, y) & \lambda c(x, z) & -3\lambda & \lambda c(y, z) \\ c(z, -x) & c(x, -y) & \lambda c(y, z) & -2 - \lambda \end{pmatrix},$$

in which $c(\alpha, \beta) \equiv \cos(\text{sgn}(\alpha)k_\alpha + \text{sgn}(\beta)k_\beta)$ for $\alpha, \beta = x, y, z$ and $\lambda \equiv J'_N/J_N$. A nonunitary Bogoliubov transformation is not necessary because of the ferromagnetic ground state. Diagonalization of H_{free} gives the magnon dispersions $\varepsilon_n(\mathbf{k})$ and the magnon eigenstates $|u_n(\mathbf{k})\rangle$. In the following we present results for $s = 1/2$, $J_N = 1$ meV, and $\lambda = 0.8$; the lattice constant is set to unity.

The magnon band structure is made up of four bands, consistent with the four basis atoms of the pyrochlore lattice [Fig. 1(b) shows the high-symmetry lines along which the spectrum is shown in Fig. 1(c)]. For isotropic exchange ($\lambda = 1$; see central inset), the two topmost bands are dispersionless and the lower two bands are mirror images of each other. For $\lambda < 1$ [$\lambda = 0.8$ in Fig. 1(c)], one of the formerly dispersionless bands (green) becomes dispersive; this leads to a crossing with band 2 (red; counted from below) at a single \mathbf{k} point on the Γ -K line (marked N_{23}). Additionally, the crossing N_{12} of band 1 (blue) and band 2 (red), which is at the W point for $\lambda = 1$, is shifted along the W-L line for $\lambda < 1$. These degeneracies are part of

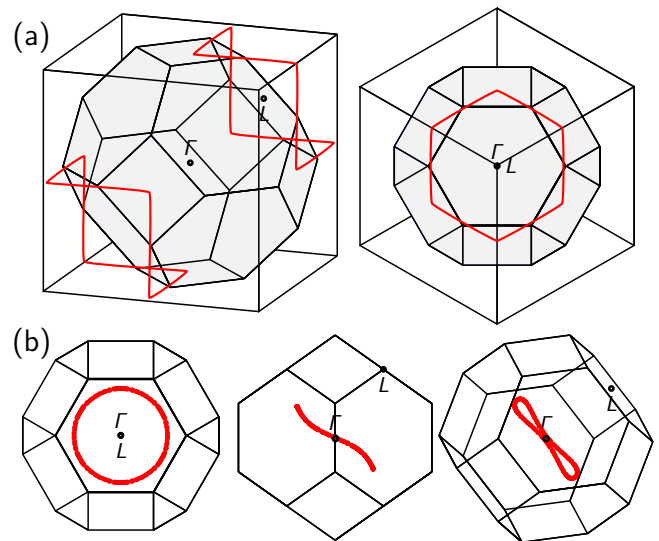


FIG. 2. Perspective views of the nodal lines (red lines) (a) N_{12} and (b) N_{23} in the fcc BZ. The high-symmetry points Γ and L are indicated for all perspectives. Parameters as in Fig. 1(c).

the nodal lines shown in Fig. 2. In the following we label the nodal lines by $N_{\mu\nu}$, in which μ (ν) stands for the energetically lower (higher) band forming the nodal line.

N_{12} is best depicted on the cube circumscribing the fcc Brillouin zone [BZ; Fig. 2(a)]. It does not lie exactly on the cube's faces but is set off by a tiny amount towards the BZ center. For decreasing λ , N_{12} keeps contracting until it becomes more and more ring-like; it is moved toward the hexagonal faces of the BZ until it vanishes in the L point for $\lambda = 0$ (which is the limit of noninteracting kagome layers).

N_{23} has its center at the Γ point [Fig. 2(b)], its diameter increases for decreasing λ . It too is not a planar ring in k space, but shows modulations that are consistent with the threefold rotational symmetry of the $[111]$ direction (Γ -L line).

Please note that the third and fourth bands are degenerate along Γ -L [green and brown bands in Fig. 1(c)], forming an “open” line of degeneracies along a high-symmetry direction (“open” is meant in the same sense as open orbits on a Fermi surface). This line is, however, not topologically protected (see the following section); its shape is not dependent on λ .

III. SYMMETRY AND TOPOLOGY ANALYSIS

Nodal lines are differentiated by their protecting symmetry [30,34]. A type-1 nodal line is protected by mirror symmetry and thus has to lie within a mirror plane. A type-2 nodal line is protected by the simultaneous presence of inversion and time-reversal symmetry in a system without SOI; it may appear in generic positions in k space. In the following we show that the magnon nodal lines are of type 2.

The free-magnon Hamiltonian considered here is time-reversal invariant because there is no complex hopping (in contrast to the case with DMI [5,21]); due to the ferromagnetic ground state, inversion symmetry is also present. In combination, these symmetries imply that the Berry curvature [35,36]

$$\Omega_n(\mathbf{k}) = i\langle \nabla_{\mathbf{k}} u_n(\mathbf{k}) | \times | \nabla_{\mathbf{k}} u_n(\mathbf{k}) \rangle \quad (5)$$

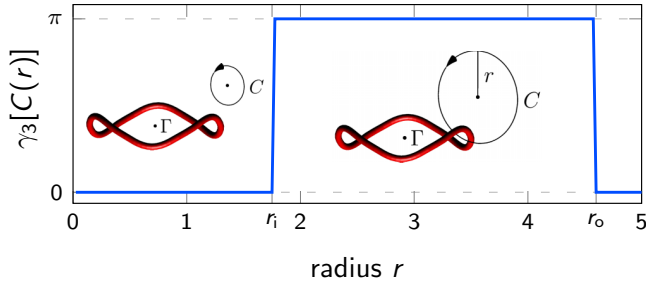


FIG. 3. Integrated Berry phase of band 3 in dependence on the radius r of the loop C . The center of C is chosen well outside the nodal line (left inset). The nodal line (red) becomes “woven” with C if its radius exceeds r_1 (right inset). For $r > r_0$ the nodal line and C are again separated.

and consequently the Chern numbers

$$C_n = \frac{1}{2\pi} \int_S \Omega_n(\mathbf{k}) \cdot \mathbf{e} \, dS \quad (6)$$

vanish, thereby suggesting a topologically trivial situation (\mathbf{e} is the \mathbf{k} -dependent local normal of a closed surface S). However, the nontrivial topology of a nodal line is identified by the Berry phase integrated along an arbitrary closed loop C [29,30],

$$\gamma_n[C] = i \int_C \langle u_n(\mathbf{k}) | \nabla_{\mathbf{k}} u_n(\mathbf{k}) \rangle d\mathbf{k}. \quad (7)$$

If C and the nodal line are intertwined (sketched in Fig. 3), $\gamma_n[C] = \pi$ (nontrivial), otherwise $\gamma_n[C] = 0$ (trivial).

To prove the nontrivial topology of the nodal lines, we compute $\gamma_n[C(r)]$ of the first and third bands in dependence on the radius r of a circle C . Figure 3 shows as an example $\gamma_3[C(r)]$, but we note that the argument is valid also for $\gamma_1[C(r)]$. The center of C is chosen such that it is well separated from the nodal line N_{23} . Hence, the nodal line does not puncture the surface enclosed by C and $\gamma_3[C(r)] = 0$ (left inset in Fig. 3). The increasing of r leads to the interweaving of the nodal line and C (right inset) once the critical radius r_1 is reached: $\gamma_3[C(r)] = \pi$. Upon a further increase of r the nodal line and C become separated again and $\gamma_3[C(r)]$ falls back to zero for $r > r_0$. This topology analysis reveals that the nodal lines are of type 2. Please see the Appendix for a detailed discussion of the \mathbb{Z}_2 topological invariants associated with the nodal lines.

The degeneracy of bands 3 and 4 along Γ -L is accidental: the Berry phase γ_4 of the fourth band is zero for any loop C . An arbitrarily small perturbation which preserves symmetry would lift the degeneracy [30]; e. g., one could vary the exchange interaction between any of the kagome sites 1, 2, or 4 [see Fig. 1(a)].

IV. SURFACE STATES

The surface magnon dispersion is analyzed in terms of the spectral density $N_p(\varepsilon, \mathbf{k})$ which is computed for a semi-infinite geometry by Green’s function renormalization [37]. The renormalization proceeds as follows. For the chosen (111) surface, the pyrochlore lattice is decomposed into principal layers (PLs) which are parallel to that surface. The principal

layers are chosen in such a way that the Hamiltonian matrix of the semi-infinite system comprises only interactions within a PL and among adjacent PLs. In the infinite set of equations for the PL-resolved Green’s-function matrix the inter-PL interactions are iteratively reduced (renormalized). After a few iterations the entire Hamiltonian matrix becomes effectively block diagonal which allows to compute the spectral densities

$$N_p(\varepsilon, \mathbf{k}) = -\frac{1}{\pi} \lim_{\eta \rightarrow 0^+} \text{Im}[\text{Tr} G_{pp}(\varepsilon + i\eta, \mathbf{k})] \quad (8)$$

of PL p from the Green’s function block G_{pp} . A finite η (here 0.001 meV) ensures convergence and introduces broadening. Hence we have access to the bulk spectral density ($p = \infty$) and to that of any other PL, in particular that of the surface ($p = 0$).

The perspective views given in Fig. 2 in which Γ and L coincide [right in Fig. 2(a); left in Fig. 2(b)] reflect the rotational symmetry of both the nodal lines and the hexagonal BZ of the (111) surface. The argumentation given below is also valid for other surfaces with nontrivial projections of the nodal lines.

The bulk magnon spectrum appears as broad features upon projection onto the (111) surface (cf. the extended green regions in Fig. 4); surface states show up as comparatively sharp features. Constant-energy cuts of the surface magnon spectrum at energies close to the nodal line N_{23} are plotted in Fig. 4(a) [the corresponding energies are indicated in Fig. 4(b)]. For the lowest energy, there is no surface state and only bulk states are visible [bottom constant-energy cut in Fig. 4(a)]. At the energy for which only N_{23} is present, the projected bulk states form a closed ring in the surface BZ [top constant-energy cut in Fig. 4(a)]. Additionally, DSS₂₃ which is associated with N_{23} produces a ring-like feature whose extension shrinks toward \bar{K} with decreasing energy. The cut of the surface magnon spectrum along high-symmetry lines of the surface BZ [Fig. 4(b)] shows two points of N_{23} : one on the $\bar{\Gamma}$ - \bar{M} and another on the $\bar{\Gamma}$ - \bar{K} line. DSS₂₃ is suspended at these points, its considerable dispersion indicates that the ‘membrane is stretched quite loosely’. Figures 4(c) and 4(d) show the same scenario for the projection of N_{12} and DSS₁₂: with decreasing energy, DSS₁₂ shrinks towards $\bar{\Gamma}$.

The (111) surface of the pyrochlore lattice allows for two terminations: a kagome or a triangular layer. The results discussed up to here were obtained for the triangular termination. Considering the kagome termination [Figs. 4(e) and 4(f)], there is no difference in the bulk contributions but a major variation in the DSSs, here exemplified by DSS₁₂. If we call the region about the $\bar{\Gamma}$ point the inside of the projected N_{12} , we find DSS₁₂ now in its exterior. This fundamental dependence on the surface termination has also been observed for electronic NLSMs, for example, in the alkaline-earth stannides, germanides, and silicides [29].

V. DISCUSSION

A. Effect of the Dzyaloshinskii-Moriya interaction

For the electronic NLSMs, SOI has to be absent [29,34] or at least very weak because otherwise the nodal lines would be lifted and other topological states could occur. The same is valid for the magnon nodal lines: the pyrochlore lattice

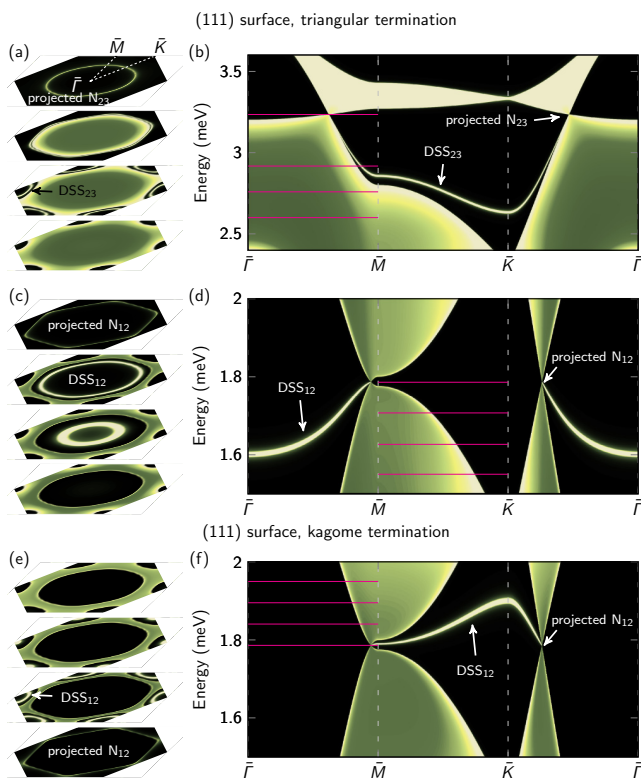


FIG. 4. Magnons at the (111) surface of an anisotropic pyrochlore ferromagnet for two surface terminations; Panels (a–d) show results for a triangular termination (top and central row), while (e) and (f) show results for a kagome termination (bottom row). The surface spectral density $N_0(\epsilon, \mathbf{k})$ is represented as a color scale (black: zero; white: maximum). Bulk magnons appear as broad features, surface states as sharp light lines. Panels (a), (c), and (e) show constant-energy cuts through the entire surface Brillouin zone for energies indicated by magenta lines in (b), (d), and (f), respectively. Panels (b), (d), and (f) display spectral densities along high-symmetry directions of the surface Brillouin zone. The projected nodal lines N_{12} and N_{23} and the respective drumhead surface states DSS_{12} and DSS_{23} are marked. Parameters as in Fig. 1(c).

allows for a nonzero DMI which would break the time-reversal symmetry [21]. Thus, the inevitable combination of inversion and time-reversal symmetry would be removed and nodal lines could not exist [49]. Instead, the magnon bands would carry nonzero Chern numbers and topological surface states would appear. Other topological states are likely, e.g., Weyl points [21,38].

The above discussion applies solely to ferromagnets. For frustrated antiferromagnets, a (synthetic) SOI is introduced to the free-magnon Hamiltonian by a nontrivial spin chirality in nonzero magnetic field rather than by DMI [39–41].

B. Experimental considerations

To prove the existence of magnon nodal lines, one could utilize either a direct or an indirect approach.

Considering a direct mapping, e.g., by inelastic neutron scattering for the bulk magnons [42] and electron energy loss spectroscopy for the surface magnons [43], we propose to

tune the anisotropy (imbalance of J_N and J'_N) by applying strain. As the diameter of the nodal line is sensitive to the ratio J'_N/J_N , it will increase or decrease accordingly; such a behavior can be detected in the experiments. If samples with different surface termination can be grown, one could utilize the strong dependence of the DSSs on the termination [cf. Figs. 4(d) and 4(f)].

In view of an indirect approach, one could think of transverse transport, for instance, the magnon Hall effect. However, these effects require a nonzero Berry curvature which is ruled out by the simultaneous presence of inversion and time-reversal symmetry required for an NLSM. We recall that most of the ferromagnetic pyrochlores exhibit a sizable DMI; examples are $\text{Lu}_2\text{V}_2\text{O}_7$, $\text{In}_2\text{Mn}_2\text{O}_7$, and $\text{Ho}_2\text{V}_2\text{O}_7$ [16,17]. Thus, the measurement of the magnon Hall effect can be used for the identification of samples with negligible DMI, which are likely to exhibit magnon nodal lines; possible candidates include the ferromagnetic pyrochlore manganates [44] and the chromium spinels [45].

The Hamiltonian (1) is surprisingly simple as it involves only an exchange interaction, which suggests that magnon NLSMs could be quite common and not restricted to the pyrochlore lattice. The examination of this conjecture is beyond the scope of this study which serves as a proof of principle; further theoretical and experimental work is clearly necessary. However, one rule can be readily formulated: the magnetic unit cell must contain more than one atom, which excludes Bravais lattices.

VI. CONCLUSION

With the prediction of magnon NLSMs the correspondence of electronic and magnonic topologically nontrivial systems in ferromagnets is completed. The term “semimetal” does not respect the bosonic nature of magnons and therefore is, strictly speaking, meaningless. However, the topological features—here: nodal lines and drumhead surface states—exist irrespective of fermion or boson statistics. The pendant of topological Dirac semimetals cannot be realized for magnons in ferromagnets because the twofold degeneracy of the bands is forbidden.

ACKNOWLEDGMENT

This work is supported by SPP 1666 of Deutsche Forschungsgemeinschaft (DFG).

APPENDIX: \mathbb{Z}_2 TOPOLOGICAL INVARIANTS FOR NODAL LINES

Another way to identify nodal lines in inversion-symmetric crystals has been presented in Ref. [28]: Kim *et al.* introduced \mathbb{Z}_2 invariants based on parity eigenvalues at parity-invariant momenta (or time-reversal invariant momenta, TRIMs)

$$\Gamma_{i=n_1n_2n_3} = \frac{1}{2}(n_1\mathbf{b}_1 + n_2\mathbf{b}_2 + n_3\mathbf{b}_3) \quad (\text{A1})$$

($n_j = 0, 1$, \mathbf{b}_j reciprocal lattice vector, and $j = 1, 2, 3$). The Berry phase ω on a contour C_{ab} which connects two TRIMs Γ_a and Γ_b and which is built from two time-reversed paths is

TABLE I. Parity eigenvalues ξ_1 (quarter filling) and $\xi_1\xi_2$ (half filling) at the eight time-reversal invariant momenta (TRIMs) Γ_i , with $i = \{n_1n_2n_3\}$; cf. Eq. (A1).

TRIM	n_1	n_2	n_3	ξ_1	$\xi_1\xi_2$
Γ_1	0	0	0	+	+
Γ_2	1	1	0	+	-
Γ_3	1	0	1	+	-
Γ_4	0	1	1	+	-
Γ_5	1	1	1	-	-
Γ_6	1	0	0	+	-
Γ_7	0	1	0	+	-
Γ_8	0	0	1	+	-

given by

$$\omega(C_{ab}) = \exp\left(i \sum_n \gamma_n[C_{ab}]\right) = \xi_a \xi_b, \quad (\text{A2})$$

in which $\xi_a = \prod_n \xi_n(\Gamma_a)$ and $\xi_n(\Gamma_a)$ is the parity eigenvalue of the n th band at Γ_a . For electrons, one would restrict the sum and the product over n to the occupied states; for magnons (or generally for bosons), the product is over all bands below the bands of interest. More precisely, for the nodal line between the first and second (second and third) bands, the product is over the first (first and second) band. For convenience, we adopt the fermionic terms “quarter filling” and “half filling” although they have no meaning for magnons.

Following Ref. [28], the Berry phase of a contour connecting four TRIMs reads $\omega(\partial S_{abcd}) = \xi_a \xi_b \xi_c \xi_d$, which counts the number $N(S_{abcd})$ of nodal lines that pierce the enclosed surface S_{abcd} ; from

$$(-1)^{N(S_{abcd})} = \omega(\partial S_{abcd}) \quad (\text{A3})$$

follows that $\xi_a \xi_b \xi_c \xi_d = -1$ indicates an odd number of nodal lines piercing through S_{abcd} .

The parity eigenvalues are evaluated as proposed by the authors or Ref. [46]: choosing site 3 as a center of inversion [see Fig. 1(a)], the parity operator in momentum space reads

$$P_k = \text{diag}(e^{-i\mathbf{a}_1 \cdot \mathbf{k}}, e^{-i\mathbf{a}_2 \cdot \mathbf{k}}, 1, e^{-i\mathbf{a}_3 \cdot \mathbf{k}}), \quad (\text{A4})$$

with $\mathbf{a}_1 = a(1, 1, 0)/2$, $\mathbf{a}_2 = a(1, 0, 1)/2$, and $\mathbf{a}_3 = a(0, 1, 1)/2$. The parity eigenvalues $\xi_n(\Gamma_i)$ ($n = 1, \dots, 4$; $i = 1, \dots, 8$) of the magnon eigenfunctions $|\mathbf{u}_n(\mathbf{k})$ at the TRIM Γ_i are

numerically evaluated according to [47]

$$P_{\Gamma_i} |\mathbf{u}_n(\Gamma_i)\rangle = \xi_n(\Gamma_i) |\mathbf{u}_n(\Gamma_i)\rangle. \quad (\text{A5})$$

The relevant parity eigenvalues for “quarter” and “half filling” are given in Table I.

We now discuss selected examples of invariant surfaces S_{abcd} and the respective products of parity eigenvalues (Fig. 5). Consider first S_{1234} [Fig. 5(a)]: for N_{12} (quarter filling), the parity eigenvalues at $\Gamma_1, \Gamma_2, \Gamma_3$, and Γ_4 are given in the column “ ξ_1 ” of Table I. All of these parity eigenvalues are positive, indicating that S_{1234} is a trivial plane with respect to N_{12} : the nodal line does not pierce S_{1234} , which is in accordance with the graphical presentation in Fig. 5(a) (the blue line never touches the green surface). However, N_{23} (red line) clearly pierces through S_{1234} at \mathbf{k} and $-\mathbf{k}$. Hence, we expect a negative parity eigenvalue product, which is corroborated by the numerics: An inspection of the column $\xi_1\xi_2$ in Table I tells that even parity is only present at Γ_1 , while odd parity is found for the other TRIMs. This means that an invariant surface S_{abcd} is nontrivial with respect to N_{23} if and only if it contains Γ_1 . This is the case for S_{1234} , S_{1357} , and S_{1368} [Figs. 5(a), 5(b), and 5(c)], respectively, but not for S_{5678} , S_{2356} , and S_{2378} [Figs. 5(d), 5(e), and 5(f)], respectively. Returning to N_{12} , we find odd parity only at Γ_5 (column ξ_1 in Table I). Thus, only the invariant surfaces containing Γ_5 exhibit a negative parity product [Figs. 5(b), 5(d), and 5(e)].

The \mathbb{Z}_2 invariants ($\nu_0; \nu_1\nu_2\nu_3$), defined by [28,48]

$$(-1)^{\nu_0} = \prod_{n_j=0,1} \xi_{n_1n_2n_3}, \quad (\text{A6})$$

$$(-1)^{\nu_{i=1,2,3}} = \prod_{\substack{n_j \neq i=0,1 \\ n_i=1}} \xi_{n_1n_2n_3}, \quad (\text{A7})$$

comprise the strong (ν_0) topological index and the weak topological indices ($\nu_{i=1,2,3}$) [48]. The \mathbb{Z}_2 invariants of N_{12} (quarter filling) read (1; 111), those for N_{23} (half filling) read (1; 000). Thus, both nodal lines are strong ($\nu_0 = 1$). The trivial weak indices for N_{23} indicate that it is located around the Γ point, while N_{12} is located around an L point.

We now address topological phase transitions, that is, the change of ($\nu_0; \nu_1\nu_2\nu_3$) upon variation of $\lambda \in (0, 1)$ [50]. It turns out that the phase (1; 111) for quarter filling (N_{12}) is robust, while the phase (1; 000) at half filling (N_{23}) changes into the weak phase (0; 111) present for $\lambda < 0.618034$. This is understood from Fig. 6: for decreasing λ , the diameter of N_{23}

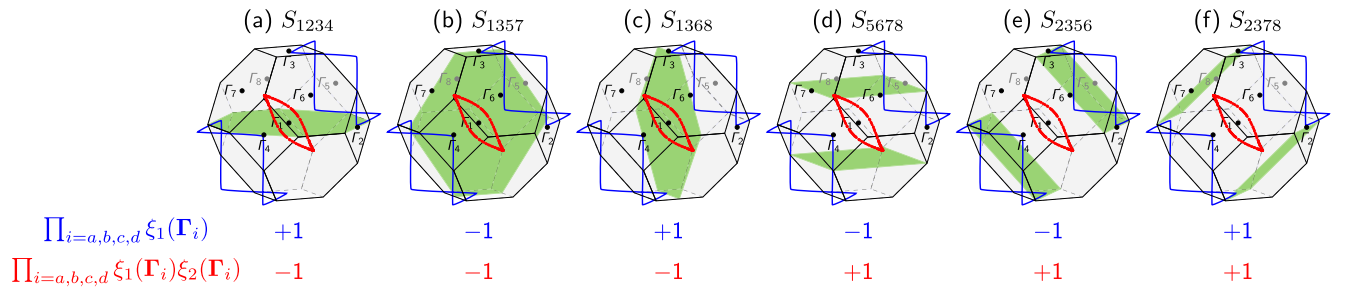


FIG. 5. Magnon nodal lines and invariant planes. N_{12} (blue), N_{23} (red), and selected invariant planes S_{abcd} (green) containing four TRIMs Γ_i ($i = a, b, c, d$) are depicted and the product of parity eigenvalues denoted below.

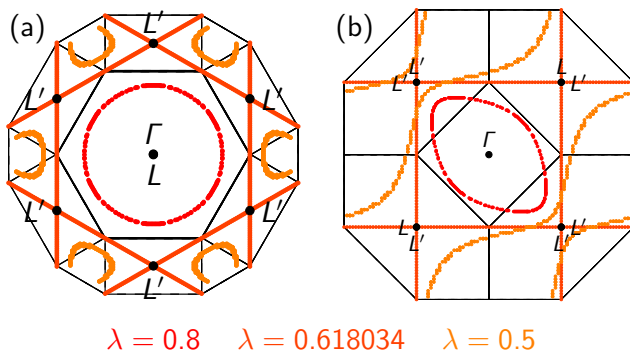


FIG. 6. Lifshitz transition of nodal line N_{23} upon variation of the anisotropy parameter λ . View along (a) [111] and (b) [100] directions.

increases until it touches the Brillouin zone boundary at the other L points, labeled L' (red and orange curves in Fig. 6).

Since the L' points are TRIMs, the local parity eigenvalues of the second band at $\Gamma_{6,7,8}$ may change sign, and consequently, the \mathbb{Z}_2 invariants may change as well. The further increase of N_{23} causes a Lifshitz transition, i.e., it splits into two line nodes, both of which are open (yellow curve in Fig. 6) but nontrivial as we have checked numerically by the calculation of $\gamma_3[C(r)]$.

The above finding lends for a classification of nodal lines: open nodal lines are topologically weak ($\nu_0 = 0$) in the sense that the formation of an open or closed surface projection of a nodal line depends on the surface normal [compare Figs. 6(a) and 6(b)]. This is fully in line with electronic \mathbb{Z}_2 topological insulators, for which $\nu_0 = 1$ guarantees a topological surface state on any surface. For $\nu_0 = 0$, the weak indices $(\nu_1\nu_2\nu_3) = (111)$ can then be understood as Miller indices, indicating a surface normal with nontrivial projection of the nodal line (closed loop); i.e., the [111] direction [cf. Fig. 6(a)].

-
- [1] H. Hasan and C. Kane, *Rev. Mod. Phys.* **82**, 3045 (2010).
- [2] L. Zhang, J. Ren, J.-S. Wang, and B. Li, *Phys. Rev. B* **87**, 144101 (2013).
- [3] I. Dzyaloshinsky, *J. Phys. Chem. Solids* **4**, 241 (1958).
- [4] T. Moriya, *Phys. Rev.* **120**, 91 (1960).
- [5] H. Katsura, N. Nagaosa, and P. A. Lee, *Phys. Rev. Lett.* **104**, 066403 (2010).
- [6] A. Mook, J. Henk, and I. Mertig, *Phys. Rev. B* **89**, 134409 (2014).
- [7] A. Mook, J. Henk, and I. Mertig, *Phys. Rev. B* **90**, 024412 (2014).
- [8] A. Mook, J. Henk, and I. Mertig, *Phys. Rev. B* **91**, 174409 (2015).
- [9] A. Mook, J. Henk, and I. Mertig, *Phys. Rev. B* **91**, 224411 (2015).
- [10] H. Lee, J. H. Han, and P. A. Lee, *Phys. Rev. B* **91**, 125413 (2015).
- [11] F. D. M. Haldane, *Phys. Rev. Lett.* **61**, 2015 (1988).
- [12] Y. Hatsugai, *Phys. Rev. B* **48**, 11851 (1993).
- [13] Y. Hatsugai, *Phys. Rev. Lett.* **71**, 3697 (1993).
- [14] R. Chisnell, J. S. Helton, D. E. Freedman, D. K. Singh, R. I. Bewley, D. G. Nocera, and Y. S. Lee, *Phys. Rev. Lett.* **115**, 147201 (2015).
- [15] S. A. Owerre, *J. Phys.: Condens. Matter* **28**, 386001 (2016).
- [16] Y. Onose, T. Ideue, H. Katsura, Y. Shiomi, N. Nagaosa, and Y. Tokura, *Science* **329**, 297 (2010).
- [17] T. Ideue, Y. Onose, H. Katsura, Y. Shiomi, S. Ishiwata, N. Nagaosa, and Y. Tokura, *Phys. Rev. B* **85**, 134411 (2012).
- [18] R. Matsumoto and S. Murakami, *Phys. Rev. B* **84**, 184406 (2011).
- [19] R. Matsumoto and S. Murakami, *Phys. Rev. Lett.* **106**, 197202 (2011).
- [20] F.-Y. Li, Y.-D. Li, Y. B. Kim, L. Balents, Y. Yu, and G. Chen, *Nat. Commun.* **7**, 12691 (2016).
- [21] A. Mook, J. Henk, and I. Mertig, *Phys. Rev. Lett.* **117**, 157204 (2016).
- [22] X. Wan, A. M. Turner, A. Vishwanath, and S. Y. Savrasov, *Phys. Rev. B* **83**, 205101 (2011).
- [23] S.-Y. Xu, N. Alidoust, I. Belopolski, Z. Yuan, G. Bian, T.-R. Chang, H. Zheng, V. N. Strocov, D. S. Sanchez, G. Chang *et al.*, *Nat. Phys.* **11**, 748 (2015).
- [24] G. P. Mikitik and Y. V. Sharlai, *Phys. Rev. B* **73**, 235112 (2006).
- [25] A. A. Burkov, M. D. Hook, and L. Balents, *Phys. Rev. B* **84**, 235126 (2011).
- [26] R. Yu, H. Weng, Z. Fang, X. Dai, and X. Hu, *Phys. Rev. Lett.* **115**, 036807 (2015).
- [27] H. Weng, Y. Liang, Q. Xu, R. Yu, Z. Fang, X. Dai, and Y. Kawazoe, *Phys. Rev. B* **92**, 045108 (2015).
- [28] Y. Kim, B. J. Wieder, C. L. Kane, and A. M. Rappe, *Phys. Rev. Lett.* **115**, 036806 (2015).
- [29] H. Huang, J. Liu, D. Vanderbilt, and W. Duan, *Phys. Rev. B* **93**, 201114 (2016).
- [30] C. Fang, H. Weng, X. Dai, and Z. Fang, *Chinese Phys. B* **25**, 117106 (2016).
- [31] M. Elhadjal, B. Canals, R. Sunyer, and C. Lacroix, *Phys. Rev. B* **71**, 094420 (2005).
- [32] V. N. Kotov, M. Elhadjal, M. E. Zhitomirsky, and F. Mila, *Phys. Rev. B* **72**, 014421 (2005).
- [33] T. Holstein and H. Primakoff, *Phys. Rev.* **58**, 1098 (1940).
- [34] M. Hirayama, R. Okugawa, T. Miyake, and S. Murakami, *arXiv:1602.06501*.
- [35] M. V. Berry, *Proc. R. Soc. London A* **392**, 45 (1984).
- [36] J. Zak, *Phys. Rev. Lett.* **62**, 2747 (1989).
- [37] J. Henk and W. Schattke, *Comput. Phys. Commun.* **77**, 69 (1993).
- [38] Y. Su, X. S. Wang, and X. R. Wang, *arXiv:1609.01500*.
- [39] S. A. Owerre, *J. Phys.: Condens. Matter* **29**, 03LT01 (2016).
- [40] S. A. Owerre, *arXiv:1609.03563*.
- [41] S. A. Owerre, *arXiv:1608.04561*.
- [42] M. Mena, R. S. Perry, T. G. Perring, M. D. Le, S. Guerrero, M. Storni, D. T. Adroja, C. Rüegg, and D. F. McMorrow, *Phys. Rev. Lett.* **113**, 047202 (2014).
- [43] K. Zakeri, Y. Zhang, and J. Kirschner, *J. Electron Spectrosc. Relat. Phenom.* **189**, 157 (2013).
- [44] J. S. Gardner, M. J. P. Gingras, and J. E. Greedan, *Rev. Mod. Phys.* **82**, 53 (2010).

- [45] A. N. Yaresko, *Phys. Rev. B* **77**, 115106 (2008).
- [46] H.-M. Guo and M. Franz, *Phys. Rev. Lett.* **103**, 206805 (2009).
- [47] M. Kurita, Y. Yamaji, and M. Imada, *J. Phys. Soc. Jpn.* **80**, 044708 (2011).
- [48] L. Fu, C. L. Kane, and E. J. Mele, *Phys. Rev. Lett.* **98**, 106803 (2007).
- [49] In a recent study, Su *et al.* considered anisotropy in combination with DMI and its effects on magnon Weyl points [38]. However, the authors did not discuss the case of zero DMI and did not identify nodal lines.
- [50] $\lambda > 1$ ($J'_N > J_N$) allows for nodal lines as well. However, an analysis of this parameter range does not provide further insight.

5.4. Magnon Transport from Atomistic Spin Dynamics Simulations

The focus of the previous publications was on the topological classification of magnon spectra and the transverse transport of magnons in the limit of low temperatures, that is, low compared to the Curie temperature, where the spin-boson transformation (Holstein-Primakoff transformation in Sec. 2.4.3) is a reasonable approximation. The conductivities were evaluated by k -space integrals over Berry's curvature, which, in turn, is calculated from the one-magnon Bloch wave functions. Apart from neglecting magnon-magnon interactions, this approach suffers from another drawback: some interesting magnetic phases do not exist at zero temperature, thereby ruling out a linear spin-wave approximation and the calculation of Berry's curvature. A famous example for such a magnetic phase is the skyrmion crystal phase (Sec. 3.4), which exhibits the topological magnon Hall effect.

Here, the development of a novel approach to magnon transport is presented. It is based on atomistic spin dynamics simulations, in which the time evolution of a single spin is governed by the stochastic Landau-Lifshitz-Gilbert (sLLG) equation (Sec. 4.3). The main idea is as follows: after reaching thermal equilibrium (either by Monte Carlo simulations, Sec. 4.2, or the sLLG equation, Sec. 4.3), a long-time evolution according to the sLLG equation is performed. The total spin and heat current are calculated at every instance of time and stored. Finally, the current-current correlation functions and from these the linear-response transport tensors are calculated according to the Kubo formula (Sec. 3.3). For instance, the thermal conductivity of a spin chain is given by [182]

$$\kappa = \frac{1}{k_B T^2} \int_0^\infty \lim_{N \rightarrow \infty} \frac{1}{Na} \langle J_{\text{th}}(t) J_{\text{th}}(0) \rangle dt, \quad (5.1)$$

if both an external magnetic field and single-ion anisotropies are absent (a lattice constant, J_{th} heat current, N number of spins).

This ansatz is borrowed from equilibrium molecular dynamics simulations (EMD) of the thermal conductivity of nonmagnetic matter (see, for example, Ref. [183]) and was firstly carried over to magnetic matter in Ref. [182], where the magnon thermal conductivity of spin chains was studied. Here, this approach is generalized to higher spatial dimensions to access *transverse* magnon transport. Additional inclusion of spin transport grants access to *all* of the magnon transport phenomena shown in Tables 3.3 or 3.4.

The evaluation of eq. (5.1) requires the calculation of ensemble-averaged current correlation function. In EMD simulations this is done by generating a number of initial conditions taken from the canonical ensemble, which is simulated by application of a thermostat. Then, the thermostat is switched off and the configurations are developed according to pure Hamilton dynamics (microcanonical ensemble). The average of the correlation function is taken over all of these ensembles.

In principle, such a routine is the most rigorous numerical evaluation of Kubo's formula and could be followed for the spin dynamics, too (and it was followed in Refs. [182] and [184]). However, this routine does not capture the influence of, e. g., magnon-phonon interactions on the magnon transport, because the Gilbert damping α is neglected in microcanonical simulations. Only the pure magnon transport can be accessed. In reality, however, the magnon bath is never truly uncoupled and interactions with other (quasi-)particles are omnipresent. Since a comparison of the simulated conductivities with the experimental ones is pursued, it was decided to perform the ensemble average as a time average over a single cluster which evolves under the influence of a thermostat. Thus, instead of Hamilton dynamics ($\alpha = 0$, microcanonical ensemble), Langevin dynamics ($\alpha \neq 0$, canonical ensemble) was utilized to calculate the correlation functions in eq. (5.1).

To quantify the difference of the two approaches, tests were performed. The magnon thermal conductivity of a ferromagnetically coupled spin chain [eq. (5.1)] was evaluated by both methods. For the Hamilton dynamics, *many thousand* initial spin cluster configurations were taken from the canonical ensemble. They were evolved according to pure Hamilton dynamics (no thermostat, no damping, only spin precession). The correlation function was calculated for every configuration and, finally, the average over all ensembles was taken. For the Langevin dynamics, *a single* spin cluster was evolved in the presence of a heat bath. The ensemble average of the correlation functions was taken as a time average.

Such calculations were performed for selected values of the damping parameter α ; results are shown in Fig. 5.2. For large α , the Langevin dynamics (colored data sets) differs a lot from the Hamilton dynamics (black data set) but it converges to the Hamilton dynamics as $\alpha \rightarrow 0$ (compare lilac and black data set). This is in agreement with the observation that by setting $\alpha = 0$ in the sLLG [cf. eq. (4.22)], only the precessional motion remains. For the

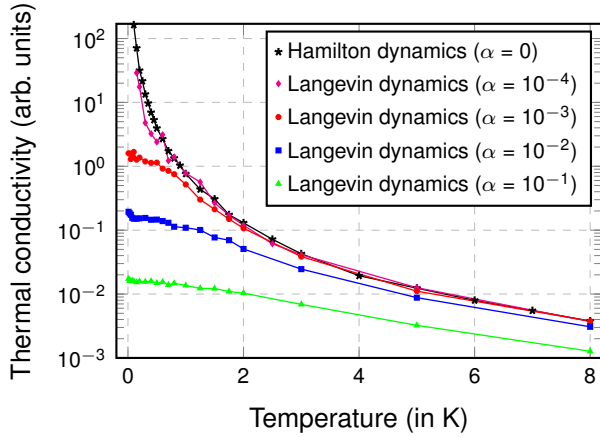


Fig. 5.2: Comparison of temperature profiles of the thermal conductivity of a ferromagnetically coupled chain for selected values of α . Black curve: $\alpha = 0$ coincides with pure Hamilton dynamics (microcanonical ensemble). Colored curves: Langevin dynamics (canonical ensemble) in the presence of a heat bath.

explanation of the overall trend of the thermal conductivity with temperature (especially, in the low-temperature limit), please confer the discussion in *Pub. 5*.

From this test, the following is concluded:

- The results of Hamilton dynamics, which describes magnon-number conserving processes, can be modeled by Langevin dynamics in the limit of vanishing Gilbert damping. Thus, it is possible to perform the ensemble average as a time average which is computationally favorable.
- It is judged that the Langevin dynamics beyond the limit of small Gilbert damping yields physically meaningful results for the correlation functions, because it phenomenologically describes magnon-number-nonconserving interactions with other (quasi-)particles. The drop of the thermal conductivity for increasing damping complies very well with the physical intuition that magnons with a short lifetime and short mean free path contribute less to transport.
- The microscopic details of the aforementioned interactions remain hidden. Thus, the Gilbert damping enters the calculations as a parameter, which has to be estimated from experimental data. For future work, an extension of the presented model to spin-lattice dynamics is suggested.

This new approach was applied to two different spin Hamiltonians. First, the topological magnon insulator on the kagome ferromagnet was set up, which is also featured in *Pubs. 1* and *2* to examine the similarities and differences between the new approach and the established linear spin-wave approximation. Second, the spin spiral ground state of the J_1 - J_3 model (Sec. 2.3) was studied, which turns into a skyrmion crystal at elevated temperatures (Sec. 4.2.2). The skyrmion crystal phase is shown to feature the topological versions of the anomalous transverse transport, that is, “topological magnon Hall effects”, which is in agreement with the emergent electrodynamics for magnons (see Sec. 3.4.2).

5.4.1. Spin dynamics simulations of topological magnon insulators: From transverse current correlation functions to the family of magnon Hall effects

For a general test of the method, the topological magnon insulator on the ferromagnetic kagome lattice was revisited, because it is understood very well in the linear spin-wave approximation (*Pubs. 1, 2*). Parameters were taken from experiments on Cu(1,3-benzenedicarboxylate) [89], a recently discovered topological magnon insulator that exhibits the thermal Hall effect of magnons [185]. Thus, there were two different standards—linear spin-wave theory and experimental results—by which the method was judged.

To verify that the set up spin cluster is a topological magnon insulator, the dynamical structure factor was calculated. It clearly showed the band gaps between the magnon bulk bands and in addition the topological edge magnons. Moreover, the transverse-current correlation functions were shown to be nonzero only if DMI was included. This indicates nonzero off-diagonal conductivity tensor elements due to broken \mathcal{T} symmetry. For the

5. Publications

longitudinal and transverse thermal conductivity, values with the same order of magnitude as their experimental counterparts were obtained. Apart from the low-temperature limit, the dependence of the conductivities on temperature and magnetic field agree with experiment.

The major advantages of the method were found to be the following:

1. *All* transport tensors are fully accessible by only *one* simulation. Thus, longitudinal and transverse transport in any direction are simultaneously studied in equilibrium. This is in contrast to a nonequilibrium steady-state simulation, where a field gradient (for instance, a temperature gradient) is applied in a certain direction and the resulting net currents are measured, allowing only for the determination of selected transport tensor elements. The latter suffers also from the need of applying a temperature difference large enough to obtain results that clearly differ from thermal noise. Thus, one is not strictly in the linear-response limit.
2. It is completely based on the spin “language” rather than on the boson “language”, and it naturally includes all orders of magnon-magnon interactions.
3. It is not restricted to zero (or very low) temperature, facilitating the treatment of the ferromagnet-to-paramagnet phase transition and magnetic phases stabilized by thermal fluctuations, for instance, skyrmion crystals (see *Pub. 6*).

However, there are also disadvantages of the presented method, which are due to the *classical* nature of atomistic spin dynamics simulations. In particular, the Boltzmann distribution, which is used to model the influence of temperature, drastically overemphasizes spin fluctuations at small temperatures, leading to a mismatch between numerically and experimentally obtained conductivities in the low-temperature limit.

All in all, it is concluded that this method complements the linear spin-wave approach. While the latter works well at low temperatures, it is insufficient (or even impossible to apply) at high temperatures. The opposite is true for the present approach: it facilitates the treatment of higher temperatures but the obtained results exhibit deviations from experimental results in the low-temperature limit. Yet, the method is reliable for the calculation of the Hall angles, because they are ratios of transverse and longitudinal transport tensor elements, such that the low-temperature trend cancels out in the quotient.

Spin dynamics simulations of topological magnon insulators: From transverse current correlation functions to the family of magnon Hall effects

Alexander Mook,¹ Jürgen Henk,² and Ingrid Mertig^{1,2}¹Max-Planck-Institut für Mikrostrukturphysik, D-06120 Halle (Saale), Germany²Institut für Physik, Martin-Luther-Universität Halle-Wittenberg, D-06099 Halle (Saale), Germany

(Received 14 September 2016; revised manuscript received 19 October 2016; published 28 November 2016)

We demonstrate theoretically that atomistic spin dynamics simulations of topological magnon insulators (TMIs) provide access to the magnon-mediated transport of both spin and heat. The TMIs, modeled by kagome ferromagnets with Dzyaloshinskii-Moriya interaction, exhibit nonzero transverse-current correlation functions from which conductivities are derived for the entire family of magnon Hall effects. Both longitudinal and transverse conductivities are studied in dependence on temperature and on an external magnetic field. A comparison between theoretical and experimental results for Cu(1,3-benzenedicarboxylate), a recently discovered TMI, is drawn.

DOI: [10.1103/PhysRevB.94.174444](https://doi.org/10.1103/PhysRevB.94.174444)

I. INTRODUCTION

Transport phenomena of the Hall type, i.e., a system shows a response perpendicular to an external force, are in the focus of modern condensed matter physics, in particular since the discovery of the quantum Hall effect [1]. Theory relates the associated Hall conductivities with nontrivial topologies of the electronic states; hence, topological insulators are investigated with great effort today [2]. While electronic topological insulators were starting at first, recent publications address bosonic particles: Hall effects of phonons [3], triplons [4], and magnons [5] were discovered or predicted, amongst others [6,7]. In particular, the experimental discovery [5] and the theoretical explanation [8–11] of the magnon Hall effect caused attention, as it revealed nontrivial topologies of the magnon dispersion relations which are brought about by the Dzyaloshinskii-Moriya (DM) interaction. The existence of topological nontrivial edge magnons [12] suggests that these “topological magnon insulators” (TMIs) may be important for future spintronics applications. Especially the ferromagnetic kagome lattice has been intensively studied because it is not only a feature-rich toy model [12–17] but also realized in nature: recently, Cu(1,3-benzenedicarboxylate) [Cu(1,3-bdc)] was identified as a TMI [18,19] exhibiting a magnon Hall effect [20].

In this paper, we show that various Hall-type transport phenomena in TMIs can be captured by classical atomistic spin dynamics simulations. Focusing on kagome ferromagnets which approximate Cu(1,3-bdc), we calculate dynamical structure factors which allow to identify topological edge magnons; in accordance with the bulk-boundary correspondence [14,21,22], the existence of topological edge magnons proves that the bulk magnons are topologically nontrivial. Furthermore, we derive expressions for the spin and thermal currents from which transport coefficients are calculated within linear-response theory; more precisely, we study both longitudinal and transverse conductivities for spin and heat transport. By comparing computed transverse thermal conductivities with those obtained in experiment [20], we identify qualitative differences between the classical and the quantum-mechanical treatment of spins.

By the above approach we access the family of magnon Hall effects (Table I) without relying on the boson language of spin

waves. This sets our study apart from previous ones, see for example Refs. [5,8,12–17,23,24]. Up to now, only the magnon Hall effect (which, strictly speaking, is a magnon Righi-Leduc effect) has been experimentally confirmed [5,20,25].

The paper is organized as follows. In Sec. II A, we introduce the kagome lattice and the Hamiltonian that models Cu(1,3-bdc). After deriving the bond currents and explaining the numerical methods in Secs. II B and II C, respectively, results are presented in Sec. III. First, we discuss the dynamical structure factor and the topological edge magnons (III A). Then we analyze the current correlation functions and the time-averaged bond currents (III B). Finally, the dependencies of the conductivity tensors on temperature and on an applied magnetic field are studied and compared with experimental data (III C). We conclude with Sec. IV.

II. THEORETICAL ASPECTS

A. Effective Hamiltonian for Cu(1,3-bdc)

Cu(1,3-bdc) is a metal-organic hybrid kagome magnet [18]; its chemical structure is depicted in Fig. 1(a). The magnetic constituents are stacked Cu²⁺ kagome layers [brown triangles in Fig. 1(a)], which are separated by an organic ligand. The spin of the Cu sites is $s = \hbar/2$.

Inelastic neutron scattering revealed the magnon dispersion from which exchange parameters have been deduced [19]. Adjacent kagome planes are very weakly antiferromagnetically coupled (according to Ref. [27] the ratio of interplane to intraplane interactions is about -0.003), which suggests to treat in good approximation the three-dimensional (3D) system as a stack of uncoupled layers. Within each layer, nearest-neighbor interactions dominate. Consequently, an effective spin Hamiltonian

$$H = \frac{1}{2} \sum_{\langle ij \rangle} [-J_{ij} s_i \cdot s_j + \mathbf{D}_{ij} \cdot (s_i \times s_j)] - B \sum_i s_i^z \quad (1)$$

of a two-dimensional (2D) ferromagnetic nearest-neighbor kagome lattice model is appropriate. $J_{ij} > 0$ and \mathbf{D}_{ij} are the exchange parameter and the DM vector that couple spin s_i with spin s_j , respectively. B is an external magnetic field in the z direction, that is, orthogonal to the kagome plane (xy plane).

TABLE I. The family of magnon Hall effects and the nomenclature of magnon-mediated transverse transport phenomena.

Force	Transverse response	
	Spin current	Heat current
magnetic-field gradient	magnon spin Hall effect (MSHE)	magnon Ettingshausen effect (MEE)
temperature gradient	magnon Nernst effect (MNE)	magnon Hall effect (MHE)

In experiments, a small magnetic field of about 50 mT perpendicular to the kagome layers is necessary to fully align the spins out of plane [19]. This indicates the presence of a mechanism that causes the in-plane orientation of the spins. For the time being, we do not include any easy-plane anisotropy as its energy is much smaller than that of the exchange parameters.

The kagome lattice is built from corner-sharing equilateral triangles hosting Cu atoms [Fig. 1(b)]. The three basis sites per unit cell (red dots) feature the $s = \hbar/2$ spins, each of which has four nearest neighbors at a distance of 0.4554 nm (Ref. [18]). All of the neighbors are equivalent, hence, the J_{ij} can be replaced by the single parameter J .

For a strict 2D geometry, Moriya's symmetry rules [28] allow for DM vectors orthogonal to the kagome plane. In Cu(1,3-bdc), however, kagome planes are not mirror planes of the crystal [cf. Fig. 1(a)]; thus, the DM vectors may have nonzero in-plane components [29]. Although their experimental results could be reproduced successfully without in-plane components, the authors of Ref. [19] note that the limited experimental resolution does not allow to rule out a band gap caused by these components. Bearing this in mind, we present results for vanishing in-plane components

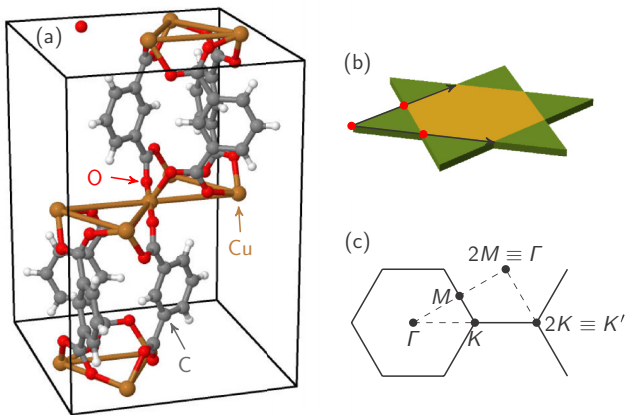


FIG. 1. Kagome planes of Cu(1,3-benzenedicarboxylate). (a) Chemical structure of Cu(1,3-benzenedicarboxylate) with parallel kagome planes built from Cu^{2+} ions (brown triangles); hydrogen atoms are shown as white spheres. Crystal data are taken from Ref. [18] and Jmol [26] was used for visualization. (b) Artistic sketch of the kagome lattice, which consists of equilateral triangles (green) and hexagons (yellow). The basis vectors of the hexagonal lattice (black arrows) and the three basis sites (red dots) are indicated. (c) Hexagonal Brillouin zone with high-symmetry points Γ , M , and K . The points $2K$ and $2M$ are shown in addition.

($\mathbf{D}_{ij} = -\mathbf{D}_{ji} = D\hat{z}$ with $D/J = 0.15$) but comment on their influence at appropriate places.

The quantum-mechanical version of the Hamiltonian (1) is often treated within the linear spin-wave approximation (LSWA): after performing the Holstein-Primakoff transformation [30], only terms quadratic in the boson operators are taken into account. A subsequent Fourier transformation yields the part of the Hamiltonian that can be diagonalized and from which the magnon band structure is obtained. Due to the ferromagnetic ground state a nonunitary Bogoliubov transformation is not necessary. Magnon-magnon interactions are neglected in the LSWA as these are at least of third order in the boson operators. The Dzyaloshinskii-Moriya interaction causes complex hopping matrix elements that introduce gaps in the magnon spectrum [5,8]; on top of this, the Abelian Berry curvature [31,32] yields nonzero topological invariants [12] which are not directly accessible in a classical approach. The Berry curvature is nonzero because the time-reversal symmetry of the boson Hamiltonian is broken; it results in an anomalous velocity which drives the transverse response to an applied temperature gradient. The transverse conductivities are given as Brillouin zone integrals over the weighted Berry curvature [9–11,33,34].

In what follows, we demonstrate that the classical version of the Hamiltonian (1) captures the transverse transport effects. The approach is based on atomistic spin dynamics simulations, which may be considered, loosely speaking, as a “brute force” method since it includes all orders of magnon-magnon interactions.

B. Spin and heat transport in a Heisenberg magnet with Dzyaloshinskii-Moriya interactions

Assuming an electrically insulating sample, two driving forces remain that act on the magnetic moments: a magnetic-field gradient ∇B and a temperature gradient ∇T . Linear response theory relates the spin current density \mathbf{j}_s and the thermal current density \mathbf{j}_{th} to these forces,

$$\begin{pmatrix} \mathbf{j}_s \\ \mathbf{j}_{\text{th}} \end{pmatrix} = \begin{pmatrix} L_{s,s} & L_{s,\text{th}} \\ L_{\text{th},s} & L_{\text{th},\text{th}} \end{pmatrix} \begin{pmatrix} \nabla B \\ -\nabla T/T \end{pmatrix}. \quad (2)$$

For 2D systems, the transport coefficients $L_{n,m}$ ($n, m = s, \text{th}$) are 2×2 tensors. Using the Onsager relation $L_{s,\text{th}} = L_{\text{th},s}$, the spin conductivity

$$\sigma \equiv L_{s,s},$$

the magnetothermal conductivity

$$\xi \equiv \frac{1}{T} L_{s,s}^{-1} L_{s,\text{th}},$$

and the thermal conductivity

$$\kappa \equiv \frac{1}{T}(L_{\text{th,th}} - TL_{s,\text{th}}\xi)$$

can be defined for the temperature T .

In accordance with the fluctuation-dissipation theorem, the Kubo formula of linear response theory links the autocorrelation of equilibrium fluctuations of the currents (capital \mathbf{J} 's are the currents corresponding to the respective current densities \mathbf{j}) to the $L_{n,m}$ (e.g., Ref. [35]),

$$L_{n,m}^{\mu\nu} = \frac{1}{k_B T} \int_0^\infty \lim_{A \rightarrow \infty} \frac{1}{A} \langle J_n^\mu(t) J_m^\nu(0) \rangle dt. \quad (3)$$

$\langle \cdot \rangle$ denotes the ensemble average, N is the total number of spins, A the total area of the sample, and k_B the Boltzmann constant. $\mu, \nu = x, y$ index the elements of the 2×2 transport tensors. Longitudinal (transverse) transport is described by diagonal (off-diagonal) elements $\mu = \nu$ ($\mu \neq \nu$).

The currents in Eq. (3) are derived for classical spins in the following (for the quantum-mechanical case confer Ref. [17]). For DM vectors along the z axis, the Hamiltonian (1) is rewritten as $H = \sum_i h_i$ with

$$h_i = -Bm_i^z + \frac{1}{2} \sum_{j \in N(i)} [-J_{ij} \mathbf{m}_i \cdot \mathbf{m}_j + D_{ij} \hat{\mathbf{z}} \cdot (\mathbf{m}_i \times \mathbf{m}_j)]. \quad (4)$$

$N(i)$ is the set of neighbors interacting with spin \mathbf{m}_i at position \mathbf{r}_i . Each \mathbf{m}_i is a three-dimensional unit vector. We use \mathbf{m} instead of \mathbf{s} to differentiate classical from quantum-mechanical spins. The units of magnetic moments are condensed in the exchange parameters, the magnetic field is consequently measured in units of energy.

Since both energy and the z component of the total magnetic moment $M^z \equiv \sum_i m_i^z$ are conserved in Eq. (4), the continuity equations

$$\begin{aligned} \frac{\partial M^z}{\partial t} + \nabla \cdot \mathbf{J}_s &= 0, \\ \frac{\partial H}{\partial t} + \nabla \cdot \mathbf{J}_{\text{th}} &= 0 \end{aligned}$$

hold. \mathbf{J}_s can be regarded as the (charge-neutral) analog of the charge current of electrons; the term ‘‘magnon current’’ also applies. Following Ref. [36], we introduce the currents

$$\begin{aligned} \mathbf{J}_s &\equiv \sum_i \mathbf{r}_i \frac{\partial m_i^z}{\partial t}, \\ \mathbf{J}_{\text{th}} &\equiv \sum_i \mathbf{r}_i \frac{\partial h_i}{\partial t}. \end{aligned}$$

Utilizing the equation of motion $\partial \mathbf{m}_i / \partial t = -\gamma \mathbf{m}_i \times \partial H / \partial \mathbf{m}_i$ (γ gyromagnetic ratio), the spin current reads

$$\mathbf{J}_s = \sum_{i < j} \mathbf{J}_s^{i \rightarrow j}, \quad (5)$$

with the bond spin current

$$\mathbf{J}_s^{i \rightarrow j} = \gamma \mathbf{r}_{ij} [J_{ij} (m_i^x m_j^y - m_i^y m_j^x) + D_{ij} (m_i^x m_j^x + m_i^y m_j^y)] \quad (6)$$

($\mathbf{r}_{ij} \equiv \mathbf{r}_i - \mathbf{r}_j$).

The thermal current $\mathbf{J}_{\text{th}} = \mathbf{J}_{\text{th}}^{\text{field}} + \mathbf{J}_{\text{th}}^{\text{inter}}$ is decomposed into two contributions (see Appendix A for a detailed derivation). The magnetization contribution

$$\mathbf{J}_{\text{th}}^{\text{field}} = -B \sum_{i < j} \mathbf{J}_s^{i \rightarrow j} = -B \mathbf{J}_s \quad (7)$$

is the coupling to the external magnetic field. The interaction contribution reads

$$\mathbf{J}_{\text{th}}^{\text{inter}} = -\frac{\gamma}{2} \sum_{\Delta_{ijk}} [\mathbf{r}_{ik} (A_{ijk} - B_{ijk} + B_{kji}) + \text{cyc}(i, j, k)]. \quad (8)$$

with

$$\begin{aligned} A_{ijk} &= J_{ij} J_{jk} \mathbf{m}_i \cdot (\mathbf{m}_j \times \mathbf{m}_k) + D_{ij} D_{jk} \hat{\mathbf{z}} \cdot (\mathbf{m}_i \times \mathbf{m}_k) (\mathbf{m}_j \cdot \hat{\mathbf{z}}), \\ B_{ijk} &= J_{ij} D_{jk} (\mathbf{m}_i \times \mathbf{m}_j) \cdot (\mathbf{m}_k \times \hat{\mathbf{z}}). \end{aligned}$$

The summations $\sum_{i < j}$ ($\sum_{\Delta_{ijk}}$) are over each pair (triple) of spins without double counting; ‘‘cyc(i, j, k)’’ in Eq. (8) means that the preceding term in the sum is repeated twice but with indices changed in cyclic order ($i \rightarrow j \rightarrow k \rightarrow i$).

C. Numerical methods

The computation of the conductivities requires several steps. In the first step, a cluster of randomized magnetic moments is thermalized for the given temperature T using either standard Monte Carlo simulations (Metropolis algorithm [37]) or the stochastic Landau-Lifshitz-Gilbert (sLLG) equation [38].

In the sLLG equation

$$(1 + \alpha^2) d\mathbf{m}_i = -(1 + \alpha \mathbf{m}_i \times) [\mathbf{m}_i \times (\mathbf{B}_i d\tau + G d\mathbf{W}_i)], \quad (9)$$

the moment \mathbf{m}_i is subject to precession about the local net magnetic field $\mathbf{B}_i = \mathbf{B} - \partial H / \partial \mathbf{m}_i$ and to Gilbert damping. The strength α of the Gilbert damping is in general a nonlocal symmetric 3×3 tensor but approximated here by a local scalar; this is justified by the collinear ground state. The coupling to a heat bath at temperature T is provided by a white-noise field \mathbf{b}_i with $G d\mathbf{W}_i = \mathbf{b}_i d\tau$; \mathbf{W}_i is an isotropic vector Wiener process and $G^2 = 2\alpha k_B T / (B^{\text{ref}} \mu_B)$ a dimensionless diffusion constant; B^{ref} is a reference field determining the scale of dimensionless time τ and μ_B is Bohr's magneton. The numerical integration of the sLLG equation is performed with an implicit midpoint method which preserves the length of each moment.

In the next step of the computation, the ensemble average of the correlation functions is performed. This can be done by two strategies.

(1) The ensemble average is literally performed by thermalizing *several thousands* of clusters and subsequently calculating their time evolution by conservative spin dynamics [i.e., the sLLG Eq. (9) with $\alpha = 0$]. The influence of the temperature is only due to the random initial conditions which differ for each ensemble. This protocol was followed, for example, in Refs. [39,40] to describe spin chains.

(2) Because the white-noise fields \mathbf{b}_i preserve the ergodicity, the ensemble average can be replaced by a time average, provided that the temporal evolution is sufficiently long. The thermalization of a *single* cluster is followed by

a long-time evolution according to the sLLG Eq. (9) with $\alpha \neq 0$. The currents are evaluated and stored at each time step. After choosing a time subinterval that is long enough for the correlations to drop to zero, the correlation functions are evaluated. The ensemble average is taken by successively shifting the subinterval by one integration step as many times as allowed by the total integration time.

In this work, we follow strategy 2 because, with regard to experiments, the magnons are coupled to other baths (e. g., to phonons and electrons). The Gilbert damping α mimics all of these couplings without specifying their detailed origin (e. g., spin-phonon coupling [41]). A typical time integration is performed over at least 20 ns up to 64 ns, that is, several million time steps of 1 fs have to be performed. The interval in which the correlation functions are calculated depends on the Gilbert damping α : the larger α , the faster the correlation functions drop to zero (see Sec. III B). In the limit $\alpha \rightarrow 0$ we expect this approach converge to the results obtained by strategy 1. To corroborate this conjecture, we compare both strategies for a chain of ferromagnetically coupled moments; the results, presented in Appendix B, show that it holds for a one-dimensional system.

Regardless of whether strategy 1 or strategy 2 is applied, numerical time integration of the current correlation functions has to be performed to determine the transport coefficients. We discuss this issue in Appendix C.

III. RESULTS AND DISCUSSION

We present and discuss results for the ferromagnetic nearest-neighbor kagome model with DM vectors and an external magnetic field in the z direction. If not stated otherwise, the experimentally determined ratio $D/J = 0.15$ (Ref. [19]) of exchange to DM interaction is used to mimic Cu(1,3-bdc). The exchange parameters are chosen such that the experimentally determined critical temperature $T_c \approx 1.8$ K (Ref. [20]) is well reproduced ($J = 0.3$ meV, $D = 0.045$ meV). Since the transport simulations are computationally very demanding, the cluster size has to be restricted, what causes a residual magnetization at temperatures above the critical temperature (finite-size effect); we comment on the influence of the cluster size in Sec. III B.

To the best of our knowledge, the Gilbert damping α of Cu(1,3-bdc) is not known but can be estimated as follows. The magnon lifetime is given by $\tau = (2\alpha\omega)^{-1}$. Taking $\hbar\omega \approx \hbar\bar{\omega} \approx 1$ meV, i.e., approximately half of the total width of the magnon spectrum, and $\tau \approx \hbar/\Gamma$ approximated from the experimental band broadening ($\Gamma = 0.03$ meV, Ref. [19]), we deduce $\alpha = \Gamma/(2\hbar\bar{\omega}) \approx 0.015$, which is a reasonable value.

A. Topology of bulk magnons and topological edge magnons

To show that the kagome ferromagnet is a TMI, we utilize the bulk-boundary correspondence (rather than computing topological invariants in the quantum-mechanical framework; cf. Sec. II A). Magnon band structures are determined from the dynamical structure factor

$$S(\omega, \mathbf{k}) = \frac{1}{2\pi} \int_{-\infty}^{\infty} \exp(i\omega t) \langle \mathbf{m}(\mathbf{k}, t) \cdot \mathbf{m}(\mathbf{k}, 0) \rangle dt,$$

where $\mathbf{m}(\mathbf{k}, t)$ is the lattice Fourier transform of the spin configuration at time t . The influence of the sample edges can be switched on or off by applying either open or periodic boundary conditions to the cluster.

For periodic boundary conditions, only the three bulk bands show up [Figs. 2(a) and 2(b)], as expected for the kagome lattice with its three sites per unit cell. The bulk spectra agree with those obtained in the LSWA [8]. A small Zeeman shift of the entire spectra to higher energies is caused by the external magnetic field. There are no band gaps if the magnetic field is in-plane (a); however, gaps open up for an out-of-plane field (b). Notice that although the dynamical structure factor of the first and second band (counted from below) decreases about the K point in (a), it stays nonzero, indicating the absence of a band gap. The dependence of the band-gap opening on the field direction reproduces nicely the experiments reported in Ref. [19]. We recall that an in-plane component of the DM vectors would introduce a small gap. The missing first optical mode in Fig. 2(a) for the ΓK direction is explained by destructive interference caused by the atomic basis [42,43].

For open boundary conditions, additional magnon branches appear within the bulk-band gaps (Fig. 2(c); cf. Ref. [44]). We distinguish two kinds of gap states: those that connect adjacent

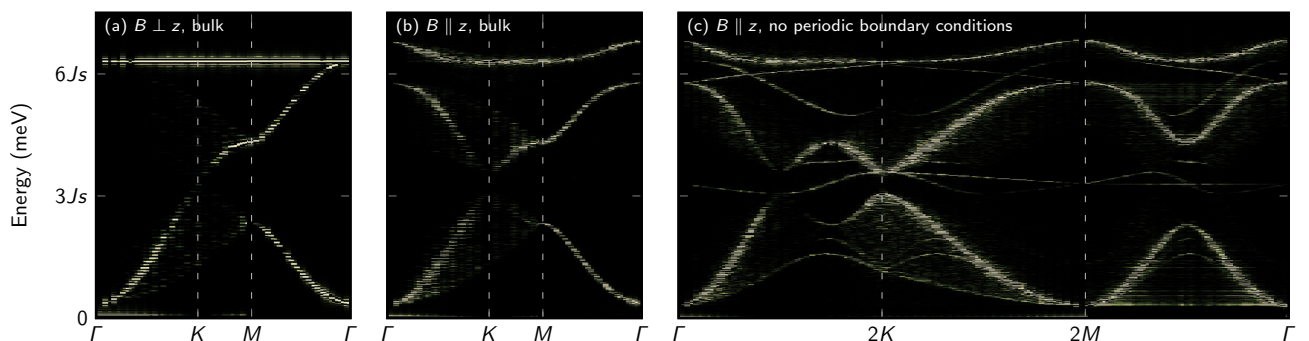


FIG. 2. Dynamical structure factor of a kagome ferromagnet with Dzyaloshinskii-Moriya interaction with periodic (a and b) and with open (c) boundary conditions [the extended zone scheme is shown in Fig. 1(c)]. A magnetic field is applied in-plane (a) or perpendicular (b and c) to the two-dimensional cluster. $J = 0.3$ meV, $D = 0.045$ meV, $B = 0.1$ meV, $T = 0.01$ K, $\alpha = 0.001$, and $N = 14700$.

bulk bands and those that do not. The existence of the latter is understood from the reduced coordination number at the edges which causes that the local order parameter may not point in the direction of the net magnetization; as a result, a magnon band becomes energetically separated from the bulk bands. Such an edge magnon is conventional or topologically trivial: it can be shifted in energy by modifying the exchange parameters at the edge [14]; in particular, it can be moved into the bulk-band regime.

More interesting is the first kind of gap states. As shown previously [12–14,45], the LSWA predicts the bulk bands to be topologically nontrivial, i.e., their Chern numbers are nonzero. More precisely, they read ± 1 , 0, and ∓ 1 for the bottom, middle and top band for the chosen exchange parameters (their sign depends on the sign of D). According to the bulk-boundary correspondence [14,21,22], the nontrivial topology causes topological edge magnons that connect adjacent bulk bands. The winding number of a band gap, which is the sum of all Chern numbers of the bulk bands below this gap, translates into the number of topological edge magnons within this gap. This rule yields one nontrivial edge magnon in each gap for the present system [12,14]. In contrast to conventional edge magnons, the topological ones cannot be shifted out of the band gap by modifying the exchange parameters at the edge [14].

The above considerations are fully in line with the two additional modes in each gap, shown in Fig. 2(c). The topological modes are unidirectionally circulating the sample. Hence edge states at opposite edges have opposite propagation direction. Being projected onto the chosen lines in reciprocal space they appear as (two) bands with opposite group velocity.

More than two topological states per gap were found in Ref. [44]. We think this is explained by using DM vectors with components compliant with the full symmetry of the 3D system. Comparison with the LSWA is not obvious for such a setup because the LSWA accounts only for the component of the DM vectors parallel to the applied magnetic field (here: z direction). The other components enter via terms of third order in the magnon operators and cause damping as well as band broadening [46]. Further theoretical work is suggested to concur topology and magnon interactions.

B. Spin and heat currents

We now discuss selected results which illustrate the influence of the cluster size N , the DM interaction D , the Gilbert damping α , and the temperature T . On top of that, time-averaged bond thermal currents are addressed with respect to the origin of nonzero transverse current correlation functions for $D \neq 0$. We focus on the correlation function of thermal currents and stress that its discussion applies to the spin correlation function as well.

1. Current correlation functions

The system size N is important when identifying finite-size effects. Since $\langle J_{\text{th}}^x(0)J_{\text{th}}^x(0) \rangle > 0$, the longitudinal correlation functions are in any case positive at $t = 0$ [Fig. 3(a)]. A closer inspection of the correlation function suggests that it decays on two time scales: a short-time decay (< 1 ps) and a long-time

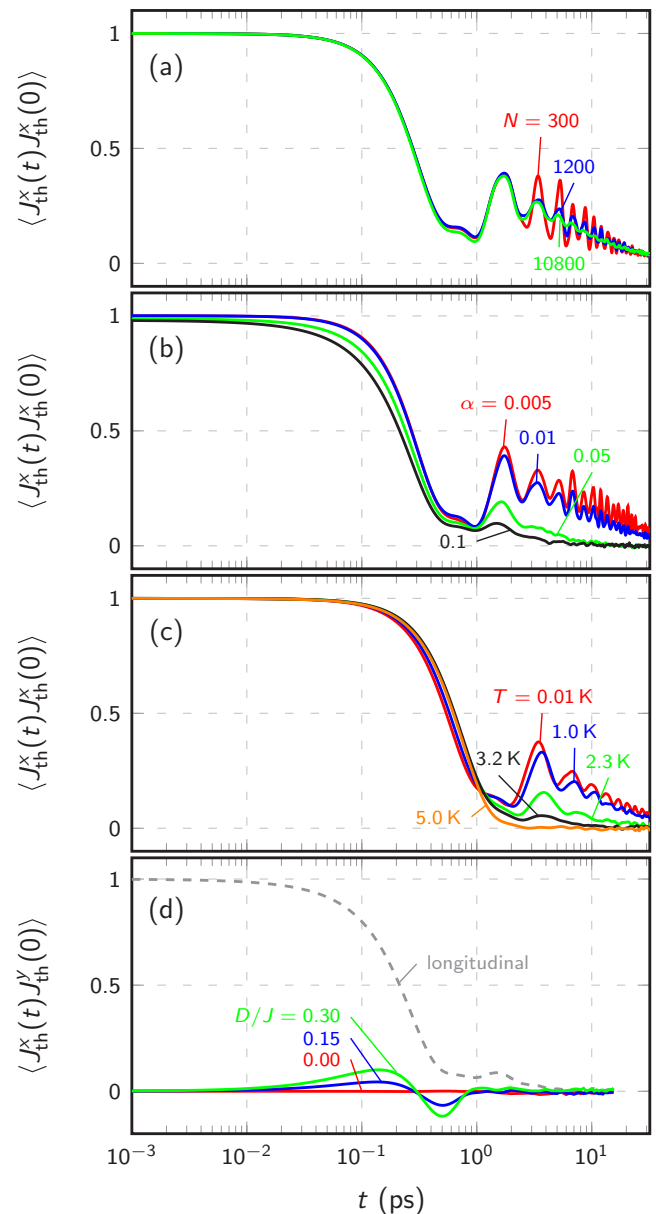


FIG. 3. Effect of various parameters on (normalized) thermal current correlation functions. (a) Longitudinal correlation function for selected cluster sizes N ; $T = 0.2$ K, $\alpha = 0.01$, $D = 0$, $J = 0.6$ meV, and $B = 0.1$ meV. (b) Longitudinal correlation function for selected Gilbert damping parameters α ; $T = 0.2$ K, $N = 1200$, $D = 0$, $J = 0.6$ meV, and $B = 0.1$ meV. (c) Longitudinal correlation function for selected temperatures T ; $D = 0$, $\alpha = 0.015$, $N = 2700$, $J = 0.3$ meV, and $B = 0.1$ meV. (d) Transverse correlation function for selected Dzyaloshinskii-Moriya interactions D . For comparison, the longitudinal correlation function is plotted (gray dashed line); $T = 0.2$ K, $\alpha = 0.1$, $N = 1200$, $J = 0.6$ meV, and $B = 0.1$ meV.

decay (≈ 100 ps); the latter exhibits oscillations. Apparently, the short-time behavior does not depend on N but the long-time behavior does because the amplitude of the oscillations decreases for increasing system size. Thus the oscillations are numerical artifacts that we will analyze in the following.

The magnon lifetimes are influenced by the Gilbert damping α : the larger the damping, the faster the current correlation drops to zero [Fig. 3(b)]. Upon increasing α the oscillations at large times are reduced. Thus α is a crucial parameter when quantitatively comparing theory with experiment.

The correlation function of the thermal *phonon* current exhibits two decay time scales, too [47]. The fast decay is attributed to optical and the slow decay to acoustic phonons [48]. This picture may apply for magnons as well since there are optical and acoustic magnons contributing to transport. However, a two-stage decay was observed also in systems without optical phonon modes [49], which is interpreted in the context of phonon mean free paths.

We clarify this point by analyzing the temperature dependence of the longitudinal thermal correlation function [Fig. 3(c)]. Apparently, the long-time decay is strongly reduced upon increasing the temperature (in particular, for $T \gtrsim 2 \text{ K} > T_c$), whereas the short-time decay shows minor dependence. This finding suggests that the magnons in the ferromagnetic phase (small T) cause long-time correlation. On the other hand, the short-time correlation survives even in the paramagnetic phase. Since the Gilbert damping and the temperature are related by the stochastic fields b_i in the sLLG equation, they evidently cause similar trends.

Neither damping nor temperature has a strong effect on the frequency of the long-time oscillations, in contrast to the exchange parameter J . The comparison of the oscillations in Figs. 3(a) and 3(c) tells that a decrease of J reduces the frequency. More precisely, $J = 0.6 \text{ meV}$ in (a) yields $\omega \approx 3.31 \text{ THz}$, whereas $J = 0.3 \text{ meV}$ in (c) gives $\omega \approx 1.99 \text{ THz}$. Both frequencies are about the mean-field Larmor frequencies $\omega_{\text{MF}} = 4J/\hbar$, which read 3.65 THz and $\approx 1.82 \text{ THz}$, respectively. Notwithstanding, these oscillations cancel out in the time integration and, hence, are irrelevant for the transport coefficients (Appendix C).

We conclude that the system size N influences the correlation function in two ways. First, the correlation function might show oscillations; second, the finite size of the system causes a residual magnetization at $T > T_c$. Thus, even in the paramagnetic phase, the correlation might introduce a contribution of magnons to the transport. It turned out that $N = 4800$, used in all further calculations, is a good compromise between finite-size effects and computation time.

Finally, we turn to the transverse current correlation function that equals zero at all times for $D = 0$ [red curve in Fig. 3(d)]. For zero DM interaction, the system's spectrum is not gapped and topologically trivial: the Berry curvature vanishes and so does the transverse conductivity. Only for $D \neq 0$ a plus/minus feature shows up, whose amplitude increases with D (blue and green curves). These findings compare well with those obtained within the LSWA. Compared to the longitudinal correlation function (gray dashed line), the transverse correlation function is much smaller. Hence the transverse transport is less efficient than the longitudinal one.

Since $\langle J_{\text{th}}^x(t)J_{\text{th}}^y(0) \rangle = -\langle J_{\text{th}}^y(t)J_{\text{th}}^x(0) \rangle$, the tensors $L_{n,m}$ are antisymmetric. If the sign of D is reversed, the sign of the transverse correlation function is reversed as well; consequently, the transverse transport takes place in opposite

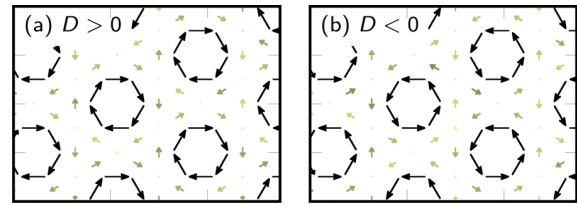


FIG. 4. Time-averaged bond thermal currents for $D > 0$ (a, left) and $D < 0$ (b, right). The darker and longer the arrows, the larger the associated bond current. Only a part of the sample is depicted. $T = 0.8 \text{ K}$, $B = 0.5 \text{ meV}$, $D/J = \pm 0.5$, and $\alpha = 0.015$.

direction. This is in line with the observation within the LSWA that the Chern numbers of the magnon bulk bands are reversed too [12,13].

2. Currents in real space

In the preceding, we showed that a transverse current correlation function being nonzero requires a nonzero DM interaction D . This qualitative difference between transport with and without DM interaction reveals itself likewise in real space. The definitions (6) and (8) allow to partition the total currents into bond currents. While the bond spin current is already given by Eq. (6), the thermal current (8) is split into terms of the form $-\mathbf{r}_{ik}(A_{ijk} - B_{ijk} + B_{kji})/2$. This definition relates sites i and k that do not have to be nearest neighbors; they only need to share a common neighbor j .

The effect of the DM interaction shows up clearly in the time-averaged bond currents [Fig. 4; only the thermal current is shown, as it involves the spin current via $\mathbf{J}_{\text{th}}^{\text{field}}$; see Eq. (7)]. For $D = 0$, all bond currents average to zero (not shown) but for $D \neq 0$ there are currents circulating in the triangles (greenish arrows) and hexagons (black arrows). The sign of D determines the orientation of the circulation [arrows in (a) and (b)]. In thermal equilibrium, the time average of the net current per hexagon remains zero, so does the net thermal current of the entire sample.

The circulating current relates currents along the x and the y directions. This directionality of the bond currents causes a nonzero transverse correlation for $D \neq 0$. Changing the sign of D reverses the handedness of the circulation and the sign of the correlation functions.

Following the interpretation of Refs. [9–11], the circulating currents are a result of the self-rotation of propagating magnon wave packets. Their rotation induces angular momentum and is caused by the Berry curvature which is brought about by the nonzero DM interaction. Recall that the orbital motion of electrons generates circulating charge currents, which is accompanied by a magnetic moment. Analogously, the self-rotation of magnons (which are charge-neutral) can be thought of as a circulating spin current, which gives rise to a polarization charge.

C. Dependence of conductivities on an external magnetic field and on temperature

Before turning to the dependence of the conductivities on the temperature and an applied magnetic field B , we recall that simulations cannot be performed for $B = 0$, as the net moment

is not forced to point along the z direction. The derivation of the spin current, however, relies on a net moment in z direction [Eq. (6)]; the term $D_{ij}(m_i^x m_j^x + m_i^y m_j^y)$ would give a nonphysical contribution to the spin current.

For comparison with experiment, we derive conductivities for 3D samples from the conductivities computed for the 2D samples. This is achieved by dividing the 2D conductivities by the spacing $c \approx 0.797$ nm of the kagome layers in Cu(1,3-bdc) [18]. Thereby, the thermal conductivity recovers its usual unit W/Km. The magnetothermal conductivity is given in units of meV/K, the magnon number conductivity σ is multiplied by \hbar in order to obtain the spin conductivity.

1. Longitudinal transport

The longitudinal spin conductivity σ^{xx} and the thermal conductivity κ^{xx} are strictly positive [Figs. 5(a)–5(d)]. With increasing temperature, both conductivities drop [(a) and (c)] because both the magnetic order and the magnons vanish. At low temperatures, σ^{xx} falls linearly to zero (a) but κ^{xx} approaches a constant (c).

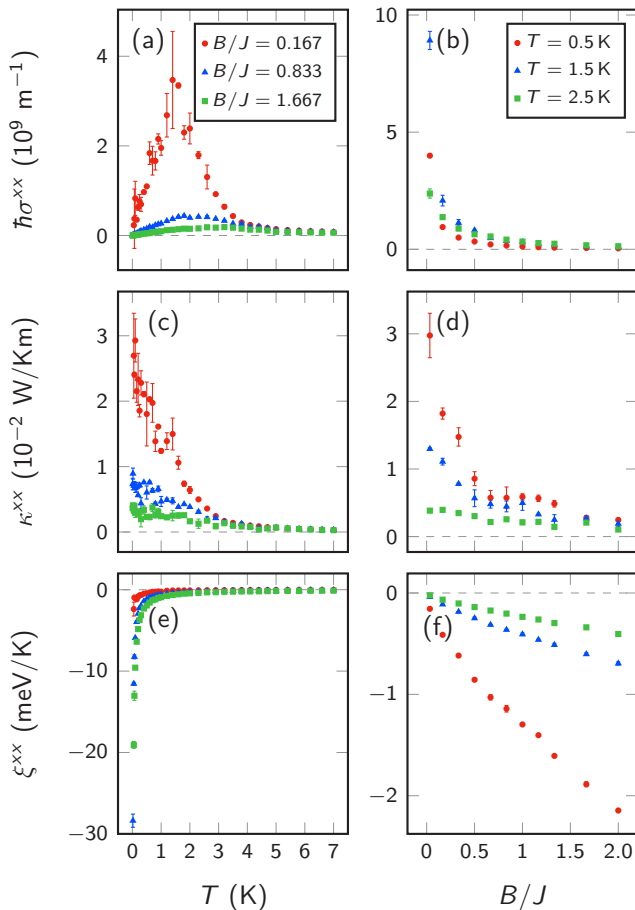


FIG. 5. Longitudinal conductivities vs temperature (left column) and applied magnetic field (right column). The spin conductivity [(a) and (b), top row], the thermal conductivity [(c) and (d), center row], and the magnetothermal conductivity [(e) and (f), bottom row] are computed for $N = 4800$, $J = 0.3$ meV, $D = 0.045$ meV, and $\alpha = 0.015$.

Concerning the dependence on the magnetic field [(b) and (d)], both conductivities decay with increasing field because, loosely speaking, the magnetic field “freezes out” the magnons. The LSWA predicts an exponential decay for κ^{xx} (Ref. [50]), which is roughly reproduced well below T_c [$T = 0.5$ K, red curve in (d)]. Such a trend is also observed in experiment and utilized to distinguish the spin from the phonon contribution to transport [20]. The order of magnitude of κ^{xx} (10^{-2} W/Km) agrees very well with that determined from experiments [20].

For $B \neq 0$, the magnetic thermopower ξ^{xx} (longitudinal magnetothermal conductivity) is negative [(e) and (f)], which indicates that the transport is mediated by spin-down particles (relative to the z direction); within this respect, recall that each magnon reduces the net magnetization by $1\hbar$. ξ^{xx} is proportional to T^{-1} (e) and B (f), in agreement with Ref. [51]. ξ^{xx} tends to zero for $B \rightarrow 0$ because the spin and thermal current are uncorrelated in this case: the contribution $-B\mathbf{J}_s$ to the thermal current vanishes.

2. Transverse transport

We now turn to the Hall-type transport properties (Fig. 6). The order of magnitude of κ^{xy} (10^{-4} W/Km) agrees very well

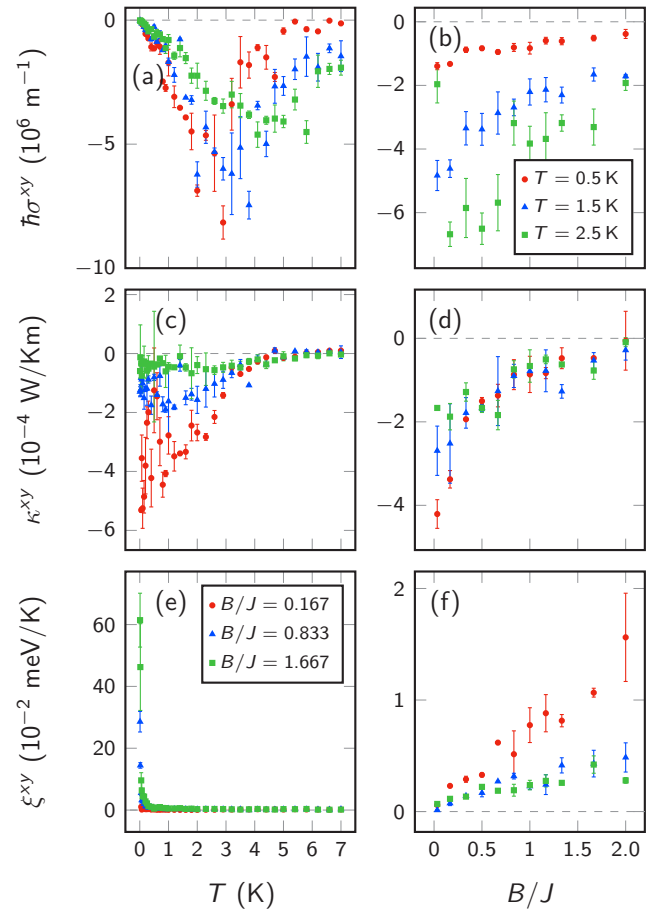


FIG. 6. Same as Fig. 5 but for the transverse conductivities. $\epsilon = 0.1$ was used for the numerical time integration of the transverse current correlation functions (see Appendix C).

with experimental results [20]. As both the longitudinal and the transverse thermal conductivity show the correct order of magnitude, the classical treatment predicts the proper order of the magnon Hall angle $\kappa^{xy}/\kappa^{xx} \approx 10^{-2}$. All of the transverse conductivities show the same T and B dependence as their respective longitudinal pendants. The signs of σ^{xy} and κ^{xy} “encode” the direction of the transverse current.

3. Low-temperature limit, quantum corrections, and comparison with experiment

The present approach shares essential features with lattice molecular-dynamics simulations to access the thermal conductivity of phonons [52]. For both magnons and phonons, the quantization of energy (and spin) as well as the zero-point energy are neglected. Furthermore, the Bose-Einstein distribution is replaced by the Boltzmann distribution. Thus one may anticipate that the temperature dependencies of the thermal conductivity in theory and experiment differ at low temperatures. An example is $\kappa \rightarrow 0$ in the quantum case and $\kappa \rightarrow \infty$ in the classical case (Ref. [53]).

We find the same situation: $T \rightarrow 0$ yields $\kappa \rightarrow \infty$ for $\alpha = 0$ and $\kappa \rightarrow \text{const.}$ for $\alpha \neq 0$ [Figs. 5(c) and 6(c), as well as Appendix B]. Since the LSWA predicts $\kappa \propto T^2$ in the low-temperature limit (in three dimensions) [50], which implies $\kappa \rightarrow 0$ for $T \rightarrow 0$, the mismatch is self-evident. In particular, the Wiedemann-Franz law, which should also hold for magnon-mediated transport [51] is violated; $\kappa/(\sigma T)$ diverges like T^{-2} for small T .

The very reason for the above disparity is found in the correlation functions, all of which increase like T^2 for small T . Thus all of the transport coefficients $L_{n,m}$ increase like T [Eq. (3)], implying $\sigma \sim T$, $\xi \sim T^{-1}$, and $\kappa \sim \text{const.}$ for $T \rightarrow 0$. This suggests that the Boltzmann distribution causes these temperature dependencies because it models the Bose distribution well at high but poorly at low T .

An established “quantum correction” post-processes the phonon thermal conductivity computed from molecular dynamics simulations [54]. The main idea is to map the classical system to its quantum-mechanical analog with the same energy. This mapping allows to renormalize the temperature scale and thereby recovers $\kappa \rightarrow 0$ for $T \rightarrow 0$.

In Ref. [55], the coupling of three-dimensional spin-lattice dynamics to a quantum heat bath was considered; for pure spin dynamics, a quantum fluctuation-dissipation ratio is derived from the magnon dispersion $\varepsilon(\mathbf{k})$ and the Bose-Einstein distribution $\rho(\varepsilon(\mathbf{k}), T)$. A new simulation temperature T_{sim} can be defined via

$$k_B T_{\text{sim}}(T) = \frac{\Omega}{(2\pi)^3} \int_{\text{BZ}} \varepsilon(\mathbf{k}) \rho(\varepsilon(\mathbf{k}), T) d^3k \quad (10)$$

as a function of the actual temperature T ; here, Ω is the volume per atom. For a ferromagnet at low T , we can set $\varepsilon(\mathbf{k}) \propto k^2$ and replace the integration over the BZ by an integration over a sphere, that is, $\int_{\text{BZ}} d^3k \rightarrow \int_0^\infty k^2 dk$. This yields the rescaling $T_{\text{sim}}(T) \propto T^{5/2}$, which would yield $\kappa \rightarrow 0$. However, the global rescaling of the temperature axis does not change the ratio κ/σ as the correlation functions still increase with T_{sim}^2 . Thus the Wiedemann-Franz law cannot be recovered by a mere rescaling of the temperature.

Furthermore, the above correction scheme does not properly resolve the divergence of the transverse conductivities since the divergence is not exclusively due to the classical approximation. A direct application of the Kubo formula for the transverse thermal conductivity yields a nonphysical divergence for $T \rightarrow 0$ because the temperature gradient drives besides the transversal heat current in addition circulating heat currents [56]. The latter are not experimentally accessible and their “polarization” contributions (Sec. III B 2) have to be removed. Thus performing a quantum correction that pushes the thermal conductivity to zero for $T = 0$ without proper treatment of the circulating currents seems questionable. For this reason, we refrain from using any of the quantum corrections; the classical description leads to a divergence of the thermal conductivity, which is lifted by the Gilbert damping but not brought to exactly zero. This is in contrast to the experimentally determined thermal conductivities reported in the literature [5,20,25]. Although the strict limit $T \rightarrow 0$ cannot be taken in experiments, the trend of the thermal conductivities is $\kappa \rightarrow 0$, as expected from the LSWA for both κ_{xx} and κ_{xy} . The different temperature dependencies become crucial in particular when the prominent sign change of κ_{xy} with magnetic field and temperature [20] is considered. It is not captured by the classical treatment.

The preceding raises the question to which minimum temperature the present approach gives a good approximation. The usual requirement $k_B T \gg \hbar\omega$ for the classical limit cannot be satisfied in the ferromagnetic phase since T_C is an upper boundary for T . For Cu(1,3-bdc), both $k_B T_C \approx 0.155$ meV and $\hbar\omega \approx 1$ meV indicate that quantum effects may dominate the transport properties in the entire temperature range up to T_C . This does also hold for the topological magnon insulator Lu₂V₂O₇, with $k_B T_C \approx 6.03$ meV (Ref. [5]) and $\hbar\omega \approx 15$ meV (Ref. [57]). On top of that, both systems feature spins with $s = \hbar/2$ which are far from the classical limit $S \rightarrow \infty$. It seems that the TMIs, which show Hall-type magnon transport are poorly modeled by classical spins, a hardly surprising observation as magnetism is intrinsically of quantum-mechanical nature. This sets magnons apart from phonons. In favor of a classical treatment, we want to stress that the order of magnitude of the thermal conductivity is in very good agreement with those determined in experiment and that the existence of the transverse transport phenomena is captured.

IV. CONCLUSION AND OUTLOOK

We demonstrated that atomistic spin dynamics simulations can capture the transverse transport in topological magnon insulators. The presented approach grants access to the complete family of magnon Hall effects and is able to estimate the correct order of magnitude of the Hall angles. It offers an additional perspective by means of a classical treatment.

With regard to transverse transport there are several systems which could be studied by this method. For once, the topological magnon insulators with honeycomb lattice [23,24] are of interest since the thermal Hall effect vanishes for a collinear antiferromagnetic ground state but the magnon spin Nernst effect persists [58,59]. Second, the method may be extended to noncollinear spin textures; in particular, skyrmion crystals are appealing inasmuch as topological Hall effects of

magnons [60–65] and topological magnon states have been predicted [66].

ACKNOWLEDGMENTS

Fruitful discussions with Danny Thonig are acknowledged. This work is supported by SPP 1666 of Deutsche Forschungsgemeinschaft (DFG).

APPENDIX A: SPIN AND THERMAL CURRENTS

With the Hamiltonian

$$H = \frac{1}{2} \sum_{ij} [-J_{ij} \mathbf{m}_i \cdot \mathbf{m}_j + D_{ij} \hat{\mathbf{z}} \cdot (\mathbf{m}_i \times \mathbf{m}_j)] - B \sum_i m_i^z, \quad (\text{A1})$$

which contains the DM interaction ($D_{ij} = -D_{ji}$) and an external magnetic field B along the z direction, the equation of motion $\dot{\mathbf{m}}_i = -\mathbf{m}_i \times \partial_{\mathbf{m}_i} H$ becomes

$$\dot{\mathbf{m}}_i = \mathbf{m}_i \times \left[\sum_{j \in \mathcal{N}(i)} (J_{ij} \mathbf{m}_j - D_{ij} \mathbf{m}_j \times \hat{\mathbf{z}}) + B \hat{\mathbf{z}} \right] \quad (\text{A2})$$

($\gamma = 1$ for the sake of clarity). From this equation, we derive expressions for spin and thermal currents that were used in the numerical calculations.

1. Spin current

In Eq. (A1), the z component of the total spin is conserved. Hence, the spin current is defined as

$$\mathbf{J}_s = \sum_i \mathbf{r}_i (\hat{\mathbf{z}} \cdot \dot{\mathbf{m}}_i),$$

which, using Eq. (A2), can be expressed as

$$\begin{aligned} \mathbf{J}_s &= \sum_i \mathbf{r}_i \sum_{j \in \mathcal{N}(i)} [J_{ij} (m_i^x m_j^y - m_i^y m_j^x) \\ &\quad + D_{ij} (m_i^x m_j^x + m_i^y m_j^y)] \\ &= \sum_{i < j} \underbrace{\mathbf{r}_{ij} [J_{ij} (m_i^x m_j^y - m_i^y m_j^x) + D_{ij} (m_i^x m_j^x + m_i^y m_j^y)]}_{=\mathbf{J}_s^{i \rightarrow j}} \end{aligned}$$

with the bond spin current $\mathbf{J}_s^{i \rightarrow j}$ and $\mathbf{r}_{ij} \equiv \mathbf{r}_i - \mathbf{r}_j$.

If in-plane components of the DM vectors (more generally: components orthogonal to the applied magnetic field) would be included in the Hamiltonian, no component of the total spin would be conserved and the continuity equation for the spin would include torques, i.e., sources or sinks of spin. An additional torque response to a thermal gradient was predicted in Ref. [33].

2. Thermal current

The energy of the system is conserved and the associated energy current (thermal current) reads

$$\mathbf{J}_{\text{th}} = \sum_i \mathbf{r}_i \dot{h}_i, \quad (\text{A3})$$

where

$$h_i = \frac{1}{2} \sum_{j \in \mathcal{N}(i)} [-J_{ij} \mathbf{m}_i \cdot \mathbf{m}_j + D_{ij} \hat{\mathbf{z}} \cdot (\mathbf{m}_i \times \mathbf{m}_j)] - B \hat{\mathbf{z}} \cdot \mathbf{m}_i \quad (\text{A4})$$

is the energy of the magnetic moment \mathbf{m}_i . With Eq. (A2), its time derivative

$$\begin{aligned} \dot{h}_i &= \frac{1}{2} \sum_{j \in \mathcal{N}(i)} [-J_{ij} \dot{\mathbf{m}}_i \cdot \mathbf{m}_j - J_{ij} \mathbf{m}_i \cdot \dot{\mathbf{m}}_j + D_{ij} \hat{\mathbf{z}} \cdot (\dot{\mathbf{m}}_i \times \mathbf{m}_j) \\ &\quad + D_{ij} \hat{\mathbf{z}} \cdot (\mathbf{m}_i \times \dot{\mathbf{m}}_j)] - B \hat{\mathbf{z}} \cdot \dot{\mathbf{m}}_i \end{aligned}$$

becomes

$$\begin{aligned} \dot{h}_i &= -B \hat{\mathbf{z}} \cdot \left\{ \mathbf{m}_i \times \left[\sum_{j \in \mathcal{N}(i)} (J_{ij} \mathbf{m}_j - D_{ij} \mathbf{m}_j \times \hat{\mathbf{z}}) + B \hat{\mathbf{z}} \right] \right\} - \frac{1}{2} \sum_{j \in \mathcal{N}(i)} J_{ij} \left\{ \mathbf{m}_i \times \left[\sum_{k \in \mathcal{N}(i)} (J_{ik} \mathbf{m}_k - D_{ik} \mathbf{m}_k \times \hat{\mathbf{z}}) + B \hat{\mathbf{z}} \right] \right\} \cdot \mathbf{m}_j \\ &\quad - \frac{1}{2} \sum_{j \in \mathcal{N}(i)} J_{ij} \mathbf{m}_i \cdot \left\{ \mathbf{m}_j \times \left[\sum_{l \in \mathcal{N}(j)} (J_{jl} \mathbf{m}_l - D_{jl} \mathbf{m}_l \times \hat{\mathbf{z}}) + B \hat{\mathbf{z}} \right] \right\} \\ &\quad + \frac{1}{2} \sum_{j \in \mathcal{N}(i)} D_{ij} \hat{\mathbf{z}} \cdot \left(\left\{ \mathbf{m}_i \times \left[\sum_{k \in \mathcal{N}(i)} (J_{ik} \mathbf{m}_k - D_{ik} \mathbf{m}_k \times \hat{\mathbf{z}}) + B \hat{\mathbf{z}} \right] \right\} \times \mathbf{m}_j \right) \\ &\quad + \frac{1}{2} \sum_{j \in \mathcal{N}(i)} D_{ij} \hat{\mathbf{z}} \cdot \left(\mathbf{m}_i \times \left\{ \mathbf{m}_j \times \left[\sum_{l \in \mathcal{N}(j)} (J_{jl} \mathbf{m}_l - D_{jl} \mathbf{m}_l \times \hat{\mathbf{z}}) + B \hat{\mathbf{z}} \right] \right\} \right). \quad (\text{A5}) \end{aligned}$$

Next, we inspect terms which include $\sum_{j \in \mathcal{N}(i)}$ and $\sum_{k \in \mathcal{N}(i)}$, namely,

$$- \sum_{j \in \mathcal{N}(i)} \sum_{k \in \mathcal{N}(i)} J_{ij} \{ [\mathbf{m}_i \times (J_{ik} \mathbf{m}_k - D_{ik} \mathbf{m}_k \times \hat{\mathbf{z}})] \cdot \mathbf{m}_j \}$$

and

$$\sum_{j \in \mathcal{N}(i)} \sum_{k \in \mathcal{N}(i)} D_{ij} \hat{\mathbf{z}} \cdot \{[\mathbf{m}_i \times (J_{ik} \mathbf{m}_k - D_{ik} \mathbf{m}_k \times \hat{\mathbf{z}})] \times \mathbf{m}_j\}.$$

The contributions from pairs (j,k) and (k,j) cancel each other, which is evident by writing

$$\begin{aligned} & - \sum_{j \in \mathcal{N}(i)} \sum_{k \in \mathcal{N}(i)} [J_{ij} J_{ik} \mathbf{m}_j \cdot (\mathbf{m}_i \times \mathbf{m}_k) - D_{ik} D_{ij} \hat{\mathbf{z}} \cdot (\mathbf{m}_j \times \mathbf{m}_k)(\mathbf{m}_i \cdot \hat{\mathbf{z}})] \\ & - J_{ij} D_{ik} (\mathbf{m}_j \times \mathbf{m}_i) \cdot (\mathbf{m}_k \times \hat{\mathbf{z}}) + J_{ik} D_{ij} (\mathbf{m}_k \times \mathbf{m}_i) \cdot (\mathbf{m}_j \times \hat{\mathbf{z}}). \end{aligned}$$

The first and second terms are antisymmetric upon exchange of j and k , the third and fourth terms are each other's negative under the aforementioned index exchange.

The remaining terms in Eq. (A5) are grouped with respect to the kinds of energy (the Heisenberg exchange J , DM interaction D , and external magnetic field B),

$$\dot{h}_i = \dot{h}_i^{(JJ)} + \dot{h}_i^{(JD)} + \dot{h}_i^{(DD)} + \dot{h}_i^{(JB)} + \dot{h}_i^{(DB)},$$

with

$$\dot{h}_i^{(JJ)} = -\frac{1}{2} \sum_{j \in \mathcal{N}(i)} \sum_{l \in \mathcal{N}(j)} J_{ij} J_{jl} \mathbf{m}_i \cdot (\mathbf{m}_j \times \mathbf{m}_l),$$

$$\dot{h}_i^{(JD)} = +\frac{1}{2} \sum_{j \in \mathcal{N}(i)} \sum_{l \in \mathcal{N}(j)} \{J_{ij} D_{jl} \mathbf{m}_i \cdot [\mathbf{m}_j \times (\mathbf{m}_l \times \hat{\mathbf{z}})] + J_{jl} D_{ij} \hat{\mathbf{z}} \cdot [\mathbf{m}_i \times (\mathbf{m}_j \times \mathbf{m}_l)]\},$$

$$\dot{h}_i^{(DD)} = -\frac{1}{2} \sum_{j \in \mathcal{N}(i)} \sum_{l \in \mathcal{N}(j)} D_{ij} D_{jl} \hat{\mathbf{z}} \cdot [\mathbf{m}_i \times (\mathbf{m}_j \times \{\mathbf{m}_l \times \hat{\mathbf{z}}\})],$$

$$\dot{h}_i^{(DB)} = +\frac{1}{2} \sum_{j \in \mathcal{N}(i)} B D_{ij} \hat{\mathbf{z}} \cdot [(\mathbf{m}_i \times \hat{\mathbf{z}}) \times \mathbf{m}_j] + \frac{1}{2} \sum_{j \in \mathcal{N}(i)} B D_{ij} \hat{\mathbf{z}} \cdot [\mathbf{m}_i \times (\mathbf{m}_j \times \hat{\mathbf{z}})] + \sum_{j \in \mathcal{N}(i)} B D_{ij} \hat{\mathbf{z}} \cdot [\mathbf{m}_i \times (\mathbf{m}_j \times \hat{\mathbf{z}})],$$

$$\dot{h}_i^{(JB)} = -\sum_{j \in \mathcal{N}(i)} J_{ij} B \hat{\mathbf{z}} \cdot (\mathbf{m}_i \times \mathbf{m}_j) - \frac{1}{2} \sum_{j \in \mathcal{N}(i)} J_{ij} B \mathbf{m}_j \cdot (\mathbf{m}_i \times \hat{\mathbf{z}}) - \frac{1}{2} \sum_{j \in \mathcal{N}(i)} J_{ij} B \mathbf{m}_i \cdot (\mathbf{m}_j \times \hat{\mathbf{z}}).$$

These terms are simplified now one by one.

With the spin chirality $\chi_{ijl} \equiv \mathbf{m}_i \cdot (\mathbf{m}_j \times \mathbf{m}_l)$, it follows:

$$\dot{h}_i^{(JJ)} = -\frac{1}{2} \sum_{j \in \mathcal{N}(i)} \sum_{l \in \mathcal{N}(j)} J_{ij} J_{jl} \chi_{ijl}.$$

Note that $\chi_{ijl} = \chi_{jli} = \chi_{lij} = -\chi_{jil} = -\chi_{ilj} = -\chi_{lji}$.

Using $\mathbf{a} \cdot [\mathbf{b} \times (\mathbf{c} \times \mathbf{d})] = (\mathbf{a} \times \mathbf{b}) \cdot (\mathbf{c} \times \mathbf{d})$, one obtains

$$\dot{h}_i^{(JD)} = +\frac{1}{2} \sum_{j \in \mathcal{N}(i)} \sum_{l \in \mathcal{N}(j)} [J_{ij} D_{jl} \xi_{ijl} + J_{jl} D_{ij} \xi_{lji}],$$

where $\xi_{ijl} \equiv (\mathbf{m}_i \times \mathbf{m}_j) \cdot (\mathbf{m}_l \times \hat{\mathbf{z}})$. Note that $\xi_{ijl} = -\xi_{jil}$.

$\dot{h}_i^{(DB)}$ is rewritten as

$$\dot{h}_i^{(DB)} = -\sum_{j \in \mathcal{N}(i)} B D_{ij} (m_j^x m_i^y + m_j^y m_i^x).$$

A similar form is found for

$$\dot{h}_i^{(JB)} = -\sum_{j \in \mathcal{N}(i)} J_{ij} B (m_i^x m_j^y - m_i^y m_j^x).$$

One might be tempted to neglect $\dot{h}_i^{(DD)}$ since it is second order in the DM interaction and often $D \ll J$. However, we account for this contribution as well. Making use of

$$\psi_{ijl} \equiv \hat{\mathbf{z}} \cdot [\mathbf{m}_i \times (\mathbf{m}_j \times \{\mathbf{m}_l \times \hat{\mathbf{z}}\})] = \hat{\mathbf{z}} \cdot (\mathbf{m}_i \times \mathbf{m}_l)(\mathbf{m}_j \cdot \hat{\mathbf{z}}),$$

we obtain

$$\dot{h}_i^{(DD)} = -\frac{1}{2} \sum_{j \in \mathcal{N}(i)} \sum_{l \in \mathcal{N}(j)} D_{ij} D_{jl} \psi_{ijl}.$$

Note that $\psi_{ijl} = -\psi_{lji}$.

Returning to the definition (A3) and plugging in the time derivatives of the local energy, we arrive at

$$\begin{aligned} \mathbf{J}_{\text{th}} &= \underbrace{\sum_i \mathbf{r}_i (\dot{h}_i^{(JB)} + \dot{h}_i^{(DB)})}_{=\mathbf{J}_{\text{th}}^{\text{field}}} \\ &+ \underbrace{\sum_i \mathbf{r}_i (\dot{h}_i^{(JJ)} + \dot{h}_i^{(JD)} + \dot{h}_i^{(DD)})}_{=\mathbf{J}_{\text{th}}^{\text{inter}}}. \end{aligned}$$

The term

$$\mathbf{J}_{\text{th}}^{\text{field}} = -B \sum_{i < j} \mathbf{J}_s^{i \rightarrow j} \quad (\text{A6})$$

involves the magnetic field and is the origin of magnetothermal coupling which generates a magnetic analog of the Seebeck effect.

Replacing the index l by k recasts the interaction contribution

$$\begin{aligned} \mathbf{J}_{\text{th}}^{\text{inter}} &= -\frac{1}{2} \sum_i \mathbf{r}_i \sum_{j \in \mathcal{N}(i)} \sum_{k \in \mathcal{N}(j)} (J_{ij} J_{jk} \chi_{ijk} - J_{ij} D_{jk} \xi_{ijk} \\ &\quad - D_{ij} J_{jk} \xi_{kji} + D_{ij} D_{jk} \psi_{ijk}) \\ &= -\frac{1}{2} \sum_i \mathbf{r}_i \sum_{j \in \mathcal{N}(i)} \sum_{k \in \mathcal{N}(j)} (A_{ijk} - B_{ijk} + B_{kji}), \end{aligned}$$

where

$$A_{ijk} \equiv J_{ij} J_{jk} \chi_{ijk} + D_{ij} D_{jk} \psi_{ijk},$$

($A_{ijk} = -A_{kji}$) and

$$B_{ijk} \equiv J_{ij} D_{jk} \xi_{ijk}.$$

Each triple $\{i, j, k\}$ of spins contributes

$$\begin{aligned} &\mathbf{r}_{ik}(A_{ijk} - B_{ijk} + B_{kji}) \\ &\quad + \mathbf{r}_{ji}(A_{jki} - B_{jki} + B_{ikj}) \\ &\quad + \mathbf{r}_{kj}(A_{kij} - B_{kij} + B_{jik}) \end{aligned}$$

to the thermal current. Defining

$$\mathbf{J}_{\text{th}}^{i \rightarrow j \rightarrow k} \equiv \mathbf{r}_{ik}(A_{ijk} - B_{ijk} + B_{kji}),$$

the interaction contribution reads

$$\mathbf{J}_{\text{th}}^{\text{inter}} = -\frac{1}{2} \sum_{\Delta_{ijk}} \underbrace{(\mathbf{J}_{\text{th}}^{i \rightarrow j \rightarrow k} + \mathbf{J}_{\text{th}}^{j \rightarrow k \rightarrow i} + \mathbf{J}_{\text{th}}^{k \rightarrow i \rightarrow j})}_{\equiv \mathbf{J}_{\text{th}}^{ijk}},$$

where the summation is over each triple of spins without double counting. $\mathbf{J}_{\text{th}}^{ijk}$ can be understood as a plaquette thermal current.

APPENDIX B: EFFECT OF GILBERT DAMPING ON THERMAL CONDUCTIVITIES

As discussed in Sec. II C, there are two strategies to evaluate the ensemble averages. Strategy 1 relies on the Hamilton dynamics and can be understood as *intrinsic* since only magnon-magnon interactions are considered. In contrast, the *extrinsic* strategy 2 includes in addition the coupling of the magnons to external baths; the interactions with the other quasiparticles are modeled by the Gilbert damping.

To compare both strategies, we address the thermal conductivity

$$\kappa = \frac{1}{k_B T^2} \int_0^\infty \lim_{N \rightarrow \infty} \frac{1}{Na} \langle J_{\text{th}}(t) J_{\text{th}}(0) \rangle dt$$

for $B = 0$ of a chain of ferromagnetically coupled spins (Refs. [39,40]; lattice constant a). We simulated a chain of $N = 500$ spins coupled by $J = 1$ meV. For strategy 1, the average is performed over 4000 ensembles, for strategy 2, the integration over time was performed for up to 42 ns. The computed thermal current correlation functions are approximated well by an exponential, $b \exp(-t/\tau)$; thus, $\kappa = b\tau L/(Nk_B T^2)$.

For the intrinsic strategy 1, κ diverges in the limit $T \rightarrow 0$ (black line in Fig. 7; note the double-logarithmic scale), in agreement with Ref. [39]. This divergence is removed if a

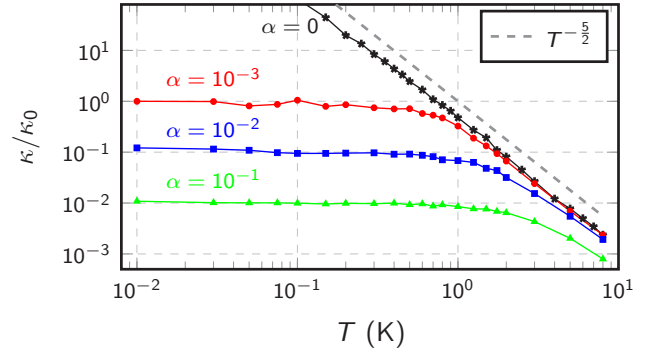


FIG. 7. Thermal conductivities of a chain of ferromagnetically coupled spins for $B = 0$ vs temperature for selected Gilbert damping constants α . Data are normalized to $\kappa_0 \equiv \kappa(0.01 \text{ K})$ for $\alpha = 10^{-3}$.

nonzero Gilbert damping α is introduced (strategy 2), no matter how small (colored lines). The thermal conductivity in the low-temperature regime increases approximately by one order of magnitude when α is decreased by one order of magnitude. At high temperatures, the conductivities behave like $T^{-5/2}$ (gray dashed line). We note in passing that the thermal conductivities shown here are similar to those in Ref. [40] for a chain with disorder. An exception is that we find $\kappa \rightarrow \text{const.}$ for $T \rightarrow 0$, whereas $\kappa \rightarrow 0$ in Ref. [40]; the latter recovers the Wiedemann-Franz law of magnon transport [51].

APPENDIX C: NUMERICAL INTEGRATION OF CURRENT CORRELATION FUNCTIONS

As a short-hand notation, we define $C_{\mu\nu}(t) \equiv \langle J^\mu(t) J^\nu(0) \rangle$ ($\mu, \nu = x, y$) and drop the index that differentiates between spin (s) and heat (th). The longitudinal correlation functions ($\mu = \nu$) decay on two time scales (Sec. III B), which leads to

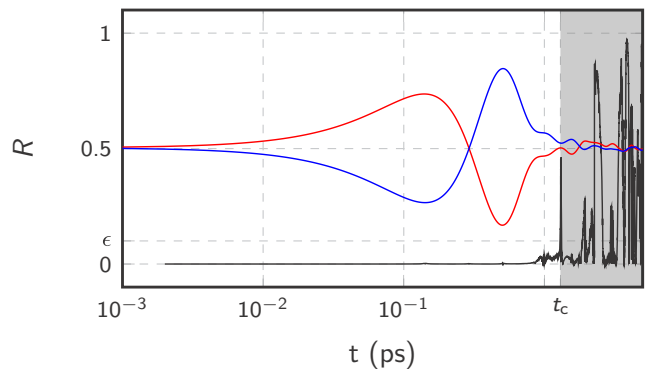


FIG. 8. Determination of the cut-off time t_c . Quality measure R (black curve) vs time for the transverse thermal-current correlation functions (red and blue curves; not true to scale) with a given error $\epsilon = 0.1$. The gray area ($t > t_c$) is excluded from the numerical integration. $J = 0.3$ meV, $D = 0.045$ meV, $T = 0.1$ K, $B = 0.1$ meV, and $N = 300$.

approximate

$$C_{\mu\mu}(t) \approx a_1 \exp\left(-\frac{t}{\tau_1}\right) + a_2 \exp\left(-\frac{t}{\tau_2}\right),$$

whose integral from time $t = 0$ to ∞ is evaluated analytically. The parameters a_1 , a_2 , τ_1 , and τ_2 are determined by a least-squares fit to the numerical data. Such a procedure is quite common in analyses of thermal conductivities of phonons [49].

In contrast to the longitudinal correlation function, the transverse correlation functions are integrated directly. The relation $C_{xy}(t) = -C_{yx}(t)$ is not strictly fulfilled in the numerical computations, in particular at large times t . Hence we introduce a measure for the numerical quality of the computed correlation functions, from which a cutoff time t_c is

deduced. With

$$E(f(x), g(x)) \equiv -\frac{2f(x)g(x)}{[f(x)]^2 + [g(x)]^2},$$

we define this measure by

$$R(t) \equiv \frac{1}{4} \left| E\left(\frac{\dot{C}_{xy}(t)}{C_{xy}(t)}, \frac{\dot{C}_{yx}(t)}{C_{yx}(t)}\right) + E(\dot{C}_{xy}(t), \dot{C}_{yx}(t)) \right. \\ \left. + E(C_{xy}(t), C_{yx}(t)) - 1 \right|$$

($0 \leq R(t) \leq 1$). Ideally, $R(t) = 0$. The integration of the correlation function is then performed numerically from $t = 0$ up to t_c , with t_c being the shortest time for which $R(t_c) > \epsilon$. $\epsilon > 0$ determines the error of the computed nondiagonal elements. This procedure is visualized in Fig. 8.

-
- [1] K. von Klitzing, *Rev. Mod. Phys.* **58**, 519 (1986).
 [2] H. Hasan and C. Kane, *Rev. Mod. Phys.* **82**, 3045 (2010).
 [3] C. Strohm, G. L. J. A. Rikken, and P. Wyder, *Phys. Rev. Lett.* **95**, 155901 (2005).
 [4] J. Romhányi, K. Penc, and R. Ganesh, *Nat. Comms.* **6**, 6805 (2015).
 [5] Y. Onose, T. Ideue, H. Katsura, Y. Shiomi, N. Nagaosa, and Y. Tokura, *Science* **329**, 297 (2010).
 [6] M. Hirschberger, J. W. Krizan, R. J. Cava, and N. P. Ong, *Science* **348**, 106 (2015).
 [7] P. Ben-Abdallah, *Phys. Rev. Lett.* **116**, 084301 (2016).
 [8] H. Katsura, N. Nagaosa, and P. A. Lee, *Phys. Rev. Lett.* **104**, 066403 (2010).
 [9] R. Matsumoto and S. Murakami, *Phys. Rev. Lett.* **106**, 197202 (2011).
 [10] R. Matsumoto and S. Murakami, *Phys. Rev. B* **84**, 184406 (2011).
 [11] R. Shindou, R. Matsumoto, S. Murakami, and J.-i. Ohe, *Phys. Rev. B* **87**, 174427 (2013).
 [12] L. Zhang, J. Ren, J.-S. Wang, and B. Li, *Phys. Rev. B* **87**, 144101 (2013).
 [13] A. Mook, J. Henk, and I. Mertig, *Phys. Rev. B* **89**, 134409 (2014).
 [14] A. Mook, J. Henk, and I. Mertig, *Phys. Rev. B* **90**, 024412 (2014).
 [15] A. Mook, J. Henk, and I. Mertig, *Phys. Rev. B* **91**, 174409 (2015).
 [16] A. Mook, J. Henk, and I. Mertig, *Phys. Rev. B* **91**, 224411 (2015).
 [17] H. Lee, J. H. Han, and P. A. Lee, *Phys. Rev. B* **91**, 125413 (2015).
 [18] E. A. Nytko, J. S. Helton, P. Müller, and D. G. Nocera, *J. Am. Chem. Soc.* **130**, 2922 (2008).
 [19] R. Chisnell, J. S. Helton, D. E. Freedman, D. K. Singh, R. I. Bewley, D. G. Nocera, and Y. S. Lee, *Phys. Rev. Lett.* **115**, 147201 (2015).
 [20] M. Hirschberger, R. Chisnell, Y. S. Lee, and N. P. Ong, *Phys. Rev. Lett.* **115**, 106603 (2015).
 [21] Y. Hatsugai, *Phys. Rev. B* **48**, 11851 (1993).
 [22] Y. Hatsugai, *Phys. Rev. Lett.* **71**, 3697 (1993).
 [23] S. A. Owerre, *J. Appl. Phys.* **120**, 043903 (2016).
 [24] S. A. Owerre, *J. Phys.: Condens. Matter* **28**, 386001 (2016).
 [25] T. Ideue, Y. Onose, H. Katsura, Y. Shiomi, S. Ishiwata, N. Nagaosa, and Y. Tokura, *Phys. Rev. B* **85**, 134411 (2012).
 [26] Jmol: an open-source JAVA viewer for chemical structures in 3D. <http://www.jmol.org/>.
 [27] R. Chisnell, J. S. Helton, D. E. Freedman, D. K. Singh, F. Demmel, C. Stock, D. G. Nocera, and Y. S. Lee, *Phys. Rev. B* **93**, 214403 (2016).
 [28] T. Moriya, *Phys. Rev.* **120**, 91 (1960).
 [29] M. Elhajal, B. Canals, and C. Lacroix, *Phys. Rev. B* **66**, 014422 (2002).
 [30] T. Holstein and H. Primakoff, *Phys. Rev.* **58**, 1098 (1940).
 [31] M. V. Berry, *Proc. R. Soc. London A* **392**, 45 (1984).
 [32] J. Zak, *Phys. Rev. Lett.* **62**, 2747 (1989).
 [33] A. A. Kovalev and V. Zyuzin, *Phys. Rev. B* **93**, 161106 (2016).
 [34] J. H. Han and H. Lee, *J. Phys. Soc. Jpn.* **86**, 011007 (2017).
 [35] R. Kubo, M. Toda, and N. Hashitsume, *Statistical Physics II*, Springer Series in Solid-State Sciences Vol 31 (Springer, Berlin, Heidelberg, 1991).
 [36] G. D. Mahan, *Many-Particle Physics* (Plenum, New York, 2000).
 [37] N. Metropolis, A. W. Rosenbluth, M. N. Rosenbluth, A. H. Teller, and E. Teller, *J. Chem. Phys.* **21**, 1087 (1953).
 [38] B. Skubic, J. Hellsvik, L. Nordström, and O. Eriksson, *J. Phys.: Condens. Matter* **20**, 315203 (2008).
 [39] A. V. Savin, G. P. Tsironis, and X. Zotos, *Phys. Rev. B* **72**, 140402 (2005).
 [40] B. Jenčič and P. Prelovšek, *Phys. Rev. B* **92**, 134305 (2015).
 [41] D. Thonig and J. Henk, *New J. Phys.* **16**, 013032 (2014).
 [42] A. Taroni, A. Bergman, L. Bergqvist, J. Hellsvik, and O. Eriksson, *Phys. Rev. Lett.* **107**, 037202 (2011).
 [43] L. Bergqvist, A. Taroni, A. Bergman, C. Etz, and O. Eriksson, *Phys. Rev. B* **87**, 144401 (2013).
 [44] M. Pereiro, D. Yudin, J. Chico, C. Etz, O. Eriksson, and A. Bergman, *Nat. Comms.* **5**, 4815 (2014).
 [45] K. Ohgushi, S. Murakami, and N. Nagaosa, *Phys. Rev. B* **62**, R6065(R) (2000).
 [46] A. L. Chernyshev and P. A. Maksimov, *Phys. Rev. Lett.* **117**, 187203 (2016).

- [47] A. J. C. Ladd, B. Moran, and W. G. Hoover, *Phys. Rev. B* **34**, 5058 (1986).
- [48] J. Che, T. Çağın, W. Deng, and W. A. Goddard, *J. Chem. Phys.* **113**, 6888 (2000).
- [49] A. McGaughey and M. Kaviani, *Int. J. Heat Mass Transf.* **47**, 1783 (2004).
- [50] J. Callaway, *Quantum Theory of the Solid State* (Academic Press, London, 1974).
- [51] K. Nakata, P. Simon, and D. Loss, *Phys. Rev. B* **92**, 134425 (2015).
- [52] D. C. Rapaport, *The Art of Molecular Dynamics Simulations*, 2nd ed. (Cambridge University Press, Cambridge, UK, 2004).
- [53] A. Khan, I. Navid, M. Noshin, H. Uddin, F. Hossain, and S. Subrina, *Electronics* **4**, 1109 (2015).
- [54] J. E. Turney, A. J. H. McGaughey, and C. H. Amon, *Phys. Rev. B* **79**, 224305 (2009).
- [55] C. H. Woo, H. Wen, A. A. Semenov, S. L. Dudarev, and P.-W. Ma, *Phys. Rev. B* **91**, 104306 (2015).
- [56] T. Qin, Q. Niu, and J. Shi, *Phys. Rev. Lett.* **107**, 236601 (2011).
- [57] M. Mena, R. S. Perry, T. G. Perring, M. D. Le, S. Guerrero, M. Storni, D. T. Adroja, C. Rüegg, and D. F. McMorrow, *Phys. Rev. Lett.* **113**, 047202 (2014).
- [58] V. A. Zyuzin and A. A. Kovalev, *Phys. Rev. Lett.* **117**, 217203 (2016).
- [59] R. Cheng, S. Okamoto, and D. Xiao, *Phys. Rev. Lett.* **117**, 217202 (2016).
- [60] K. A. van Hoogdalem, Y. Tserkovnyak, and D. Loss, *Phys. Rev. B* **87**, 024402 (2013).
- [61] M. Mochizuki, X. Z. Yu, S. Seki, N. Kanazawa, W. Koshibae, J. Zang, M. Mostovoy, Y. Tokura, and N. Nagaosa, *Nat. Mater.* **13**, 241 (2014).
- [62] C. Schütte and M. Garst, *Phys. Rev. B* **90**, 094423 (2014).
- [63] Y.-T. Oh, H. Lee, J.-H. Park, and J. H. Han, *Phys. Rev. B* **91**, 104435 (2015).
- [64] S. Komineas and N. Papanicolaou, *Phys. Rev. B* **92**, 064412 (2015).
- [65] A. A. Kovalev, *Phys. Rev. B* **89**, 241101 (2014).
- [66] A. Roldán-Molina, A. S. Nunez, and J. Fernández-Rossier, *New J. Phys.* **18**, 045015 (2016).

5.4.2. Magnon transport in noncollinear spin textures: Anisotropies and topological magnon Hall effects

With the advantages and disadvantages of the novel approach analyzed for an established topological magnon insulator, a different spin Hamiltonian was turned to. Here, the J_1 - J_3 model on a triangular lattice was studied, whose ground state is not ferromagnetic but a spin spiral phase (confer Sec. 2.3). Importantly, thermal fluctuations stabilize a skyrmion crystal phase (confer Sec. 4.2.2), which exhibits the family of *topological* magnon Hall effects (confer Sec. 3.4.2). This phase does not “survive” down to zero temperature and, thus, cannot be treated by the linear spin-wave approximation.

While previous work on the topological Hall effect of magnons (see Refs. [147–149]) considered chiral skyrmion crystals, that is, the skyrmions possess a fixed handedness due to DMI, nonchiral skyrmions were studied here. They are originated by frustration (due to antiferromagnetic exchange on a triangular lattice as explained in Sec. 2.3), which cannot be modeled in the continuum approach to magnetism. In this regard, the present case is the “purest” of the topological magnon Hall effects, because they are solely due to the topological charge of the self-generated magnetic texture, and are not superimposed by a spin-orbit contribution due to DMI [128]. Furthermore, exchange frustration allows for very small skyrmions (down to about three lattice constants), which—for DMI-induced skyrmions—could only be formed for unphysically strong DMI. Thus, the considered model grants access to a limit which has not been considered before.

It is demonstrated that the atomistic spin dynamics approach to magnon transport can be successfully applied to noncollinear magnetic textures, exemplified by a spin spiral and skyrmion crystal. For the spin spiral, a large anisotropy in the longitudinal transport associated with magnon propagation along and across the wave fronts of the spiral was identified. When the external magnetic field is increased, a magnetic phase transition to the skyrmion crystal phase is observed and the anisotropy in the longitudinal transport vanishes. Instead, nonzero transverse-current correlation functions are observed, indicating transverse transport, which is in qualitative agreement with the magnon electrodynamics (Sec. 3.4.2). Both the longitudinal anisotropy in the spin spiral phase and the thermal Hall angle in the skyrmion crystal phase were studied in dependence on the spiral’s pitch (skyrmion size). The optimal skyrmion size for maximizing the topological thermal magnon Hall angle was identified. The latter can be orders of magnitude larger than in the case of the topological magnon insulator on the Kagome lattice, which was studied in the previous publication.

Magnon transport in noncollinear spin textures: Anisotropies and topological magnon Hall effects

Alexander Mook,¹ Borge Göbel,^{1,2} Jürgen Henk,² and Ingrid Mertig^{1,2}

¹Max-Planck-Institut für Mikrostrukturphysik, D-06120 Halle (Saale), Germany

²Institut für Physik, Martin-Luther-Universität Halle-Wittenberg, D-06099 Halle (Saale), Germany

(Received 7 September 2016; published 3 January 2017)

We analyze signatures of noncollinear spin textures in the magnon transport of both spin and heat by means of atomistic spin dynamics. The influence of the spin texture is demonstrated for a spin spiral and for a skyrmion lattice on a frustrated antiferromagnet. Spin spirals show an anisotropy in the longitudinal transport, whereas skyrmion lattices exhibit transverse transport, which is interpreted in terms of topology and establishes skyrmion-induced versions of magnon Hall effects. The conductivities depend sensitively on the spiral pitch and on the skyrmion size; we predict magnon Hall angles as large as 60%.

DOI: 10.1103/PhysRevB.95.020401

Introduction. Skyrmions are particle-like magnetic textures with nontrivial winding [1,2]; they are frequently featured in today's condensed matter research because they produce a topological contribution to the Hall effect of electrons [3] or magnons [4–8]. In the case of magnons, a transverse thermal current \mathbf{J}_{th} is predicted upon application of a temperature gradient ∇T to a skyrmion crystal (SkX) phase [4,5]. This “topological magnon Hall effect” (TMHE) or “topological magnon Righi-Leduc effect” is solely due to the topological charge

$$w = \frac{1}{4\pi} \int \mathbf{n}(\mathbf{r}) \cdot [\partial_x \mathbf{n}(\mathbf{r}) \times \partial_y \mathbf{n}(\mathbf{r})] d^2r \quad (1)$$

of the magnetic texture $\mathbf{n}(\mathbf{r})$. The TMHE has three relatives since magnons do not only carry heat but also spin: the “topological magnon spin Nernst effect” (TMSNE) comprises a transverse spin current \mathbf{J}_s due to an applied temperature gradient; its Onsager reciprocal is the “topological magnon spin Ettingshausen effect” (TMSEE). If the spin current is generated by a magnetic field gradient ∇B [9] the term “topological magnon spin Hall effect” (TMSHE) applies. Combined, they form the family of topological magnon Hall effects (Table I). The “topological” effects originate from the self-generated magnetic texture rather than from spin-orbit interactions which explicitly enter the Hamiltonian (this is the case for the “nontopological” magnon Hall effects on, for example, the ferromagnetic kagome or pyrochlore lattices [10–13]).

Linear response theory captures these effects by coupling the gradients (forces) to the current densities,

$$\begin{pmatrix} \mathbf{J}_s \\ \mathbf{J}_{\text{th}} \end{pmatrix} = \begin{pmatrix} L_{s,s} & L_{s,\text{th}} \\ L_{\text{th},s} & L_{\text{th},\text{th}} \end{pmatrix} \begin{pmatrix} \nabla B \\ -\nabla T/T \end{pmatrix}. \quad (2)$$

The generalized transport coefficients, i.e., the tensors $L_{m,n}$ ($m, n = s, \text{th}$), define the spin conductivity $\sigma \equiv L_{s,s}$, the magnetothermal conductivity $\xi \equiv T^{-1} L_{s,s}^{-1} L_{s,\text{th}}$, and the thermal conductivity $\kappa \equiv T^{-1} (L_{\text{th},\text{th}} - L_{s,\text{th}} L_{s,s}^{-1} L_{s,\text{th}})$ at temperature T . For a two-dimensional (2D) sample, the conductivities are 2×2 tensors. The TMHE, TMSNE, and TMSHE are quantified by σ_{xy} , ξ_{xy} , and κ_{xy} , respectively.

In this Rapid Communication, we identify signatures of noncollinear spin textures in the magnon transport by means of atomistic spin dynamics, focusing on spin spirals (Sp²)

and skyrmion lattices. The conductivities are evaluated as time integrals of current correlation functions (CCFs) in the Kubo formula [14]. We generalize the approach reported in Refs. [15,16] to a 2D frustrated magnet on a triangular lattice which exhibits a Sp² ground state; it features a helicity-degenerate SkX phase stabilized by an external magnetic field and by thermal fluctuations.

The longitudinal conductivities in the Sp² phase reveal a strong anisotropy due to the broken rotational symmetry of the lattice. Furthermore, the transverse conductivities in the SkX phase are finite, which proves the existence of the topological Hall effects of magnons. Both phenomena are studied in dependence on the strength of an external magnetic field and on the spiral pitch which mediates between the collinear ferromagnetic and an antiferromagnetic phase; magnon Hall angles as large as 60% are predicted. Our results call for experimental verification.

Theoretical aspects. We focus on noncollinear magnetic textures induced by frustrations and described within a 2D classical Heisenberg model. Its Hamiltonian

$$H = \sum_i h_i, \quad h_i = -Bn_i^z - \frac{1}{2} \sum_{j \in N(i)} J_{ij} \mathbf{n}_i \cdot \mathbf{n}_j, \quad (3)$$

includes the isotropic symmetric exchange (J_{ij}) and the Zeeman energy due to a magnetic field $\mathbf{B} = B\hat{z}$ applied orthogonal to the lattice (in the xy plane). $N(i)$ is the set of all interacting neighbors of spin \mathbf{n}_i (\mathbf{n}_i unit vector at position \mathbf{r}_i). The conservation of both the z component of the total spin and the energy allows us to formulate corresponding continuity equations and currents [17]: the total spin current $\mathbf{J}_s \equiv \sum_i \mathbf{r}_i \partial n_i^z / \partial t$ and the total thermal current $\mathbf{J}_{\text{th}} \equiv \sum_i \mathbf{r}_i \partial h_i / \partial t$. Using $\dot{\mathbf{n}}_i = -\gamma \mathbf{n}_i \times \partial H / \partial \mathbf{n}_i$ (γ gyromagnetic ratio) with $\partial H / \partial \mathbf{n}_i = -B\hat{z} - \sum_{j \in N(i)} J_{ij} \mathbf{n}_j$, these currents read

$$\mathbf{J}_s = \gamma \sum_{i < j} J_{ij} \mathbf{r}_{ij} \hat{z} \cdot (\mathbf{n}_i \times \mathbf{n}_j), \quad (4)$$

$$\begin{aligned} \mathbf{J}_{\text{th}} = & -B\mathbf{J}_s - \gamma \sum_{\Delta_{ijk}} \frac{\chi_{ijk}}{2} [J_{ij} J_{jk} \mathbf{r}_{ik} + J_{jk} J_{ki} \mathbf{r}_{ji} \\ & + J_{ki} J_{ij} \mathbf{r}_{kj}] \end{aligned} \quad (5)$$

with the spin chirality $\chi_{ijk} \equiv \mathbf{n}_i \cdot (\mathbf{n}_j \times \mathbf{n}_k)$ and $\mathbf{r}_{ij} \equiv \mathbf{r}_i - \mathbf{r}_j$. The summation $\sum_{i < j} (\sum_{\Delta_{ijk}})$ is over each pair (triple) of spins

TABLE I. Family of topological magnon Hall effects. For the nomenclature, see the text.

force	transverse response	
	spin current	heat current
∇B	TMSHE	TMSEE
∇T	TMSNE	TMHE

without double counting. The term $-B\mathbf{J}_s$ of \mathbf{J}_{th} describes the coupling of the spin current to the magnetic field; it gives rise to the magnetothermal conductivity, i.e., the magnetic analog of the thermopower.

In Ref. [18], the Hamiltonian (3) was applied to frustrated spins on a triangular lattice, brought about by positive nearest ($J_1 > 0$) and negative third-nearest neighbor couplings ($J_3 < 0$). As long as $-4 < J_1/J_3 < 0$, the ground state is a spin spiral with ordering vector $|\mathbf{q}| = 2 \arccos[(1 + \sqrt{1 - 2J_1/J_3})/4]$ (lattice constant set to unity) along any of the three third-nearest neighbor directions. The magnetic phase diagram (spanned by T and B) contains besides this single- q (Sp^2) phase coherent superpositions of two (double- q) and three (SkX, triple- q) spin spirals. Since Dzyaloshinskii-Moriya interaction (DMI) [19,20] is absent, the spin texture lacks a fixed handedness; in particular, the SkX phase is both helicity- and vorticity-degenerate; i.e., $w = 1$ and $w = -1$ are equally likely. Yet, once a spin configuration is randomly chosen, an energy barrier separates the topologically opposite configurations.

Transport properties are studied by means of the classical Kubo formula of linear response theory [14],

$$L_{m,n}^{\mu\nu} = \int_0^\infty \frac{1}{Ak_B T} [C_{m,n}^{\mu\nu}(t) - \langle J_m^\mu(\infty)J_n^\nu(0) \rangle] dt; \quad (6)$$

$m, n = s, th$, and $\mu, \nu = x, y$; A and k_B are the sample's area and the Boltzmann constant, respectively. $\langle J_m^\mu(\infty)J_n^\nu(0) \rangle$ has to be subtracted from the CCF $C_{m,n}^{\mu\nu}(t) = \langle J_m^\mu(t)J_n^\nu(0) \rangle$ to account for those CCFs that do not drop to zero because of a persistent contribution caused by noncollinear magnetic textures [21,22]. For example, a Sp^2 would yield a finite \mathbf{J}_s even without thermal excitations [cf. Eq. (4)].

After thermalizing (annealing) a spin cluster by Monte Carlo simulations, the ensemble average $\langle \cdot \rangle$ in Eq. (6) is evaluated as a time average. The time evolution obeys the stochastic Landau-Lifshitz-Gilbert equation [23]

$$(1 + \alpha^2)d\mathbf{n}_i = -(1 + \alpha\mathbf{n}_i \times) [\mathbf{n}_i \times (\mathbf{B}_i d\tau + Dd\mathbf{W}_i)]. \quad (7)$$

The precession of each moment about its effective field $\mathbf{B}_i = -\partial H/\partial \mathbf{n}_i$ is damped. The Gilbert damping α is in general a nonlocal and symmetric 3×3 tensor but assumed here as a scalar. This approximation disregards the anisotropy of the damping due to the noncollinearity of the magnetic texture [24,25], and, thus, becomes better the smaller $|\mathbf{q}|$. As domain wall velocities decrease by texture-induced damping [26], the present method presumably overestimates the conductivities; hence, we address mainly Hall angles rather than conductivities.

Temperature is included by an additional white-noise field \mathbf{b}_i with $Dd\mathbf{W}_i = \mathbf{b}_i d\tau$, where \mathbf{W}_i is an isotropic vector

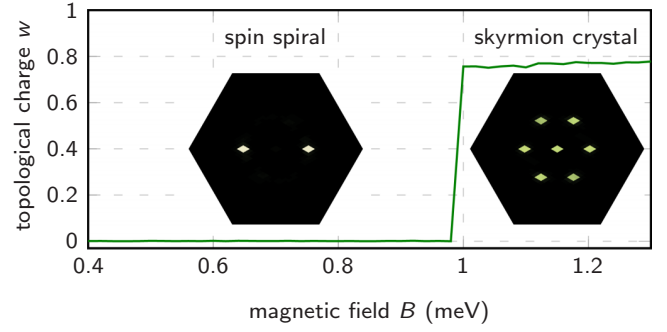


FIG. 1. Topological charge w per skyrmion for $\lambda = 4$ versus external magnetic field B . A topological phase transition from the Sp^2 phase to the SkX phase takes place at $B \approx 1$ meV. Insets show the respective static structure factor in the structural Brillouin zone. $J_1 = 1.171572875$ meV, $J_3 = -1$ meV, $T = 3$ K, and $N \times N = 1600$.

Wiener process and $D^2 = 2\alpha k_B T / (2\mu_B B^{\text{ref}})$ a dimensionless diffusion constant (μ_B Bohr's magneton). B^{ref} is a reference field determining the scale of dimensionless time τ . For the numerical integration an implicit midpoint method is used.

The spin cluster is evolved according to Eq. (7); the currents \mathbf{J}_s and \mathbf{J}_{th} are evaluated and stored at each time step. Subsequently, the correlation functions and, finally, the transport tensors are calculated. The numerical computations showed that a total integration time of 20 ns up to 64 ns, used for all results presented below, is sufficient to converge the correlation functions.

Results and discussion. This Rapid Communication focuses on differences between the Sp^2 and the SkX phases. Relying on finite clusters, the magnetic texture has to be commensurate: the ratio J_1/J_3 is chosen such that the skyrmion lattice fits exactly. For a pitch $\lambda = 2\pi/|\mathbf{q}|$ of the Sp^2 , $3N^2/(4\lambda^2)$ skyrmions fit into an $N \times N$ triangular lattice. The skyrmion lattice vectors are rotated by $\pi/6$ with respect to the structural lattice vectors and are larger by a factor of $2\lambda/\sqrt{3}$.

Since the Sp^2 is the ground state and the SkX phase requires elevated temperatures and a finite magnetic field B , the magnetic phase diagram is traversed by varying B at a given T (Fig. 1). For $\lambda = 4$, the SkX phase is formed for $B \geq 1$ meV; larger skyrmions would require smaller critical fields. Due to thermal fluctuations and the quite small size of the skyrmions, the computed topological charge w is underestimated (≈ 0.8 instead of 1). The static structure factor $\langle \mathbf{n}^*(\mathbf{k}) \cdot \mathbf{n}(\mathbf{k}) \rangle$ [$\mathbf{n}(\mathbf{k})$ lattice Fourier transform of the magnetic texture] retrieves the ordering vectors: a single pair of ordering vectors (two spots) for the Sp^2 phase and three pairs (six spots) in the SkX phase (the central, seventh spot belongs to the ferromagnetic contribution). A further increase of B leads to the double- q phase and, finally, to the field-polarized phase [18] (not shown).

Concerning transport, we focus on the thermal CCF and note that the following discussion is qualitatively valid for the other CCFs, too. The Sp^2 breaks the sixfold structural rotational symmetry about the z axis. We consider samples with \mathbf{q} along the x axis to facilitate the discussion. This broken symmetry yields $C_{th,th}^{xx} \neq C_{th,th}^{yy}$ [red and blue curves as well as vertical arrow in Fig. 2(a)]. Since $C_{th,th}^{xy} = C_{th,th}^{yx} = 0$

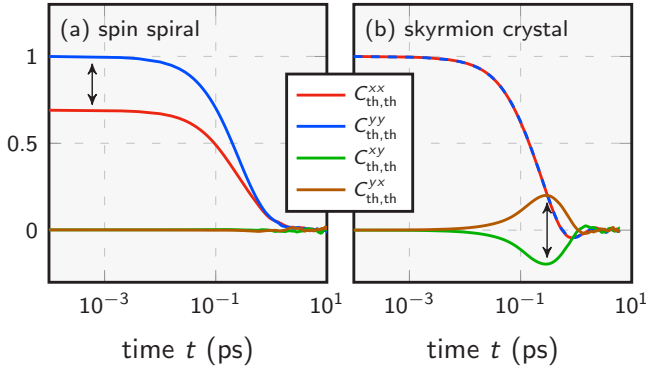


FIG. 2. Time dependence of the longitudinal (blue: $C_{th,th}^{xx}$, red: $C_{th,th}^{yy}$) and transverse (green: $C_{th,th}^{xy}$, brown: $C_{th,th}^{yx}$) thermal current correlation functions in the Sp^2 (a) and in the SkX phase (b). The CCFs are normalized to their value at $t = 0$. Vertical arrows indicate signatures unique to the respective magnetic phase. Parameters as in Fig. 1 with $B = 0.6$ meV and $B = 1.2$ meV in the Sp^2 and SkX phase, respectively.

(green and brown curves) there is no transverse transport [27]. Furthermore, the longitudinal spin correlation function along \mathbf{q} does not drop to zero (not shown) since the Sp^2 introduces a persistent contribution to the microscopic currents which is removed to determine the true transport [Eq. (6)].

The SkX phase maintains $C_{th,th}^{xx} = C_{th,th}^{yy}$ because of the rotational symmetry of the triangular lattice is not broken [Fig. 2(b)]. Most notably, the off-diagonal part of the transport tensor is antisymmetric and nonzero [$C_{th,th}^{xy} = -C_{th,th}^{yx} \neq 0$; green and brown curves as well as vertical arrow in Fig. 2(b)] which indicates transverse transport.

The above signatures due to the magnetic textures— $C_{th,th}^{xx} \neq C_{th,th}^{yy}$ and $C_{th,th}^{xy} = C_{th,th}^{yx} = 0$ for the Sp^2 but $C_{th,th}^{xx} = C_{th,th}^{yy}$ and $C_{th,th}^{xy} = -C_{th,th}^{yx} \neq 0$ for the SkX—show up also in the dependence of the conductivities on the external magnetic field (Fig. 3). $\sigma_{\mu\mu}$ and $\kappa_{\mu\mu}$ [red and blue symbols, respectively, in Figs. 3(a) and 3(c)] are positive. $\xi_{\mu\mu}$ being negative (b) implies that the transport is dominated by spin-down particles (relative to \mathbf{B}), which is readily understood by the magnons having largely spin antiparallel to the net magnetization which itself is along \mathbf{B} .

In the Sp^2 phase ($B \lesssim 1$ meV), $\sigma_{xx} > \sigma_{yy}$ [red and blue symbols, respectively, and vertical arrow in (a)] translates to $|\xi_{xx}| < |\xi_{yy}|$ [see (b)] since $\xi = T^{-1}\sigma^{-1}L_{s,th}$. This relation, although less prominent, is “transferred” to $\kappa_{xx} < \kappa_{yy}$ [see (c)]. Thus, we conclude that thermal and spin transport are differently influenced: thermal transport along the ordering vector \mathbf{q} is less efficient than perpendicular to it, whereas the opposite holds for spin transport.

This anisotropy is lost (red and blue curves coincide) once the SkX phase is reached ($B \gtrsim 1$ meV). The transverse conductivities (green and brown symbols in Fig. 3), which are approximately zero within the Sp^2 phase, take on small but nonzero values. They are antisymmetric; that is, an xy and a yx element differ in sign but not in modulus. Thus, all of the transverse transport phenomena mentioned above are present.

Longitudinal transport does not depend on whether a skyrmion ($w > 0$) or an antiskyrmion lattice ($w < 0$) is formed

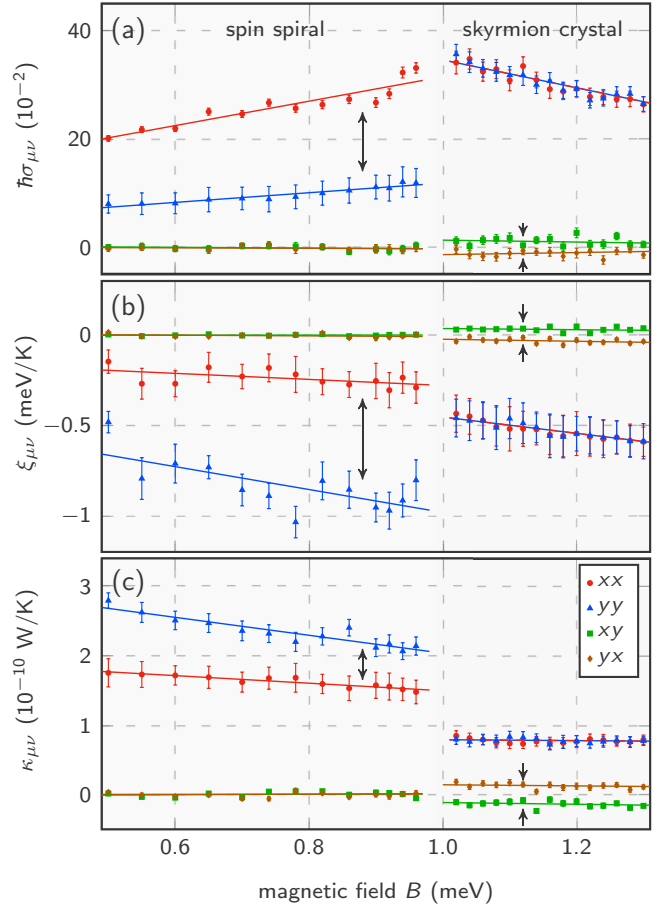


FIG. 3. Spin conductivity $\sigma_{\mu\nu}$ (a), magnetothermal conductivity $\xi_{\mu\nu}$ (b), and thermal conductivity $\kappa_{\mu\nu}$ (c) versus external magnetic field for $\lambda = 4$ ($\mu, \nu = x, y$). Parameters as in Fig. 1, Gilbert damping $\alpha = 0.05$, σ multiplied by \hbar . Lines are guides to the eye; vertical arrows indicate signatures unique to the respective magnetic phase.

during annealing. However, the sign of w determines the sign of the transverse CCFs and of the transverse conductivities. This feature is explained by the “emergent electrodynamics” of magnons, originally derived for electrons [3]. A local coordinate transformation to the reference frame of the skyrmion texture recasts Eq. (7) to look formally like an equation describing charged particles in (fictitious) electromagnetic fields [4,5,28,29]. In particular, an emergent magnetic field B_{em} along the z direction is identified, which contains the local contribution to w [Eq. (1)]. Inversion of w inverts B_{em} , the emergent Lorentz force, and, consequently, the transverse transport direction.

Restricting ourselves to samples with $w > 0$, we discuss the effect of the pitch λ on both the transport anisotropy—quantified by κ^{xx}/κ^{yy} —in the Sp^2 phase and on the magnon Hall transport in the SkX phase. The stabilization of large skyrmions requires different exchange parameters, temperatures, and magnetic fields. This implies that a direct comparison of transverse conductivities is barely meaningful. Therefore, we focus on the (thermal) magnon Hall angle κ_{xy}/κ_{xx} because it is accessed easily in experiments [11,30,31]; its discussion applies also to the other conductivities.

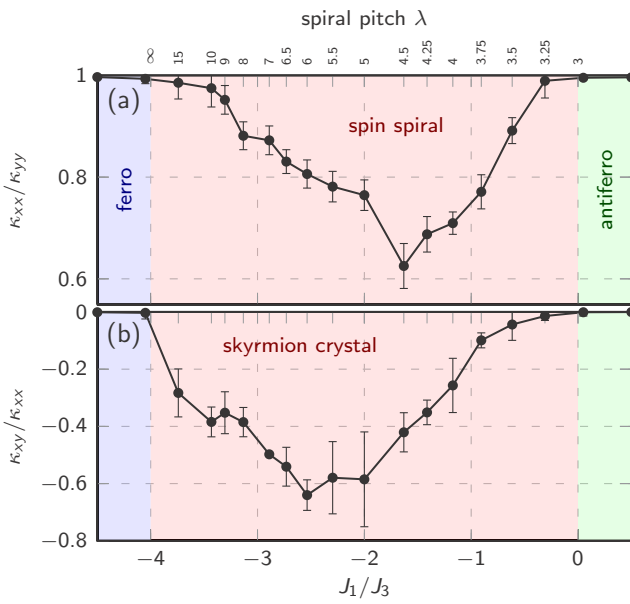


FIG. 4. (a) Longitudinal transport anisotropy κ_{xx}/κ_{yy} in the Sp^2 phase. The ordering vector is along the x direction. (b) Magnon Hall angle κ_{xy}/κ_{xx} in the SkX phase versus J_1/J_3 ($J_1 > 0$). Three magnetic phases are indicated: collinear ferromagnetic phase (blue, “ferro”), Sp^2/SkX phase (red), and the antiferromagnetic phase (green, “antiferro”). For $-4 < J_1/J_3 < 0$ the ratio J_1/J_3 translates into the Sp^2 pitch λ and the corresponding skyrmion size. Cluster sizes were chosen such that the magnetic textures are commensurate. B and T had to be varied for the formation of the SkX phase; $\alpha = 0.05$. For the Sp^2 phase the magnetic field is half as large as in the SkX phase.

For the variation of the magnetic texture two limits have to be noted: (i) λ decreases for $J_1/J_3 \nearrow 0$ until it is so small that the spatial frequency of the lattice sites is too small to sample the Sp^2 , and an antiferromagnetic phase is formed; and (ii) λ increases for $J_1/J_3 \searrow -4$ up to infinity, which generates a collinear ferromagnetic order for $J_1/J_3 \leq -4$.

Neither the ferromagnetic nor the antiferromagnetic phase breaks the structural symmetry of the triangular lattice; therefore, $\kappa^{xx}/\kappa^{yy} = 1$ is found [Fig. 4(a)]. Only within the Sp^2 phase ($-4 < J_1/J_3 < 0$) an anisotropy of up to ≈ 0.7 is identified and reached at $\lambda = 4 \sim 5$.

While the magnon Hall angle κ_{xy}/κ_{xx} is zero in the (collinear) ferromagnetic and antiferromagnetic phases [Fig. 4(b)], it is negative in the SkX phase, showing a minimum of about -60% at $\lambda = 5 \sim 6.5$. Its absolute value is much larger than in systems showing the (nontopological) MHE (ferromagnetic kagome lattice: $\approx 10^{-2}$ [12,13,31,32]; pyrochlore lattice: $\approx 10^{-3}$ [11,30]). The increase of $|\kappa_{xy}/\kappa_{xx}|$ with decreasing λ down to $\lambda \approx 6$ is explained by the increasing

skyrmion density (decreased skyrmion size) and the increasing density of B_{em} (the same trend is found for electrons [33]). Although the skyrmion density increases as $J_1/J_3 \nearrow 0$ (further decrease of λ), the Hall angle drops to zero, which we attribute to the quite coarse sampling underestimating w and B_{em} .

Concerning the temperature dependence of the conductivities, we recall that the spins are treated classically: spin and energy are not quantized; the Boltzmann distribution is used. This ansatz is “borrowed” from molecular dynamics simulations [34] for the evaluation of the phonon thermal conductivity; one of its drawbacks is that κ diverges for $T \rightarrow 0$ [35]. *Ad hoc* “quantum corrections” restore the limit $\kappa \rightarrow 0$ [37] and could be implemented here as well. However, care has to be taken for κ_{xy} ; it diverges not alone because of the classical treatment but also because a direct application of the Kubo formula yields a nonphysical divergence for $T \rightarrow 0$. The latter is attributed to circulating heat currents [38] which are not experimentally observable, so their contribution has to be removed. Hence, “quantum corrections” without proper removal of circulating currents appear questionable but have to be applied for models which feature a SkX phase at $T = 0$ [39,40]; in the present case, which requires elevated temperatures, quantum corrections are not necessary. In particular, we point out that our numerical results obey Onsager’s reciprocity relation.

Outlook. The identified signatures of the noncollinear magnetic textures in the magnon transport of spin and heat are accessible in experiments. The magnon spin Hall effect or the magnon spin Nernst effect require measuring spin currents, using the inverse spin Hall effect [41].

To measure the transverse thermal conductivity, we suggest an electrically insulating material that exhibits a spin spiral as ground state and which features a SkX phase at an elevated external magnetic field; examples are Cu_2OSeO_3 [42] and $\text{BaFe}_{1-x-0.05}\text{Sc}_x\text{Mg}_{0.05}\text{O}_{19}$ [43], both of which show SkX phases induced by DMI rather than by frustration. Nonetheless, when traversing the phase boundary between the Sp^2 and the SkX phase by increasing the magnetic field, the longitudinal transport anisotropy should abruptly vanish and transverse thermal transport should set in [Fig. 3(c)]. For small skyrmions, magnon Hall angles are expected orders of magnitudes larger than in systems showing the (nontopological) MHE [11,30,31].

It is conceivable to extend the numerical method to three dimensions and to include magnetocrystalline anisotropies. Taking into account the DMI would allow us to apply the approach to topological magnon insulators [10–13,31,32,44–52] and to DMI-induced SkX phases exhibiting an additional spin-orbit contribution to the transverse conductivities [4].

Acknowledgments. This work is supported by SPP 1666 of Deutsche Forschungsgemeinschaft (DFG).

[1] S. Mühlbauer, B. Binz, F. Jonietz, C. Pfleiderer, A. Rosch, A. Neubauer, R. Georgii, and P. Boni, *Science* **323**, 915 (2009).
[2] N. Nagaosa and Y. Tokura, *Nat. Nanotechnol.* **8**, 899 (2013).

[3] T. Schulz, R. Ritz, A. Bauer, M. Halder, M. Wagner, C. Franz, C. Pfleiderer, K. Everschor, M. Garst, and A. Rosch, *Nat. Phys.* **8**, 301 (2012).

- [4] K. A. van Hoogdalem, Y. Tserkovnyak, and D. Loss, *Phys. Rev. B* **87**, 024402 (2013).
- [5] M. Mochizuki, X. Z. Yu, S. Seki, N. Kanazawa, W. Koshibae, J. Zang, M. Mostovoy, Y. Tokura, and N. Nagaosa, *Nat. Mater.* **13**, 241 (2014).
- [6] C. Schütte and M. Garst, *Phys. Rev. B* **90**, 094423 (2014).
- [7] Y.-T. Oh, H. Lee, J.-H. Park, and J. H. Han, *Phys. Rev. B* **91**, 104435 (2015).
- [8] S. Komineas and N. Papanicolaou, *Phys. Rev. B* **92**, 064412 (2015).
- [9] S. Fujimoto, *Phys. Rev. Lett.* **103**, 047203 (2009).
- [10] H. Katsura, N. Nagaosa, and P. A. Lee, *Phys. Rev. Lett.* **104**, 066403 (2010).
- [11] Y. Onose, T. Ideue, H. Katsura, Y. Shiomi, N. Nagaosa, and Y. Tokura, *Science* **329**, 297 (2010).
- [12] A. Mook, J. Henk, and I. Mertig, *Phys. Rev. B* **89**, 134409 (2014).
- [13] H. Lee, J. H. Han, and P. A. Lee, *Phys. Rev. B* **91**, 125413 (2015).
- [14] R. Kubo, M. Toda, and N. Hashitsume, *Statistical Physics II* (Springer, Berlin, 1991).
- [15] A. V. Savin, G. P. Tsironis, and X. Zotos, *Phys. Rev. B* **72**, 140402 (2005).
- [16] B. Jenčič and P. Prelovšek, *Phys. Rev. B* **92**, 134305 (2015).
- [17] G. D. Mahan, *Many-Particle Physics* (Springer Science+Business Media, 2000).
- [18] T. Okubo, S. Chung, and H. Kawamura, *Phys. Rev. Lett.* **108**, 017206 (2012).
- [19] I. Dzyaloshinsky, *J. Phys. Chem. Solids* **4**, 241 (1958).
- [20] T. Moriya, *Phys. Rev.* **120**, 91 (1960).
- [21] F. Schuetz, P. Kopietz, and M. Kollar, *Eur. Phys. J. B* **41**, 557 (2004).
- [22] G. Tatara, *Phys. Rev. B* **92**, 064405 (2015).
- [23] B. Skubic, J. Hellsvik, L. Nordström, and O. Eriksson, *J. Phys.: Condens. Matter* **20**, 315203 (2008).
- [24] Z. Yuan, K. M. D. Hals, Y. Liu, A. A. Starikov, A. Brataas, and P. J. Kelly, *Phys. Rev. Lett.* **113**, 266603 (2014).
- [25] C. A. Akosa, I. M. Miron, G. Gaudin, and A. Manchon, *Phys. Rev. B* **93**, 214429 (2016).
- [26] J. Foros, A. Brataas, Y. Tserkovnyak, and G. E. W. Bauer, *Phys. Rev. B* **78**, 140402 (2008).
- [27] $C_{th,th}^{xy} = C_{th,th}^{yx} \neq 0$ if \mathbf{q} were not aligned with one of the Cartesian axes; a principal-axis transformation would then be necessary.
- [28] A. A. Kovalev, *Phys. Rev. B* **89**, 241101 (2014).
- [29] U. Güngördü and A. A. Kovalev, *Phys. Rev. B* **94**, 020405 (2016).
- [30] T. Ideue, Y. Onose, H. Katsura, Y. Shiomi, S. Ishiwata, N. Nagaosa, and Y. Tokura, *Phys. Rev. B* **85**, 134411 (2012).
- [31] M. Hirschberger, R. Chisnell, Y. S. Lee, and N. P. Ong, *Phys. Rev. Lett.* **115**, 106603 (2015).
- [32] R. Chisnell, J. S. Helton, D. E. Freedman, D. K. Singh, R. I. Bewley, D. G. Nocera, and Y. S. Lee, *Phys. Rev. Lett.* **115**, 147201 (2015).
- [33] N. Nagaosa, J. Sinova, S. Onoda, A. H. MacDonald, and N. P. Ong, *Rev. Mod. Phys.* **82**, 1539 (2010).
- [34] D. Rapaport, *The Art of Molecular Dynamics Simulation* (Cambridge University Press, Cambridge, UK, 2004).
- [35] For magnons, this divergence is only found for a perfect crystal for $\alpha = 0$ [15]. For $\alpha > 0$, $\kappa \rightarrow \text{const.}$, and disorder yields $\kappa \rightarrow 0$ [16]. The latter recovers the Wiedemann-Franz law of magnon transport [36].
- [36] K. Nakata, P. Simon, and D. Loss, *Phys. Rev. B* **92**, 134425 (2015).
- [37] J. E. Turney, A. J. H. McGaughey, and C. H. Amon, *Phys. Rev. B* **79**, 224305 (2009).
- [38] T. Qin, Q. Niu, and J. Shi, *Phys. Rev. Lett.* **107**, 236601 (2011).
- [39] A. O. Leonov and M. Mostovoy, *Nat. Commun.* **6**, 8275 (2015).
- [40] A. Roldán-Molina, A. S. Nunez, and J. Fernández-Rossier, *New J. Phys.* **18**, 045015 (2016).
- [41] E. Saitoh, M. Ueda, H. Miyajima, and G. Tatara, *Appl. Phys. Lett.* **88**, 182509 (2006).
- [42] S. Seki, X. Z. Yu, S. Ishiwata, and Y. Tokura, *Science* **336**, 198 (2012).
- [43] X. Yu, M. Mostovoy, Y. Tokunaga, W. Zhang, K. Kimoto, Y. Matsui, Y. Kaneko, N. Nagaosa, and Y. Tokura, *Proc. Natl. Acad. Sci. USA* **109**, 8856 (2012).
- [44] R. Matsumoto and S. Murakami, *Phys. Rev. Lett.* **106**, 197202 (2011).
- [45] R. Matsumoto and S. Murakami, *Phys. Rev. B* **84**, 184406 (2011).
- [46] R. Shindou, R. Matsumoto, S. Murakami, and J.-i. Ohe, *Phys. Rev. B* **87**, 174427 (2013).
- [47] L. Zhang, J. Ren, J.-S. Wang, and B. Li, *Phys. Rev. B* **87**, 144101 (2013).
- [48] A. Mook, J. Henk, and I. Mertig, *Phys. Rev. B* **90**, 024412 (2014).
- [49] E. A. Nytko, J. S. Helton, P. Müller, and D. G. Nocera, *J. Am. Chem. Soc.* **130**, 2922 (2008).
- [50] R. Cheng, S. Okamoto, and D. Xiao, *Phys. Rev. Lett.* **117**, 217202 (2016).
- [51] V. A. Zyuzin and A. A. Kovalev, *Phys. Rev. Lett.* **117**, 217203 (2016).
- [52] A. Mook, J. Henk, and I. Mertig, *Phys. Rev. B* **94**, 174444 (2016).

In the course of this thesis fundamental topological properties of magnon spectra and the associated transverse transport phenomena were theoretically studied. Topological invariants calculated within the framework of linear spin-wave theory revealed the magnon band structures to be topologically nontrivial. This led to the identification of several magnonic pendants of electronic topological materials. Moreover, atomistic spin dynamics simulations were used to study longitudinal and transverse magnon transport in topological magnon insulators and skyrmion lattices.

With respect to the issues raised in the introduction (Sec. 1), the following conclusions can be drawn.

- ▷ The study of a ferromagnetic “topological magnon insulator” on the two-dimensional kagome lattice showed that a topological phase transition as well as a variation of temperature can lead to a sign change of the transverse thermal conductivity. Since the Bose-Einstein distribution function makes all states contribute to transport, the relative population of states contributing positively and negatively to the transverse conductivity determines its sign. For example, a sign change with temperature was found experimentally in Cu(1,3-benzenedicarboxylate) [185].

The bulk-boundary correspondence was exemplarily studied for different Chern-insulator phases of the kagome topological magnon insulator. Unidirectional topologically protected magnon edge states were identified. They might be used as “magnon highways” in magnonic devices: an external excitation by a terahertz frequency within the magnon band gap will exclusively excite the topologically protected boundary states, which can only propagate in one direction. Thus, information is carried along the edge and the lifetime of the topological magnons determines the range of information transmission.

The theory of “topological magnon (Chern) insulators” can be generalized to nonferromagnetic phases as, for instance, noncoplanar phases [27, 90] and skyrmion lattices [186]. One of the most interesting open questions is that concerning the magnonic pendant to \mathbb{Z}_2 topological insulators. Since a pseudo-Kramers degeneracy is mandatory, Néel-ordered antiferromagnets appear promising: the combined symmetry of spin reversal and sublattice exchange leads to a two-fold band degeneracy associated with magnons of opposite spin. The associated helical magnon edge states, whose propagation direction is locked to the spin, would allow for a pure edge spin current, because there is zero net magnon flow.

- ▷ By generalizing the classification of topological magnon materials to three dimensions, $\text{Lu}_2\text{V}_2\text{O}_7$ and other ferromagnetic pyrochlore oxides were predicted to be “topological magnon Weyl semimetals”. They feature zero-dimensional band touchings, i. e., Weyl points, and magnon surface arcs, both of which can be rotated in reciprocal space by an external magnetic field. Inelastic neutron scattering experiments were suggested for the experimental verification.

For the future and concerning transport, it appears to be of great interest to study the external excitation of the Weyl magnons by a terahertz frequency. The electronic negative longitudinal magnetoresistance of electrons might have a magnonic relative, if a considerable Weyl magnon population can be ensured. Moreover, the search for ferromagnetic “magnon nodal-line semimetals”, which were predicted here, should be focused on materials with negligible spin-orbit interaction and a non-Bravais crystal structure. A transport signature of nodal-line magnons is yet to be found.

- ▷ To evaluate magnon transport beyond the limit of low temperatures, a novel method was developed, which is based on the Kubo formula and atomistic spin dynamics simulations. It naturally includes all orders of magnon-magnon interactions and avoids the spin-boson transformation, and the calculation of a Berry curvature. It was applied to the ferromagnetic topological magnon insulator Cu(1,3-benzenedicarboxylate); the numerically determined thermal Hall angle was of the same order of magnitude as that found in experiments. Furthermore, this method was utilized to study the magnon transport in a magnetic phase

6. Conclusion and Outlook

which is not stable at zero temperature and, thus, escapes a linear spin-wave description: a skyrmion lattice. An optimal skyrmion size for maximizing the topological Hall angles was identified.

The numerical evaluation of the transport tensors based on atomistic spin dynamics simulations can be utilized to study the influence of disorder and defects. Fundamental questions concerning the stability of topological edge or surface states upon breaking translational symmetry could be addressed. Moreover, this would allow to quantify the *extrinsic* contribution to the transverse magnon transport. As in the case of electrons, the Berry curvature contribution is *intrinsic* (it is determined from the band structure), while “skew scattering” and “side jump” at defects are regarded extrinsic. For the spin Hall effect of electrons, it was shown that there are limits, in which these extrinsic contributions dominate over the intrinsic contributions [187]. An “engineering” of the transverse magnon transport appears close at hand.

In summary, the single-particle treatment of magnons shows striking similarities to that of electrons. Thus, at low temperatures, both the classification of topologically nontrivial materials and the anomalous Hall-type transport phenomena can be carried over from electrons to magnons. Moreover, atomistic spin dynamics simulations were shown to capture the transverse transport properties even at elevated temperatures. Thus, it is expected that the topological invariants obtained within the single-particle *ansatz* possess physical meaning in the interacting limit as well. Since it is envisioned to utilize magnonic devices at room temperature, future work should address the meaning of topological invariants in the presence of magnon-magnon interactions.

APPENDIX A

NUMERICAL CALCULATION OF THE SKYRMION NUMBER

For the numerical evaluation of the skyrmion number w , partial derivatives of the magnetic texture $\mathbf{n}(\mathbf{r})$ (\mathbf{n} unit vector) have to be estimated [cf. eq. (3.40), $\mathbf{n} = \mathbf{m}/|\mathbf{m}|$]. Three algorithms were implemented and tested.

(a) *Trigonometric gradient estimation.* Since a skyrmion lattice can be represented as a superposition of spin spirals, a trigonometric gradient estimation is appropriate. The trigonometric polynomial

$$\mathbf{n}(\mathbf{r}_i) = \sum_{\mathbf{k} \in \text{BZ}} \mathbf{n}_{\mathbf{k}} \exp(i \mathbf{k} \cdot \mathbf{r}_i) \quad (\text{A.1})$$

contains the coefficients $\mathbf{n}_{\mathbf{k}}$ that can be determined by Fourier transformation of the spin configuration. One then takes the partial derivative

$$\partial_{\alpha} \mathbf{n}(\mathbf{r}_i) = i \sum_{\mathbf{k} \in \text{BZ}} k_{\alpha} \mathbf{n}_{\mathbf{k}} \exp(i \mathbf{k} \cdot \mathbf{r}_i), \quad (\text{A.2})$$

($\alpha = x, y$) which enters eq. (3.40).

(b) *First-order least squares gradient estimation.* Given the set $N(i)$ of $N > 2$ neighbors of site i , the over-determined equation system for the first-order estimate of the gradient of each Cartesian spin component $n_{\beta}(\mathbf{r}_i)$ ($\beta = x, y, z$) at \mathbf{r}_i reads $D_i \mathbf{g}_i = \Delta \mathbf{n}_i$ [188]. The difference matrix

$$D_i = \begin{pmatrix} \Delta_1^i x & \Delta_1^i y \\ \vdots & \vdots \\ \Delta_N^i x & \Delta_N^i y \end{pmatrix}, \quad (\text{A.3})$$

contains the Cartesian components $\Delta_j^i \alpha = \alpha_j - \alpha_i$ ($\alpha = x, y$) of the distance vector $\mathbf{r}_j - \mathbf{r}_i$ between site i and site $j \in N(i)$. The gradient vector $\mathbf{g}_i = (\partial_x n_{\beta}(\mathbf{r}_i), \partial_y n_{\beta}(\mathbf{r}_i))^T$ contains the sought partial derivatives of the spin texture, and $\Delta \mathbf{n}_i = (\Delta_1^i n_{\beta}, \dots, \Delta_N^i n_{\beta})^T$ is a vector of differences of Cartesian spin components $\Delta_j^i n_{\beta} = n_{\beta}(\mathbf{r}_j) - n_{\beta}(\mathbf{r}_i)$ with $j \in N(i)$. The solution of this equation system is approximated by the linear least squares method for each Cartesian component of the spins.

(c) *Non-conserving first-order least squares gradient estimation.* The former algorithm can be formulated in a non-conserving way by replacing [188]

$$D_i \rightarrow D'_i = \begin{pmatrix} \Delta_1^i x & \Delta_1^i y & 1 \\ \vdots & \vdots & \vdots \\ \Delta_N^i x & \Delta_N^i y & 1 \end{pmatrix}, \quad (\text{A.4})$$

and $\mathbf{g}_i \rightarrow \mathbf{g}'_i = (\partial_x n_{\beta}(\mathbf{r}_i), \partial_y n_{\beta}(\mathbf{r}_i), \delta n_{\beta}(\mathbf{r}_i))^T$, where $\delta n_{\beta}(\mathbf{r}_i)$ is a correction to the actual $n_{\beta}(\mathbf{r}_i)$. Simply put, an interpolated surface calculated by that algorithm does not (in general) contain the data points.

Test *Integration over a single skyrmion.* A triangular cluster of size $L \times L$ with *one* (anti)skyrmion was set up by superimposing three spin spirals. The results of the numerical integration with algorithms (a), (b), and (c) are presented in Tab. A.1.

There is an obvious trend that the results get better the larger the skyrmion. The more sites there are for sampling the skyrmion, i. e., the finer the integration mesh, the more accurate is the numerical result.

The trigonometric integration is superior; even skyrmions of size 6×6 are detected with a relative error less than 3%. Since the triangular lattice is inversion symmetric, algorithms (b), and (c) are of second-order accuracy. Both of them yield skyrmion numbers larger than one half for a 6×6 skyrmion. Thus, they can be used for the identification of skyrmions, when high accuracy is not needed. Besides, they are much faster than the trigonometric fit, because they do not need a Fourier transformation.

A. Numerical calculation of the skyrmion number

Table A.1.: Performance test of the skyrmion number integration algorithms: (a) trigonometric gradient estimation, (b) first-order least squares gradient estimation, and (c) nonconserving first-order least squares gradient estimation. A single (anti)skyrmion state ($|w| = 1$) on a triangular lattice was set up. The numerically estimated skyrmion number $|w|$ and the relative error are given in dependence on different cluster sizes $L \times L$. The absolute value of w is given, because the results apply to skyrmions as well as antiskyrmions.

cluster	(a) trigonometric		(b) 1st-order LS		(c) n. 1st-order LS	
	$ w $	rel. err.	$ w $	rel. err.	$ w $	rel. err.
4×4	0.8267	17.33 %	0.2940	70.60 %	0.6443	35.57 %
6×6	0.9751	2.49 %	0.6352	36.48 %	0.8695	13.05 %
8×8	0.9976	0.24 %	0.7711	22.89 %	0.9461	5.39 %
10×10	0.9997	0.03 %	0.8449	15.51 %	0.9694	3.06 %
20×20	1.0000	$< 10^{-7}$	0.9579	4.21 %	0.9979	0.21 %
30×30	1.0000	$< 10^{-10}$	0.9810	1.90 %	0.9994	0.06 %
40×40	1.0000	$< 10^{-10}$	0.9892	1.08 %	0.9997	0.03 %
50×50	1.0000	$< 10^{-10}$	0.9931	0.69 %	0.9999	0.01 %

- [1] I. Žutić, J. Fabian, and S. Das Sarma. Spintronics: Fundamentals and applications. *Rev. Mod. Phys.*, 76:323–410, Apr 2004.
- [2] C. Hu. *Modern Semiconductor Devices for Integrated Circuits*. Prentice Hall, Upper Saddle River, 2010.
- [3] M. N. Baibich, J. M. Broto, A. Fert, F. N. Van Dau, F. Petroff, P. Etienne, G. Creuzet, A. Friederich, and J. Chazelas. Giant Magnetoresistance of (001)Fe/(001)Cr Magnetic Superlattices. *Phys. Rev. Lett.*, 61:2472–2475, Nov 1988.
- [4] G. Binasch, P. Grünberg, F. Saurenbach, and W. Zinn. Enhanced magnetoresistance in layered magnetic structures with antiferromagnetic interlayer exchange. *Phys. Rev. B*, 39:4828–4830, Mar 1989.
- [5] M. Jullière. Tunneling between ferromagnetic films. *Physics Letters A*, 54(3):225–226, Sep 1975.
- [6] A. V. Chumak, V. I. Vasyuchka, A. A. Serga, and B. Hillebrands. Magnon spintronics. *Nature Physics*, 11(6):453–461, 2015.
- [7] A. D. Karenowska, A. V. Chumak, A. A. Serga, and B. Hillebrands. Magnon Spintronics. *Handbook of Spintronics*, pages 1505–1549, 2016.
- [8] E. Hall. XVIII. On the “Rotational Coefficient” in Nickel and Cobalt. *Philosophical Magazine Series 5*, 12(74):157–172, Sep 1881.
- [9] S. Onoda, N. Sugimoto, and N. Nagaosa. Quantum transport theory of anomalous electric, thermoelectric, and thermal Hall effects in ferromagnets. *Phys. Rev. B*, 77:165103, Apr 2008.
- [10] G. Sundaram and Q. Niu. Wave-packet dynamics in slowly perturbed crystals: Gradient corrections and Berry-phase effects. *Phys. Rev. B*, 59:14915–14925, Jun 1999.
- [11] N. Nagaosa, J. Sinova, S. Onoda, A. H. MacDonald, and N. P. Ong. Anomalous Hall effect. *Rev. Mod. Phys.*, 82:1539–1592, May 2010.
- [12] M. V. Berry. Quantal Phase Factors Accompanying Adiabatic Changes. *Proc. R. Soc. London A*, 392(1802):45–57, Mar 1984.
- [13] J. Zak. Berry’s phase for energy bands in solids. *Phys. Rev. Lett.*, 62:2747–2750, Jun 1989.
- [14] Y. Onose, T. Ideue, H. Katsura, Y. Shiomi, N. Nagaosa, and Y. Tokura. Observation of the Magnon Hall Effect. *Science*, 329(5989):297–299, Jul 2010.
- [15] H. Katsura, N. Nagaosa, and P. A. Lee. Theory of the Thermal Hall Effect in Quantum Magnets. *Phys. Rev. Lett.*, 104(6):066403, Feb 2010.
- [16] I. Dzyaloshinsky. A thermodynamic theory of “weak” ferromagnetism of antiferromagnetics. *J. Phys. Chem. Sol.*, 4(4):241, 1958.
- [17] T. Moriya. Anisotropic Superexchange Interaction and Weak Ferromagnetism. *Phys. Rev.*, 120:91, 1960.
- [18] R. Matsumoto and S. Murakami. Rotational motion of magnons and the thermal Hall effect. *Phys. Rev. B*, 84(18):184406, Nov 2011.
- [19] R. Matsumoto and S. Murakami. Theoretical Prediction of a Rotating Magnon Wave Packet in Ferromagnets. *Phys. Rev. Lett.*, 106(19):197202, May 2011.

Bibliography

- [20] R. Matsumoto, R. Shindou, and S. Murakami. Thermal Hall effect of magnons in magnets with dipolar interaction. *Phys. Rev. B*, 89:054420, Feb 2014.
- [21] J. H. Han and H. Lee. Spin Chirality and Hall-Like Transport Phenomena of Spin Excitations. *Journal of the Physical Society of Japan*, 86(1):011007, Jan 2017.
- [22] L. Zhang. Berry curvature and various thermal Hall effects. *New Journal of Physics*, 18(10):103039, 2016.
- [23] L. Zhang, J. Ren, J.-S. Wang, and B. Li. Topological magnon insulator in insulating ferromagnet. *Phys. Rev. B*, 87(14):144101, Apr 2013.
- [24] D. J. Thouless, M. Kohmoto, M. P. Nightingale, and M. den Nijs. Quantized Hall Conductance in a Two-Dimensional Periodic Potential. *Phys. Rev. Lett.*, 49:405–408, Aug 1982.
- [25] K. von Klitzing. The quantized Hall effect. *Rev. Mod. Phys.*, 58:519–531, Jul 1986.
- [26] F. D. M. Haldane. Model for a Quantum Hall Effect without Landau Levels: Condensed-Matter Realization of the Parity Anomaly. *Phys. Rev. Lett.*, 61(18):2015–2018, Oct 1988.
- [27] R. Shindou, R. Matsumoto, S. Murakami, and J.-i. Ohe. Topological chiral magnonic edge mode in a magnonic crystal. *Phys. Rev. B*, 87:174427, May 2013.
- [28] X. S. Wang, Y. Su, and X. R. Wang. Topologically protected unidirectional edge spin waves and beam splitter. *Phys. Rev. B*, 95:014435, 2017.
- [29] X. Wan, A. M. Turner, A. Vishwanath, and S. Y. Savrasov. Topological semimetal and Fermi-arc surface states in the electronic structure of pyrochlore iridates. *Phys. Rev. B*, 83:205101, May 2011.
- [30] X. Huang, L. Zhao, Y. Long, P. Wang, D. Chen, Z. Yang, H. Liang, M. Xue, H. Weng, Z. Fang, X. Dai, and G. Chen. Observation of the Chiral-Anomaly-Induced Negative Magnetoresistance in 3D Weyl Semimetal TaAs. *Phys. Rev. X*, 5:031023, Aug 2015.
- [31] C.-L. Zhang, S.-Y. Xu, I. Belopolski, Z. Yuan, Z. Lin, B. Tong, G. Bian, N. Alidoust, C.-C. Lee, S.-M. Huang, and et al. Signatures of the Adler-Bell-Jackiw chiral anomaly in a Weyl fermion semimetal. *Nature Communications*, 7:10735, Feb 2016.
- [32] D. T. Son and B. Z. Spivak. Chiral anomaly and classical negative magnetoresistance of Weyl metals. *Phys. Rev. B*, 88:104412, Sep 2013.
- [33] W. Heisenberg. Zur Theorie des Ferromagnetismus. *Zeitschrift für Physik*, 49(9-10):619–636, 1928.
- [34] W. Nolting and A. Ramakanth. *Quantum Theory of Magnetism*. Springer, Berlin, 2009.
- [35] P. A. M. Dirac. Quantum Mechanics of Many-Electron Systems. *Proceedings of the Royal Society A: Mathematical, Physical and Engineering Sciences*, 123(792):714733, Apr 1929.
- [36] C. Herring. *Direct Exchange between Well-Separated Atoms*, volume 2b of *Magnetism*. Academic Press, New York, 1966.
- [37] A. Liechtenstein, M. Katsnelson, V. Antropov, and V. Gubanov. Local spin density functional approach to the theory of exchange interactions in ferromagnetic metals and alloys. *Journal of Magnetism and Magnetic Materials*, 67(1):65–74, May 1987.
- [38] L. Szunyogh, L. Udvardi, J. Jackson, U. Nowak, and R. Chantrell. Atomistic spin model based on a spin-cluster expansion technique: Application to the IrMn₃/Co interface. *Phys. Rev. B*, 83:024401, Jan 2011.
- [39] T. Yildirim, A. B. Harris, A. Aharony, and O. Entin-Wohlman. Anisotropic spin Hamiltonians due to spin-orbit and Coulomb exchange interactions. *Phys. Rev. B*, 52:10239–10267, Oct 1995.

- [40] R. F. L. Evans, W. J. Fan, P. Chureemart, T. A. Ostler, M. O. A. Ellis, and R. W. Chantrell. Atomistic spin model simulations of magnetic nanomaterials. *Journal of Physics: Condensed Matter*, 26(10):103202, Feb 2014.
- [41] L. Udvardi, L. Szunyogh, K. Palotás, and P. Weinberger. First-principles relativistic study of spin waves in thin magnetic films. *Phys. Rev. B*, 68:104436, Sep 2003.
- [42] C. Lacroix, P. Mendels, and F. Mila. *Introduction to Frustrated Magnetism*. Springer, Berlin, 2011.
- [43] E. Ising. Beitrag zur Theorie des Ferromagnetismus. *Zeitschrift für Physik*, 31(1):253–258, Feb 1925.
- [44] B. Cullity and C. Graham. *Introduction to Magnetic Materials*. Wiley New Jersey, 2011.
- [45] K. Yosida. *Theory of Magnetism*. Springer, Berlin, 1996.
- [46] M. Maksymenko, V. R. Chandra, and R. Moessner. Classical dipoles on the kagome lattice. *Phys. Rev. B*, 91:184407, May 2015.
- [47] P. Millet, F. Mila, F. C. Zhang, M. Mambrini, A. B. Van Oosten, V. A. Pashchenko, A. Sulpice, and A. Stepanov. Biquadratic Interactions and Spin-Peierls Transition in the Spin-1 Chain LiVGe_2O_6 . *Phys. Rev. Lett.*, 83:4176–4179, Nov 1999.
- [48] K. Majumdar, D. Furton, and G. S. Uhrig. Effects of ring exchange interaction on the Néel phase of two-dimensional, spatially anisotropic, frustrated Heisenberg quantum antiferromagnet. *Phys. Rev. B*, 85:144420, Apr 2012.
- [49] J. M. Luttinger and L. Tisza. Theory of Dipole Interaction in Crystals. *Phys. Rev.*, 70:954–964, Dec 1946.
- [50] J. M. Luttinger. A Note on the Ground State in Antiferromagnetics. *Phys. Rev.*, 81:1015–1018, Mar 1951.
- [51] D. Litvin. The Luttinger-Tisza method. *Physica*, 77(2):205–219, Oct 1974.
- [52] T. Okubo, S. Chung, and H. Kawamura. Multiple- q States and the Skyrmion Lattice of the Triangular-Lattice Heisenberg Antiferromagnet under Magnetic Fields. *Phys. Rev. Lett.*, 108:017206, Jan 2012.
- [53] C. Mudry. *Lecture Notes on Field Theory in Condensed Matter Physics*. World Scientific Publishing Company, Singapore, 2014.
- [54] N. Ashcroft and N. Mermin. *Festkörperphysik*. De Gruyter, Oldenburg, 2001.
- [55] Y. Nambu. Quasi-Particles and Gauge Invariance in the Theory of Superconductivity. *Phys. Rev.*, 117:648–663, Feb 1960.
- [56] J. Goldstone. Field theories with “Superconductor” solutions. *Il Nuovo Cimento*, 19(1):154–164, Jan 1961.
- [57] J. Goldstone, A. Salam, and S. Weinberg. Broken Symmetries. *Phys. Rev.*, 127:965–970, Aug 1962.
- [58] A. Auerbach. *Interacting Electrons and Quantum Magnetism*. Springer, New York, 1994.
- [59] N. Majlis. *The Quantum Theory of Magnetism*. World Scientific Publishing, Philadelphia, 2007.
- [60] F. J. Dyson. General Theory of Spin-Wave Interactions. *Phys. Rev.*, 102:1217–1230, Jun 1956.
- [61] E. Rastelli. *Statistical Mechanics of Magnetic Excitations*. World Scientific Publishing, Philadelphia, Nov 2011.
- [62] T. Holstein and H. Primakoff. Field Dependence of the Intrinsic Domain Magnetization of a Ferromagnet. *Phys. Rev.*, 58:1098–1113, Dec 1940.
- [63] P. Mohn. *Magnetism in the Solid State: An Introduction*. Springer Series in Solid-State Sciences. Springer, Berlin, 2002.

Bibliography

- [64] N. N. Bogoljubov. On a new method in the theory of superconductivity. *Il Nuovo Cimento*, 7(6):794–805, Mar 1958.
- [65] J. G. Valatin. Comments on the theory of superconductivity. *Il Nuovo Cimento*, 7(6):843–857, Mar 1958.
- [66] R. M. White, M. Sparks, and I. Ortenburger. Diagonalization of the Antiferromagnetic Magnon-Phonon Interaction. *Phys. Rev.*, 139:A450–A454, Jul 1965.
- [67] Y. Aharonov and D. Bohm. Significance of Electromagnetic Potentials in the Quantum Theory. *Phys. Rev.*, 115:485–491, Aug 1959.
- [68] Y. Aharonov and J. Anandan. Phase change during a cyclic quantum evolution. *Phys. Rev. Lett.*, 58:1593–1596, Apr 1987.
- [69] C. L. Kane and E. J. Mele. Quantum Spin Hall Effect in Graphene. *Phys. Rev. Lett.*, 95:226801, Nov 2005.
- [70] H. Hasan and C. Kane. Colloquium: Topological insulators. *Rev. Mod. Phys.*, 82:3045, 2010.
- [71] T. Schulz, R. Ritz, A. Bauer, M. Halder, M. Wagner, C. Franz, C. Pfleiderer, K. Everschor, M. Garst, and A. Rosch. Emergent electrodynamics of skyrmions in a chiral magnet. *Nature Physics*, 8(4):301304, Feb 2012.
- [72] K. Everschor-Sitte and M. Sitte. Real-space Berry phases: Skyrmion soccer (invited). *Journal of Applied Physics*, 115(17):172602, May 2014.
- [73] A. A. Kovalev. Skyrmionic spin Seebeck effect via dissipative thermomagnonic torques. *Phys. Rev. B*, 89:241101, Jun 2014.
- [74] S. T. Bramwell. Spin Ice State in Frustrated Magnetic Pyrochlore Materials. *Science*, 294(5546):1495–1501, Nov 2001.
- [75] C. Castelnovo, R. Moessner, and S. L. Sondhi. Magnetic monopoles in spin ice. *Nature*, 451(7174):42–45, Jan 2008.
- [76] L. Savary and L. Balents. Quantum spin liquids: a review. *Reports on Progress in Physics*, 80(1):016502, Nov 2016.
- [77] J. K. Asbóth, L. Oroszlány, and A. Pályi. A Short Course on Topological Insulators. *Lecture Notes in Physics*, 2016.
- [78] D. Xiao, M.-C. Chang, and Q. Niu. Berry phase effects on electronic properties. *Rev. Mod. Phys.*, 82:1959–2007, Jul 2010.
- [79] M. Fruchart and D. Carpentier. An introduction to topological insulators. *Comptes Rendus Physique*, 14(9-10):779–815, Nov 2013.
- [80] J. Cayssol. Introduction to Dirac materials and topological insulators. *Comptes Rendus Physique*, 14(9-10):760–778, Nov 2013.
- [81] C. Kane. *Topological Band Theory and the Z_2 Invariant*. Elsevier, Oxford, 2013.
- [82] Y. Hatsugai. Edge states in the integer quantum Hall effect and the Riemann surface of the Bloch function. *Physical Review B*, 48(16):11851–11862, Oct 1993.
- [83] Y. Hatsugai. Chern number and edge states in the integer quantum Hall effect. *Physical Review Letters*, 71(22):3697–3700, Nov 1993.
- [84] S. A. Owerre. A first theoretical realization of honeycomb topological magnon insulator. *J. Phys.: Condens. Matter*, 28(38):386001, Jul 2016.

- [85] J. Fransson, A. M. Black-Schaffer, and A. V. Balatsky. Magnon Dirac materials. *Phys. Rev. B*, 94:075401, Aug 2016.
- [86] S. K. Kim, H. Ochoa, R. Zarzuela, and Y. Tserkovnyak. Realization of the Haldane-Kane-Mele Model in a System of Localized Spins. *Phys. Rev. Lett.*, 117:227201, Nov 2016.
- [87] A. A. Kovalev, V. A. Zyuzin, and B. Li. Pumping of magnons in a Dzyaloshinskii-Moriya ferromagnet. *Phys. Rev. B*, 95:165106, Apr 2017.
- [88] G. Jotzu, M. Messer, R. Desbuquois, M. Lebrat, T. Uehlinger, D. Greif, and T. Esslinger. Experimental realization of the topological Haldane model with ultracold fermions. *Nature*, 515(7526):237–240, Nov 2014.
- [89] R. Chisnell, J. S. Helton, D. E. Freedman, D. K. Singh, R. I. Bewley, D. G. Nocera, and Y. S. Lee. Topological Magnon Bands in a Kagome Lattice Ferromagnet. *Phys. Rev. Lett.*, 115:147201, Sep 2015.
- [90] S. A. Owerre. Topological thermal Hall effect in frustrated kagome antiferromagnets. *Phys. Rev. B*, 95:014422, Jan 2017.
- [91] B. Singh, A. Sharma, H. Lin, M. Z. Hasan, R. Prasad, and A. Bansil. Topological electronic structure and Weyl semimetal in the TlBiSe₂ class of semiconductors. *Phys. Rev. B*, 86:115208, Sep 2012.
- [92] S.-M. Huang, S.-Y. Xu, I. Belopolski, C.-C. Lee, G. Chang, B. Wang, N. Alidoust, G. Bian, M. Neupane, C. Zhang, and et al. A Weyl Fermion semimetal with surface Fermi arcs in the transition metal monopnictide TaAs class. *Nature Communications*, 6:7373, Jun 2015.
- [93] H. Weng, C. Fang, Z. Fang, B. A. Bernevig, and X. Dai. Weyl Semimetal Phase in Noncentrosymmetric Transition-Metal Monophosphides. *Phys. Rev. X*, 5:011029, Mar 2015.
- [94] S.-Y. Xu, I. Belopolski, N. Alidoust, M. Neupane, G. Bian, C. Zhang, R. Sankar, G. Chang, Z. Yuan, C.-C. Lee, and et al. Discovery of a Weyl fermion semimetal and topological Fermi arcs. *Science*, 349(6248):613–617, Jul 2015.
- [95] B. Q. Lv, H. M. Weng, B. B. Fu, X. P. Wang, H. Miao, J. Ma, P. Richard, X. C. Huang, L. X. Zhao, G. F. Chen, Z. Fang, X. Dai, T. Qian, and H. Ding. Experimental Discovery of Weyl Semimetal TaAs. *Phys. Rev. X*, 5:031013, Jul 2015.
- [96] C. Fang, H. Weng, X. Dai, and Z. Fang. Topological nodal line semimetals. *Chinese Physics B*, 25(11):117106, 2016.
- [97] H. Huang, J. Liu, D. Vanderbilt, and W. Duan. Topological nodal-line semimetals in alkaline-earth stannides, germanides, and silicides. *Phys. Rev. B*, 93:201114, May 2016.
- [98] G. Xu, H. Weng, Z. Wang, X. Dai, and Z. Fang. Chern Semimetal and the Quantized Anomalous Hall Effect in HgCr₂Se₄. *Phys. Rev. Lett.*, 107:186806, Oct 2011.
- [99] C. Fang, Y. Chen, H.-Y. Kee, and L. Fu. Topological nodal line semimetals with and without spin-orbital coupling. *Phys. Rev. B*, 92:081201, Aug 2015.
- [100] G. Bian, T.-R. Chang, R. Sankar, S.-Y. Xu, H. Zheng, T. Neupert, C.-K. Chiu, S.-M. Huang, G. Chang, I. Belopolski, and et al. Topological nodal-line fermions in spin-orbit metal PbTaSe₂. *Nature Communications*, 7:10556, Feb 2016.
- [101] L. M. Schoop, M. N. Ali, C. Straer, A. Topp, A. Varykhalov, D. Marchenko, V. Duppel, S. S. P. Parkin, B. V. Lotsch, and C. R. Ast. Dirac cone protected by non-symmorphic symmetry and three-dimensional Dirac line node in ZrSiS. *Nature Communications*, 7:11696, May 2016.
- [102] L. Fu. Topological Crystalline Insulators. *Phys. Rev. Lett.*, 106:106802, Mar 2011.

Bibliography

- [103] Z. Wang, A. Alexandradinata, R. J. Cava, and B. A. Bernevig. Hourglass fermions. *Nature*, 532(7598):189–194, Apr 2016.
- [104] S. M. Young, S. Zaheer, J. C. Y. Teo, C. L. Kane, E. J. Mele, and A. M. Rappe. Dirac Semimetal in Three Dimensions. *Phys. Rev. Lett.*, 108:140405, Apr 2012.
- [105] E. H. Hall. On a New Action of the Magnet on Electric Currents. *American Journal of Mathematics*, 2(3):287, Sep 1879.
- [106] R. Karplus and J. M. Luttinger. Hall Effect in Ferromagnetics. *Phys. Rev.*, 95:1154–1160, Sep 1954.
- [107] C. Cercignani. *The Boltzmann Equation and Its Applications*. Springer, New York, 1988.
- [108] J. Callaway. *Quantum Theory of the Solid State*. Academic Press, London, 1974.
- [109] D. M. Rowe. *CRC Handbook of Thermoelectrics*. Informa UK, Boca Raton, Jul 1995.
- [110] R. Kubo. Statistical-Mechanical Theory of Irreversible Processes. I. General Theory and Simple Applications to Magnetic and Conduction Problems. *Journal of the Physical Society of Japan*, 12(6):570–586, Jun 1957.
- [111] E. S. R. Gopal. *Statistical Mechanics and Properties of Matter; Theory and Applications*. Ellis Horwood, Hemel Hempstead, 1974.
- [112] L. Onsager. Reciprocal Relations in Irreversible Processes. I. *Phys. Rev.*, 37:405–426, Feb 1931.
- [113] Y. Aharonov and A. Casher. Topological Quantum Effects for Neutral Particles. *Phys. Rev. Lett.*, 53:319–321, Jul 1984.
- [114] S. M. Al-Jaber, X. Zhu, and W. C. Henneberger. Interaction of a moving magnetic dipole with a static electric field. *European Journal of Physics*, 12(6):268, 1991.
- [115] J. Anandan. Electromagnetic effects in the quantum interference of dipoles. *Physics Letters A*, 138(8):347–352, 1989.
- [116] F. Meier and D. Loss. Magnetization Transport and Quantized Spin Conductance. *Phys. Rev. Lett.*, 90:167204, Apr 2003.
- [117] A. A. Kovalev and Y. Tserkovnyak. Thermomagnonic spin transfer and Peltier effects in insulating magnets. *EPL (Europhysics Letters)*, 97(6):67002, 2012.
- [118] V. Basso, E. Ferraro, and M. Piazza. Thermodynamic transport theory of spin waves in ferromagnetic insulators. *Phys. Rev. B*, 94:144422, Oct 2016.
- [119] D. Xiao, Y. Yao, Z. Fang, and Q. Niu. Berry-Phase Effect in Anomalous Thermoelectric Transport. *Phys. Rev. Lett.*, 97:026603, Jul 2006.
- [120] D. L. Bergman and V. Oganessian. Theory of Dissipationless Nernst Effects. *Phys. Rev. Lett.*, 104:066601, Feb 2010.
- [121] T. Yokoyama and S. Murakami. Transverse magnetic heat transport on the surface of a topological insulator. *Phys. Rev. B*, 83:161407, Apr 2011.
- [122] H. Lee, J. H. Han, and P. A. Lee. Thermal Hall effect of spins in a paramagnet. *Phys. Rev. B*, 91:125413, Mar 2015.
- [123] S. Fujimoto. Hall Effect of Spin Waves in Frustrated Magnets. *Phys. Rev. Lett.*, 103:047203, Jul 2009.
- [124] M. Hirschberger, J. W. Krizan, R. J. Cava, and N. P. Ong. Large thermal Hall conductivity of neutral spin excitations in a frustrated quantum magnet. *Science*, 348(6230):106–109, Apr 2015.

- [125] I. Sodemann and L. Fu. Quantum Nonlinear Hall Effect Induced by Berry Curvature Dipole in Time-Reversal Invariant Materials. *Phys. Rev. Lett.*, 115:216806, Nov 2015.
- [126] K. Nakata, J. Klinovaja, and D. Loss. Magnonic quantum Hall effect and Wiedemann-Franz law. *Phys. Rev. B*, 95:125429, Mar 2017.
- [127] B. Xu, T. Ohtsuki, and R. Shindou. Integer quantum magnon Hall plateau-plateau transition in a spin-ice model. *Phys. Rev. B*, 94:220403, Dec 2016.
- [128] K. A. van Hoogdalem, Y. Tserkovnyak, and D. Loss. Magnetic texture-induced thermal Hall effects. *Phys. Rev. B*, 87:024402, Jan 2013.
- [129] S. A. Owerre. Magnon Hall effect in AB-stacked bilayer honeycomb quantum magnets. *Phys. Rev. B*, 94:094405, Sep 2016.
- [130] R. Cheng, S. Okamoto, and D. Xiao. Spin Nernst Effect of Magnons in Collinear Antiferromagnets. *Phys. Rev. Lett.*, 117:217202, Nov 2016.
- [131] A. A. Kovalev and V. Zyuzin. Spin torque and Nernst effects in Dzyaloshinskii-Moriya ferromagnets. *Phys. Rev. B*, 93:161106, Apr 2016.
- [132] T. H. R. Skyrme. A Non-Linear Theory of Strong Interactions. *Proceedings of the Royal Society A: Mathematical, Physical and Engineering Sciences*, 247(1249):260–278, Sep 1958.
- [133] T. H. R. Skyrme. A Unified Model of K- and Formula-mesons. *Proceedings of the Royal Society A: Mathematical, Physical and Engineering Sciences*, 252(1269):236–245, Sep 1959.
- [134] T. H. R. Skyrme. A Non-Linear Field Theory. *Proceedings of the Royal Society A: Mathematical, Physical and Engineering Sciences*, 260(1300):127–138, Feb 1961.
- [135] T. H. R. Skyrme. Particle States of a Quantized Meson Field. *Proceedings of the Royal Society A: Mathematical, Physical and Engineering Sciences*, 262(1309):237–245, Jul 1961.
- [136] A. N. Bogdanov and D. A. Yablonskii. Thermodynamically stable “vortices” in magnetically ordered crystals. The mixed state of magnets. *Zh. Eksp. Teor. Fiz.*, 95:178, 1989.
- [137] S. Mühlbauer, B. Binz, F. Jonietz, C. Pfleiderer, A. Rosch, A. Neubauer, R. Georgii, and P. Boni. Skyrmion Lattice in a Chiral Magnet. *Science*, 323(5916):915–919, Feb 2009.
- [138] S. Seki, X. Z. Yu, S. Ishiwata, and Y. Tokura. Observation of Skyrmions in a Multiferroic Material. *Science*, 336(6078):198–201, Apr 2012.
- [139] N. Nagaosa and Y. Tokura. Topological properties and dynamics of magnetic skyrmions. *Nature Nanotechnology*, 8(12):899–911, 2013.
- [140] G. Catalan, J. Seidel, R. Ramesh, and J. F. Scott. Domain wall nanoelectronics. *Rev. Mod. Phys.*, 84:119–156, 2012.
- [141] I. Kézsmárki, S. Bordács, P. Milde, E. Neuber, L. M. Eng, J. S. White, H. M. Rønnow, C. D. Dewhurst, M. Mochizuki, K. Yanai, and et al. Néel-type skyrmion lattice with confined orientation in the polar magnetic semiconductor GaV4S8. *Nature Materials*, 14(11):1116–1122, Sep 2015.
- [142] W. Koshibae and N. Nagaosa. Theory of antiskyrmions in magnets. *Nature Communications*, 7:10542, 2016.
- [143] R. Bamler. *Phase-Space Berry Phases in Chiral Magnets: Skyrmion Charge, Hall Effect, and Dynamics of Magnetic Skyrmions*. PhD thesis, University of Cologne, 2016.
- [144] A. Neubauer, C. Pfleiderer, B. Binz, A. Rosch, R. Ritz, P. G. Niklowitz, and P. Böni. Topological Hall Effect in the A Phase of MnSi. *Phys. Rev. Lett.*, 102:186602, May 2009.

Bibliography

- [145] V. K. Dugaev, P. Bruno, B. Canals, and C. Lacroix. Berry phase of magnons in textured ferromagnets. *Phys. Rev. B*, 72:024456, Jul 2005.
- [146] M. Mochizuki, X. Z. Yu, S. Seki, N. Kanazawa, W. Koshibae, J. Zang, M. Mostovoy, Y. Tokura, and N. Nagaosa. Thermally driven ratchet motion of a skyrmion microcrystal and topological magnon Hall effect. *Nature Materials*, 13(3):241–246, Jan 2014.
- [147] J. Iwasaki, A. J. Beekman, and N. Nagaosa. Theory of magnon-skyrmion scattering in chiral magnets. *Phys. Rev. B*, 89:064412, Feb 2014.
- [148] C. Schütte and M. Garst. Magnon-skyrmion scattering in chiral magnets. *Phys. Rev. B*, 90:094423, Sep 2014.
- [149] Y.-T. Oh, H. Lee, J.-H. Park, and J. H. Han. Dynamics of magnon fluid in Dzyaloshinskii-Moriya magnet and its manifestation in magnon-Skyrmion scattering. *Phys. Rev. B*, 91:104435, Mar 2015.
- [150] J. Henk and W. Schattke. A subroutine package for computing Greens functions of relaxed surfaces by the renormalization method. *Comp. Phys. Commun.*, 77(1):69–83, Sep 1993.
- [151] A. Bödicker, W. Schattke, J. Henk, and R. Feder. Interface electronic structure by the renormalization method: theory and application to Sb/GaAs. *J. Phys.: Condens. Matter*, 6(10):1927–1940, Mar 1994.
- [152] D. P. Landau and K. Binder. *A Guide to Monte Carlo Simulations in Statistical Physics*. Cambridge University Press, Cambridge, 2009.
- [153] N. Metropolis, A. W. Rosenbluth, M. N. Rosenbluth, A. H. Teller, and E. Teller. Equation of State Calculations by Fast Computing Machines. *The Journal of Chemical Physics*, 21(6):1087–1092, 1953.
- [154] M. Creutz. Overrelaxation and Monte Carlo simulation. *Physical Review D*, 36(2):515–519, Jul 1987.
- [155] B. Göbel. Topologische Eigenschaften von Skyrmionen. *Master Thesis, Martin Luther University of Halle-Wittenberg*, 2016.
- [156] U. Nowak, R. W. Chantrell, and E. C. Kennedy. Monte Carlo Simulation with Time Step Quantification in Terms of Langevin Dynamics. *Phys. Rev. Lett.*, 84:163–166, Jan 2000.
- [157] X. Z. Cheng, M. B. A. Jalil, and H. K. Lee. Time-quantified Monte Carlo algorithm for interacting spin array micromagnetic dynamics. *Phys. Rev. B*, 73:224438, Jun 2006.
- [158] M. d’ Aquino, C. Serpico, G. Coppola, I. D. Mayergoyz, and G. Bertotti. Midpoint numerical technique for stochastic Landau-Lifshitz-Gilbert dynamics. *Journal of Applied Physics*, 99(8):08B905, Apr 2006.
- [159] B. Skubic, J. Hellsvik, L. Nordström, and O. Eriksson. A method for atomistic spin dynamics simulations: implementation and examples. *Journal of Physics: Condensed Matter*, 20(31):315203, 2008.
- [160] G. Bertotti, I. Mayergoyz, and C. Serpico. *Nonlinear Magnetization Dynamics in Nanosystems*. Elsevier, Oxford, 2009.
- [161] M. Lakshmanan. The fascinating world of the Landau-Lifshitz-Gilbert equation: an overview. *Philosophical Transactions of the Royal Society A: Mathematical, Physical and Engineering Sciences*, 369(1939):1280–1300, Feb 2011.
- [162] M. O. A. Ellis, R. F. L. Evans, T. A. Ostler, J. Barker, U. Atxitia, O. Chubykalo-Fesenko, and R. W. Chantrell. The Landau-Lifshitz equation in atomistic models. *Low Temperature Physics*, 41(9):705–712, Sep 2015.
- [163] T. Gerhardt. *Micromagnetic Simulations of Ferromagnetic Domain Walls in Nanowires*. PhD thesis, University of Hamburg, 2014.

- [164] T. Gilbert. Abstracts of Papers to be Presented at the 1955 Thanksgiving Meeting at the University of Chicago, Chicago, Illinois, November 25 and 26, 1955. *Phys. Rev.*, 100:1235–1235, Nov 1955.
- [165] T. Gilbert. Classics in Magnetism A Phenomenological Theory of Damping in Ferromagnetic Materials. *IEEE Transactions on Magnetics*, 40(6):3443–3449, Nov 2004.
- [166] L. D. Landau and E. M. Lifshitz. Theory of the dispersion of magnetic permeability in ferromagnetic bodies. *Phys. Z. Sowjetunion*, 8:153, 1935.
- [167] K. Capelle and B. L. Gyorffy. Exploring dynamical magnetism with time-dependent density-functional theory: From spin fluctuations to Gilbert damping. *Europhysics Letters (EPL)*, 61(3):354–360, Feb 2003.
- [168] R. Wieser. Description of a dissipative quantum spin dynamics with a Landau-Lifshitz/Gilbert like damping and complete derivation of the classical Landau-Lifshitz equation. *The European Physical Journal B*, 88(3), Mar 2015.
- [169] W. F. Brown. Thermal Fluctuations of a Single-Domain Particle. *Phys. Rev.*, 130:1677–1686, Jun 1963.
- [170] J. Hellsvik. *Atomistic Spin Dynamics, Theory and Applications*. PhD thesis, Uppsala University, Materials Theory, 2010.
- [171] C. Gardiner. *Handbook of Stochastic Methods for Physics, Chemistry and the Natural Sciences*. Springer, Berlin, 2004.
- [172] B. Skubic. *Spin Dynamics and Magnetic Multilayers*. PhD thesis, Uppsala University, Department of Physics, 2007.
- [173] D. A. Garanin. Self-consistent Gaussian approximation for classical spin systems: Thermodynamics. *Phys. Rev. B*, 53:11593–11605, May 1996.
- [174] R. E. Watson, M. Blume, and G. H. Vineyard. Spin Motions in a Classical Ferromagnet. *Phys. Rev.*, 181:811–823, May 1969.
- [175] P. Peczak, A. M. Ferrenberg, and D. P. Landau. High-accuracy Monte Carlo study of the three-dimensional classical Heisenberg ferromagnet. *Phys. Rev. B*, 43:6087–6093, Mar 1991.
- [176] C. Holm and W. Janke. Critical exponents of the classical three-dimensional Heisenberg model: A single-cluster Monte Carlo study. *Phys. Rev. B*, 48:936–950, Jul 1993.
- [177] S. A. Owerre. Magnonic Dirac Semimetal in Quantum Magnets. *arXiv:1610.08869*, October 2016.
- [178] F.-Y. Li, Y.-D. Li, Y. B. Kim, L. Balents, Y. Yu, and G. Chen. Weyl magnons in breathing pyrochlore antiferromagnets. *Nature Communications*, 7:12691, Sep 2016.
- [179] T. Ideue, Y. Onose, H. Katsura, Y. Shiomi, S. Ishiwata, N. Nagaosa, and Y. Tokura. Effect of lattice geometry on magnon Hall effect in ferromagnetic insulators. *Phys. Rev. B*, 85(13):134411, Apr 2012.
- [180] A. L. Chernyshev and P. A. Maksimov. Damped Topological Magnons in the Kagome-Lattice Ferromagnets. *Phys. Rev. Lett.*, 117:187203, Oct 2016.
- [181] Y. Kim, B. J. Wieder, C. L. Kane, and A. M. Rappe. Dirac Line Nodes in Inversion-Symmetric Crystals. *Phys. Rev. Lett.*, 115:036806, Jul 2015.
- [182] A. V. Savin, G. P. Tsironis, and X. Zotos. Thermal conductivity of a classical one-dimensional Heisenberg spin model. *Phys. Rev. B*, 72:140402, Oct 2005.
- [183] M. Tuckerman. *Statistical Mechanics: Theory and Molecular Simulation*. Oxford University Press, Oxford, 2010.

Bibliography

- [184] B. Jenčič and P. Prelovšek. Spin and thermal conductivity in a classical disordered spin chain. *Phys. Rev. B*, 92:134305, Oct 2015.
- [185] M. Hirschberger, R. Chisnell, Y. S. Lee, and N. P. Ong. Thermal Hall Effect of Spin Excitations in a Kagome Magnet. *Phys. Rev. Lett.*, 115:106603, Sep 2015.
- [186] A. Roldán-Molina, A. S. Nunez, and J. Fernández-Rossier. Topological spin waves in the atomic-scale magnetic skyrmion crystal. *New Journal of Physics*, 18(4):045015, 2016.
- [187] C. Herschbach, D. V. Fedorov, M. Gradhand, and I. Mertig. Colossal spin Hall effect in ultrathin metallic films. *Phys. Rev. B*, 90:180406, Nov 2014.
- [188] J. A. Belward, I. W. Turner, and M. Ili. On derivative estimation and the solution of least squares problems. *Journal of Computational and Applied Mathematics*, 222(2):511–523, 2008.

LIST OF PUBLICATIONS

- A. Mook, J. Henk, and I. Mertig
Magnon Hall effect and topology in kagome lattices: A theoretical investigation
Physical Review B **89**, 134409 (2014).
- A. Mook, J. Henk, and I. Mertig
Edge states in topological magnon insulators
Physical Review B **90**, 024412 (2014).
- A. Mook, J. Henk, and I. Mertig
Topologically nontrivial magnons at an interface of two kagome ferromagnets
Physical Review B **91**, 224411 (2015).
- A. Mook, J. Henk, and I. Mertig
Magnon waveguide with nanoscale confinement constructed from topological magnon insulators
Physical Review B **91**, 174409 (2015).
- A. Mook, J. Henk, and I. Mertig
Tunable magnon Weyl points in ferromagnetic pyrochlores
Physical Review Letters **117**, 157204 (2016).
- A. Mook, J. Henk, and I. Mertig
Topological Magnon Insulators: Chern numbers and surface magnons
Proceedings SPIE 9931, Spintronics IX, 993134 (2016).
- A. Mook, J. Henk, and I. Mertig
Spin dynamics simulations of topological magnon insulators: From transverse current correlation functions to the family of magnon Hall effects
Physical Review B **94**, 174444 (2016).
- A. Mook, B. Göbel, J. Henk, and I. Mertig
Magnon transport in noncollinear spin textures: Anisotropies and topological magnon Hall effects
Physical Review B Rapid Communications **95**, 020401(R) (2017).
- A. Mook, J. Henk, and I. Mertig
Magnon nodal-line semimetals and drumhead surface states in anisotropic pyrochlore ferromagnets
Physical Review B **95**, 014418 (2017).
- B. Göbel, A. Mook, J. Henk, and I. Mertig
Unconventional topological Hall effect in skyrmion crystals caused by the topology of the lattice
Physical Review B **95**, 094413 (2017).
- B. Göbel, A. Mook, J. Henk, and I. Mertig
Signatures of Lattice Geometry in Quantum and Topological Hall Effect
Preprint on arXiv:1704.00567, submitted to the New Journal of Physics (2017).

Personal Information

Name Alexander Mook
Sex Male
Birth October 26, 1989 in Magdeburg, Germany
Nationality German
Address Robert-Franz-Ring 8
 06108 Halle (Saale), Germany

Education

since 11/2013 PhD studies at the “Max Planck Institute of Microstructure Physics”, Halle (Saale) and the “Martin Luther University Halle-Wittenberg”, Halle (Saale)
Supervisor: Prof. Dr. Ingrid Mertig

10/2011 – 11/2013 Study of Physics at the “Martin Luther University Halle-Wittenberg”, Halle (Saale)
 Master thesis: “Magnon Hall Effect”
 Master’s degree (M.Sc., final grade: 1.0)

10/2008 – 09/2011 Study of Physics at the “Martin Luther University Halle-Wittenberg”, Halle (Saale)
 Bachelor thesis: “Intrinsic Anomalous Hall Effect as a Fermi surface property”
 Bachelor’s degree (B.Sc., final grade: 1.3)

08/2000 – 07/2008 High school, “Werner-von-Siemens-Gymnasium”, Magdeburg

08/1996 – 07/2000 Elementary school, “Wilhelm-Weitling-Grundschule”, Magdeburg

Academic Career

since 11/2013 Research Assistant at the “Max Planck Institute of Microstructure Physics”, Halle (Saale) and the “Martin Luther University Halle-Wittenberg”, Halle (Saale)
 in the group of Prof. Dr. Ingrid Mertig

10/2011 – 10/2013 Student Assistant at the “Martin Luther University Halle-Wittenberg”, Halle (Saale)
 in the group of Prof. Dr. Ingrid Mertig

EIDESSTATTLICHE ERKLÄRUNG

Hiermit erkläre ich, Alexander Mook, gemäß §5 der Promotionsordnung der Naturwissenschaftlichen Fakultäten I, II und III der Martin-Luther-Universität Halle-Wittenberg die vorliegende Arbeit *Topological Magnon Materials and Transverse Magnon Transport* selbständig und ohne fremde Hilfe verfasst, keine anderen als die von mir angegebenen Quellen und Hilfsmittel benutzt und die den benutzten Werken wörtlich oder inhaltlich entnommenen Stellen als solche kenntlich gemacht zu haben. Ich erkläre, die Angaben wahrheitsgemäß gemacht, keine vergeblichen Promotionsversuche unternommen und keine Dissertation an einer anderen wissenschaftlichen Einrichtung zur Erlangung eines akademischen Grades eingereicht zu haben. Ich bin weder vorbestraft noch sind gegen mich Ermittlungsverfahren anhängig.

Halle (Saale), October 16, 2017
Alexander Mook